Characterisation and phononic image reconstruction of gold nanorods

Shakila Naznin

A thesis presented for the degree of
Doctor of Philosophy

Faculty of Engineering
The University of Nottingham

May 2023

I would like to dedicate this thesis to the people who lost their lives due to COVID-19.

Acknowledgements

Abstract

The optical and mechanical properties of metal nanoparticles depend mostly on their sizes and shapes. However, a non-destructive size characterisation technique for metal nanoparticles which can work in any external environment with high precision is currently unavailable. It is well known that optical microscopy is diffraction limited which means that two close objects are not resolvable because of the bending of light waves while passing through small apertures. The resolution of an optical system is limited to a few hundred nanometres for visible wavelengths, even using the highest available numerical aperture (1.4). This PhD research focused on both these problems: the unavailability of a precise and non-destructive size characterisation technique for metal nanoparticles applicable for all environments and the resolution limit of optical microscopy.

In this PhD work, size, orientation, and location of gold nanorods were determined to reconstruct their acoustic or phononic images in both air and water media by using time-resolved pump-probe picosecond ultrasonics. Metal nanoparticles are of sub-optical dimensions and a large number of them can be placed inside the same optical point spread function. Using acoustic frequencies and orientation differences of gold nanorods, it was possible to separate and image them, even inside the same optical point spread function.

The approach involved the exploitation of gold nanorods as optoacoustic transducers when they were excited by focused circularly polarised femtosecond optical pump pulses. They became hot and vibrated due to the created stress, producing acoustic waves in the GHz range. Circularly polarised focused probe pulses were transmitted through them, and the modulation of the scattered probe light intensity caused by the vibration was used to determine their vibrational frequencies. These vibrational frequencies were then converted into sizes by using an established analytical model developed by Hu et al. (2003). A polarisation-controlled detection system was developed to change the polarisation of the probe light to determine the orientation of the rod. The nanorods were scanned spatially during the experiments and later an amplitude map of the scanned area at the frequency of the rod was extracted. Then, the centroid algorithm was applied to find the location of the rod. Experimental parameters such as pump and probe wavelengths were estimated by simulating the optical and mechanical responses of gold nanorods. A non-commercial Matlab code package SMARTIES and a commercial finite element model

tool COMSOL Multiphysics were used to simulate the optical response of gold nanorods in specific external environments. The mechanical responses of gold nanorods were simulated by using an established analytical model developed by Hu et al. (2003) and finite element models designed by using COMSOL Multiphysics.

In this thesis, it was found that the characterised sizes of gold nanorods in both air and water media were close to the sizes measured from the scanning electron microscopy (SEM) images. Obtained worst-case length and width precisions were approximately 1 nm and 0.3 nm compared to SEM measurements, respectively. The size characterisation results presented in this thesis showed that the worst case SEM precision was ± 36 nm. However, the SEM measurement was a function of human error because measurements were done manually from the pixels of the SEM images. In addition, the precision of SEM measurements also depends on the setting of the machine, noise, magnification, contrast, and aberration, among others. The reconstructed acoustic images of gold nanorods also matched reasonably well with the SEM images. Obtained minimum location and angle precisions were 2 nm and $0.4°$, respectively. The result presented in this thesis showed that the minimum angle precision was $\pm 7°$ from SEM. The results showed that the proposed technique was in good agreement with the SEM.

The proposed technique can work with high precision in any external medium without requiring a vacuum environment and conductive surface. Its applicability to the water environment also suggests that the technique can be used in bio-environments. Hence, the technique is simple, non-destructive and ideal for imaging living specimens.

The motivation behind this PhD research was to help make progress towards a phonon-based super-resolution imaging technique in biology. Although imaging biological nanostructures using gold nanorods was out of the scope of this PhD work, the achievements of the present work are significant steps towards offering a phonon based super-resolution imaging technique that can image biological nanostructures.

Achievements

During my PhD, I have some publications with my group which are described below:

1. Rafael Fuentes-Domínguez, **Shakila Naznin**, Salvatore La Cavera III, Richard Cousins, Fernando Pérez-Cota, Richard J. Smith, and Matt Clark. Polarization sensitive super-resolution phononic reconstruction of nanostructures. *ACS Photonics*, 9(6): 1919-1925, 2022.

2. Rafael Fuentes-Domínguez, **Shakila Naznin**, Leonel Marques, Fernando Pérez-Cota, Richard J. Smith, and Matt Clark. Characterising the size and shape of metallic nano-structures by their acoustic vibrations. *Nanoscale*, 12(26):14230-14236, 2020.

3. Fernando Pérez-Cota, Salvatore La Cavera III, **Shakila Naznin**, Rafael Fuentes-Domínguez, Richard J. Smith, and Matt Clark. Apparent attenuation by opto-acoustic defocus in phonon microscopy. *Photoacoustics*, 19:100180, 2020.

4. Fernando Pérez-Cota, Rafael Fuentes-Domínguez, Salvatore La Cavera III, William Hardiman, Mengting Yao, Kerry Setchfield, Emilia Moradi, **Shakila Naznin**, Amanda Wright, Kevin F Webb, et al. Picosecond ultrasonics for elasticity-based imaging and characterisation of biological cells. Journal of Applied Physics, 128(16):160902, 2020.

5. Fuentes-Domínguez, Rafael, Fernando Pérez-Cota, **Shakila Naznin**, Leonel Marques, Richard J. Smith, and Matt Clark. "Nano ultrasonic measurements of nanoparticles." In AIP Conference Proceedings, 2102 (1), p. 020027. AIP Publishing LLC, 2019.

6. Rafael Fuentes-Domínguez, Fernando Pérez-Cota, **Shakila Naznin**, Richard J. Smith, and Matt Clark. Super resolution imaging using nano-bells. *Scientific reports*, 8(1):1-9, 2018.

Oral Presentations titled 'Gold nanorod opto-acoustic transducer'

1. Shakila Naznin, Rafael Fuentes-Domínguez, Fernando Pérez-Cota, Richard J. Smith, and Matt Clark. International congress on ultrasonics (ICU), 3-6 September 2019, VIVES, Brugges, Belgium.

2. Shakila Naznin, Rafael Fuentes-Domínguez, Fernando Pérez-Cota, Richard J. Smith, and Matt Clark. RCNDE ESR event 8-10 July, 2019, Imperial College London, UK.

3. Shakila Naznin, Rafael Fuentes-Domínguez, Fernando Pérez-Cota, Richard J. Smith, and Matt Clark. Annual CDT conference, 1st May, 2018, Manchester, UK.

4. Shakila Naznin, Rafael Fuentes-Domínguez, Fernando Pérez-Cota, Richard J. Smith, and Matt Clark. Laser Ultrasonics, 9-13 July 2018, University of Nottingham, Nottingham, UK.

5. Shakila Naznin, Rafael Fuentes-Domínguez, Fernando Pérez-Cota, Richard J. Smith, and Matt Clark. Optics+Ultrasound IV, 23 Nov 2017, University of Strathclyde, UK.

6. Shakila Naznin, Rafael Fuentes-Domínguez, Fernando Pérez-Cota, Richard J. Smith, and Matt Clark. Lunchtime Seminar (2017, 2018, 2020), Optics and Photonics group, University of Nottingham, UK.

Contents

List of Figures

Chapter 1

Introduction

This chapter describes the background problems on which this PhD project is focussed. Also, the motivation, aim and objectives of this research work are mentioned. In addition, the whole thesis structure is presented. This chapter clearly portrays the existing problems and the significance of this research.

1.1   Problem statement and motivation

This PhD research focused on two research problems. One of them was the unavailability of a precise and non-destructive size characterisation technique for metal nanoparticles that can work in any external environment. Metal nanoparticles have been of special interest for decades because of their different attractive properties that can be used in different applications such as sensing [1–4], photothermal therapy [5–8], drug delivery [9–11], optoelectronics [12–15], imaging [16–20] and optical data storage [21–26], among others. The optical and mechanical properties of metal nanoparticles depend mostly on their sizes and shapes [27–30]. The size of metal nanoparticles can be measured by various techniques such as electron microscopy [31–33], atomic force microscopy (AFM) [34–38], dynamic light scattering [39–42] and UV-VIS (Ultraviolet-Visible) spectroscopy [43–45], among others. However, all of these techniques can not work in all media with high precision without damaging the sample and some of them are very expensive.

Scanning electron microscopy (SEM) and transmission electron microscopy (TEM) can characterise and image nanostructures with a resolution of 10 nm [31] and 0.1 nm [32],

respectively by using a focused electron beam. Such a high resolution is achievable by using these techniques because the electron beam has a very short wavelength. However, conventional SEM and TEM require a vacuum environment and conductive coating on the sample. Hence, these techniques are expensive, destructive, and cannot work in all environments. In addition, the sample preparation methods for these techniques are very complex, especially in TEM, which can also damage the sample. Atomic force microscopy can characterise and image metal nanoparticles with a high resolution where the 3D image of the surface is constructed by measuring the force between a sharp tip attached at the end of a cantilever and the surface of the sample. It offers 0.1 nm resolution similar to transmission electron microscopy (TEM) but can work in any external environment [34]. It is a valuable tool that can measure physical and living biological structures [35]. However, the measurement in AFM is affected by the tip-convolution effect. Using a sharp tip can be a solution to this problem but the sharp tip can damage the sample. In addition, the single scan image size in AFM is limited to 150 μm by 150 μm area [38]. In contrast, dynamic light scattering (DLS) is a non-invasive technique that measures the size and distribution of particles in a solution by detecting the intensity change of the scattered light due to the Brownian motion of particles caused by the collision with solvent molecules [39–42]. Although the DLS technique is fast, it provides an average measurement which is very sensitive to contamination and aggregation. It cannot predict small size differences between the particles and can only work when particles are immersed in a liquid [39, 41]. In addition, it is possible to measure size across the range of ≈ 0.3 nm to ≈ 10 μm by DLS technique [39]. UV-VIS spectroscopy is a fast, simple, and cost-effective technique. However, it provides average measurements, considers many particles at the same time and can only work when particles are immersed in a liquid [43–45]. It can be understood from the discussion that it is necessary to have a precise and non-destructive size characterisation technique for metal nanoparticles which can work in all environments.

The other research problem on which this PhD research focused on was the limitation of optical microscopy. The resolution, which means the ability to separate closely spaced fine features, is an important factor in imaging. The objective of any imaging technique is to provide the highest possible resolution to resolve fine details. Electron microscopy and atomic force microscopy can offer high resolution in imaging but suffers from some

problems as mentioned above. Optical microscopy is non-destructive if it is not in the ultraviolet (UV) range and also cost-effective. However, it cannot give in-depth information about the sample and is seriously limited in resolution. Diffraction or bending of light occurs when the light waves pass through the circular opening of lenses and hence optical microscopy is diffraction limited. The resolution in conventional optical imaging is limited to $0.61\lambda_{optical}/NA$ according to the Rayleigh criteria where $\lambda_{optical}$ is the optical wavelength and NA is the numerical aperture of the objective lens. Hence, the resolution of an optical system is limited to a few hundred nanometres even when the highest available NA (1.4) is used. This resolution is not sufficient for imaging, especially for biological samples that have poor optical contrast. It has always been a research interest to defeat this barrier. To defeat the optical diffraction barrier, engineering of point spread function (PSF) was done to achieve super-resolution in imaging such as confocal microscopy [46], structured illumination microscopy (SIM) [47–49], stimulated emission depletion (STED) [50–52], among others. In addition, single-molecule localisation techniques are available that offer super-resolution such as stochastic optical reconstruction microscopy (STORM) [53–55], photo-activated localisation microscopy (PALM) [46], among others. These techniques are based on the localisation of a single emitter where the wide PSF can be localised with precision.

Frequently used super-resolution techniques are based on fluorophores such as STED, STORM and PALM. Fluorophores require typically high light intensities, which can change the chemical property of fluorophores and they bleach. As a result, the imaging capability of the techniques deteriorates with time and repetition. This problem is severe for cell imaging because cells may die because of the high photon dose. Therefore, alternatives to fluorescent-based techniques have been tried by researchers such as spatial modulation spectroscopy (SMS) [56] and photo-thermal microscopy [57]. All the above methods rely on the optical properties of either fluorophores or nanostructures to provide super-resolution.

However, it is possible to use phonons to achieve super-resolution using time-resolved pump-probe spectroscopy. It has been possible to characterise the size and shape of metal nanoparticles [58, 59], as well as resolve them with super-optical resolution [60]. Metal nanoparticles are of sub-optical dimensions and a large number of them can be placed inside the optical point spread function. They also do not bleach and can allow long

time efficient imaging. Nanoparticles can also be inserted into cells easily and are bio-compatible [61–63]. In [60], acoustic frequencies of nanospheres were used to resolve them below the optical diffraction limit. The limitation was that the technique failed to identify and separate two spheres of the same size because they produced the same frequencies.

In this PhD work, acoustic frequencies of gold nanorods (GNRs) were used to separate them as long as their frequencies did not overlap. Gold nanorods were chosen because unlike spheres, they are sensitive to their orientation to the light or the polarisation of light. Hence, it is possible to turn them 'on' and 'off' by changing the polarisation of light. In addition to resonant frequencies, orientations of nanorods can be used to identify and separate them. So, it is possible to separate two nanorods of the same size (same frequencies) using their orientation difference.

There is a limit to the number of particles or frequencies that can be measured simultaneously within one PSF. This capacity can be increased if the amount of information from the particle increases to separate them simultaneously. A nanorod has two main vibrational modes, whereas a sphere has only one main vibrational mode. Two vibrational frequencies, longitudinal and breathing modes, give information about the length and width of the nanorod respectively and give more degrees of freedom to separate particles using frequencies. So, it is possible to detect more particles in the PSF simultaneously and increase the capacity of the system using nanorods (shown in the appendix A.2 through a simulation).

The long-term motivation behind this PhD work was to help make progress towards a phonon-based super-resolution imaging technique in biology. Imaging any biological structure with gold nanorods was out of the scope of this work. However, the achievements of the present work are significant steps to offer a phonon-based super-resolution imaging technique that can image biological nanostructures. Gold nanorods can be used as labels like fluorophores used in STORM or PALM and the proposed technique can be used to image living biological cells with super-optical resolution. Imaging cells in this way may be more stable than fluorescence microscopy because nanoparticles do not bleach like fluorophores. As the technique is phonon-based, it will not damage cells and can also provide mechanical information about the surrounding environment.

There are many challenges applying the proposed technique to image biological cells

such as proper functionalisation of gold nanorods, binding of gold nanorods to a cell, thermal effect of gold nanorods on a cell, imaging speed relative to the cell survival time, among others. Despite these challenges, the proposed phonon-based image reconstruction technique might find a way to become popular as a super-resolution imaging technique for biology in the future.

1.2 Aim and objectives of the thesis

The aim of this PhD research was to develop methods and instrumentation to enable the characterisation of gold nanorods and reconstruct their phononic images using time-resolved pump-probe picosecond laser ultrasonics. By measuring the size, orientation, and location of gold nanorods using a combination of optical and GHz ultrasound measurements, I was able to reconstruct their phononic images, even when multiple gold nanorods were inside the same optical point spread function and thus could resolve them with super-optical resolution.

I executed the following research objectives to achieve the aim of this PhD work.

1. Simulation of the optical responses of gold nanorods of different sizes in different external media.

2. Estimation of wavelengths and powers from the simulations to excite and detect gold nanorods in a specific laser system.

3. Simulation of the mechanical responses of gold nanorods to estimate their vibrational frequencies. The frequency estimation also helped to select the size of gold nanorods for experiments.

4. Carrying out experiments using the time-resolved pump-probe picosecond laser ultrasonics and measuring the vibrational frequencies of gold nanorods.

5. Conversion of the vibrational frequencies to sizes by using an analytical model.

6. Addition of new capabilities to the laser system to change the polarisation of the probe light for determining the orientation of gold nanorods.

7. Utilisation of the vibrational frequencies and orientations of gold nanorods as tags to identify, separate, and locate them, even inside the same optical point spread function.

8. Estimation of the size, location and orientation precisions of the proposed technique.

9. Reconstruction of the phononic images of gold nanorods by combining all three obtained parameters: size, orientation, and location.

10. Comparison of the reconstructed phononic images of gold nanorods with the images available from the scanning electron microscopy (SEM) and estimation of the accuracies.

1.3 Thesis structure

The structure of the thesis is as follows

1. Chapter 1 **"Introduction"**: This chapter presents the background problems on which this PhD research was focused and describes the importance of this work. In addition, aim and objectives of this project are provided. Also, the thesis structure is presented.

2. Chapter 2 **"Literature Review"**: This chapter introduces the relevant theories and reviews the state-of-the-art technologies that form the foundation of this thesis. Unique properties, applications, synthesis and fabrication methods of metal nanoparticles are discussed here. Afterwards, available characterisation techniques of metal nanoparticles such as electron microscopy, atomic force microscopy, dynamic light scattering, UV-VIS spectroscopy, picosecond laser ultrasonics are reviewed. Moreover, various generation/detection techniques of laser ultrasonics and vibrational modes of metal nanoparticles are discussed. In addition, resolution limit of optical microscopy and available super-resolution imaging techniques are reviewed.

3. Chapter 3 **"Modelling"**: In this chapter, gold nanorods are modelled as opto-acoustic transducers. Analytical and finite element modelling tools are used to sim-

ulate the optical and mechanical properties of gold nanorods to investigate their behaviours for different sizes, shapes and external media.

4. Chapter 4 **"Instrumentation and experimental methods"**: This chapter describes the instrumental and experimental methods in detail which were used in this research. Pump-probe spectroscopy and experimental setup are explained in detail with schematics and diagrams. In addition, different signal processing steps are explained step-by-step which were used to determine the size, orientation and location of gold nanorods. Moreover, used sample preparation methods and scanning electron microscopy techniques are described briefly.

5. Chapter 5 **"Phononic image reconstruction of gold nanorods by characterising their sizes, angles and locations"**: In this chapter, phononic image reconstruction of gold nanorods are shown by combining their sizes, angles and locations. The size of gold nanorods are determined in air and water media first. Precision of the size measurements are estimated and the predicted sizes are also compared with the sizes measured from the SEM images. Moreover, angle measurements of gold nanorods are shown by using basic examples. Precisions of the angle measurements are also estimated and the predicted angles of the rods are compared with the angles measured from the SEM images. Finally, location information of the rods is extracted and phononic images of the rods are reconstructed. The reconstructed images are then compared with the previously captured SEM images. It is also shown that the proposed technique can image gold nanorods with super-optical resolution.

6. Chapter 6 **"Phononic image reconstruction of GNRs fabricated by EBL and thermal effect on gold nanorods"**: In this chapter, size, angle and location of gold nanorods fabricated by electron beam lithography (EBL) are determined to reconstruct their phononic images. In addition, thermal effect on EBL fabricated and synthesised gold nanorods is shown. Also, possible ways to minimise the thermal effect on gold nanorods are discussed.

7. Chapter 7 **"Conclusions and future works"**: In this last chapter, the whole PhD

project is summarised. Moreover, key findings, challenges, long term motivation and contributions to knowledge of this research work are discussed. Afterwards, some promising future works are also recommended based on this research. The limitations of the proposed technique are also explained.

Chapter 2

Literature review

2.1 Introduction

The purpose of this chapter is to introduce relevant theories and review the state-of-the-art technologies that form the foundation of this research. Firstly, the properties and promising applications of metal nanoparticles are discussed. Next, different synthesis and fabrication methods of metal nanostructures are briefly explained because in this research, gold nanorods prepared by both wet chemical process and electron beam lithography (EBL) are used. Then, available characterisation techniques for metal nanoparticles are described comparatively. The fundamentals of laser ultrasonics and its applications are also reviewed. Then, the basics of vibrational frequencies of metal nanoparticles are reviewed together with interesting research works in which vibrational frequencies of metal nanoparticles were used. Next, the limit of resolution of optical microscopy and various available super-resolution imaging techniques are presented. The chapter concludes with a brief discussion on the thermal effect on gold nanorods and biological cells.

2.2 Metal nanostructures

Metal nanoparticles have been used for a long time in stained glass, pottery, mosaics, etc. where different sizes and types of metal nanoparticles were used to present different colours of light. One popular example is the 'Lycurgus Cup' made by Roman glass workers in the 4th Century [64]. The cup looks green when it is viewed normally but red when

light is shined through it. The reason behind this mystery is the presence of silver and gold nanoparticles in the glass and the light interaction with them. In the reflected light, the small particles are coarse enough to reflect the green light. However, in transmission, small particles scatter the blue end of the spectrum more than the red end and the cup looks red in the eye. Although the use of nanoparticles is very ancient, the purpose and mechanism were not clearly explained until Michael Faraday presented in the Bakerian Lecture of the Royal Society entitled "Experimental Relations of Gold (and other Metals) to Light" [65] in 1857 in London. He first showed the suspension of gold nanoparticles in a solution and mentioned different colours of different gold nanoparticles. Hence, he is considered the pioneer of colloidal chemistry, and his experiments are counted as the birth of modern nanotechnology. However, the reason behind this effect was not fully understood until Gustav Mie explained theoretically the absorption and scattering of spherical gold nanoparticles in 1908 [66] by solving Maxwell's equations. His theory is known as the Mie theory and is the foundation of describing small metal particles. Gans extended Mie's theory to prolate and oblate spheroidal particles averaged over all the orientations [67].

The light interaction happens in an interesting way when the size of a bulk metal is brought down to the nanoscale. Hence, the optical properties of metal nanoparticles are strongly dependent on their sizes, shapes, and external environments [27–30]. The attractive and distinct properties of metal nano-particles arise because of a special physical phenomenon called localised surface plasmon resonance (LSPR) which is the oscillation of free electrons in metal [68, 69]. This phenomenon occurs when the size of a particle is smaller than the wavelength of light. When light interacts with nanoparticles, charge separation occurs near the surface between free conduction electrons (electron cloud) and ionic core due to the incident electric field as shown in figure 2.1. However, these separated opposite charges also feel attractive force according to Coulomb's law. As a result, a restoring force is created to bring back the charges together. Exposed charges at the surface are connected like a spring and oscillate back and forth continuously when illuminated by light. The maximum condition of this oscillation happens when the natural frequency of the particle and the frequency of the incident light match. The resonant frequency or plasma frequency is determined by the equation

$$\omega_p = \sqrt{\frac{ne^2}{m\epsilon_0}} \tag{2.1}$$

where n is the electron density, e is the electron charge, m is the electron mass and ϵ_0 is the permittivity of free space. The created field at the surface is stronger than the incident field and thus localised enhancement occurs. For this reason, metal nanoparticles work as strong absorbers and scatterers. This field decays exponentially from the surface.
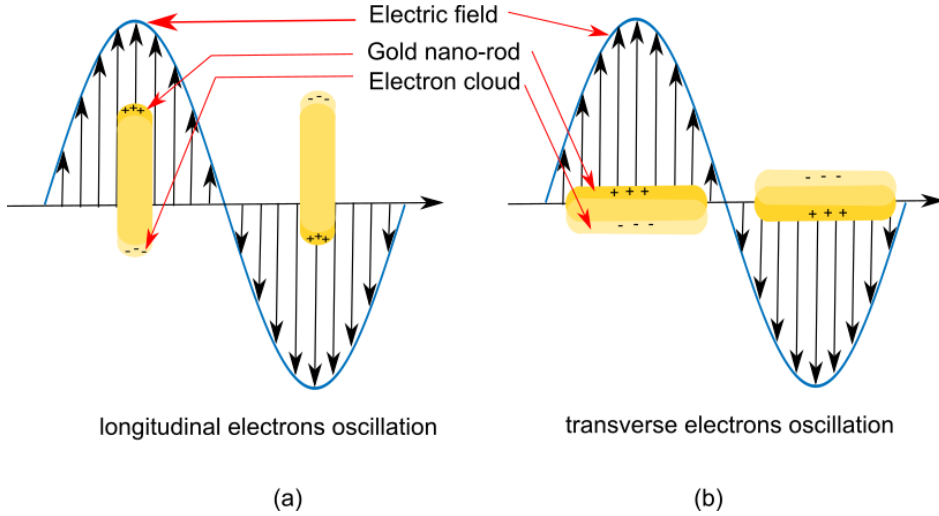
Figure 2.1: Localised surface plasmon resonance (LSPR) of GNR. (a) Longitudinal electrons oscillations. (b) Transverse electrons oscillations.

The electron density at the surface of the nanoparticles depends on their sizes, shapes, metal types, and external media [69]. Hence, it is possible to tune the localised surface plasmon resonance frequency by changing the mentioned parameters for different applications. Nanorod is asymmetric in shape and hence two localised surface plasmon bands occur, longitudinal LSPR and transverse LSPR where electron oscillations are along the length and width of the nanorod respectively, as shown in figure 2.1 (a) and (b). Nanorod is used in different applications for its extremely sensitive LSPR.

2.3 Applications of metal nanostructures

Metal nanostructures are of extreme interest and used in different applications, such as sensing [1–4], photothermal therapy [5–8], drug delivery [9–11], optoelectronics [12–15], imaging [16–20], optical data storage [21–26], among others.
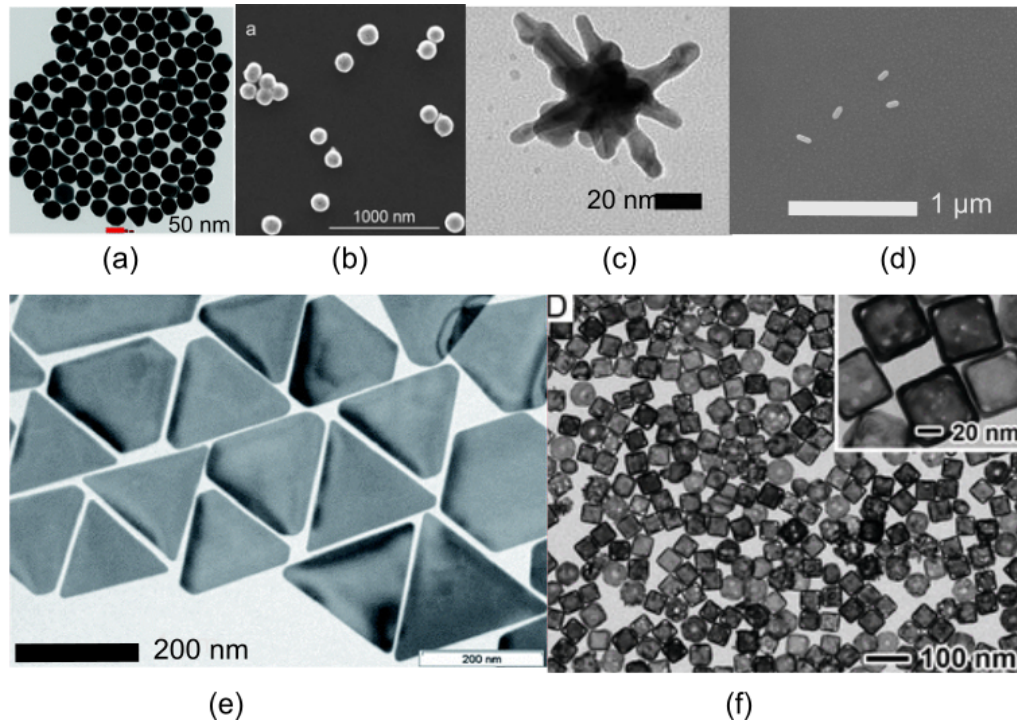
Figure 2.2: Different sizes and shapes of metallic nanostructures. (a) SEM image of gold nanospheres. Reproduced with permission [70]. (b) SEM image of Au/SiO_2 nanoshells. Reprinted with permission [71]. (c) TEM image of a gold nanostar (60nm). Reproduced with permission [72]. (d) SEM image of gold nanorods (112 nm by 40 nm). (e) TEM micrograph of bare gold nano-triangles. Reproduced with permission [73]. (f) TEM image of gold nanocages (edge length ∼ 50 nm). Reprinted with permission [74].

Different sizes and shapes of metal nanoparticles such as nanospheres [70, 75], nanoshells [71, 76], nanostars [72, 77], nanorods [1, 2], nanotriangles [73, 78], nanocages [74, 79], etc. are being used in different applications due to their attractive properties. The scanning electron microscopy (SEM) and transmission electron microscopy (TEM) images of different metal nanoparticles are shown in figure 2.2. Some applications of metal nano-particles are discussed below.

2.3.1 Sensing

Metallic nanoparticles have gained popularity as LSPR-based sensors. These sensors are highly sensitive, simple to fabricate and easily tunable by changing their sizes, shapes and materials to apply for different sensing applications. Gold nanorods are more attractive sensors because they have a high quality factor (Q) and can be tuned from visible to near-infrared (NIR) wavelength regions. Gold nanorods have been used as local environment

sensors [2], biosensors [3], and chemical sensors [4], among others. The working principle of a nanoparticle sensor is that the LSPR wavelength shifts due to the change in the refractive index of the surrounding medium and this shift can be used for sensing the external environment. The LSPR shift of a gold nanorod due to the change in the surrounding medium is shown through simulations in chapter 3 in section 3.3.1.1. The change in the refractive index of the external medium practically can happen due to the addition of chemicals, binding of molecules, flow of gas, etc.

2.3.2   Photothermal therapy (PTT) and drug delivery

Metal nanoparticles are being used widely in photothermal therapy [5–8]. Photothermal therapy is a process where photosensitiser agents are activated by light to create heat which is used to kill cancer cells. The enhanced absorption and scattering cross-sections of metal nanoparticles than photo-absorbing dyes make photo-thermal therapy more efficient, reliable and less destructive. The nanoparticles conjugated with antibodies attach to cancer or tumour cells and the particles are excited externally with a laser. The strong scattered light by particles helps to diagnose the cancer cells where the absorbed light introduces local heat which kills the cancer cells. Gold nanoparticles are more frequently used than other metallic particles because of their chemical or biological stability, and low cytotoxicity [62], among others.

In biomedical applications, near infrared light is used because it can penetrate the body. Hence, gold nanorods are extremely popular in PTT because they can be activated by NIR [80].

Small metal nanoparticles can be easily inserted into the cell. They can also be used as drug carriers and the photo-thermal effect can be utilised to release drugs efficiently [9–11]. When nano-particles become hot during the laser irradiation, the drugs are released to the target cancer cells. Nano-particles have also been used to release genes and bio-molecules [81, 82].

2.3.3   Imaging

Gold nanoparticles are widely used for imaging, especially gold nanorods are attractive for their efficient and tunable absorption and scattering in the NIR that can penetrate

the biological tissue [16–20]. They are more stable and strong absorbers and scatterers than fluorescent molecules. Hence, gold nanorods are attractive probes for in vitro and in vivo imaging. The bio-medical imaging modes for GNRs include two-photon enhanced luminescence (TPL) [17], dark field microscopy [18], optical coherence tomography (OCT) [19], and photoacoustic tomography (PAT) [20], among others.

2.4 Synthesis and fabrication of gold nanorods

It is challenging to produce metal nanostructures and several techniques have been proposed to prepare different sizes and shapes of nanostructures with stability and efficiency. There are different methods to synthesise gold nanorods and the prepared nanorods have been used successfully in many applications as mentioned before. These methods have achieved a good control over production but it is still hard to scale or modify the shape. On the other hand, there are lithographic approaches to fabricate gold nanorods like electron beam lithography (EBL), focused ion beam (FIB), etc. These techniques offer more flexibility to get desired sizes and distributions of nanorods on the sample. However, these techniques are expensive, time-consuming and it is not possible to fabricate very complex shapes effectively. On the other hand, different complex shapes like bi-pyramids have been made using the synthesis process. Both methods are described briefly below.

2.4.1 Wet chemical synthesis

Different wet chemical synthesis methods of metal nanoparticles have been reported at different times. The seed-mediated growth method is the most popular among all methods used for the synthesis of gold nanorods because of its simplicity, high quality, better yield, better size control and structural modification flexibility [83]. It was first demonstrated by Jana et al. in 2001 [84]. The seed solution was prepared by the reduction of gold salt $HAuCl_4$ with $NaBH_4$ in the presence of sodium citrate. The seed solution was added to a growth solution containing $HAuCl_4$, cetyl-trimethyl ammonium bromide (CTAB), ascorbic acid, and $AgNO_3$. To change the aspect ratio of nanorods, different volumes of seed solution were added to the growth solution. Later the group proposed a modified approach (three-step method) without using $AgNO_3$ to increase the aspect ratio of gold

nanorods up to 25 [85]. Later an improved method was demonstrated by Nikobakth and El-Sayed by replacing sodium citrate with a stronger CTAB stabiliser in the seed formation process and adjusting the number of silver ions to control the aspect ratio [86]. A co-surfactant, benzyldimethylhexadecylammonium chloride (BDAC) was introduced later in the growth solution to increase the aspect ratio. The method demonstrated by Nikobakth and El-Sayed is mostly used for synthesising GNRs for sensor applications [87]. Several optimisation techniques have also been proposed and demonstrated at different times, for example, broadening LPB tunable range [88], seedless synthesis [89], etc. Several other methods were reported even before the seed-mediated process like electrochemical method [90], photochemical method [91], template method [92], etc. The gold nanorods (immersed in solution) were bought from Nanopartz for the experiments of this research and were synthesised using the seed-mediated process by the manufacturer. The SEM image of some nanorods purchased from Nanopartz can be seen in figure 2.2 (d). Different shapes of metal nanoparticles such as nanorods, nanotriangles, nanocages, nanospheres, nanostars, bipyramids, nanoshells have successfully been fabricated using the wet chemical synthesis process and used for different purposes [93], [94].

2.4.2 Focussed ion beam (FIB)

Focussed ion beam (FIB) is a direct writing technique that uses a fine focused ion beam (generally Ga^+) to fabricate structures by milling, implantation, deposition and ion-based etching. It is an extremely high resolution technique (5 nm) [95]. It is being used to fabricate different plasmonic nanostructures [96–99] frequently.

The drawback of this technique is that it can often damage the sample or modify the sample properties by the heavy ions. It is also very expensive and slow. A simple schematic of a FIB machine is shown in figure 2.3 for the case of milling where heavy ions from the FIB column hit the surface of the sample and sputter the atoms out. It is also possible to deposit materials by introducing a gas injection system (GIS) that provides gas molecules. These molecules get adsorbed on the surface of the sample and decomposed by the incident ion beam that results in local deposition of the material. The imaging can be done by detecting secondary electrons generated by either the ion beam or the electron beam. Though the resolution in FIB imaging is higher than the SEM, imaging is done by

the SEM preferably to avoid the sample damage.
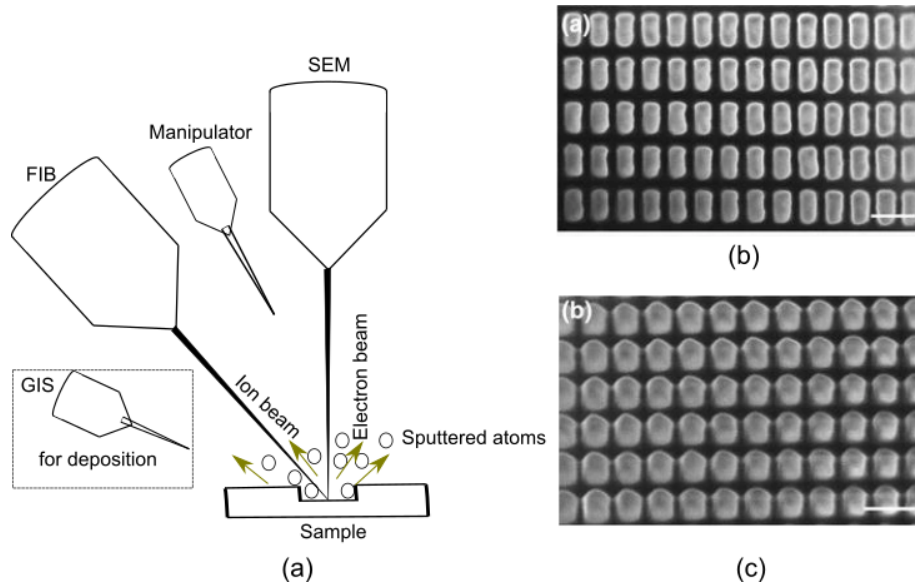
Figure 2.3: Nano-fabrication by focused ion beam (FIB) lithography. (a) A simple schematic of a FIB machine system. (b)(c) Top and 45 degree tilted view SEM images of Au^{2+} milled pattern where rectangular nanoparticles are 190 nm by 100 nm with a gap of $\sim$50 nm between adjacent particles. Reprinted with permission [97].

2.4.3 Electron beam lithography (EBL)

Feature size in photo-lithography is limited to the optical diffraction limit defined by the Rayleigh criteria. According to this criteria, feature size, a is defined by the formulae, a=1.22 λ/NA, where λ is the optical wavelength and NA is the numerical aperture. Either wavelength needs to be very low or NA needs to be very high to reduce the feature size. However, even for sophisticated immersion lens microscopes, the NA is limited to < 1.5.

Electron beam lithography (EBL) is a direct pattern writing technique because it does not use any mask like photo-lithography. It is a lithographic process that uses a highly focused and precisely controlled electron beam to transfer the desired pattern on the substrate. The substrate has electron-sensitive resist on the surface and the electron beam changes the solubility of the resist according to the designed pattern. The exposed or non-exposed regions are then removed by immersion into a developer and in this way the desired pattern is transferred onto the substrate. The main advantage of the EBL technique is that it offers higher resolution than photo-lithography and can provide structures with sub-5 nm resolution [100, 101]. The wavelength of high-energy electrons is typically less

than 0.01 nm (0.005 nm for 50 keV) and this feature enables EBL to achieve ultra-high resolution [102]. However, the electron wavelength is not the resolution limiting factor of EBL. The achievable resolution in EBL depends on the spot size, electron scattering, secondary electron range, mechanical stability of resist and the resist development [103].

Electron beam lithography was originally developed by introducing the pattern generator and beam blanker into scanning electron microscopes. These days, modern machines are specifically designed to perform electron beam lithography with attractive features. A simple schematic of an EBL machine is shown in figure 2.4 where only basic components are shown for simplicity.
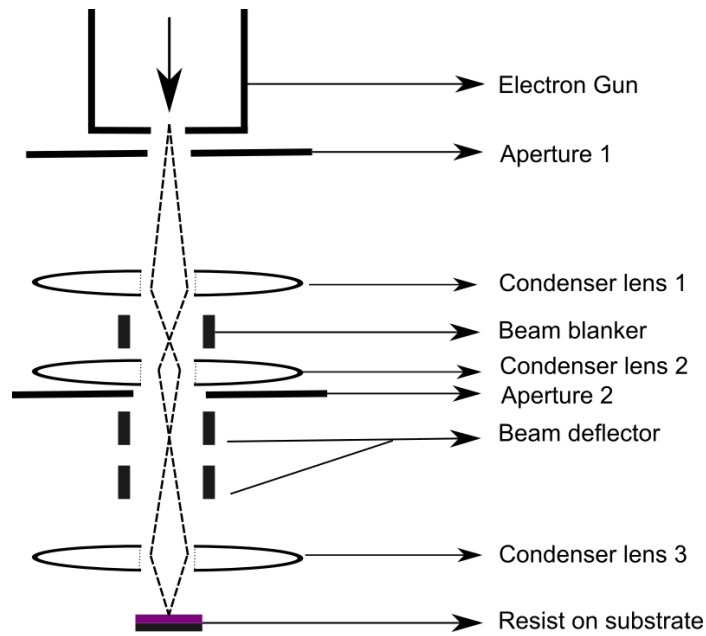
Figure 2.4: Schematic of a typical EBL machine.

An electron gun is the electron source that emits a stream of electrons on the resist for exposure. A good electronic source should have high brightness, good uniformity, stability, smaller spot size and a longer lifetime. Electron gun can be a thermionic emitter where electrons are emitted by heating the filament or a field emitter where a large electric field is used to emit electrons. Tungsten (W) and Lanthanum Hexaboride (LaB6) are commonly used as thermionic sources in low and high vacuums, respectively. A reliable thermionic emitter should have a low work function, high melting point and high mechanical strength.

The spot size of the beam is an important factor because it controls the resolution of the fabrication. Thermionic emitter produces a broad beam (10-25 μm) and strong

magnetic lenses are needed to focus the beam to a small spot size to improve the resolution compromising the intensity. Field emission electron sources offer 5 nm to 20 nm beam spot size where a strong electrostatic field is applied to the sharp tip of Tungsten wire and electrons are released by quantum mechanical tunnelling. Field emission guns (FEGs) are more popular because they offer high resolution, high brightness and longer lifetime. However, these guns are expensive because of their high vacuum requirements ($\approx 10^{-9}$ Torr). The nB5 EBL machine which was used to prepare the samples for this project has a FEG type electron gun.

Magnetic lenses are generally used instead of electrostatic lenses to focus the electron beam to a small spot size on the sample. The beam blanker turns off the beam by driving it away from the optical axis. It works according to the loaded pattern into the computer and keeps the beam on when needed during scanning. The beam deflector steers the beam across the sample to write the pattern. The scan can be either a raster scan where the beam sequentially scans the whole area of the sample or a vector scan where the beam only scans the area where features are present. The samples shown in this thesis were raster scanned. One SEM image of gold nanorods (200 nm by 80 nm) fabricated by EBL for this project is shown in figure 2.5. Fabrication methods of gold nanorods by EBL are discussed in the appendix (A.1) in detail.
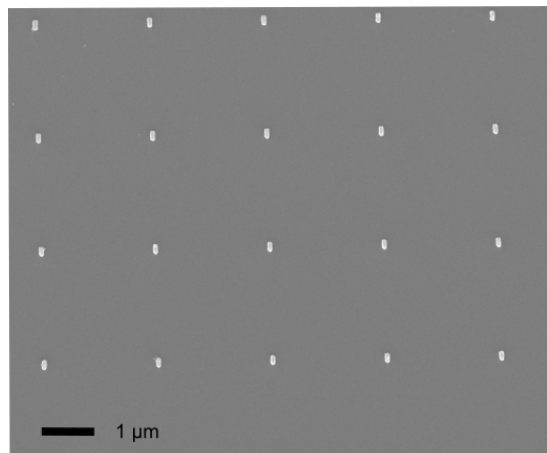
Figure 2.5: SEM image of gold nanorods (200 nm by 80 nm) fabricated by electron beam lithography (EBL).

Electron beam lithography offers more flexibility than the wet chemical synthesis process which suffers from randomness. It is also possible to control the size, shape, orientation

and distribution of nanostructures in a pattern by the EBL process. The drawback is that it is very expensive and slow. Hence, it is not popular for high-volume production.

Different plasmonic nanostructures such as nanorods, nanotriangles and nanodisks, among others have been fabricated by using EBL for different applications [104–110]. Some interesting works on EBL fabricated nanostructures are reviewed here. Neval A. Cinel et al. [104] made silver nanodisks of 30 nm to 73 nm in radius with a separation of 125 nm to 200 nm on sapphire and the array was used as an LSPR based label-free biosensor to detect biotin-avidin pair. The sensor was also applied to detect heat-killed Escherichia coli (E.coli O157:H7) bacteria, the most serious food borne infections. Refractive index sensitivity was calculated experimentally as 221-354 nm/RIU for different arrays of different sizes. Kosei Ueno et al. [105] designed sensors based on gold nanorods fabricated by EBL. The sensors were capable of detecting the change in the refractive index of the medium and the minimum detection level was in the order of 10^{-2}.

It is important to provide an adhesion layer to the deposited metal while fabricating metal nano-structures by EBL. The adhesion layer provides a binding between the metal nanostructures and the substrate. Wei-Sun Chang et al. [106] did research on the thickness of the adhesion layer of a nanodisk and demonstrated that the adhesion layer thickness can be used to tune the acoustic frequency in the GHz range. It was observed that the phonon frequency of the gold nanodisk increased when the thickness of the Titanium adhesion layer increased. This tuning effect can lead to new types of plasmon-based optomechanical devices as was proposed by the authors.

Yongbin Lin et al. [107] fabricated gold nanodots of 185 nm in diameter and 55 nm in height by EBL directly on the tip of optical communication fibres (Corning SMF-28, core 9 μm, cladding 125 μm) to make LSPR based biochemical sensors. The designed sensor provided refractive index sensitivity of 196 nm/RIU. As the Au layer was directly sputtered onto the fibre facet, the designed sensor was robust and reusable. Optical transmission through the array of nanoparticles on the tip of the sensor fibre was measured by UV-VIS spectroscopy. The gold nanodots were funtionalised with biotin at first that bound steptavidin later and a shift in LSPR was recorded from the transmission measurement. The detection limit of the sensor was found as 6 pM.

The nanostructures designed by EBL are gaining popularity in optical data storage

(ODS) media day by day. Adam B. Taylor et al. [108] fabricated three-layer ODS media using gold nanorods fabricated by EBL. It was proposed that the required readout powers can be reduced in deeper layers by twisting the GNR alignment together with the polarisation through deep layers. It was demonstrated that the extinction loss could be four-fold reduced for CW readout in a three-layer structure. The gold nanorods were 90 nm long, 30 nm wide and 30 nm thick where the centre to centre spacing between rods was 180 nm. The nanorods were fabricated using the standard EBL technique on a glass substrate and 20 μm thick SU-8 photopolymer layer was used as a spacer between each nanorod array layer.

Shaoli Zhu et al. [109] fabricated gold nanostars with 'top hats' by EBL technique on a silicon substrate. The five-point gold stars had tips with radii of about 50 nm, and a nominal height of about 40 nm. The applied exposure parameters were optimised by performing different tests with different sizes, periods and exposure doses. A bilayer resist process was used where the top and bottom layers had 2 wt% 950k PMMA and 4 wt% 495k PMMA, respectively. Reflection spectra of the fabricated nanostructures were collected by a spectrophotometer. It was observed that the presence of 'top-hat' structures changed the optical properties of the nanostructures. The use of these structures for biosensing applications was inspired by the authors.

Luis Gutierrez-Rivera et al. [110] fabricated surface enhanced Raman spectroscopy (SERS) substrates consisting of arrays of gold dots with 50, 100 and 200 nm pitches on a fused silica substrate using EBL. E-beam resist (PMMA 950K A2) was used and standard EBL procedures were followed. AquaSAVE conductive polymer was used as a conductive layer to avoid the charging effect. The fabricated SERS substrates were biofunctionalised and used to characterise immobilised protein A. Results showed that the Raman intensities became highest when the gap between the nanodots was less than 20 nm and many vibrational modes of protein A could be detected. Authors proposed to control the exposure and development parameters to optimise the nanostructures and material to design highly sensitive SERS-based biodetection devices.

Nanoparticles need to be characterised after synthesis or fabrication. Characterisation techniques of nanoparticles are discussed next.

2.5 Characterisation of metal nanostructures

There are different characterisation techniques for nanoparticles. These techniques can characterise the size, size distribution, shape, aggregation, etc. Some frequently used characterisation techniques of metal nanoparticles are described below.

2.5.1 Transmission electron microscopy (TEM) and Scanning electron microscopy (SEM)

The wavelength of an electron beam is smaller than the optical wavelength. Hence, high power electron beams are used for imaging with high resolution overcoming the optical resolution limit. Both, scanning electron microscopy and transmission electron microscopy techniques use this principle to image samples and characterise different nanostructures. Conventional SEM and TEM techniques require a high vacuum environment for operating and cannot measure living samples.

The resolution offered by the SEM is about 10 nm [31]. The three-dimensional images produced by the SEM provide topographical, morphological and compositional information. The sample should have a conductive surface for performing the SEM. These preparation methods can also damage the sample or change the property of a very sensitive sample.

The resolution offered by TEM is about 0.1 nm [32]. The two-dimensional images produced by TEM provide topographical, morphological, compositional and crystalline information. The sample preparation method for TEM is very complex because the sample needs to be ultra-thin. These preparation methods can also damage the sample. The TEM and SEM images of gold nanorods are shown in figure 2.6. Both SEM and TEM machines are expensive and need careful maintenance.
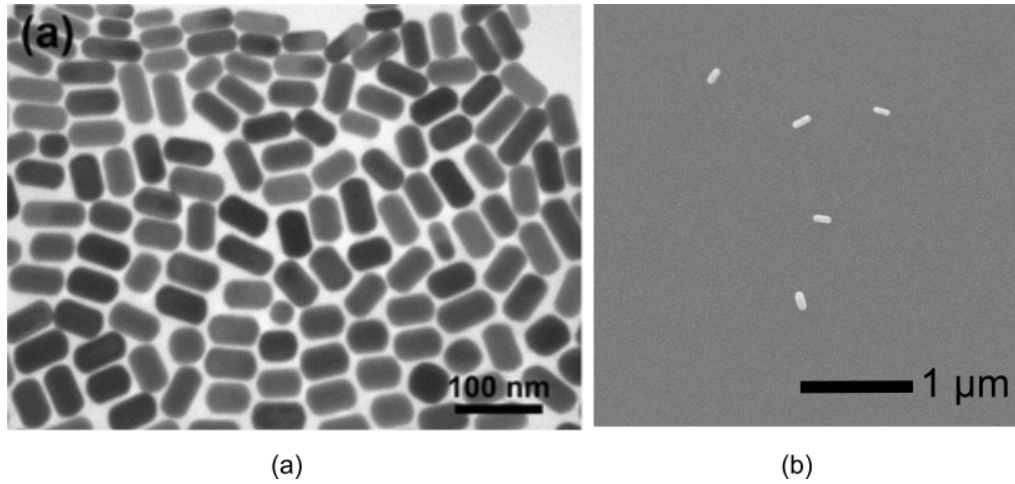
Figure 2.6: Transmission electron microscopy (TEM) and scanning electron microscopy (SEM) images of gold nanorods. (a) TEM image of gold nanorods. Reprinted by permission [33].(b) SEM image of gold nanorods taken at nmRC, UON using JEOL 7100F FEG-SEM.

2.5.2 Atomic force microscopy

Atomic Force Microscopy (AFM) is one type of Scanning Probe Microscopy (SPM) where a 3D image of the surface is constructed by measuring the force between a sharp tip attached at the end of a cantilever and the surface of the sample. It is a high resolution technique that can provide at best 0.1 nm resolution [34]. A simple schematic of AFM is shown in figure 2.7 (a). There is an arrangement of an optical system where a LASER beam is reflected from the back of the cantilever to a position photo-detector. Any deflection of the cantilever changes the position of the beam in the detector. As the cantilever raster scans the sample surface, the tip moves up and down following the contour of the surface and the resulting deflection of the cantilever is recorded in the detector to construct the 3D image of the surface. Three different types of AFM modes are contact mode (generally for solid surfaces), tapping mode (generally for ambient conditions and liquid environment) and non-contact mode (generally for biological samples and organic thin films). Single or groups of nano-particles have been imaged using the AFM technique [35–38]. An image area of gold nanorods using the AFM technique is shown in figure 2.7(b) [37]. The disadvantage of this technique is that the scanning speed is very slow that often leads to thermal drift in the image [35]. In addition, the single scan image size in AFM technique is limited to 150 μm by 150 μm area [38]. Moreover, often the measurement is affected

22

by the tip-convolution effect of AFM technique [38]. The tip convolution effect happens when the radius of curvature of the tip is the same or larger than the surface feature. In that case, the sides of the tip come before the apex of the tip during the scan. The result is a low lateral resolution and the surface feature will appear bigger than its original size. The tip may not be able to resolve close features separately. The solution is to use a sharp and robust tip but not damage the sample.
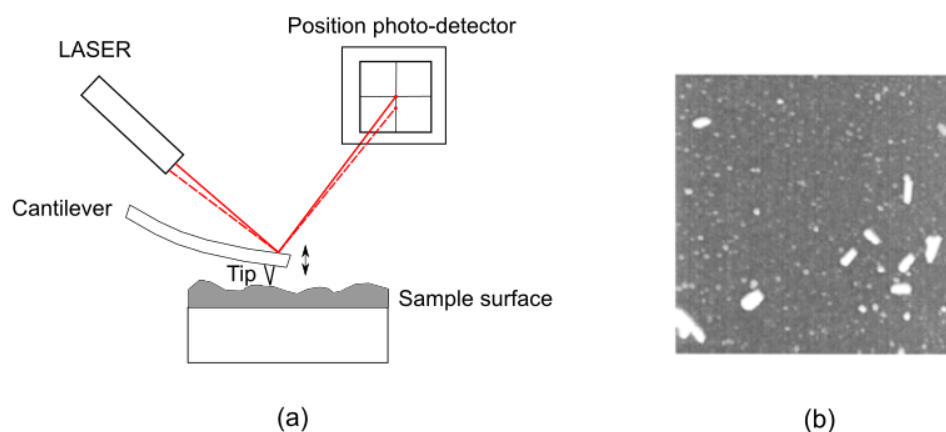
Figure 2.7: Atomic force microscopy (AFM). (a) A simple schematic of atomic force microscopy technique (AFM). (b) Image of gold nanorods using AFM technique (the image area is 1 μm by 1 μm. Reprinted with permission [37].

2.5.3 Dynamic light scattering (DLS)

Dynamic light scattering (DLS) is a non-invasive technique that measures the size and distribution of particles in a solution. It works on the principle of detecting the intensity change of the scattered light due to the Brownian motion of particles caused by the collisions with solvent molecules [39–42]. The technique measures the hydrodynamic diameter of the particles that depends on the ionic strength, surface structure and shape [39]. A simple schematic of dynamic light scattering is shown in figure 2.8 where the laser light is scattered by the particles immersed in a solution.
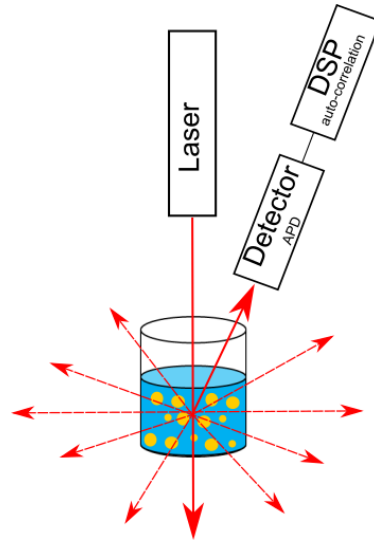
Figure 2.8: A simple schematic of dynamic light scattering (DLS) where the laser light is scattered by the particles immersed in a solution in random directions when the particles are in motion (Brownian motion) due to having a collision with the solution molecules. A photo-detector (Avalanche photo-diode, APD) is set at an angle to detect the intensity change of the light over time due to the motion of particles. The diffusion time difference of different sizes of particles is the key to size characterisation by the DLS technique. Digital signal processing (DSP) unit performs the auto-correlation of the detected signal over time to estimate the diffusion coefficient of the particles which is used in the Stokes-Einstein equation to determine the hydrodynamic size.

The light is scattered by the particles in random directions when the particles are in motion (Brownian motion) due to colliding with the solution molecules. A photo-detector (Avalanche photo-diode, APD) is set at an angle to detect the intensity change of light over time due to the motion of particles. Small particles diffuse quickly while larger particles diffuse slowly. The diffusion time difference of different sizes of particles is the key to size characterisation by the DLS technique. Digital signal processing (DSP) performs the auto-correlation of the detected signal over time to estimate the diffusion coefficient of the particle which is used in the Stokes-Einstein equation to determine the hydrodynamic size. It is possible to measure size across the range of ≈ 0.3 nm to ≈ 10 μm by DLS technique [40]. One of the disadvantages of the DLS technique is that it cannot precisely predict the small difference in size between particles [41]. Though the technique is fast, it provides an average measurement which is very sensitive to contamination and aggregation. In addition, for asymmetric particles (like nanorods), rotational diffusion rate needs to be considered also which needs further care and efficient analysis [42].

2.5.4 UV-VIS spectroscopy

Ultraviolet-visible (UV-VIS) spectroscopy or spectrophotometry is a simple and quick technique which is used to characterise metal nano-structures. The absorption or reflection as a function of wavelength is used to investigate the material, size, aggregation, size distribution and quality of nanoparticles immersed in a solution [43–45]. It is generally mentioned as UV-VIS but generally a wavelength range from 190 nm to 1100 nm is used and often called UV-VIS-NIR spectroscopy.
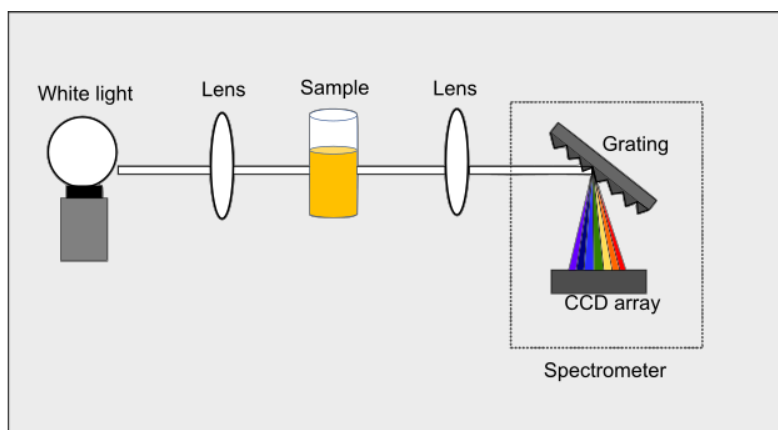
(a)
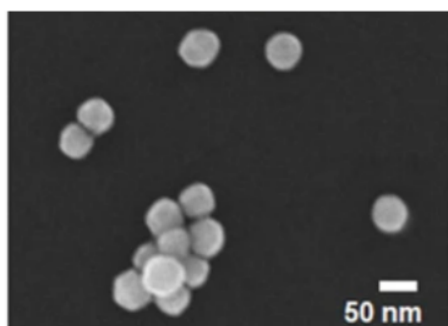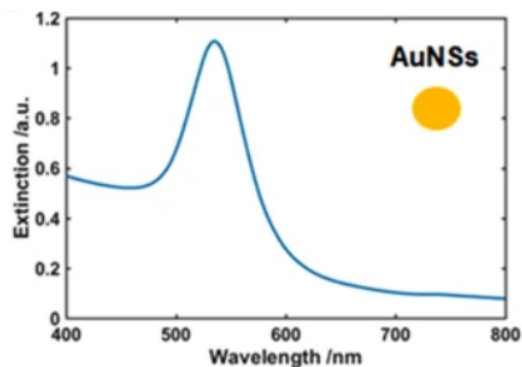
(b)   (c)

Figure 2.9: UV-VIS spectroscopy. (a) A simple schematic of a spectrophotometer. (b) SEM image of gold nanoparticles (50.3 +/- 1.7 nm). (c) UV-VIS extinction spectrum of gold nanospheres. Reproduced from [44] with permission.

The basic principle of UV-VIS spectroscopy is explained using a schematic diagram as shown in figure 2.9 (a). The light from a white light source goes through a lens to the sample. The sample absorbs, reflects and scatters selected wavelengths of the light and

light is then passed through a lens to a dispersive element, generally an optical grating. This grating acts like a monochromator and separates light by wavelength. This dispersed light is then passed to a linear camera for detecting the amount of light at each wavelength, typically using a charge-coupled device (CCD) array. This detection system allows rapid and simultaneous acquisition of a full spectrum. In this way, the intensity of light at each wavelength is measured and the absorption spectra are obtained. The SEM image of some gold nanospheres and their UV-VIS extinction spectra are shown in figure 2.9 (b) and (c), respectively. Although UV-VIS spectroscopy is a simple and fast technique, it provides average measurements and considers many particles simultaneously.

2.5.5   Laser ultrasonics

Laser ultrasonics is one technique which has made the generation and detection of high frequency acoustic waves possible. It has overcome the limitations of piezo-electric transducers such as the need for couplant, low frequency range and high sensitivity to undesired environmental conditions, among others. In this technique, light is absorbed on an opaque material (mainly metals) that causes the local thermal expansion and strain is generated in turn. Short optical pulses of a few femtoseconds generate ultrasound in the THz range [111].

Laser ultrasound based on the pump-probe technique [112] is commonly referred to as picosecond laser ultrasonics (PLU), where ultrashort laser pulses are used to generate and detect ultra-high frequency coherent acoustic pulses [113, 114]. The pump–probe architecture removes the need for extremely fast electronics and detectors. Picosecond laser ultrasonics started to develop since the first works by H. J. Maris et al. in 1984 [113]. The sample was excited with the pump laser and photo-induced changes were detected using the probe laser. The major breakthrough was the successful detection of GHz range frequency by delaying the probe pulse relative to the pump [113, 114]. The measurements were based on a metallic thin film optoacoustic transducer where acoustic waves were generated thermoelastically by the pump laser excitation and detected as variations of the reflected light intensity caused by the photoelastic effect.

Later, a picosecond interferometric detection system was proposed and demonstrated from the same group where the measurement of small attenuations and study of very thin

films using Brillouin scattering [115, 116] were shown. This interferometric technique is also known as time-resolved Brillouin scattering (TRBS) where the interference of the reflected probe beam from the sample surface and the acoustic strain is used to measure the phonon velocity and attenuation. Detail on the TRBS technique is given later in this section.

Picosecond ultrasonics is a rapid, non-contact and non-destructive label-free all optical experimental method. It can also perform measurements on multiple layers simultaneously. The high frequency can recover the low frequency range limitation of SAM (Scanning acoustic microscope) where piezoelectric transducers are used. However, the challenges are low acquisition speed, low signal-to-noise ratio (SNR) and complex pump-probe system with moving parts, among others. Transducer design and experimental set-up can be optimised to enhance SNR [117] which can improve the acquisition speed or bio-compatibility [118].

The effectiveness and popularity of the PLU technique improved dramatically with the development of ASOPS (Asynchronous optical sampling) [119, 120]. It is a technique that uses two lasers locked together where one of the lasers can be delayed relative to the other. It offers high scanning speed, faster acquisition time and high SNR. It was possible to image cells with high resolution using PLU and ASOPS in fixed 3T3 fibroblast [121] and bone marrow [122]. Though there are several challenges using PLU for cell imaging, it is proven as a non-invasive and label-free high resolution technique [118].

Picosecond laser ultrasonics along with ASOPS was also used to characterise metal nanoparticles from their vibrational modes [58–60]. In this thesis, picosecond laser ultrasonics is used to characterise and image gold nanorods. The working principle of a gold nanorod as an opto-acoustic transducer is discussed later in this section in detail.

2.5.5.1 Laser ultrasound generation

The principle of laser ultrasound generation is the absorption of optical pulses in opaque (i.e. metals) or semi-transparent materials (i.e. semiconductors and biological objects). The absorbed light converts into thermal energy and causes local thermoelastic expansion of the material near the surface. The rapid expansion creates strain pulses that propagate through the material. The generated elastic strain can be used to measure the film thick-

ness and mechanical properties of nanostructures [58–60, 113, 114]. The absorption can cause thermal expansion or thermal ablation. In a lower energy regime, only the thermal effect is observed. A theoretical description of the generation of ultrasound by laser pulses was first published in [113, 114, 123]. The theory was expanded for more complicated multi-layer structures by Osamu in [124].

Opto-acoustic transducers can be designed to strengthen optical absorption efficiency. For example, patterned transducers to generate surface waves [125], metallic thin films to examine translucent dielectrics [114], semiconductors [126] and imaging cells [118, 121].
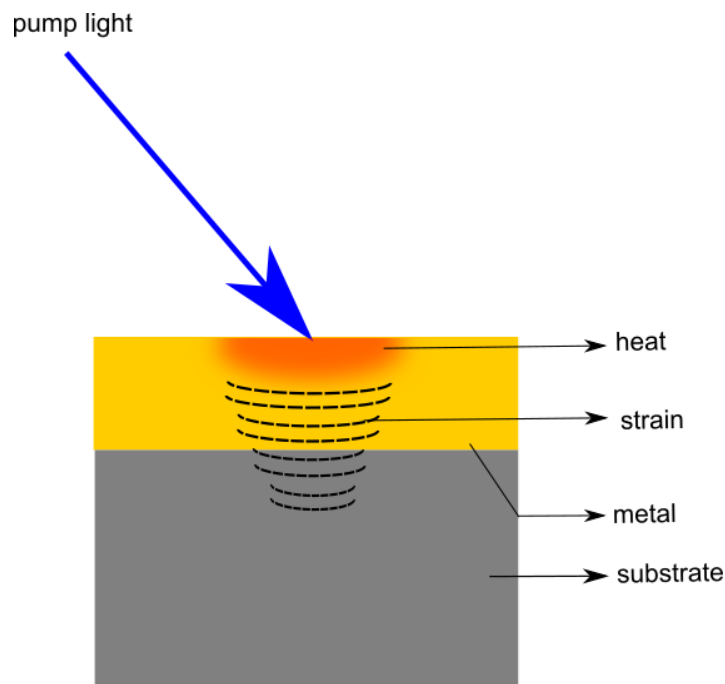
Figure 2.10: Thermoelastic generation of acoustic waves during laser illumination. Short laser light pulses are absorbed by the sample that causes a rise in the temperature which generates acoustic waves due to thermal expansion.

2.5.5.2 Laser ultrasound detection

The interaction between light and sound waves provides different ways to detect acoustic waves such as interferometry, opto-elastic effect, beam deflection, beam distortion or a combination of these. In this section, some optical detection techniques of ultrasound are discussed.

(i) Transient reflectivity using opto-elastic effect:

   Opto-elastic effect is the change of optical properties due to acoustic waves. The

refractive index changes due to the pressure associated with acoustic waves. The simple way to detect an acoustic wave through the opto-elastic effect is to monitor the optical reflectivity on the surface of a material [113, 114]. The reflectivity will change according to the change in the refractive index due to strain. Though the process is simple, the sensitivity of this method is low and high intensity beam is needed to achieve a reasonable signal-to-noise ratio. Modulation of the refractive index can also happen due to the temperature change and the effect of temperature on the intensity of the reflected signal which is called the thermal background. This thermal background can easily be removed from the desired signal by simple signal processing steps because the change of the intensity is very slow in this case. The reflectivity method is simple but it is only applicable to materials having reasonable opto-elastic co-efficient at the probe wavelength. This criterion restricts the reflectivity method to certain materials and wavelengths.

(ii) Interferometry:

Interferometry is a technique where the directly reflected beam from the sample surface and the beam reflected from the acoustic wavefront interfere with each other at the detector providing a way to measure the sound wave as shown in figure 2.11 (a). The modulation depth in this method is higher than the only reflection method because the intensity change by interferometry is higher than the intensity change provided by the refractive index modulation. Different types of interferometric configuration are possible such as two wave mixing fibres [127], free space [128], Fabry-Perot interferometer [129], Michelson [130], and Sagnac-based [131], among others. The interferometric technique is advantageous because it does not depend on photo-elastic co-efficient and works on every material that has reflectivity. The disadvantage is that the interferometers are sensitive to low frequency noise and ambient disturbances.

(iii) Beam deflection:

A knife edge detector is based on the optical deflection technique to detect the ultrasound generated by a laser. This simple and low cost technique is used to detect surface acoustic waves (SAW) [132]. When a sound wave propagates during the laser

29

illumination, the reflected beam deflects forward and backwards at the frequency of the ultrasonic waves. The reflected beam is partially blocked by a 'knife edge' as shown in figure 2.11 (b). When the beam moves perpendicular to the knife edge, the amount of light reaching the detector changes. The knife edge can be implemented in many ways, for example, by using a split photodiode and differential amplifier [133, 134]. In that case, in one part of the cycle, the signal in one detector is higher than the other and in the other part of the cycle, the opposite happens. The outputs of two detectors are subtracted using a differential amplifier (such as Op-AMP) where the difference signal is proportional to the tilt of the sample surface due to the generated acoustic waves during laser illumination. However, conventional knife edge detection works effectively when the sample surface is smooth and the reflection is specular. If the sample surface is rough, diffuse speckle patterns enter the detector. The reason is that different parts of the reflected beam having different phase components interfere constructively or destructively at the detector, called speckles. These reduce the sensitivity of the knife edge process and change randomly with the position of the speckles. This problem can be handled by CCD detectors by converting each speckle into its own split detector [134] and by developing self-adapting sensors to cope with optical speckles. [133]. However, CCD detectors are very slow.
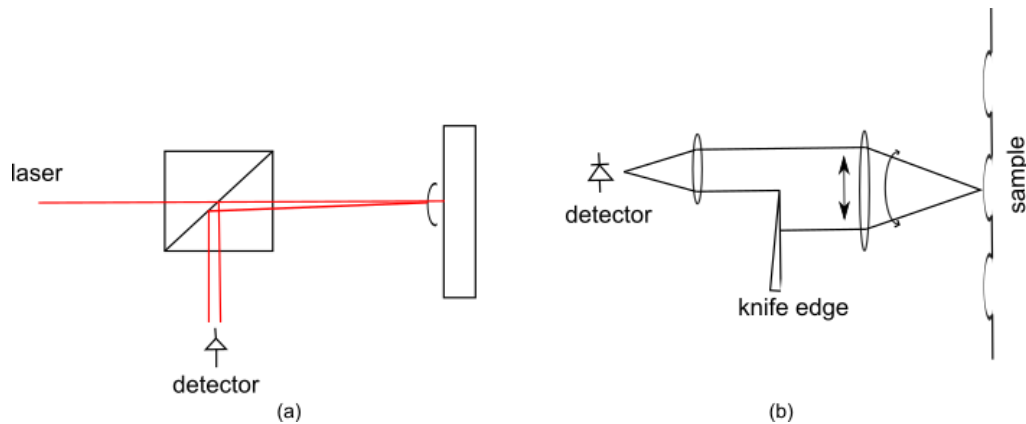
Figure 2.11: Optical detection of ultrasound. (a) Interferometric technique. (b) Knife-edge technique.

(iv) Beam distortion:

Beam distortion detection (BDD) technique is based on the change of the reflected

probe beam radius due to the propagation of acoustic waves during laser illumination. This is a simple and stable technique. A curvature of the surface forms due to the acoustics that changes the divergence of the reflected beam. An iris is placed before the detector. The power at the detector changes according to the change of the reflected probe beam radius before the iris. The signal is proportional to the surface displacement and curvature. In this way, beam distortion due to acoustics can be used to measure the surface displacement [135].

2.5.5.3   Opto-acoustic transducers

Opto-acoustic transducers can be designed by putting an absorptive layer of metal on the sample for the generation and detection of sound waves. A thin film three-layer (Au-ITO-Au) transducer was designed to generate frequencies in the GHz range [117, 121]. These transducers were activated and read optically using pulsed lasers and did not need any physical contact between the instrumentation and the transducer. The detection sensitivity can be increased by choosing the proper material, layer thickness and probe wavelength.

Gold nanorods can act as nano-sized opto-acoustic transducers if they are excited with laser pulses having appropriate parameters such as wavelength and power. The particle vibrates because of the created stress and the vibrational frequency can be determined from the modulation of the probe laser light caused by the vibration. The working principle is described below in detail.

Optical generation in the nanoparticle is based on thermal excitation. The particle absorbs the pump light (of duration equal to or less than a picosecond) and becomes hot. This rapid heating causes stress in the particle and it vibrates as shown in figure 2.12 (a). The condition for efficient absorption is that a specific size of particle of a specific material in a specific external medium needs to absorb that specific wavelength of pump light. It is important to model the optical response of the particle to know its absorption spectra in a specific external medium. If the properties of the particle (size, shape and material) need to be fixed, then the pump laser wavelength, λ_{pump} can be tuned to satisfy the absorption criteria or the external medium can be chosen accordingly. On the other hand, if the operating wavelength range of the laser is limited and the external medium is fixed,

appropriate sizes and shapes of particles of appropriate materials can be purchased or fabricated so that they can be excited using the available experimental set-up. Nanorods are sensitive to their orientation to the light and for this reason, they exhibit different absorption cross-sections for different orientations. The absorption cross-section spectra of a 112 nm by 40 nm GNR in water simulated by SMARTIES [136] is shown in figure 2.12 (b) when the polarisation of the light was along the length (blue) and the width (red) where the longitudinal LSPR and transverse LSPR were at 515 nm and 735 nm, respectively. The rod can be excited with a range of wavelengths as can be seen from the spectra but different wavelengths would have different absorption efficiencies. The generation process will be a strong function of size, medium and orientation if the longitudinal LSPR is chosen as λ_{pump}. The intermediate wavelengths can also be used for the excitation if they provide enough absorption sensitivity.

The excited particle is illuminated by another probe laser and the particle scatters light at the wavelength of the probe laser. The vibration of the particle modulates the scattered light intensity which can be detected in transmission or reflection as shown in figure 2.12 (a). The change in the scattered light carries the information about the vibration of the particle and the vibrational frequency can be extracted from the obtained raw signal after some signal processing steps. As explained before the rod needs to be sensitive to the probe laser wavelength, λ_{probe} to be detected and this needs to be checked from the scattering cross-section spectra. The scattering cross-section spectra of a 112 nm by 40 nm GNR in water is shown in figure 2.12 (c) when the polarisation of light was along the length (magenta) and the width (cyan) where the longitudinal LSPR peak was at 735 nm. The sensitivity of detection over length (change in the scattering cross-section per nm change in length) is shown in figure 2.12 (d) where it can be seen that 720 nm and 760 nm had the highest sensitivity. This sensitivity analysis is important to choose proper λ_{probe}. The sensitivity analysis of a nanorod is explained in section 3.3.4 in detail.
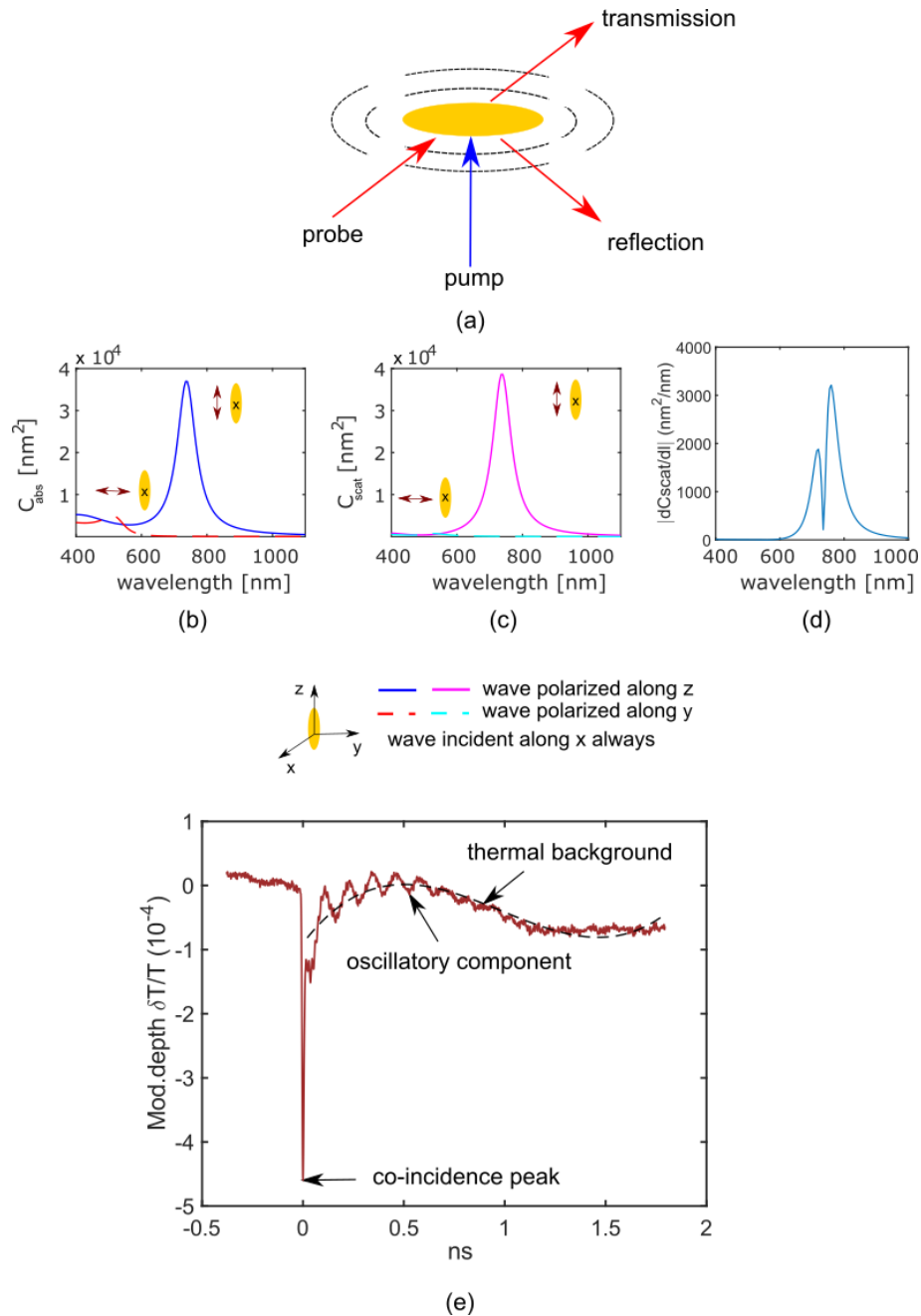
Figure 2.12: Generation and detection mechanism of a gold nanorod as an opto-acoustic transducer. (a) A schematic of a gold nanorod showing the excitation by a pump laser and detection by a probe laser. (b) Absorption cross-section spectra of a 112 nm by 40 nm GNR in water when the polarisation of light was along the length (blue colour, longitudinal LSPR peak at 735 nm) and the width (red colour, transverse LSPR peak at 515 nm). (c) Scattering cross-section spectra of a 112 nm by 40 nm GNR in water when the polarisation of light was along the length (magenta colour) and width (cyan colour). (d) Scattering sensitivity (scattering cross-section change per nm change in length) of a 112 nm by 40 nm GNR over length in water where 720 nm and 760 nm had the highest sensitivity. All the modelling results helped to choose the proper pump and probe wavelengths for the generation and detection of acoustic waves, respectively. (e) An experimental raw time trace from a gold nanorod which was obtained after exciting it with a pump laser and detecting with a probe laser.

An experimental time trace from a nanorod is shown in figure 2.12 (e) when it was excited by a pump laser and detected by a probe laser. Each time trace consists of a co-incidence peak, thermal background, background coming from laser electronics and oscillatory components on top of the thermal background. Co-incidence peak arises due to short-lived electronic effects while the pump and probe hit at the same time and the thermal background happens due to the temperature change of the particle. The oscillatory components carry the information about the vibrational frequency of the particle which is recovered by the probe pulse with time. The vibrational frequencies of the nanorod can be determined from the experimental raw trace after some signal processing steps that are explained in section 4.4.1.

2.5.5.4   Time resolved Brillouin scattering

Brillouin scattering [115] happens when the light scatters from the acoustic waves (phonons). Light scatters because the pressure associated with the acoustic waves changes the refractive index of the medium. Acoustic wave generates a Bragg grating due to opto-elastic effect. A part of the probe beam reflects from the travelling wavefront of the acoustic wave and interferes with the directly reflected probe beam (reference beam) as shown in figure 2.13. As a result, the light beam experiences a frequency shift and a temporal intensity oscillation is seen in the detected light. The mechanism is called time-resolved Brillouin scattering (TRBS)[117, 118, 124, 137–155].
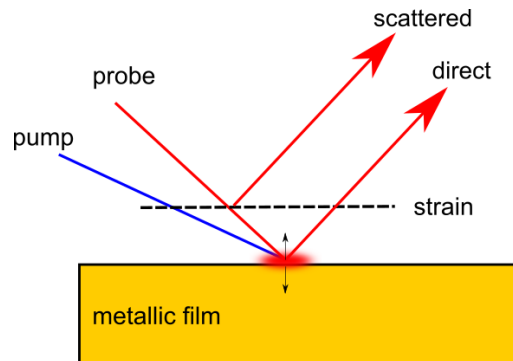
Figure 2.13: A Schematic of the time-resolved Brillouin scattering detection using PLU. The pump beam thermally generates the acoustic waves. The probe beam is reflected from the surface and acts as a reference beam where part of the probe beam is reflected by the travelling acoustic waves. In this way, direct and scattered beams interfere at the detector and temporal oscillation is seen, called Brillouin oscillations.

The frequency shift is called the Brillouin frequency and defined by

$$f_B = \frac{2n\nu}{\lambda_{probe}}cos\theta \tag{2.2}$$

where n is the refractive index of the medium, ν is the sound velocity, λ_{probe} is the probe wavelength and θ is the incident angle of the probe beam with respect to the normal. Coherent (right direction and frequency) acoustic phonons are generated to increase the amount of the scattered light by using picosecond ultrasonics and pump-probe technique.

Brillouin frequencies are generally in the GHz region. The frequency of water and glass are $\approx$5 GHz and $\approx$22 GHz respectively at 780 nm. Time-resolved Brillouin scattering technique is used to directly measure the sound velocity, acoustic impedance and sound attenuation in solid, transparent, semi-transparent and liquid media if refractive indices are known. Using this technique, measurements in metal thin films [124, 137], semiconductors [138–140], dielectrics [141–143], crystals [144, 145], liquids [146, 147] and biological cells [148–150] were performed. It was demonstrated that time-resolved Brillouin spectroscopy can achieve sub-optical axial resolution because each cycle of the detected signal corresponds spatially to one acoustic wavelength which is typically shorter than the optical wavelength [118]. However, the lateral resolution was still limited to the beam spot size. It can be improved by fabricating thin film transducers smaller than the laser spot size but the fabrication process will be complex. Metal nano-particles on the other hand are very promising as nano-sized opto-acoustic transducers which offer optical enhancement because of the LSPR, high lateral resolution and high signal-to-noise ratio. Scattering of GHz coherent acoustic phonons by silica nanoparticles in water was probed with TRBS technique [154]. When the sample is in a liquid medium, the measurement can be affected by strong Brillouin scattering in liquid. It was shown that by introducing nanoparticles as acoustic scatterers, the undesired Brillouin response of the liquid medium can be reduced. This was found advantageous to separate close Brillouin frequencies from the cell and the surrounding liquid during the elasticity characterisation of cells. The frequency of a thin film of thickness less than the optical wavelength was performed in this work without disturbance by the Brillouin interaction in the liquid. Using time-resolved Brillouin scattering, a novel optical fibre spectrometer was demonstrated in [147]. This

technique could also be applied to image in 3D through the optical fibre as presented in [155].

2.6   Vibrational modes

The elastic response of a mechanically isotropic material is defined by the Navier equation as follows:

$$\rho\frac{d^2\mathbf{u}}{dt^2} = (\lambda + 2\mu)\boldsymbol{\nabla}(\boldsymbol{\nabla}.\mathbf{u}) - \mathbf{u}\boldsymbol{\nabla} \times (\boldsymbol{\nabla} \times \mathbf{u}) \tag{2.3}$$

where $\mathbf{u}$ is the displacement factor, λ and μ are Lame elastic constants and ρ is the density. The vibrational eigenmodes correspond to its harmonic solution

$$\mathbf{u}(\mathbf{r}, t) = \mathbf{u}(\mathbf{r})\exp(i\omega t) \tag{2.4}$$

where ω will be real or imaginary depending on whether the modelling includes vibrational damping or not. The vibrational modes of metallic nanoparticles can be derived from equation 2.3 if the geometry is simple enough whereas numerical solutions are required for complex shapes. Lamb in 1881, at first computed the solutions of the Navier equation to derive undamped vibrations for stress free boundary conditions at the surface of a sphere [156]. These were extended by Dubrowskiy and Morochnik [157] to include intrinsic vibrational damping via acoustic energy transfer towards a homogeneous environment. According to these calculations, spheres have two types of vibrational modes, torsional and spheroidal. However, the excitation is uniform in time-resolved experiments on nano-spheres and excites only radial spheroidal modes.

Vibrational modes of nanostructures were first investigated through low frequency Raman scattering experiments [158]. Several modes were observed and results agreed well with the time-resolved measurements. However, the technique could not give the damping information.

Nisoli et al. first performed time-resolved measurements and investigated the acoustic vibrational modes [159]. Tin (solid) and Gallium (liquid) nanoparticles were used and femtosecond laser spectroscopy was performed. There is a considerable amount of research on the investigation of vibrational modes of metal nanospheres and obtained acoustics

modes are used to characterise them [58–60].

The optical and mechanical properties of nanoparticles are significantly dependent on their sizes and shapes. The interesting optical and mechanical properties of dumbbells were examined and explained in [160]. The optical reflection spectra of a single nanosphere and dumbbell were compared where additional modes were present in the case of the dumbbell. The modes were strongly dependent on the polarisation of light along the axis of the dumbbell. Vibrational modes were obtained using the ultrafast laser spectroscopy and it was reported that additional vibrational modes were present for dumbbells with a splitting of modes when one of the particles was bigger than the other. Importantly, an additional low frequency mode was found which was the oscillation of the centre of mass of the constituent particles along the dumbbell's long axis. The experimental results agreed with finite element method (FEM) simulations and the frequency was dependent on the contact area of the dumbbell. So, mechanical contact information can also be extracted by ultra-fast laser spectroscopy.

Radial vibrational modes of bi-metallic spherical core-shell nanoparticles and metal nano-shells embedded in different environments were studied in [161]. It was found that breathing mode frequency was always lower in metal nano-shells than solid particles of the same size but the damping was higher. It was also found that the frequency and damping rate of bimetallic nanoparticles were periodic functions of the aspect ratio but this dependence was monotonic for nanoshells. It can be understood that the vibrational properties of nanoparticles can be used to determine their composite structures, geometries and surrounding environments.

The vibrational frequency of metal nanoparticles is related to Young's modulus values of them. The Young's modulus value of a gold nanorod is a complex matter and depends on its crystal structure, growth direction, fabrication method and temperature, among others. Different researchers reported different values of Young's modulus of gold nanorods based on experiments and simulations.

Theoretical and experimental analysis of the vibrational response of cylindrical gold nanorods to ultrafast laser heating was first presented by Min Hu et al. [162]. The nanorod has two main vibrational modes, extensional mode along the long axis and breathing mode along the short axis. It was shown that Young's modulus of gold nanorod was 64 GPa,

which was lower than the value of bulk gold having Young's modulus of 79 GPa. It was also shown that the ratio of extensional and breathing mode vibrational frequencies of gold nanorod was equal to 2.32 times the aspect ratio of the rod.

Min Hu et al. again demonstrated in [163] by time-resolved spectroscopy that gold nanorods prepared by wet chemical synthesis showed lower Young's modulus than that of bulk gold.

Hristina Petrova et al. measured the vibrational response of gold nanorods by time-resolved laser spectroscopy and reported in [164] that Young's modulus of gold nanorod along [100] was 31±1GPa which was 26% lower than the bulk value $E_{[100]}$=42 GPa.

Peter Zilstra et al. measured the vibration modes of single gold nanorods and determined the elastic constants considering the crystal structure of the rods [165]. The authors concluded that the elastic constants of single particles agreed well with the bulk values. Young's modulus values of gold nanorods when the crystal directions were along [100], [110], [111] and polycrystalline were mentioned as 42 GPa, 81 GPa, 115 GPa and 78.5 GPa, respectively.

Mechanical properties of gold nanorods can also be determined by AFM as was done by Bernhard Reischl et al. [166]. It was found by using OliverPharr method that Young's moduli of the [100] terminated and [110] terminated single crystal nanorods, and the penta-twinned nanorod were 103±2 GPa, 140±2 GPa and 108±2 GPa, respectively.

The mechanical property or vibrational frequencies of anisotropic shapes like nanorods were discussed in [167]. Vibrational frequencies of silver and gold nanorods were modelled with FEM and simulated results were compared with the experimental results. It was found that the simulated results agreed well with the experimental results for the pentagonal-shaped rods rather than the cylinder-shaped. Temperature dependence of Young's modulus was also reported in this work where it was shown that Young's modulus decreased as the temperature increased.

Yong et al. investigated the ultrafast laser excitation and elastic modulus of individual gold nanorods by using integrated TTM-MD (two temperature model and molecular dynamics) in [168]. In combination with the continuum elasticity, elastic moduli of single gold nanorods were determined. It was shown that elastic modulus increased as the width of the rod increased with a trend to approach the bulk gold.

Ultrafast laser excited breathing mode vibrations and elastic properties of single and poly-crystalline gold nanorods were again studied by Yong et al. in [169] by atomistic simulations and FEM calculations. It was shown that the continuum model in the limit of an infinite rod length could be used to define the breathing mode vibrations of nanorods with an aspect ratio as small as ≈2.5, in combination with bulk material elastic constants. It was reported that the breathing mode vibrations of the penta-twinned nanorods were more affected by the crystal structure effect than the single crystal nanorod.

The effect of symmetry breaking and crystallinity on the vibrational modes of nano-objects was analysed using FEM in [170]. The evolution from nanosphere to nanorod was considered and a change in the vibrational modes was observed. The vibration of single crystal gold nanorod and nanowire were numerically investigated using Rayleigh-Ritz variational method by L. Saviot [171]. Raman spectra were calculated by considering the Brillouin scattering mechanism. It was shown that the difference between the cylindrical flat end and half-sphere end rods was negligible as long as the fundamental modes were considered. A larger difference was observed for overtones.

Vibrational response of metal nanoparticles can also be investigated without ultra-fast laser [172]. The size and distribution of gold nanorods were determined by the application of four-wave mixing (FWM) method using a continuous wave (CW) laser. The size of gold nanorods having aspect ratios of 3.8, 4 and 4.3 were characterised in an aqueous solution and the experimental results agreed well with the results simulated by the used analytical model.

Vibrational modes of nanoparticles can also be used as a sensing mechanism. Silver deposition on single nanorods was investigated by authors in [173] where it was found that the breathing mode frequency decreased (102 GHz to 79 GHz as the silver shell thickness increases from 0 nm to 4.8 ± 0.8 nm) with an increase in the silver deposition while the extensional mode remained constant up to 6 nm of shell thickness. It was also mentioned that the quality factor was not affected due to silver deposition which indicated that the introduced interface between gold and silver did not produce damping to the nanorod vibration. Vibrational modes of metal nanoparticles were measured by ultrafast laser spectroscopy and used to characterise their sizes and shapes [58, 59]. Vibrational modes can also be used to identify and locate nanoparticles inside the same optical point

spread function [60]. Acoustic vibrational modes of other shapes of nano-structures such as nanostar [174], and nanocage [175], among others were also investigated using ultrafast laser spectroscopy.

The lifetime of the acoustic vibration of metal nanoparticles depends on several factors such as acoustic impedance and viscosity of the environment, substrate effect, and crystal property, among others. Damping of single gold nanorod in different media was investigated by time-resolved pump-probe measurements in [176]. It was shown that the vibration got more damped in water than in air, specially the extensional mode. As a result, quality factor (Q) also reduced in a water medium. It was mentioned that the lubrication force between the nanoparticle and the substrate was responsible for this damping. It was demonstrated that the Q of the vibrational mode could be controlled by a thin layer of water on the nanoparticle.

The damping time and quality factor of monocrystalline colloidal and polycrystalline lithographically fabricated gold nanorods were investigated by single particle transient extinction spectroscopy in [177]. It was shown that the damping rate was much faster for lithographically prepared nanorods. The propagation of confined phonons inside the nanostructure was affected by the crystal defect, strong binding to the substrate, and surface roughness, among others. It was found that the mechanical contact between metal and substrate had no effect on damping (or quality factor Q) where intrinsic crystal defect was the main reason for fast damping. Damping of different sizes of lithography fabricated structures were compared and a constant quality factor was observed that can be helpful for optical switches and resonators. It was concluded that lithographically prepared polycrystalline nanorods show constant Q regardless of size, geometry, frequency, surface adhesion, and mode. Several research works have been done to investigate the damping of nanoparticles and the researches are still going on [178–180].

2.7 Resolution and related factors

Resolution is the ability to separate or resolve fine features that are very close in distance. The objective of any microscopy technique is to offer the best possible resolution where each microscopy technique has its own limitation. Light waves from point sources encounter diffraction while passing through the circular opening of lenses and hence optical microscopy is diffraction limited. The diffraction pattern has a bright central region with a series of concentric rings around it and is known as the Airy pattern [181, 182], named after George Biddell Airy who explained it. The focal pattern from an aberration free diffraction limited optical imaging system can be described by

$$I = I_0 \left[2 \frac{J_1(kNAr)}{kNAr} \right]^2 \qquad (2.5)$$

where I is the intensity distribution, I_0 is the maximum intensity at the centre of the airy disc, J_1 is the first order Bessel function of the first kind, $k = 2\pi/\lambda$, r is the radial coordinates of the image plane and NA is the numerical aperture of the system. The three-dimensional representation of the Airy pattern is known as the point spread function (PSF).

In figure 2.14, the images of two individual point sources (blue line) and the sum of their images (red dash) are plotted where the separation between the sources was reduced gradually. It can be seen in figure 2.14 (a) that the sum image did not differ from the individual images and two sources were resolved independently. In figure 2.14 (b) it can be seen that the distance between the sources was reduced but they were still resolvable. In contrast, the sum image differed from the individual images in figure 2.14 (c) and the presence of only one peak revealed that two objects were not resolved independently.

There are different criteria to estimate the minimum separation needed between two objects to be resolvable such as Abbe [182, 183], Rayleigh [182, 184] and Sparrow criteria [182, 185] where the last two are most commonly used.
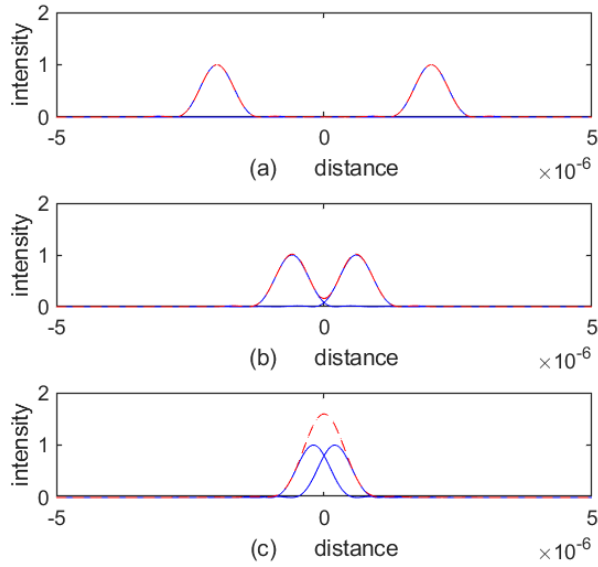
Figure 2.14: The images of two individual point sources (blue line) and the sum of their images (red dash) as the distance between the sources reduced. (a) Two individual sources (blue colour) were well separated from each other and the sum of their images (red colour) did not differ from their individual images. (b) The distance between the sources was reduced but they could be separated from each other and were resolvable. (c) The distance between the sources was very low and they could not be resolved because the sum of the image had only one peak, whereas there were two sources. (NA=0.65, λ=600 nm).
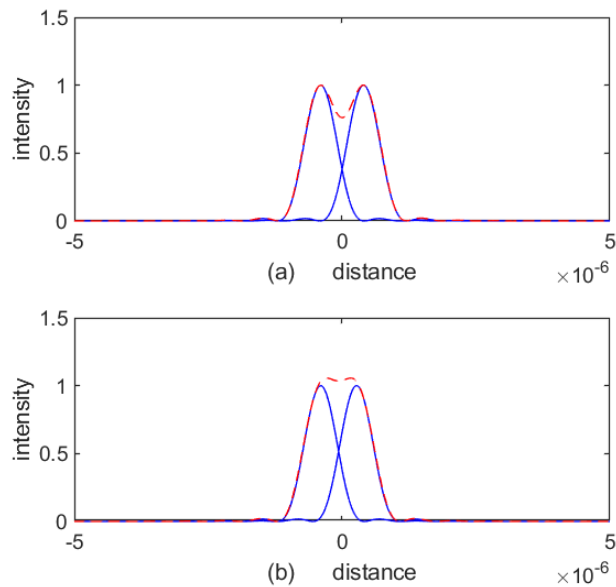
Figure 2.15: Different resolution criteria. (a) The Rayleigh Criterion. (b) The Sparrow criterion. (NA=0.65, λ=600 nm)

According to Abbe's formula, the minimum resolvable distance is

$$R_{Abbe} = \frac{\lambda}{2NA} \tag{2.6}$$

According to the Rayleigh criterion, if the centre of one Airy disc is overlapped with the first minimum of the diffraction pattern of another, two objects can be considered as just resolvable as shown in figure 2.15 (a). However, if the separation between two objects is smaller than this estimation, they will not be resolvable. This criterion is independent of the coherence of the two point sources and the separation can be mathematically expressed as

$$R_{Rayleigh} = \frac{0.61\lambda}{NA} \tag{2.7}$$

According to the Sparrow criterion, two adjacent objects are just resolvable when the intensity of the midpoint of the image has the same value as the peak value of the PSF as shown in figure 2.15 (b). This criterion applies to coherent or incoherent sources and mathematically expressed as

$$R_{Sparrow} = \frac{0.504\lambda}{NA} \tag{2.8}$$

It can be seen that the estimation of resolution is not a fixed term but is dependent on the operating wavelength and the numerical aperture. The wavelength for optical imaging is restricted to the visible spectrum and NA is limited to less than 1.5 for sophisticated immersion lenses. This leaves the resolution of optical imaging within a few hundreds of nanometers (for example, 174 nm when $\lambda = 400$ nm and NA=1.4, using the Rayleigh formula). Hence, it has always been tried to break the optical diffraction limit and offer high resolution with different techniques. Scanning electron microscopy uses very short wavelength electrons and offers very high resolution. However, it can damage the sample and it is also very expensive. Different available super-resolution imaging techniques are discussed next.

2.8 Super-resolution imaging techniques

This optical resolution is not enough for imaging, especially biological samples that have poor optical contrast. To defeat the optical diffraction barrier, engineering of PSF is done by super-resolution imaging techniques such as confocal microscopy [46], structured illumination microscopy (SIM) [47–49] and stimulated emission depletion (STED) [50–52], among others. In addition, single-molecule localisation techniques have been proposed and demonstrated to offer super-resolution such as stochastic optical reconstruction microscopy (STORM) [53–55] and photo-activated localisation microscopy (PALM) [46], among others. All these techniques are frequently used and work based on fluorophores. Non-fluorescent techniques have also been tried to defeat the optical diffraction barrier such as spatial modulation spectroscopy (SMS) [56] and photothermal microscopy [57]. All these techniques are explained briefly in this section.

2.8.1 Fluorescent-based techniques

Fluorescence microscopy is a light microscopy technique which uses fluorophores to increase the contrast for better imaging. It has become an essential tool for biomedical research because it can be used to image living cells efficiently [186–188]. Fluorescent dyes or fluorophores absorb light at a given wavelength and emit light at a longer wavelength. Fluorophores can be conjugated with antibodies or others to target a specific type of cellular structure with a high degree of specificity and high contrast.

The basic components of a fluorescent microscope are the light source, excitation filter, objective, dichroic mirror, emission filter and detector. A simple schematic of a fluorescent microscope is shown in figure 2.16. The sample is labelled with chosen fluorophores first. The light from the source is used to excite the fluorophores where the desired wavelength of light (applicable for the chosen fluorophores) is selected by the excitation filter. In this way, the excitation wavelength can be changed to excite different fluorophores. The excitation light is reflected by a dichroic mirror and focused on the sample through an objective. Fluorophores absorb light and the emitted light has a longer wavelength and low energy compared to the incident light. The dichroic mirror acts as a wavelength filter which passes the light of a longer wavelength emitted from the sample but reflects the excitation light
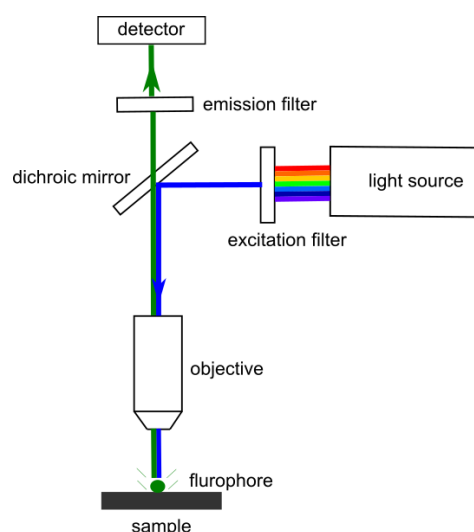
Figure 2.16: A Simple schematic of a fluorescent microscope. The excitation filter selects the desired wavelength of light that reflects from the dichroic to excite the fluorophore on the sample. Fluorophore then emits light of a longer wavelength that passes through the dichroic mirror and emission filter to the detector.

of a lower wavelength. The emission filter finally passes only the wavelengths of interest to the detector emitted by the fluorophores.

The high degree of specificity, high contrast, sensitivity and versatility of fluorescent probes have made fluorescent microscopy inevitable for live-cell imaging. However, the spatial resolution of conventional fluorescent microscopy (where all fluorophores emit at the same time) is still limited by the optical diffraction limit because when images from two fluorophores are closer than the optical diffraction limit, they are not resolvable.

2.8.1.1 Structured illumination microscopy (SIM)

Structured illumination microscopy (SIM) [47–49], is one of the super-resolution imaging techniques. It achieves super-resolution by moving the lost unobservable high frequency information (due to diffraction limit) into the observable region through the frequency mixing with a known illumination structure. The spatial illuminating structure is generated by passing the laser beam through a phase grating inside the microscope. The generated pattern is superimposed with the sample and different Moire patterns are created by rotating the illuminating pattern. All generated images with different angles are then post-processed to reconstruct the super-resolved image. In this way, it is possible to make the resolution double ($\approx$ 100 nm) [48]. It is a fast technique and can be used in

live biological imaging [49]. Optical sectioning is also possible with this technique. The disadvantages are lower resolution than other techniques, sensitivity to image artefacts and out-of-focus light, among others. A cancer cell was imaged using SIM as shown in figure 2.17 where it can be seen that the resolution was better than the wide-field and deconvolution techniques.
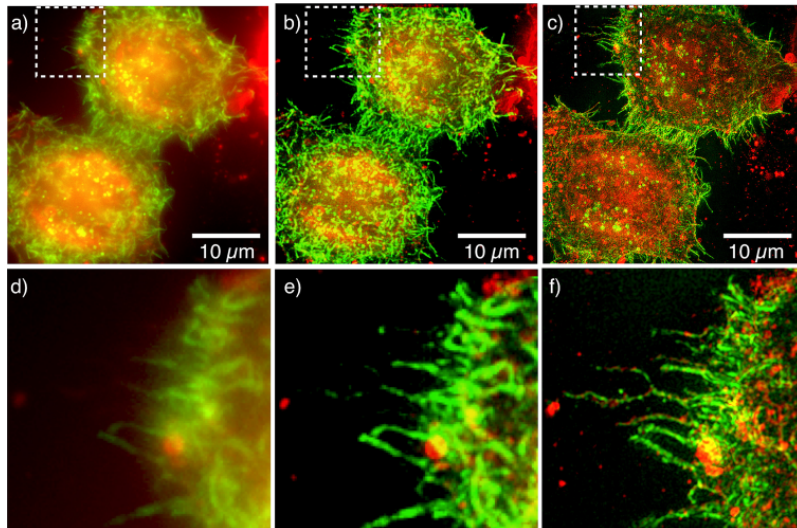
Figure 2.17: (a) Maximum intensity projection micrographs of osteosarcoma (U2OS) cells shown in wide-field epifluorescence. (b) Deconvolution of the epifluorescence data. (c) 3D SIM. The green colour channel encodes for transmembrane β-dystroglycan-eGFP subunit, while the red colour channel highlights the plasma membrane stained with CellMask orange. Magnified views of the boxes are highlighted in the upper row are shown lower row, (d)-(f). Reprinted (adapted) with permission [47].

2.8.1.2 Stimulated emission depletion microscopy (STED)

Stimulated emission depletion (STED) [50–52], proposed by Stefan W. Hell, is a super-resolution imaging technique where the area of fluorescence is reduced below the diffraction limit. In addition to the excitation beam to excite fluorophores, a doughnut-shaped depletion beam (zero intensity at centre) of high intensity is applied as shown in figure 2.18 (a) and 2.18 (b), respectively.
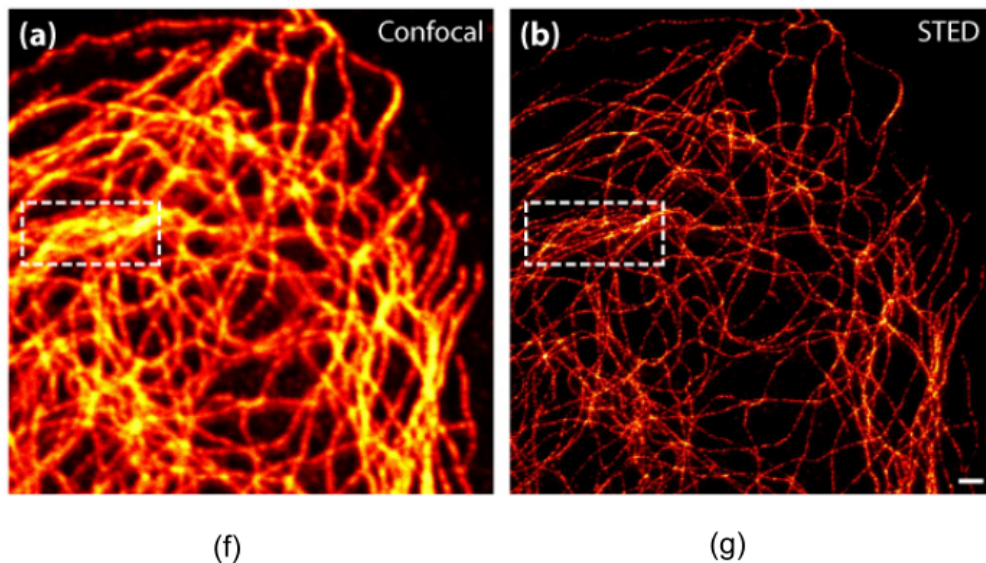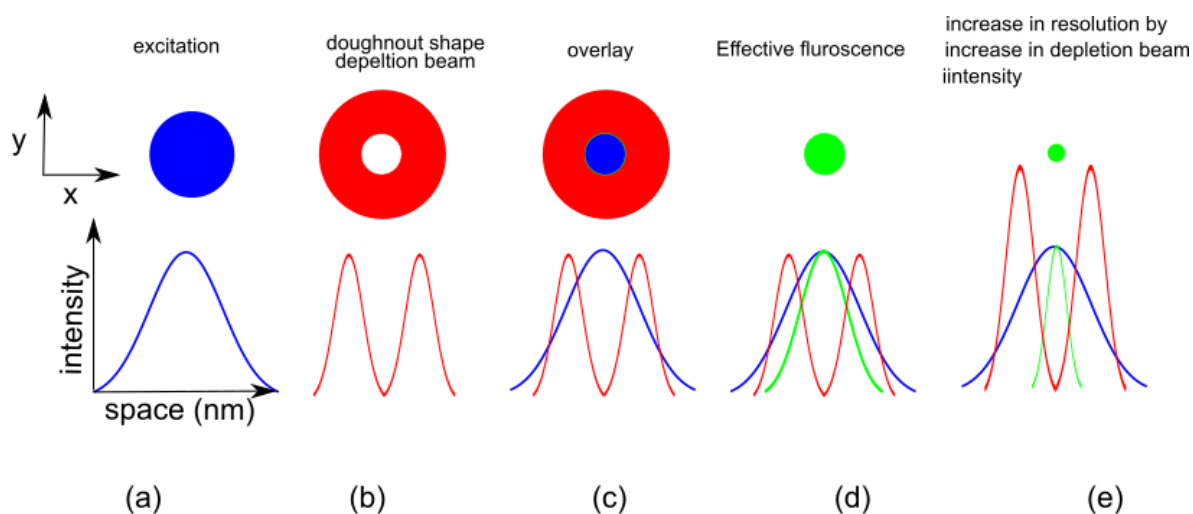
Figure 2.18: Working principle of STED. (a) Excitation beam and PSF. (b) Depletion beam (doughnut shape) and PSF where the intensity at the centre is almost zero. (c) Overlay of the excitation beam and depletion beam. Excitation only works at the inner part (centre) of the depletion beam where the outer part is suppressed by the stimulated emission and not allowed to fluoresce. (d) Reduced effective PSF from where only fluorescence happens which in turn offers super-resolution. (e) Depletion beam intensity can be increased further (saturated depletion beam) to increase the resolution more. (f) (g) Images of the microtubular network of PtK2 cells imaged with a confocal and a single-beam STED microscope, respectively. It can be seen that the confocal image provides less detail than the STED image. Reprinted with permission [51].

The depletion beam prevents the fluorophores to come back to the ground state by emitting photons but forces them to relax to a higher vibrational state. Hence, the required energy difference to fluoresce becomes lower and the photon wavelength shifts to the

red end of the spectrum. Eventually, the stimulated photons are ignored and the active fluorophore area is reduced. The result of this summation as seen in figure 2.18 (c) is that the excitation volume is reduced and focused on the centre only. The fluorophores at the centre can only fluoresce but the fluorophores outside the small circle are de-activated by the stimulated emission using the depletion beam as shown in 2.18 (d). This means that the effective PSF is smaller now and can break the diffraction limit. The resolution can be further improved by increasing the intensity of the depletion beam or saturating the depletion beam as shown in figure 2.18 (e). It can be seen that the image from STED microscopy as shown in figure 2.18 (g) is super clear than the image from confocal microscopy as shown in figure 2.18 (f). The technique has successfully been applied to image living cells and lateral resolution up to 20-40 nm has been achieved already [52].

2.8.1.3 Stochastic optical reconstruction microscopy (STORM)

Stochastic optical reconstruction microscopy (STORM) [53–55] is a fluorescent microscopy which uses single-molecule localisation microscopy (SMLM) approach to achieve a better resolution than conventional fluorescent microscopy. In conventional fluorescence microscopy, all fluorophores are excited at the same time as shown in figure 2.19 (a) and the result is a blurred image. In STORM, the main technique is to turn on and turn off fluorophores at different times so that a single fluorophore can produce a diffraction-limited spot.

It can be seen in figure 2.19 (b) that fluorophores are turned on at different times sequentially. The location of an individual fluorophore is found by using the centroid localisation algorithm and Gaussian fitting method as shown in figure 2.19 (b). In this way, a set of fluorophores is localised in each image frame and all sets are merged at last to reconstruct the final image with super-resolution as shown in figure 2.19 (c). The technique suffers from the inherent photo-bleaching problem and high acquisition time. The acquisition time can be reduced by reducing the number of measurements but at the cost of image resolution.
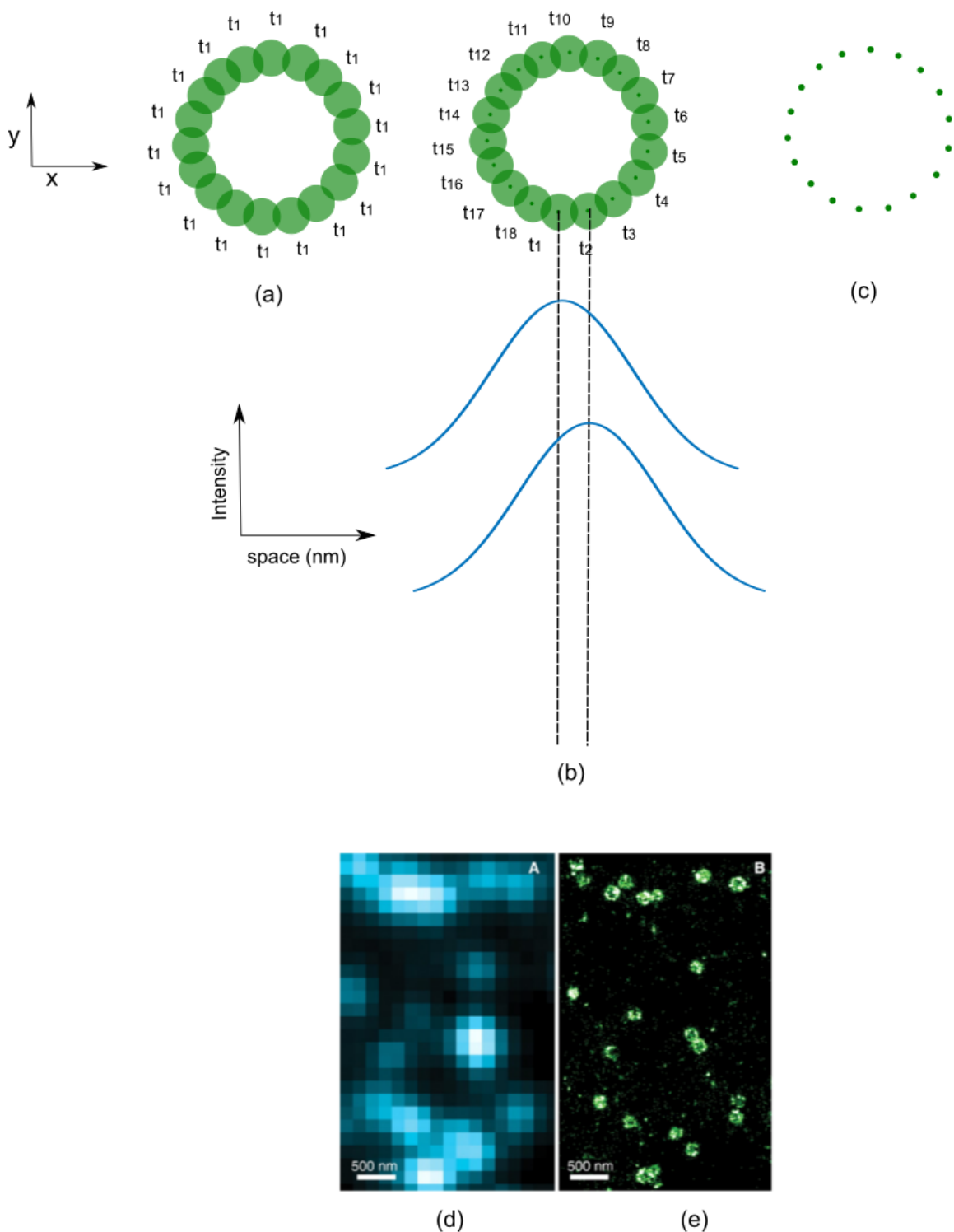
Figure 2.19: Working principle of Stochastic optical reconstruction microscopy (STORM). (a) Conventional fluorescence image where all fluorophores are excited at the same time. It is not possible to separate them if they are more close than the optical diffraction limit. (b) Different sets of fluorophores are excited at different times so that each fluorophore can produce a diffraction limited spot. Fluorophores are localised using the centroid localisation algorithm and Gaussian fitting method. (c) Localised points from all separate attempts are merged to form the final super-resolved image. (d) Conventional direct immunofluorescence image of clathrin in a region of a BS-C-1 cell. (e) The 2D STORM image of the same area, with all localisations at different z positions. Reprinted with permission [55].

49

2.8.1.4 MINFLUX and MINSTED

Another concept of super-resolution, named MINFLUX, was proposed and demonstrated in 2017 by the group of Stefan W. Hell [189, 190]. The main idea behind MINFLUX was to probe the emitters with doughnut-shaped excitation beam and use the zero intensity (centre) of the beam for the localisation while individual emitters were turned on and off sequentially. The advantages were the reduction of the amount of photons required for precise localisation and less photo-bleaching. It was shown that MINFLUX could achieve a precision of $\approx$1 nm and molecules only 6 nm apart were resolved. According to the claim from authors, MINFLUX can provide a high speed localisation technique that does not depend on wavelength and opens the door of super-resolution to low numerical aperture lenses and wavelengths outside the visible spectrum.

A similar idea of MINFLUX can also be applied to STED. A new concept based on STED named MINSTED nanoscopy [191] was offered by the group of Stefan W. Hell in late of 2020. The main difference between STED and MINSTED was that in the latter, the doughnut beam was used only for localisation, not for the separation of fluorophores. It was ensured that one fluorophore was active at a time. The minimum of the STED beam was aligned with the fluorophore and used for precise localisation. This process ensured less photo-bleaching and reached the resolution of molecular scale with fewer detected photons. It was shown that MINSTED could attain 1-3 nm of spatial resolution. Authors claimed that MINSTED can offer improved background suppression than MINFLUX and can handle higher densities of fluorophores.

One of the main disadvantages of fluorescence-based microscopy is that it requires high light intensities, which can produce optically induced damage and the fluorophores bleach. This photobleaching occurs when a fluorophore permanently loses the ability to fluoresce due to photon-induced chemical damage and covalent modification. It reduces the sample observation time during the microscopy. However, strong fluorophores can be chosen or illumination time can be decreased to reduce the photobleaching effect. Another disadvantage is that the chemicals generated from fluorophores can be toxic to living cells [192]. Therefore, it also has been tried to use alternatives to fluorescent labels to overcome these limitations.

2.8.2 Non-fluorescent based techniques

Spatial modulation spectroscopy (SMS) [56, 193] and photo-thermal microscopy [57, 194] are two non-fluorescent based techniques. In [193], SMS was used to image single organic nanoparticles doped with non-fluorescent near-IR croconaine dye. SMS images were recorded for particles within EMT-6 breast cancer cells. In SCSMS, the analyte's position is modulated relative to the diffraction limited probe which allows the acquisition of a single particle's extinction spectrum in the visible and NIR region. Photothermal microscopy (PTM) detects the small additional divergence of a transmitted probe beam through the heating induced thermal lens, i.e, the refractive index gradient around a heated nanoparticle. Confocal PTM was developed providing three-dimensional (3D) mapping and spectral identification of multiple chromophores and fluorophores in live cells [194].

In this thesis, it is proposed to use gold nanorods as alternatives to fluorophores to achieve a phonon-based super-resolution imaging technique that can image biological nanostructures. The technique will be similar to STORM and PALM but acoustic signatures of metal nanoparticles will be used instead of fluorophores. The advantage is that nanoparticles do not bleach like fluorophores and can ensure stable imaging for a long time. As in STORM subsets of fluorophores are activated and deactivated, different sets of gold nanorods can be activated and deactivated by changing the polarisation of light. The reason is that nanorods are sensitive to their orientation to the light or the polarisation of light and this property can be used to turn them 'on' and 'off'. As Gaussian function is used in STORM to locate the emitter, a Gaussian pulse and centre of mass formulae can be used to locate the nanorod. Gold nanorods can be easily functionalised and are well-tolerated by biological cells. In addition, as the technique is phonon-based, it will not damage cells and can also provide mechanical information about the surrounding environment.

2.9 Thermal effect on gold nanorods and biological cells

Metal nanoparticles are temperature sensitive. The effect of temperature on gold nanorods encapsulated in micelles was discussed in [195]. It was shown that the aspect ratio of gold nanorods decreased as the temperature increased while the width remained constant. The

reason was the different thermal instability of capping micelles of different lengths, as mentioned by the authors. Laser induced heat also reshapes and melts the gold nanorods. A theoretical model was proposed in [196] to analyse the thermal effect of gold nanorods in an aqueous medium heated with femtosecond laser pulses. Shape change of colloidal gold nanorods using femtosecond and nanosecond laser pulses was demonstrated in [197]. It was shown that femtosecond laser pulses were suitable for reshaping gold nanorods in an aqueous solution and also required 100 times less energy to melt them. Gonzalez-Rubio et al. annealed gold nanorods dispersed in an aqueous solution of a surfactant with carefully tuned ultrafast (femtosecond) laser pulses in [198]. Laser reshaping and melting can also be used in optical recording. For instance, Peter Zijlstra et al. melted gold nanorods selectively by applying different wavelengths and polarisations of light to write different patterns for optical recording [23]. From this discussion, it can be understood that the temperature change can affect the performance of gold nanorods and also this effect can be used to reshape them. The thermal effect on gold nanorod is also used in photothermal therapy [5–8] where the laser induced heat is used to damage the cancer cells. Hence, thermal effect on gold nanorods can be an advantage and also a disadvantage which depends on the application.

For this project, an excessive heat effect on gold nanorods was undesired because that can change the size, shape and frequency of them. Unfortunately, thermal effect on gold nanorods was observed during some experiments of this project, specially while using the NIR-NIR (generation-detection) set-up (please see section 6.5 of chapter 6). To avoid this problem, most of the experiments were carried out using the UV-NIR set-up with low power in this project. However, several ways can be applied to reduce the heat effect as has been proposed in section 6.6 of chapter 6.

Thermal effect on biological cells is a matter of concern. Intolerable and undesired heat can damage cells or change their natural biological processes. In [118], high resolution 3D imaging of living cells with sub-optical wavelength phonons was performed. A transducer composed of three layers (Au-ITO-AU) on a sapphire substrate was designed and optimised to enhance the thermal management. Typical average powers of 1 mW (0.3 mW at cell) in the probe (780 nm) and 0.5 mW (0.05 mW at cell) in the pump (390 nm) were applied to image live 3T3 fibroblast cells. The damage threshold of cells caused by NIR

laser pulses were reported to be safe for power densities of $1.7 \times 10^{14} \, W/m^2$ scanning a sub-micrometre spot for over 35 minutes. In the measurements of [118], the power density was approximately $8.5 \times 10^{12} \, W/m^2$ scanning a one micron spot for approximately 38 minutes which was safe. Although UV is harmful for cells, cell imaging could be done using UV with the mentioned parameters above. It was also reported that the temperature at the cell/substrate raised to $25°C$ above the room temperature for a glass substrate. In contrast, the temperature raised to $7°C$ above the room temperature for a sapphire substrate. All these ratings cannot be directly used for gold nanorods because they have different properties than plate transducers. However, an idea can be developed to apply the experimental parameters for gold nanorods. As nanorods have high absorption cross-sections, power can be lowered for them to be safe. It is possible to estimate the temperature rise for a gold nanorod as was estimated by Peter Zijlstra and co-workers in [165].

In [150], the temperature at the vicinity of a transducer was estimated through FEM simulations and it was found that the temperature was high for glass, low for sapphire, and lowest for diamond. Hence, in general, it can be said that the use of highly conductive diamond substrates for gold nanorods can reduce the heat effect on them. However, this heat reduction can only happen if the gold nanorods are bonded to the highly conductive substrate. In the case of cell imaging with gold nanorods, using highly conductive surfaces may not be beneficial because gold nanorods will be bounded to the cell, not to the substrate. Other recommended ways as mentioned in chapter 6 (section 6.6) then can be tried to reduce the heat effect so that the cells do not get affected.

2.10 Summary

Theoretical background and related research works were reviewed in this chapter. Unique characteristics, applications and preparation procedures of metal nanoparticles were presented in detail. Available characterisation techniques of metal nanoparticles, advantages and limitations of those techniques were thoroughly discussed. In addition, the theoretical background, applications and generation/detection techniques of laser ultrasonics were explained briefly. The resolution limit of optical microscopy, available super-resolution imaging techniques with their merits and demerits were also discussed. Although biologi-

cal nanostructures were not imaged by using gold nanorods in this research, the long-term motivation behind this work was to help make progress towards a phonon-based super-resolution imaging technique for biological nanostructures labelled by gold nanorods. The thermal effect of metal nanoparticles can be used in many applications such as photothermal therapy, drug delivery, optical data storage, among others. However, this heat effect can be undesired for many applications. For this research, the vibrational frequency of a gold nanorod was a significant parameter. Hence, it was not desired that the laser-induced heat changes the frequency of particles by modifying their sizes and shapes or completely damaging them. This problem can be severe in case of using gold nanorods inside biological cells. The chapter was concluded by discussing the thermal effect on gold nanorods and biological cells briefly.

Chapter 3

Modelling

3.1 Introduction

In this chapter, a short review of different available modelling tools for simulating the responses of metal nanoparticles is presented first. Then, gold nanorods are modelled as opto-acoustic transducers by using analytical and finite element method (FEM) based models [199–203]. Mainly, optical and mechanical responses of gold nanorods are described here. SMARTIES (a non-commercial Matlab code package) [136] is used as an analytical tool and COMSOL Multiphysics is used as a FEM based tool to simulate the optical responses of gold nanorods of different sizes and shapes in different external media. On the other hand, the analytical model developed by Hu et al. [162] and the FEM tool COMSOL Multiphysics are used to simulate the mechanical responses of gold nanorods of different sizes and shapes. Simulated results obtained by analytical model are also compared with FEM based approach and presented in this chapter.

3.2 Various modelling tools

Several numerical methods are available to simulate the responses of metal nanoparticles such as finite element method (FEM) [199–203], boundary element method (BEM) [204, 205], discrete dipole approximation (DDA) [206–212], finite difference time domain method (FDTD) [213–217], and T-matrix [136, 218–221], among others.

The Finite element method (FEM) is a numerical technique that solves a complex

physical phenomenon by subdividing the structure into an assembly of finite elements and provides approximate solutions of partial differential equations (PDE) over all the elements where boundary conditions are specified. This method is adaptive, accurate, flexible, less expensive and easy to model complex geometries. It can also solve different physical phenomena simultaneously, for example, coupling of heat transfer and solid mechanics modules. It has been used in several cases, such as modelling cardiac ablation [200], orthopedic mechanics [201], deformation of composite structures [202] and human liver physiology [203], among others. The choice of mesh size is very important in this method. Accurate results can be obtained by using a small mesh size but at the cost of high computational time. In contrast, a larger mesh size reduces the computational time but can give an inaccurate solution. Hence, it is important to choose a mesh size that can provide adequate accuracy and reasonable computational time. Mesh size can be made adaptive depending on regions to get more accuracy, for example, a small mesh element size can be chosen near the boundaries or curvature. The disadvantage of this method is that the approximations of domain discretisation introduce errors. It is good to compare the solutions from FEM with solutions from any analytical model so that the mesh size can be chosen properly to save computational time. Several commercial FEM-based softwares are available, such as Ansys, Abaqus, COMSOL Multiphysics etc. In this research, COMSOL Multiphysics is one of the tools which was used to obtain the optical and mechanical responses of gold nanorods. A two-dimensional geometry of a gold nanorod designed by COMSOL Multiphysics is shown in figure 3.1 where axial symmetry was used. It can be seen that the nanorod geometry was considered as one domain and then was divided into many elements (300 domain elements and 64 boundary elements) when meshing was done.
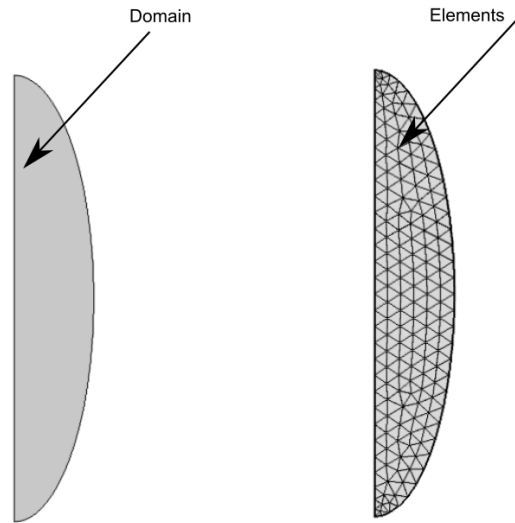
Figure 3.1: A gold nanorod geometry (2D) designed in COMSOL Multiphysics using axial symmetry. It can be seen that FEM divided the whole domain into mesh elements to provide a solution.

The discrete dipole approximation (DDA), pioneered by Purcell and Pennypacker [206], is one of the methods to compute the electromagnetic absorption and scattering of particles of arbitrary shapes. In this method, the scatterer is replaced by interacting dipoles and hence this method is also known as coupled dipole method [207]. The method became more popular since the availability of computer code DDSCAT, developed by Draine and coworkers [208]. Researchers frequently use the DDA method for metallic nanoparticles to compute the absorption/scattering spectrum [209, 210], refractive index sensitivity [211] and the effect of size and shape on the optical response [212], among others.

The finite difference time domain (FDTD) method (Yee's method) [213] is a numerical method that solves Maxwell's equations in a discrete form both in spatial and temporal domains to compute the field distribution at different locations at different times. It is simple, accurate and robust. However, the solution can be very time-consuming if the computational domain has fine grids. This method is very popular to simulate the optical properties of nanoparticles [214], breast tissue properties and distribution [215] and electromagnetic absorption in the human body [216], among others. Several simulation tools implement FDTD algorithms, such as Lumerical, OmniSim and OptiFDTD, among others.

The T-matrix (Transition matrix) method, pioneered by Peter C. Waterman, is one of the most versatile and efficient computational techniques of light scattering by non-spherical particles [218]. A variety of methods can be used to calculate the T-matrix, such as the extended boundary condition method (EBCM) [219] and the point matching method [220], among others. Spheroids modelled accurately with a robust T-matrix implementation for electromagnetic scattering (SMARTIES) is a MATLAB implementation of an improved T-matrix algorithm for the theoretical modelling of electromagnetic scattering by particles of spheroidal shape [136]. The commonly used EBCM method is applied in SMARTIES to simulate the light scattering properties of spheroidal particles [221]. It is one of the tools which was used in this research to simulate the optical response of gold nanorods.

3.3 Modelling of gold nanorods as opto-acoustic transducers

In this PhD work, gold nanorods were designed as opto-acoustic transducers where the following physical phenomena occurred:

1. The light was absorbed by gold nanorods.

2. Absorption of light created heat in the particles.

3. Heat introduced mechanical resonances of the particles.

4. Mechanical resonances were detected optically by the changes in the optical scattering cross-section due to the particle vibration.

These physical phenomena were modelled by simulation tools in this work to investigate mostly the optical and mechanical responses of gold nanorods.

3.3.1 Optical absorption

Light will be absorbed by a gold nanorod if it has the proper wavelength and power needed for that specific size or shape of rod in a specific external medium. A non-commercial Matlab code package, SMARTIES as an analytical tool and COMSOL Multiphysics as a FEM based tool were used in this research to simulate the optical responses of gold nanorods

of various sizes and shapes in different external environments for different polarisations of
light.

3.3.1.1 Analytical model

Spheroids Modelled Accurately with a Robust T-matrix Implementation for Electromagnetic Scattering (SMARTIES) is a MATLAB implementation of an improved T-matrix algorithm for the theoretical modelling of electromagnetic scattering by particles of spheroidal shape [136]. It offers user-friendly codes for fast and accurate calculations. The optical response of a nanorod depends on its size, shape, material and external medium [27–30]. Using SMARTIES, it is possible to change all the mentioned parameters except shape to investigate the optical properties of a gold nanorod.

The optical response of a gold nanorod was investigated by measuring the optical cross-section spectrum in this research work. The optical cross- section is a measure of the interaction strength of light with nano-object. Mathematically, it can be expressed as the ratio of power (absorbed/scattered) to the incident intensity. Simply, the cross-section can be defined as the effective area of interaction. The geometry of a gold nanorod is considered as a prolate spheroid in SMARTIES as shown in figure 3.2.
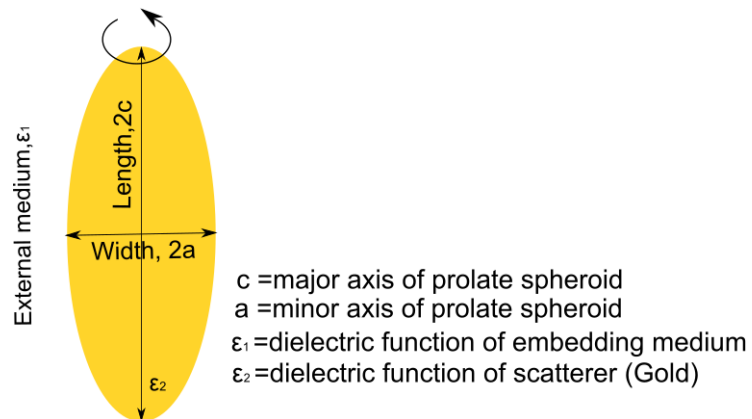
Figure 3.2: A prolate spheroid, the geometry of a gold nanorod in SMARTIES.

The absorption cross-section (C_{abs}) spectra of a 112 nm by 40 nm gold nanorod in a water medium are shown in figure 3.3 for two different polarisations of light. A nanorod is sensitive to its orientation to the light or the polarisation of light. It can be seen from figure 3.3 that the absorption cross-section was very high (blue) when the polarisation of light

was along the length of the nanorod (longitudinal mode). In contrast, the cross-section was very low (red dash) when the polarisation of light was along the width (transverse mode) of the nanorod. It can also be observed that the longitudinal LSPR peak and transverse LSPR peak of 112 nm by 40 nm GNR in water were at 735 nm and 515 nm, respectively. It can be understood from this simulation that the polarisation of light can be used to 'turn on' (generating) or 'turn off' (not generating) a nanorod.
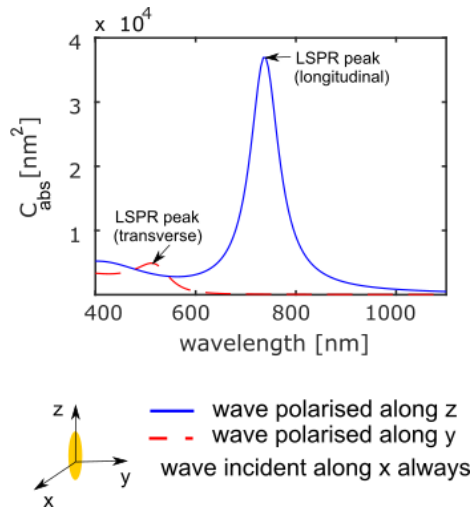
Figure 3.3: Absorption cross-section spectra of a 112 nm by 40 nm GNR in a water medium simulated by SMARTIES for different polarisations of light. It can be seen that the cross-section was very high (blue) when the polarisation of light was along the length of the nanorod but very low (red dash) when the polarisation of light was along the width of the nanorod. Longitudinal and transverse LSPR peaks were found at 735 nm and 515 nm, respectively.

Absorption cross-section spectra of GNRs for different aspect ratios and external media:

Aspect ratio (AR) of a GNR is defined as the ratio of length to width. It can be noted from the absorption cross-section spectra shown in figure 3.4 (a) that the longitudinal LSPR peak of a GNR shifted to a longer wavelength when the aspect ratio of the rod increased and vice versa. The size of a nanoparticle governs the resonant condition of its plasmon. The distance between the charges at the opposite interfaces of the particle increases when the size of the particle increases and thus the restoring force reduces. So, the resonant frequency decreases and the resonant peak shifts to the longer wavelength. In short, it can be said that larger particles oscillate at longer wavelengths. It can also be seen in figure 3.4 (a) that the width of the resonant peak broadened when the particle size increased which happened due to radiation damping [222]. Radiation damping is caused

by the directive decay of the coherent electron oscillations into photons. In contrast, it can be seen in figure 3.4 (b) that the transverse LSPR peak was almost insensitive to the change of the aspect ratio of the rod.
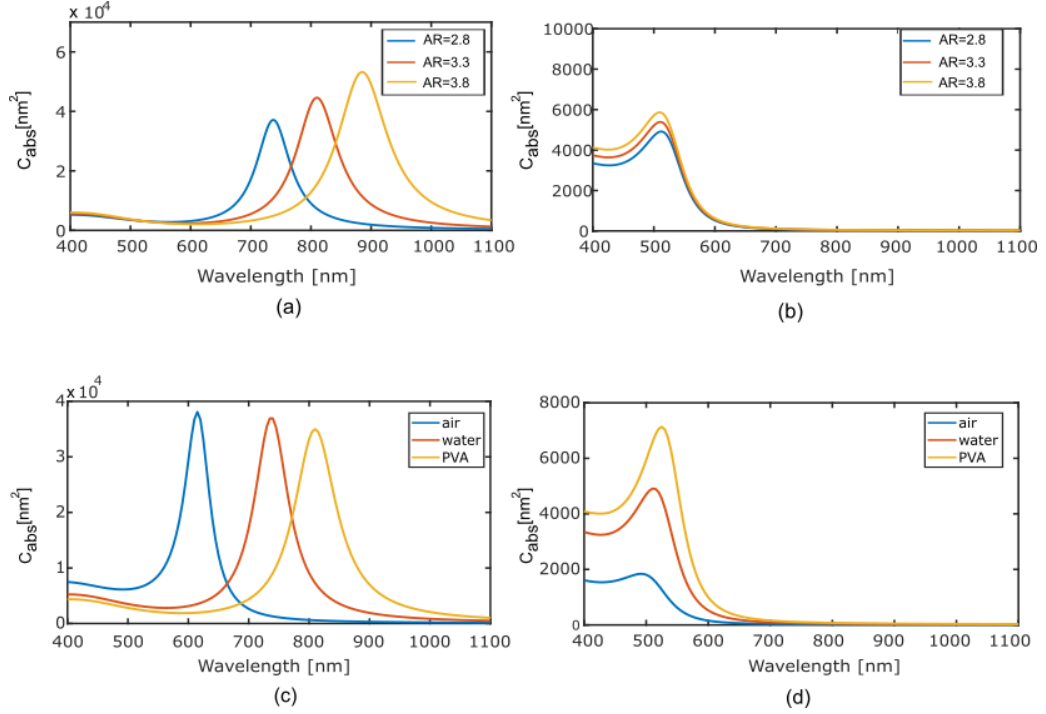
Figure 3.4: Absorption cross-section spectra of GNRs for different aspect ratios and external media. (a) Absorption cross-section spectra of GNRs for different aspect ratios showing the longitudinal LSPR peaks. (b) Absorption cross-section spectra of GNRs for different aspect ratios showing the transverse LSPR peaks. (c) Absorption cross-section spectra of a GNR (112 nm by 40 nm) in different external media showing the longitudinal LSPR peaks. (d) Absorption cross-section spectra of a GNR (112 nm by 40 nm) in different external media showing the transverse LSPR peaks. It can be seen that the LSPR peak of a GNR shifted to the longer wavelength when the aspect ratio and refractive index of the external medium increased. In contrast, transverse LSPR peak was almost insensitive to the change of the aspect ratio and external medium of the rod .

The external medium has a significant effect on the optical response of a nanorod and also in cooling dynamics of it [30]. When the external medium changes, the refractive index of the surrounding environment changes too. This effect is simulated for a 112 nm by 40 nm GNR in figure 3.4 (c) where it can be seen that the longitudinal LSPR peak shifted to a longer wavelength when the refractive index of the medium increased from 1 (air) to 1.5 (Polyvinyl alcohol). The physical explanation behind this change is that the effective resonant wavelength decreases when the refractive index of the medium increases. Hence, the probing wavelength outside the medium should increase to satisfy the resonance

condition of the rod. So, the resonant wavelength shifts to the right (longer wavelength) when the refractive index of the medium increases. Nanorod is often used as a sensor to detect any change in the external environment. For example, gold nanorod is used as a biosensor to monitor the change of the refractive index at the surface of the nanoparticle due to adherence of bio-molecules [87]. In contrast, figure 3.4 (d) shows that the shift of the transverse LSPR peak was negligible when the external medium of the rod changed.

The pump wavelength to excite a specific gold nanorod in a specific external medium can be fixed from the absorption cross-section spectrum of that gold nanorod. In this work, a wavelength at or near the LSPR peak was chosen as the pump wavelength when experiments were carried out using the NIR-NIR mode. However, most of the experiments were carried out using blue light (UV) as the pump beam in this work.

3.3.1.2 Finite element method (FEM) based models

COMSOL Multiphysics, a FEM based tool was used in this PhD work in addition to the analytical model to simulate the optical response of gold nanorods. This tool is accurate and offers flexibility to design any geometrical shape. However, it is more time consuming than SMARTIES. For this project, it was necessary to see the difference in the optical and mechanical responses of gold nanorods due to their shape diversity. In SMARTIES, gold nanorod was a prolate spheroid by default and it was not possible to change its shape. Hence, COMSOL Multiphysics was used in this work not only to confirm the results from SMARTIES but also to have some additional facilities.

A 3D finite element optical model was designed using the RF module of COMSOL Multiphysics to calculate the absorption and scattering cross-section of a gold nanorod embedded in a water medium. Cross-section can be defined mathematically as the net rate at which the electromagnetic energy, W crosses the surface of an imaginary sphere centred at the particle divided by the incident irradiation, P_{inc}. Cross-sections were calculated by using the following equations

$$\sigma_{abs} = \frac{W_{abs}}{P_{inc}} \tag{3.1}$$

$$\sigma_{sca} = \frac{W_{sca}}{P_{inc}} \tag{3.2}$$

where σ_{abs} is the absorption cross-section, σ_{sca} is the scattering cross-section, P_{inc} is the incident irradiance, W_{abs} is the energy rate absorbed by the particle and W_{sca} is the rate of scattered energy. The extinction cross-section is the summation of the scattering and absorption cross-section that estimates the total amount of energy lost from the incident field.

$$\sigma_{ext} = \sigma_{abs} + \sigma_{sca} \tag{3.3}$$

The total absorbed energy was derived by integrating the energy loss over the volume of the particle

$$W_{abs} = \iiint_{V_p} Q_{loss} \, dv \tag{3.4}$$

where the energy loss rate Q_{loss} in a particle can be expressed as:

$$Q_{loss} = \frac{1}{2} Re[\mathbf{J}_{tot} \cdot \mathbf{E}^* + j\omega \mathbf{B} \cdot \mathbf{H}^*] \tag{3.5}$$

where the total current, J_{tot} is the superposition of conduction and displacement current

$$\mathbf{J}_{tot} = \sigma \mathbf{E} + j\omega \mathbf{D} \tag{3.6}$$

where σ is the electrical conductivity, E is the electric field, ω is the angular frequency and D is electric displacement. The scattered energy was derived by the integration of the Poynting vector over an imaginary sphere around the particle

$$W_{sca} = \oiint_{s} \mathbf{P}_{sca} . \mathbf{n} dS \tag{3.7}$$

The scattered Poynting vector, $\mathbf{P}_{sca}$ can be expressed as

$$\mathbf{P}_{sca} = P_{sca}^x \hat{\mathbf{x}} + P_{sca}^y \hat{\mathbf{y}} + P_{sca}^z \hat{\mathbf{z}} \tag{3.8}$$

where $P_{sca}^x \hat{\mathbf{x}}$, $P_{sca}^y \hat{\mathbf{y}}$ and $P_{sca}^z \hat{\mathbf{z}}$ are the time averaged x, y and z component of the Poynting vector of the scattered electromagnetic field respectively. Incident irradiance, $P_{inc} = n_m \frac{E_0^2}{2Z_0}$ where n_m is the refractive index of the medium, E_0 is the incident electric field, $Z_0 = \sqrt{\frac{\mu_0}{\epsilon_0}}$ is the impedance of free space where μ_0 and ϵ_0 are the permeability and permittivity in

free space respectively.

The electromagnetic wave in the frequency domain was defined as

$$\nabla \times \mu_r^{-1}(\nabla \times \mathbf{E}) - k_0^2(\epsilon_r - \frac{j\sigma}{\omega\epsilon_0})\mathbf{E} = 0 \qquad (3.9)$$

where μ_r and ϵ_r are the relative permeability and permittivity respectively, k_0 is the free space wave number and ω is the angular frequency. The equation was simplified by using $\mu_r=1$ and $\sigma=0$ by assuming that there was no magnetic field and losses respectively. So equation 3.9 reduced to

$$\nabla \times (\nabla \times \mathbf{E}) - k_0^2\epsilon_r\mathbf{E} = 0 \qquad (3.10)$$

Electric field was defined as $E_x = E_0 \exp(-ikz)\hat{x}$, $E_y = E_0 \exp(-ikz)\hat{y}$, $E_z = E_0 \exp(-ikz)\hat{z}$ for x-polarised, y-polarised and z-polarised scattered field respectively to simulate the optical response of nanorod for different polarisations of light. The amplitude of the incident electric field E_0 was assigned to 1 V/m and $k = k_0 n_m$ is the wave number where n_m is the refractive index of the medium and k_0 is the free space wave number. The incident electric field propagation was along z.
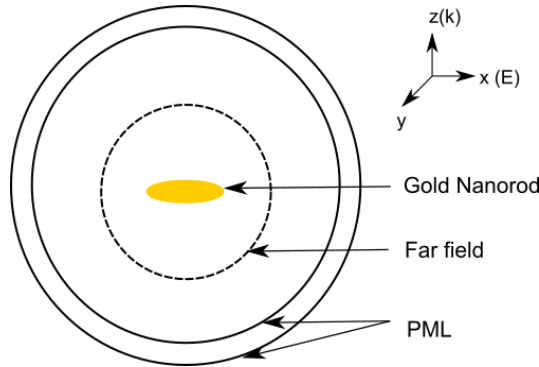
Figure 3.5: Sketch of the nanorod geometry which was designed in COMSOL Multiphysics to calculate the optical response of a gold nanorod.

A schematic of the designed geometry in COMSOL Multiphysics is shown in figure 3.5. The model was designed by following the steps listed below.

- At first, different parameters and constants were defined according to the necessity, for example, length and width of the nanorod, radius of different domains/sub-

domains, refractive index of the medium, amplitude of the incident light, incident poynting vector, wavelength range etc.

- The next step was to create the geometry where domains, sub-domains and boundaries were defined. A 3D geometry was designed where gold nanorod was represented by an ellipsoid surrounded by a perfect matched layer (PML) domain represented by a sphere having a radius of 3 times the length of the rod. The PML thickness was 0.5 times the length of the nanorod. This layer absorbs the electromagnetic waves and minimises the reflections at all frequencies and angle of incidence. A sphere having radius of 0.57 times the PML domain was used to represent the far-field and the scattered energy was calculated by integrating the Poynting vector over the sphere.

- Physics of the problem was defined by selecting the appropriate physics interface, for example, electromagnetic, thermal, mechanical etc. These interfaces contain all the underlying equations, material properties etc. Boundary conditions were also defined. The default material library of COMSOL Multiphysics was used to assign materials for different domains. Gold was assigned to the nanorod domain and water was assigned to the rest of the domains to evaluate the nanorod response in a water medium. In this model, equation 3.1, 3.2, 3.3, 3.4 and 3.7 were defined by using different default variables and functions of COMSOL Multiphysics. The propagation direction of the electromagnetic wave and the polarisation of the electric field were defined in the electromagnetic frequency domain interface. All of these steps set the conditions of the model to work.

- The next step was to create a mesh before solving. The choice of mesh size is crucial to get accurate solutions and also to avoid very time consuming solutions. The model was solved for 25752 domain elements, 4168 boundary elements and 426 edge elements. The model was also tested with increased number of mesh elements. However, the number of mesh elements were reduced later to save the computational time without compromising the accuracy of the simulation.

- Finally, the model was evaluated for the frequency domain and a parametric sweep was introduced to select a range of wavelengths for the simulation. COMSOL-

MATLAB interface was also used to simulate designed COMSOL models in this thesis where different parameters were defined by MATLAB and all results could be saved easily.
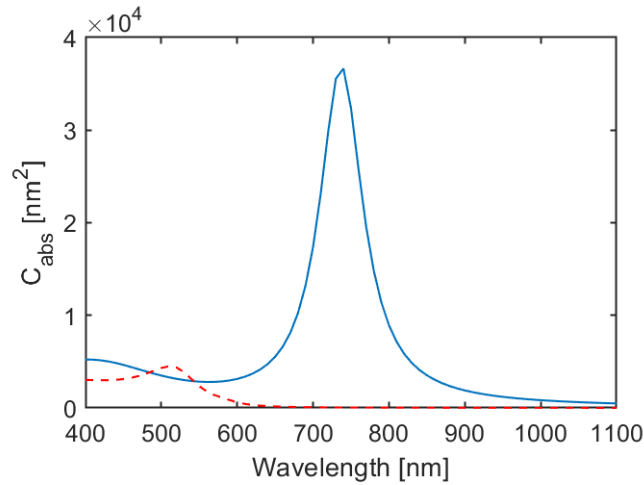
Figure 3.6: Absorption cross-section spectra of a 112 nm by 40 nm GNR in a water medium simulated by COMSOL Multiphysics for different polarisations of light. It can be seen that the cross-section was very high (blue) when the polarisation of light was along the length of the nanorod but very low (red dash) when the polarisation of light was along the width of the nanorod. Longitudinal and transverse peaks were at 740 nm and 510 nm, respectively.

The absorption cross-section spectra obtained from the designed model in COMSOL Multiphysics for a 112 nm by 40 nm GNR in a water medium is shown in figure 3.6. The cross-sections were calculated by using the equations mentioned before in this section. It can be seen that the cross-section was very high (blue) when the polarisation of light was along the length of the nanorod but very low (red dash) when the polarisation of light was along the width of the nanorod. Longitudinal and transverse peaks were found at 740 nm and 510 nm, respectively. The electric field maps corresponding to the electric field enhancement E/E_0 are shown in figure 3.7 (a) and figure 3.7 (b) evaluated at the longitudinal LSPR (740 nm) and transverse LSPR (510 nm), respectively. It can be seen that the electric field was strong along the length at the longitudinal LSPR and along the width at the transverse LSPR.
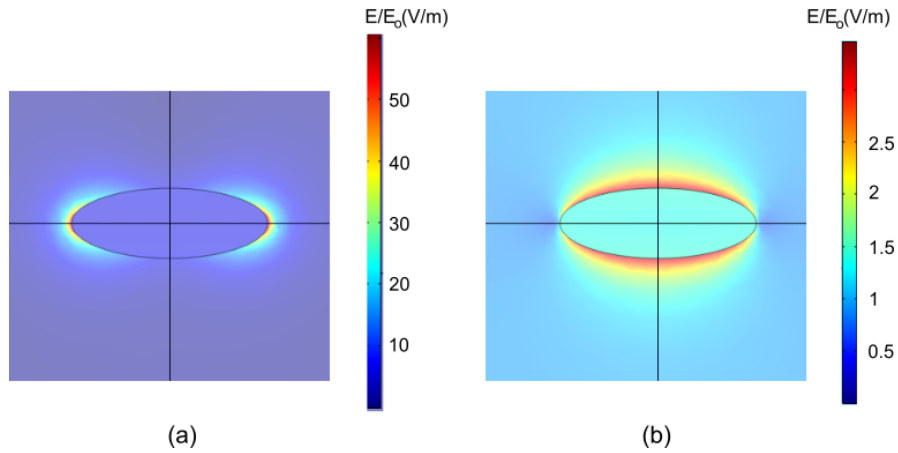
Figure 3.7: Electric field maps of a 112 nm by 40 nm GNR in water which shows the localised surface plasmon resonance obtained using finite element model. (a)(b) Electric field maps corresponding to the electric field enhancement E/E_0 evaluated at the longitudinal LSPR (740 nm) and transverse LSPR (510 nm), respectively.

It can be seen from figure 3.3 and 3.6 that the absorption cross-section spectra of a 112 nm by 40 nm GNR simulated by SMARTIES and COMSOL Multiphysics respectively are the same. The good agreement between simulated results by SMARTIES and COMSOL Multiphysics is shown later in this chapter in detail.

Change in the absorption cross-section spectrum of a GNR due to its shape diversity:

The optical response of a nanorod is a function of its shape. It is common to deal with different shapes of nanorod willingly or unwillingly due to their shape diversity, design complexity, fabrication challenges, etc. Due to shape diversity, the experimental results can deviate from the expected results. Commercially available nanorod batches can have shape diversity which is hard to avoid. In the case of fabricated nanorods, it is also challenging that every rod will come out of the same shape although they are designed and fabricated in the same way. Hence, it is important to see the effect of shape diversity to know whether the nanorod will behave as a selective absorber/detector or not. Resonant wavelength of a GNR shifts due to the change in its shape. As a result, the applied pump (excitation) and probe (detection) wavelengths may not work. If the change in the optical response of the nanorod is drastic due to its shape diversity, a different size of nanorod can be selected to adjust the optical response according to the need or optical parameters can be changed to work with the rod having a different shape. The medium can also be changed to adjust the optical response if possible. However, if the change is tolerable, the

error can be estimated due to shape diversity.

To see the effect of shape change on the optical response of a nanorod, four general and probable nanorod shapes were considered in this work, such as ellipsoid, dome, cylinder and flat. As mentioned before, COMSOL Multiphysics is flexible to design any shape of nanorod. All shapes were simulated by COMSOL Multiphysics where the ellipsoid rod was formed by an ellipsoid of length L, diameter D; the dome rod was formed by a cylinder of length L, diameter D, and capped by hemispheres of radius D/2; the cylinder rod was formed by a cylinder of length L, diameter D and the flat rod was formed by a rectangle of length L, width D and height D. All rods had a total length of 112 nm and width of 40 nm. The simulations were done in a water medium. The length and width of all rods were kept same to see the effect of shape difference only.
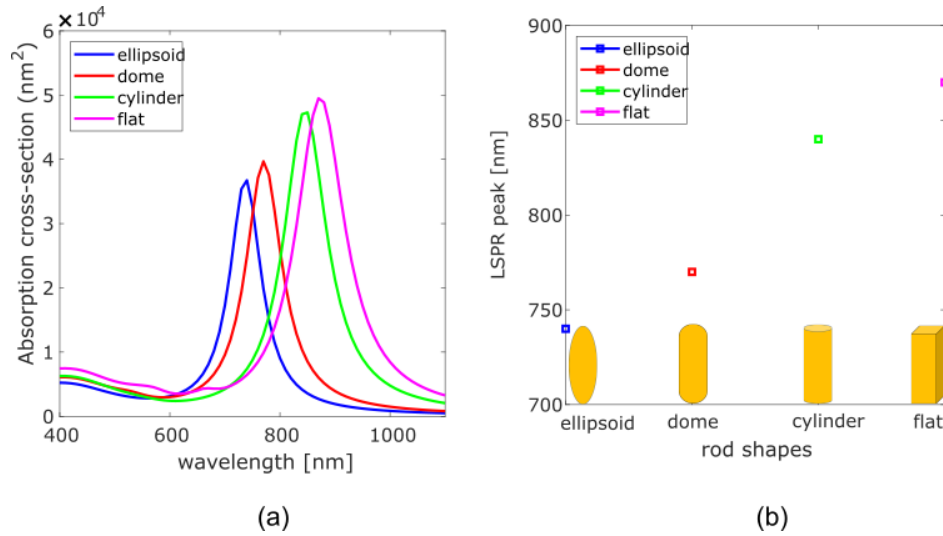
Figure 3.8: Change in the longitudinal absorption cross-section spectrum of a GNR in a water medium due to its shape diversity (ellipsoid, dome, cylinder, flat) simulated by COMSOL Multiphysics. (a) Longitudinal absorption cross-section spectra of a GNR for four different shapes. They all correspond to a total rod length of 112 nm and a width of 40 nm. (b) A shift in the longitudinal LSPR peak of GNR due to its shape diversity. It can be seen that the absorption cross-section increased and the longitudinal LSPR peak shifted to a longer wavelength as the nanorod cap flattened from ellipsoid to flat rod.

The shape of the end caps of the rod has a significant effect on the optical response of the nanorod [30]. It can be seen in figure 3.8 (a) that as the nanorod cap flattened from ellipsoid to flat rod, the absorption cross-section increased and the longitudinal LSPR peak shifted to longer wavelengths. It is clear from figure 3.8 (b) that the longitudinal LSPR peak red shifted from 740 nm to 870 nm due to the shape change in the shown order. The

trend observed was similar to the trend when the aspect ratio of nanorod increased.

3.3.2 Heat

Optical absorption causes heat in the nanorods and the heat then induces mechanical resonances or vibrations. In this thesis, the amount of heat produced by nanorod was not modelled for simplicity. Instead, the heat was given as an input to the mechanical model to calculate the vibrational modes. The amount of heat does not change the vibrational frequencies of nanorods unless it damages or melts the rod. It is good to mention that the melting of a nanorod by heat was not modelled in this work and was out of the scope of this PhD work. However, this issue was always monitored during experiments and proper steps were taken to minimise the thermal effect on nanorods. Observed thermal effect on nanorods during some experiments of this PhD work and ways to minimise the thermal effect on gold nanorods are discussed in chapter 6.

3.3.3 Mechanical resonances

Mechanical resonances of gold nanorods were investigated by using FEM models and the analytical model developed by Hu et al. [162] in this research. The analytical model was fast and FEM models were time consuming. On the other hand, the analytical model was fixed for only cylindrical nanorod but any shape could be simulated by FEM based models.

3.3.3.1 Finite element method (FEM) based models

A coupled model was designed by using the heat-transfer module and structural mechanics module of COMSOL Multiphysics to determine the vibrational frequencies of gold nanorods. The model calculated the displacement of an ellipsoidal nanorod caused by the produced heat from a heat source in the time domain. The displacement contained the information about the vibrational frequency of the nanorod which was extracted by doing a fast Fourier transform (FFT) of the obtained displacement over time. The time-dependent heat equation was defined as

$$\rho C_p \frac{\partial (T)}{\partial (t)} + \nabla \cdot q = Q \tag{3.11}$$

where ρ is the density, C_p is the specific heat capacity, T is the absolute temperature, $q = -k\nabla T$ is the heat flux, k is the thermal conductivity and $Q = Q_{source}$ where Q_{source} is the generated heat from the laser and was defined as

$$Q_{source} = Q_0\, t \exp(-t/t_0)/t_0 \tag{3.12}$$

The model was simulated for $Q_0 = 10^{18}\ W/m^3$, the power density of the pump laser and $t_0 = 100\ fs$, the pulse width of the pump laser. The value of Q_0 was arbitrary. However, this value only affected the amount of displacement, not the vibrational frequency of the nanorod.

The mechanics were defined by the equation

$$\rho \frac{\partial^2 (u)}{\partial^2 (t)} = \nabla \cdot S \tag{3.13}$$

where u is the displacement vector and S is the second Piola-Kirchhoff stress tensor. The geometry of the GNR mechanical model using 2D axial symmetry is shown in figure 3.9 where the nanorod is in free space and S is a point on the surface where the surface displacement was measured. The designed model was solved for 125 domain elements and 41 boundary elements in COMSOL Multiphysics which took 4 minutes and 3 seconds for a time interval of 1.5 ns in 0.1 ps step size. The result of the model was also compared with the result simulated with an increased number of mesh elements and similarity between both results was found. Hence, the simulation was continued with a reduced number of mesh elements to save computational time.
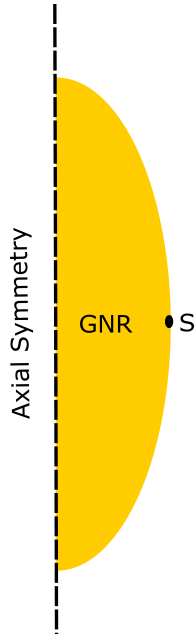
Figure 3.9: Schematic of the 2D thermal-mechanical coupled GNR model using axial symmetry. The surface displacement was measured at the point S.

The simulated results from the designed model are shown in figure 3.10. Two different sizes of nanorod (112 nm by 40 nm and 145 nm by 50 nm) were considered because these were frequently used for experiments of this PhD work. Surface displacements and FFT of surface displacements are shown in figure 3.10 (a) and figure 3.10 (d), respectively. Zoom in versions of surface displacements for higher frequency modes and lower frequency modes are shown in figure 3.10 (b) and figure 3.10 (c) respectively where corresponding FFT traces are shown in figure 3.10 (e) and figure 3.10 (f) respectively to observe more clearly. Two main vibrational modes can be seen in figure 3.10 (d), the extensional mode (f_{ext}, low frequency) which corresponds to the length and the breathing mode (f_{brth}, high frequency) which corresponds to the width. It can also be observed that f_{ext} and f_{brth} decreased when the length and width of the nanorod increased, respectively. The reason is that bigger particles oscillate at a longer wavelengths. Obtained extensional modes and breathing modes for these two GNR batches are listed in table 3.1.

Table 3.1: Vibrational modes of GNRs from the designed FEM based models.

Batch	Aspect ratio AR	Extensional mode f_{ext} GHz	Breathing mode f_{brth} GHz
(112×40) nm	2.8	10.5	64.7
(145×50) nm	2.9	8	50
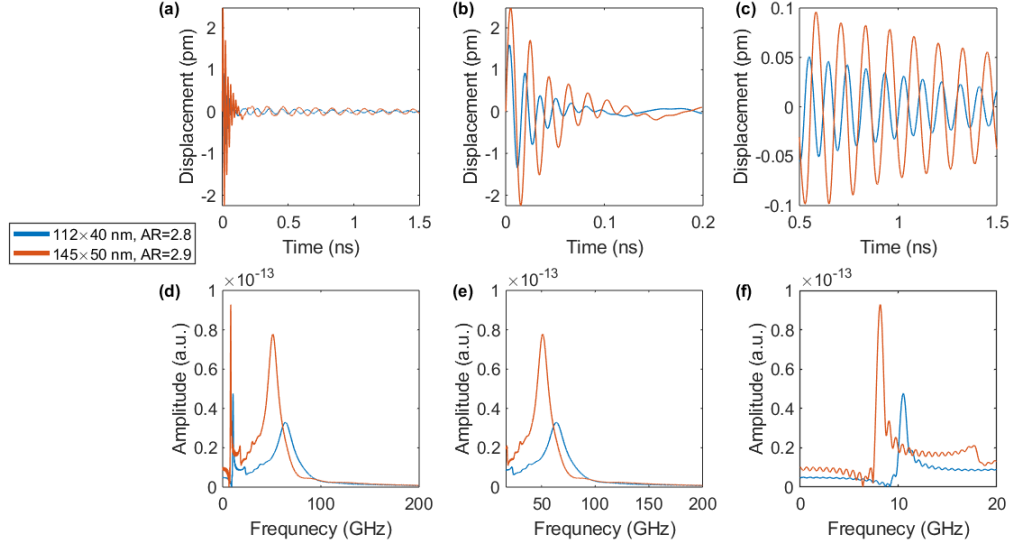
Figure 3.10: Simulated mechanical responses of 112 nm by 40 nm and 145 nm by 50 nm GNRs using COMSOL Multiphysics. (a)(d) The surface displacements and corresponding FFT traces, respectively. (b)(e) A zoom of the surface displacements to clearly see the high frequencies and corresponding FFT traces, respectively. (c)(f) A zoom of the surface displacements to clearly see the low frequencies and corresponding FFT traces, respectively. It can be seen that different sizes of GNRs produced different frequencies where low frequency (longitudinal) modes and high frequency (breathing) modes were 10.5 GHz and 64.7 GHz for a 112 nm by 40 nm GNR; 8 GHz and 50 GHz for a 145 nm by 50 nm GNR.

The vibrational modes of a 112 nm by 40 nm are shown through the displacement and stress plots in figure 3.11, simulated by COMSOL Multiphysics. The surface displacements from 0 to 0.2 ns is shown in figure 3.11 (a) which presents the high frequency components. The inset shows the stress plot at point p (0.003 ns) and q (0.01 ns) of the displacement curve. Expansion and contraction along the width of the rod can be seen at p and q points, respectively. On the other hand, the surface displacements from 0.16 to 0.21 ns is shown in figure 3.11 (b) which presents the low frequency components. The inset shows the stress plot at point m (0.16 ns) and q (0.21 ns) of the displacement curve. Contraction and expansion along the length of the rod can be seen at m and n points, respectively.
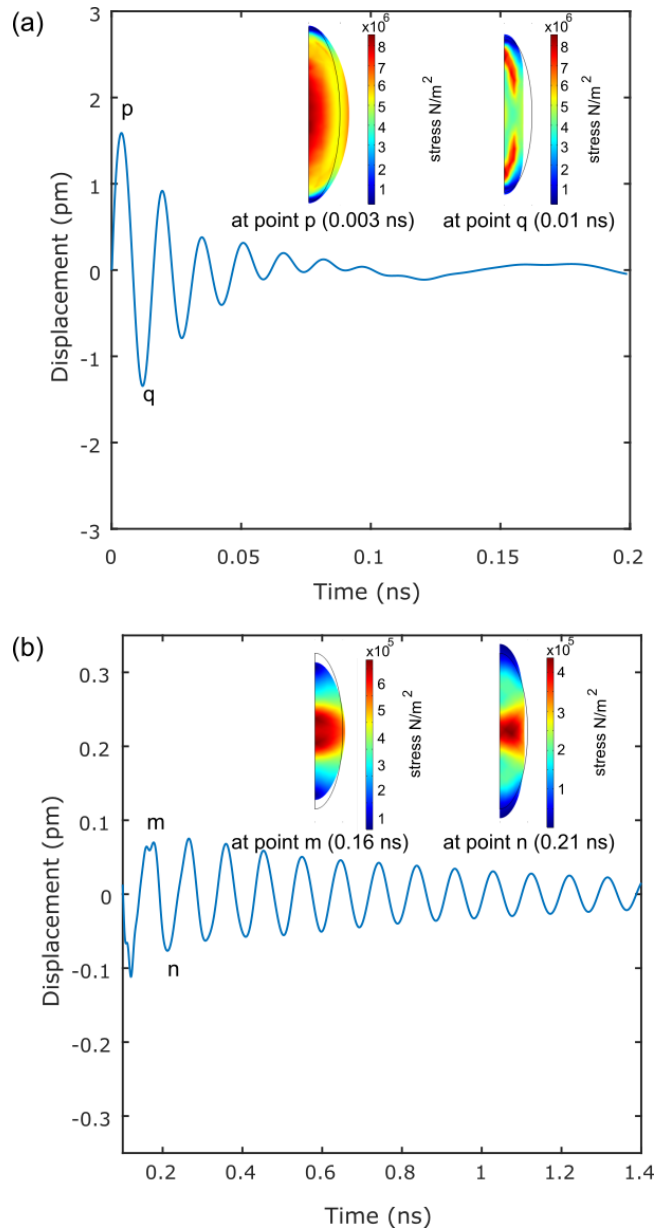
Figure 3.11: The surface displacements and stress plots of a 112 nm by 40 nm GNR simulated by COMSOL Multiphysics. (a) The surface displacements from 0 to 0.2 ns that shows the high frequency components. The inset shows the stress plot at point p (0.003 ns) and q (0.01 ns) of the displacement curve. Expansion and contraction along the width of the rod can be seen at p and q points, respectively. (b) The surface displacements from 0.1 to 1.4 ns that shows the low frequency components. The inset shows the stress plot at point m (0.16 ns) and q (0.21 ns) of the displacement curve. Contraction and expansion along the length of the rod can be seen at point m and n, respectively.

The particle was very small and only fundamental symmetric modes (extensional and breathing) were observed because the particle heating was considered as uniform. The reason is that the absorbed energy creates a cloud of hot electrons which rapidly (<1 ps)

heat the lattice provided that the particle is small or on a similar scale compared with the mean free path of the hot electrons ($\approx$20 nm). So a combination of the penetration depth of the energy absorption and the fast hot electrons means that small particles can be considered uniformly heated. However, this assumption might not be valid for bigger particles. Fundamental and higher-order symmetric and asymmetric acoustic modes can exist for gold nanorods when they are excited. However uniform excitation only excites fundamental symmetric modes strongly. Higher order modes will still be excited by rapid uniform heating but very weakly. Hence, these modes are hard to detect. It was shown in figure 3.7 that the optical field is very strong at the edges or tips of the rod. Hence, vibration of the rod causes a big change in the field.

Frequency diversity because of shape diversity of the rods:

In section 3.3.1.2, the effect of shape diversity of the rod on its optical response was described. Shape diversity of a rod can also affect the mechanical response of it. To investigate this, three dimensional FEM based models were designed using different shapes of gold nanorods using COMSOL Multiphysics following the steps mentioned before in section 3.3.1.2.

The simulation was done using a reasonable mesh size (2909 domain elements, 584 boundary elements and 84 edge elements) that took approximately 23 minutes. Two machines: machine 1 (Intel i7-6700 processor, an NVIDIA GT 720 GPU, and 64GB of RAM) and machine 2 Intel Xeon E7 4870 processors, NVIDIA KG 107 GPUs, and 1024GB of RAM) were used for the simulations. The simulated results were also compared with the results taken with a reduced mesh size (35412 domain elements, 2560 boundary elements, 180 edge elements) and no significant difference was observed between both results. However, this may not be true for nanorods of high AR. Simulations were continued with a reasonable mesh size to reduce the computational time. The extensional and breathing mode frequencies of different shapes (ellipsoid, cylinder, dome) of gold nanorods are compared in figure 3.12. Frequencies for different shapes were not miles off as can be seen from figure 3.12 (a) and 3.12 (c) for the extensional mode (f_{ext}) and breathing mode (f_{brth}), respectively. However, it is hard to understand the deviation without a zoomed view. Hence, only frequency deviations (maximum) due to the shape diversity are shown in figure 3.12 (b) and 3.12 (d) for the extensional mode and breathing mode, respectively.

It can be observed that shape diversity affected the breathing mode more than the longitudinal mode. End tip shapes of ellipsoid, cylinder and dome rods are different. This in turn changes the apparent length and width of the rod. Eventually, the frequency changes although there is no direct change in the size.
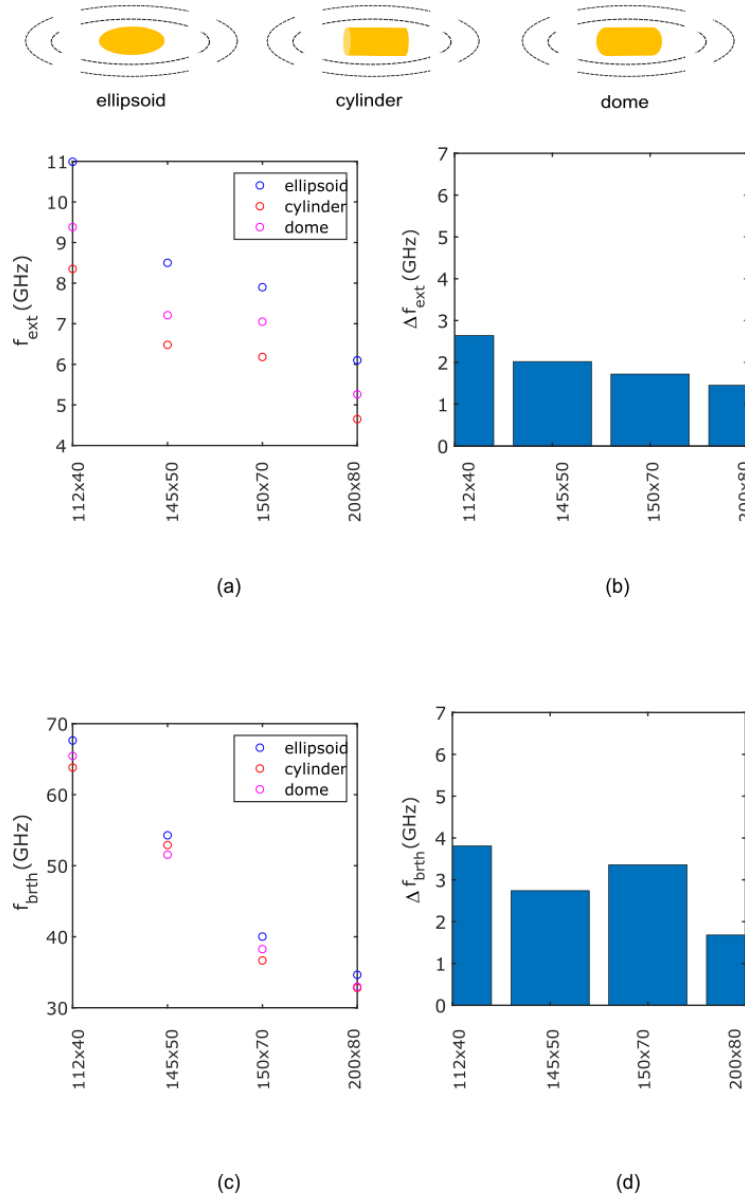
Figure 3.12: Obtained extensional and breathing mode vibrational frequencies of different shapes of gold nanorods using COMSOL Multiphysics. (a)(c) Extensional and breathing mode vibrational frequencies of ellipsoidal, cylindrical and dome shaped gold nanorods of different sizes, respectively. (b)(d) Frequency deviation of the longitudinal and breathing modes because of shape diversity. It can be seen that the shape diversity did not change the frequency drastically where it had more effect on the breathing mode rather than the extensional mode. It can also be observed that the shape diversity had more effect on smaller sizes than bigger sizes.

3.3.3.2 Analytical Model

Hu et al. developed an analytical model to calculate the extensional and breathing mode frequencies of a free-standing and elastically isotropic cylindrical rod in free space following excitation by a thermal pulse [162]. Two main vibrational frequencies exist for a cylindrical rod where the extensional mode is along the length (L) and the breathing mode is along the width (W). These frequencies can be expressed by the following equations [162]

$$f_{ext} = \frac{2m+1}{2L} \sqrt{\frac{E}{\rho}} \tag{3.14}$$

$$f_{br} = \frac{\tau_n}{\pi W} \sqrt{\frac{E(1-\upsilon)}{\rho(1+\upsilon)(1-2\upsilon)}} \tag{3.15}$$

where positive integer m is the extensional mode number, n is the radial mode number, E is Young's modulus, ρ is the density of gold, υ is the Poisson's ratio. The parameter τ_n is the nth root of the eigenvalue equation

$$\tau J_0(\tau) = \frac{1-2\upsilon}{1-\upsilon} J_1(\tau) \tag{3.16}$$

where J_0 and J_1 are Bessel functions of the first kind. The obtained eigenvalue for the fundamental mode was 2.28 by solving the above equation.

The choice of Young's modulus (E) for a gold nanorod is a part of discussion. It depends on the crystal structure and growth direction of the nanorod determined by the used synthesis process [162–167]. Different research works have been carried out to well estimate the value of Young's modulus for gold nanorods and the estimation varies according to the crystal structure and applied preparation method as discussed in section 2.6. In this thesis, both commercially available gold nanorods and nanorods fabricated by EBL were used. Hence, to avoid the complexity of different approaches to prepare gold nanorods, Young's modulus of bulk gold, 79 GPa was used. However, the sizes of gold nanorods were measured in this work for different frequently used E values to understand the effect of E on the measurements. In the case of figure 3.13, the equations were solved for E = 79 GPa, $\rho = 19300 \ kg/m^3$, $\upsilon = 0.42$, $\tau_0 = 2.28$ [162] to obtain the fundamental extensional and breathing modes for different sizes of cylindrical GNRs.
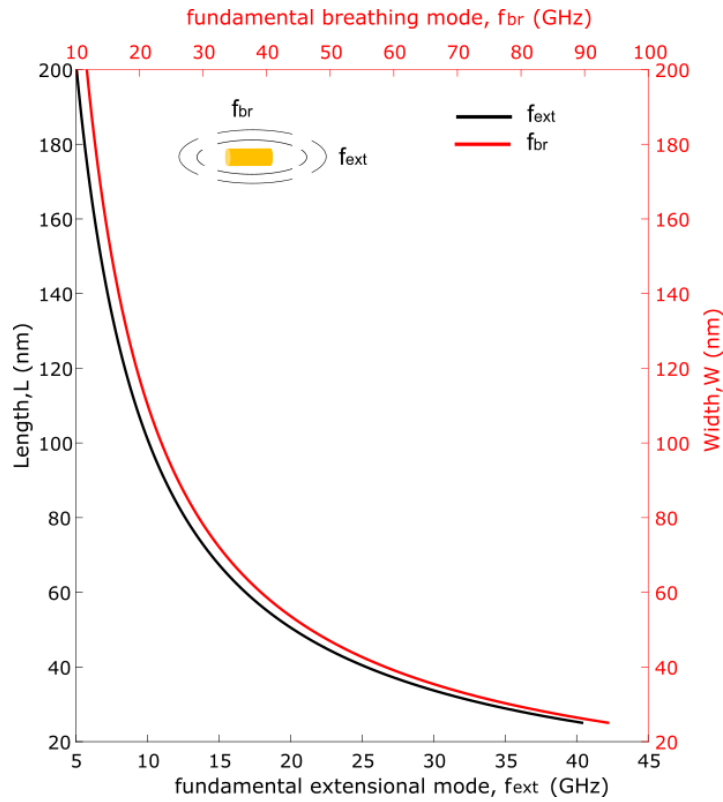
Figure 3.13: Fundamental vibrational frequencies of a cylindrical gold vs length and width predicted by the analytical model [162]. It can be seen that the extensional mode (f_{ext}) of a nanorod decreased as the length of the rod increased and the breathing mode (f_{br}) decreased as the width of a rod increased. Young's modulus of bulk gold, 79 GPa was used for this simulation.

3.3.4 Optical detection

When gold nanorods are excited with a laser, they also scatter light in addition to absorbing light. Hence, gold nanorods can be detected using the scattered light by them. The scattering cross-section spectra of a 112 nm by 40 nm GNR in water simulated by SMARTIES are shown in figure 3.14 for two different polarisations of light. It was clear from figure 3.3 and 3.6 that simulated results from SMARTIES and COMSOL match with each other. A detailed comparison between the simulated results by SMARTIES and COMSOL can be found in the next section. Hence, for simplicity, optical detection of GNR is shown here using simulated results by SMARTIES only.
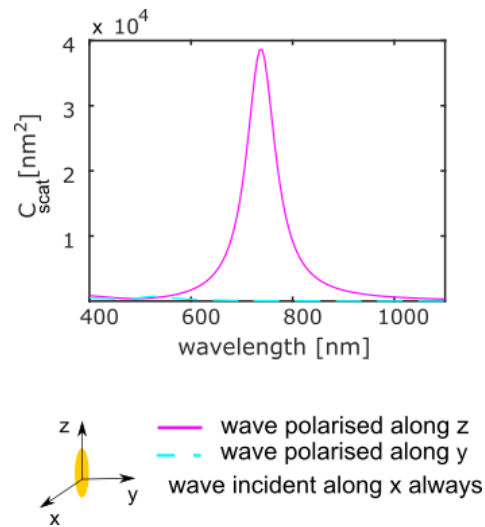
Figure 3.14: Scattering cross-section spectra of a 112 nm by 40 nm GNR in a water medium simulated by SMARTIES for different polarisations of light. It can be seen that the cross-section was very high (magenta) when the polarisation of light was along the length of the nanorod but very low (green dash) when the polarisation of light was along the width of the nanorod. Longitudinal and transverse LSPR peaks were found at 735 nm and 525 nm, respectively.

It can be seen from figure 3.14 that the scattering cross-section was very high when the polarisation of light was along the length of the rod and very low when the polarisation was along the width of the rod. The trend was similar as was shown for absorption cross-section spectra in figure 3.3. It is good to mention here that in this research, the orientation of a gold nanorod was determined by changing the polarisation of the probe light or detecting the rod from different angles.

The mechanical resonance of a gold nanorod causes an instantaneous change in its size. Hence, if a nanorod is illuminated by another probe laser, the scattered light intensity gets modulated and this change can be detected in transmission or reflection. There are many detection mechanisms available in laser ultrasonics such as transient reflectivity based [113, 114], interferometry [127–131], modulation of the scattered signal [58–60], beam deflection [132–134], beam distortion [135], among others as described in section 2.5.5.2. In this project, the detection system was based on detecting the modulation of the scattered light intensity by gold nanorods.

The probe laser wavelength needs to be optimised so that the nanorod scattering cross-section is high enough for detection. The wavelength also needs to be sensitive so that any small change in the scattering cross-section due to the vibration of the GNR is detectable. In this thesis, optical sensitivity, S_{Cscat} of a rod was defined as the change in the scattering cross-section for a 1 nm change in the length (l) or width (w) of it. Other parameters such as modulation depth (MD) and optical sensitivity with respect to signal-to-noise ratio (SNR) can also be used to evaluate the optical response. Modulation depth was defined as the optical sensitivity over the scattering cross-section, and optical sensitivity with respect to signal to noise ratio, SNR was defined as the optical sensitivity over the square root of scattering cross-section. The noise was assumed as optical shot noise. All the defined terms can be mathematically presented by the following equations

$$\text{Optical Sensitivity}, S_{Cscat} = \frac{|dCscat|}{dl} \tag{3.17}$$

$$\text{Modulation Depth, MD} = \frac{|dCscat/dl|}{Cscat} \tag{3.18}$$

$$\text{SNR} = \frac{|dCscat/dl|}{\sqrt{Cscat}} \tag{3.19}$$

The above equations are expressed for length here which are also true for width. Optical sensitivity, modulation depth and SNR of a 112 nm by 40 nm GNR in water are plotted vs wavelength in figure 3.15 (a)(b) and (c) respectively by solving the above equations for length.

It can be seen from figure 3.15 (a) that the gold nanorod had the highest optical sensitivity at 720 nm and 760 nm. These wavelengths lie almost at half of the scattering cross-section slope as shown in figure 3.14 when the polarisation of light was along the length (magenta curve) of the rod. The wavelengths where the modulation depth and SNR were maximum can be seen in figure 3.15 (b) and (c), respectively. A reasonable probe laser wavelength for a 112 nm by 40 nm GNR in water can be estimated from figure 3.15 (a) (b) and (c). Experimentally, 112 nm by 40 nm GNRs in water were detected with probe wavelength of 780 nm in this project (Table 5.2). It can be seen from figure 3.15

that the chosen wavelength was a good choice for the enhanced optical detection of the rod.
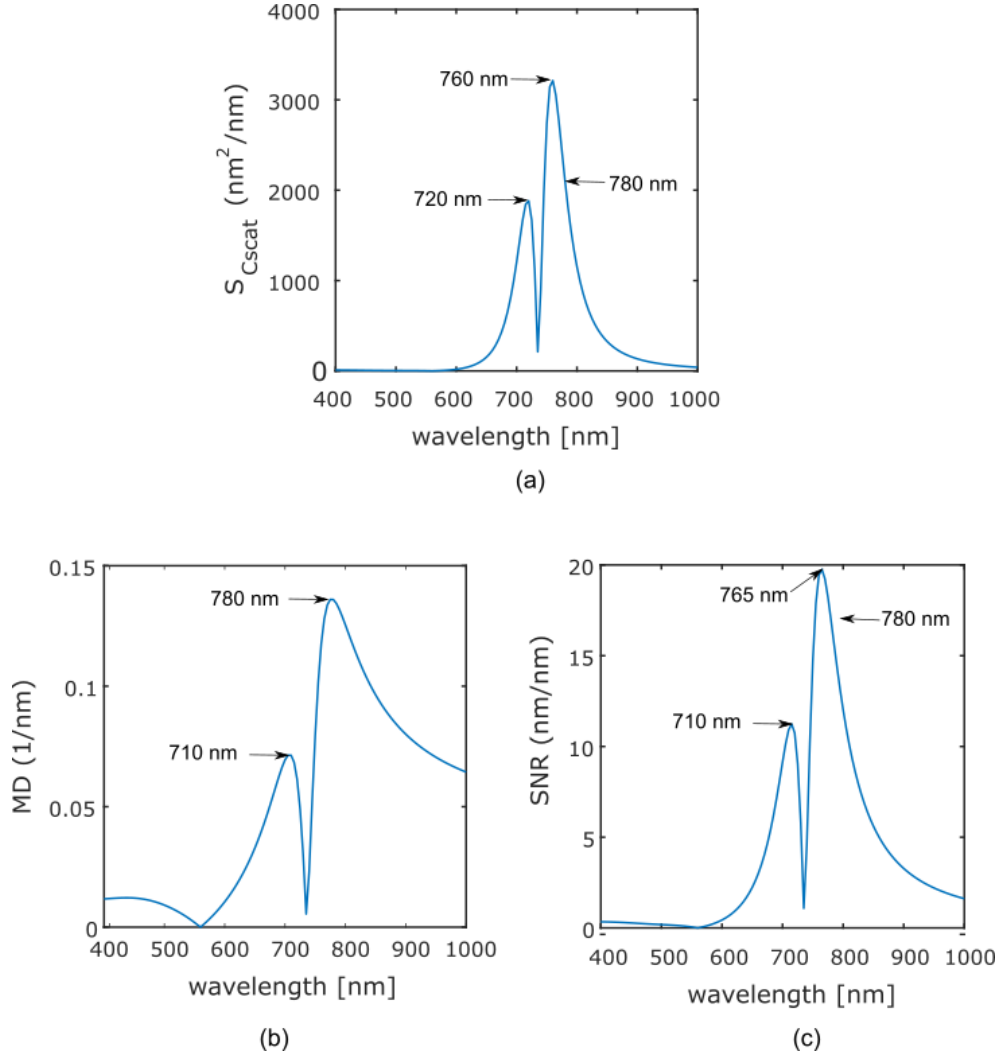
Figure 3.15: Detection sensitivity analysis of a 112 nm by 40 nm GNR in water with respect to length. (a)(b)(c) The optical sensitivity, modulation depth and SNR with respect to length respectively. Appropriate probe laser wavelength can be selected for a specific size of nanorod from the plots to enhance the optical detection.

The longitudinal LSPR peak wavelength of a GNR is the same for the absorption and scattering cross-section spectra. It is also true for the transverse LSPR peak wavelength. Hence, the shift in the longitudinal LSPR and transverse LSPR peak due to any change in the parameter of the GNR will be same for the absorption and scattering. The effect of change in the aspect ratio, external medium and shape of the rod on the absorption cross-section spectra was shown in section 3.3.1.1 before. The same effects are shown here in the case of the scattering cross-section for clarity.

Scattering cross-section spectra of GNRs for different aspect ratios and external mediums:

The scattering cross-section spectra of GNRs for different aspect ratios and external media are shown in figure 3.16 (a)(b) and (c)(d), respectively where a right shift in the longitudinal LSPR peak due to an increase in the aspect ratio and refractive index of the external medium of a GNR can be seen, as was shown previously for absorption cross-section spectra in figure 3.4. In contrast, shift in transverse LSPR peak was negligible when the aspect ratio and external medium changed. Probe wavelengths for different GNRs in different external media can be estimated by analysing the detection sensitivity of a GNR for each case as shown in figure 3.15.
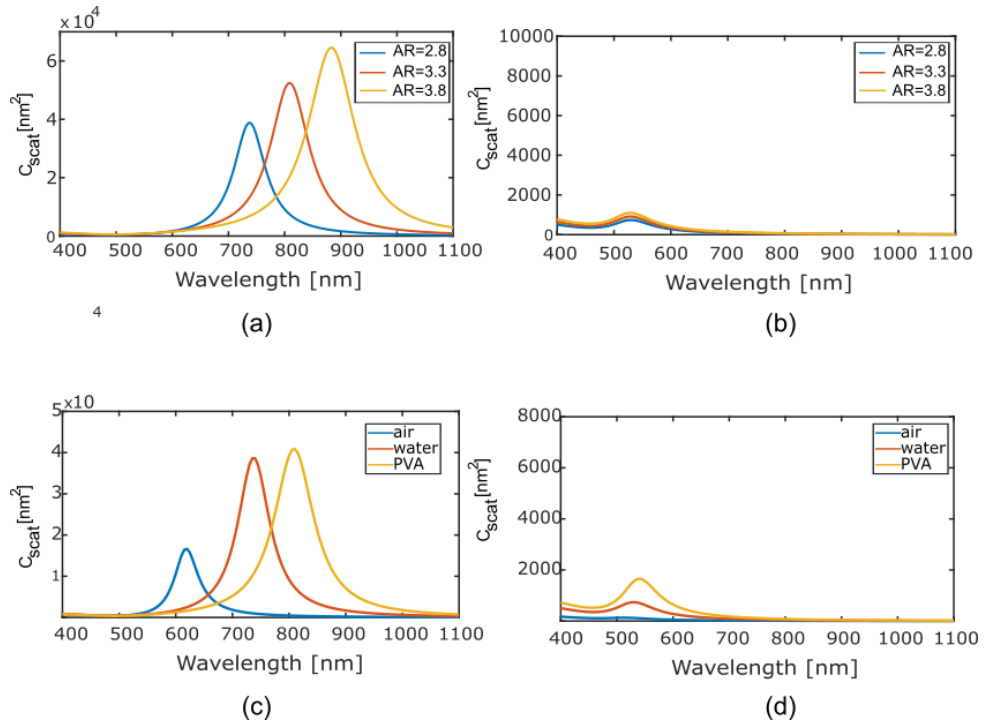
Figure 3.16: Scattering cross-section spectra of GNRs for different aspect ratios and external media. (a) Scattering cross-section spectra of GNRs for different aspect ratios showing the longitudinal LSPR peaks. (b) Scattering cross-section spectra of GNRs for different aspect ratios showing the transverse LSPR peaks. (c) Scattering cross-section spectra of a 112 nm by 40 nm GNR in different external mediums showing the longitudinal LSPR peaks. (d) Scattering cross-section spectra of a 112 nm by 40 nm GNR in different external media showing the transverse LSPR peaks. It can be seen that the LSPR peak of a GNR shifted to a longer wavelength when the aspect ratio and refractive index of the external medium increased. In contrast, the transverse LSPR peak was almost insensitive to the change in the aspect ratio and external medium of the rod.

Change in the scattering cross-section spectra of a GNR due to its shape diversity:

In section 3.3.1.2, the effect of shape diversity on the absorption cross-section spectra of GNR was shown. The results from the same model (length 112 nm, width 40 nm) are shown in figure 3.17 for the scattering cross-section spectra. As previous, it can be seen in figure 3.17 (a) that as the nanorod cap flattened from ellipsoid to flat rod, the scattering cross-section increased. The longitudinal LSPR also red shifted from 740 nm to 870 nm due to the change in shape as can be seen in figure 3.17 (b). Probe wavelengths for different shapes of GNR can be estimated by analysing the detection sensitivity of a GNR for each case as shown in figure 3.15.
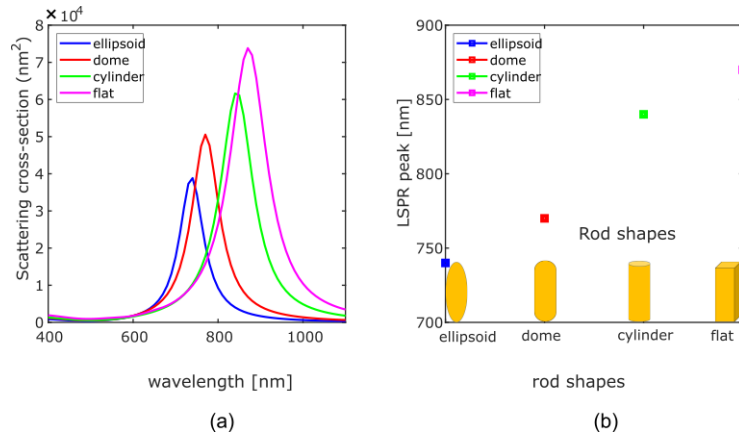
Figure 3.17: Change in the scattering cross-section spectrum of a GNR in a water medium due to shape diversity (ellipsoid, dome, cylinder, flat) simulated by COMSOL Multiphysics. (a) Scattering cross-section spectra of a GNR for four different shapes. They all correspond to a total rod length of 112 nm and a width of 40 nm. (b) A shift of the longitudinal LSPR peak of GNR due to the shape diversity. It can be seen that the scattering cross-section increased and the longitudinal LSPR shifted to a longer wavelength as the nanorod cap flattened from ellipsoid to flat rod.

3.4 Comparison of simulated results by analytical model and FEM based model

3.4.1 Optical models

SMARTIES and COMSOL Multiphysics both were used to simulate the optical properties of gold nanorods in this research work. It was very important to compare the simulated results from both models so that their accuracy could be compared and effective choice could be taken for different purposes.
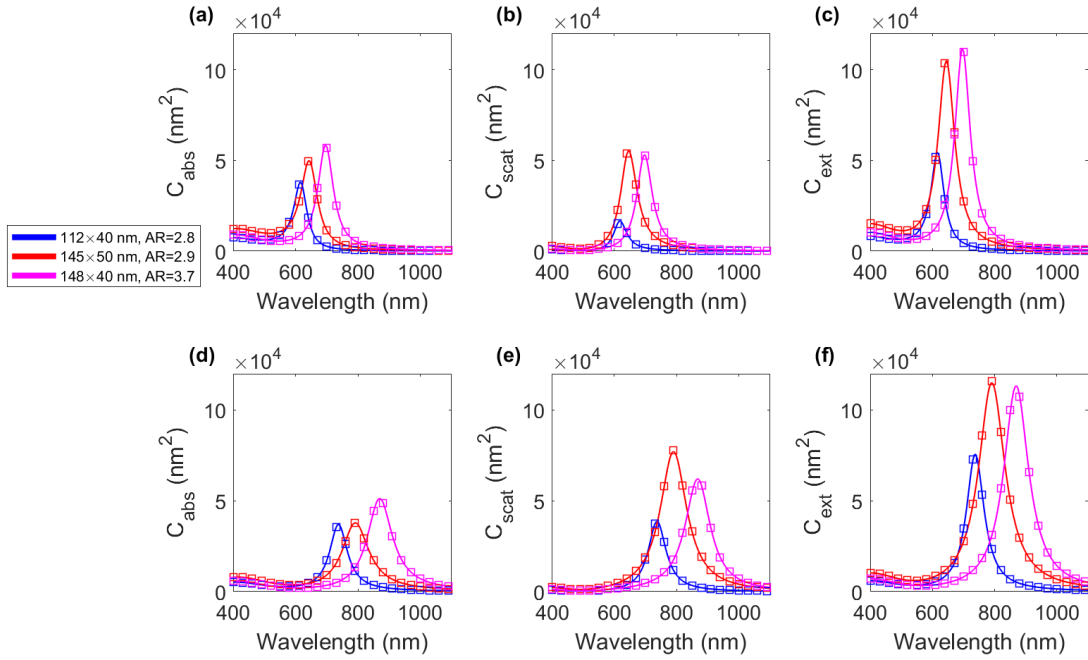
Figure 3.18: Simulation of the optical responses of GNRs (112 nm by 40 nm, 145 nm by 50 nm and 148 nm by 40 nm.) at a glance those were used in different experiments of this work. (a)(b)(c) Cross-section spectra of GNRs in an air medium. (d)(e)(f) Cross-section spectra of GNRs in a water medium. Here lines and squares represent the simulated results by SMARTIES and COMSOL Multiphysics, respectively. It can be seen that the results from SMARTIES and COMSOL Multiphysics were in good agreement with each other for both air and water media.

Optical responses of nanorods that were used in different experiments of this research are shown in figure 3.18 simulated by both SMARTIES (lines) and COMSOL Multiphysics (squares) in air (figure 3.18 (a), (b),(c)) and water (figure 3.18 (d), (e),(f)) media. This figure is helpful not only to see the optical responses of all used sizes of nanorod together but also to understand that the SMARTIES and COMSOL Multiphysics results were in good agreement with each other. It can be said that COMSOL Multiphysics and SMARTIES can be used alternatively. However, FEM models are more time consuming than analytical models. It is worth to mention that SMARTIES took only 3.56 seconds to simulate a cross-section spectra of a GNR while COMSOL Multiphysics took 18 minutes to simulate the same spectra. Hence, SMARTIES was frequently used in this work to simulate the optical responses of gold nanorods. However, there was a compromise behind this choice because SMARTIES assumes that the nanorod is of a prolate shape by default and does not allow to simulate the response of nanorod of any shape. On the other hand,

83

any type of geometry can be designed in COMSOL Multiphysics to simulate the response. However, SMARTIES is a good choice to have solutions in a reasonable time with the same accuracy as COMSOL Multiphysics provides.

3.4.2 Mechanical models

An analytical model developed by Hu et al. [162] was used in this thesis to calculate the vibrational frequency of cylindrical nanorods as shown in figure 3.13. It was also shown in figure 3.10 how vibrational frequency of an elliptical nanorod can be determined from a 2D FEM model using the axial symmetry in COMSOL Multiphysics. It was important to compare the vibrational frequencies obtained from the analytical model and FEM based models. As the analytical model was fixed for only cylinders, the comparison is shown here for a cylindrical rod.

It can be seen from figure 3.19 that the results from analytical and designed FEM models were in good agreement with each other. The extensional mode (corresponds to length) decreased from 15 GHz to 3 GHz as the length increased from 60 nm to 300 nm with a fixed width of 20 nm as shown in figure 3.19 (a) while the breathing mode (corresponds to width) was constant at 123 GHz as shown in figure 3.19 (b). On the other hand, the extensional mode was constant at 3.3 GHz when the width was varied from 20 nm to 180 nm as can be seen from figure 3.19 (c) but the breathing mode decreased from 123 GHz to 13 GHz as can be seen from figure 3.19 (d).

Analytical model and FEM based models were used according to the necessity in this work. But it is important to mention that 3D FEM modelling is very time consuming and requires high CPU memory. It took approximately 23 minutes to get the vibrational information of a gold nanorod (145 nm by 50 nm) from the designed FEM based where moderate mesh size was used. It can be more time consuming depending on the mesh size and also the size of the structure. On the other hand, the analytical model calculated the vibrational frequency of a gold nanorod within a few seconds. The limitation of the used analytical model is that it is only valid for cylindrical nanorods. In contrast, a rod of any shape can be designed and simulated using FEM based models. It is necessary because all nanorods do not come of the same shape from the synthesis and fabrication process unexpectedly.
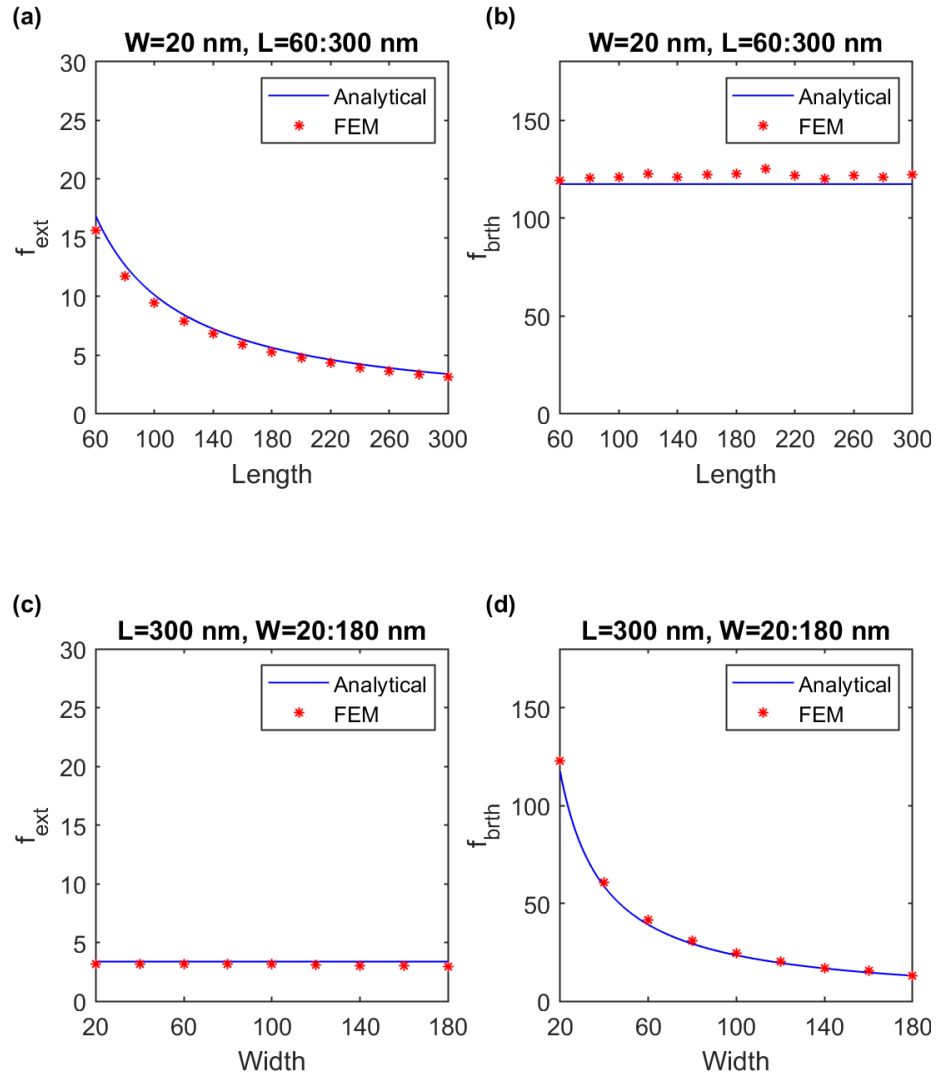
Figure 3.19: Comparison of vibrational frequencies of cylindrical gold nanorods obtained from analytical and FEM based models. (a) Extensional mode (f_{ext}) decreased dramatically as length of the rod increased. (b) Breathing mode was constant when length was increased because length and width were not coupled (independent) in a cylindrical shape. (c) Extensional mode (f_{ext}) was constant as width of the rod increased. (d) Breathing mode decreased rapidly when width was increased. It can be seen that the results from analytical and FEM based models were in good agreement with each other.

3.5 Summary

Gold nanorods were modelled as opto-acoustic transducers. Mainly, optical and mechanical responses of gold nanorods were investigated by using different modelling tools such as SMARTIES (non commercial code), COMSOL Multiphysics (commercial FEM based tool) and an analytical model developed by Hu et al. Computational time of the analytical model was faster than the finite element based model. However, finite element models offered greater design flexibility than the analytical one. It was found that results obtained from both models were in good agreement with each other. Hence, both of them were used in this research work whenever necessary. The simulated results presented in this chapter were used to select the size, shape, external medium, pump wavelength and probe wavelength of the gold nanorods for a specific experimental set-up in this research. However, the results can be used in general to fix the parameters for gold nanorods for any experimental set-up.

Chapter 4

Instrumentation and experimental methods

4.1 Introduction

This chapter is organised to describe different instrumental and experimental methods that were followed in this research. Pump-probe spectroscopy, a time-resolved technique which was used to obtain the vibrational frequency of a gold nanorod, is described first. Then, the used experimental set-up is explained in detail with appropriate diagrams. Next, the basic signal processing steps to obtain the frequency of a nanorod from the experimental raw traces are explained. Furthermore, the techniques which were followed to determine the size, orientation and location of a nanorod from the experimental results, are explained. Later in the chapter, different methods which were followed to prepare the sample with purchased gold nanorods and to fabricate gold nanorods by electron beam lithography (EBL), are described. In the last section of this chapter, the applied method to capture the images of samples by scanning electron microscopy (SEM) is described.

4.2 Pump-probe in ASOPS Configuration

Gold nanorods used in this research generated acoustic frequencies over a wide range, from ≈ 5 GHz to ≈ 70 GHz. These fast events were challenging to measure in real time due to the wide bandwidth and high attenuation. Hence, it was required to measure

87

very fast events with compatibility to be measurable in real-time scale. The pump-probe method [112] is a well-established technique to measure fast events. The principle of pump-probe spectroscopy is that the pump pulse excites the sample and the induced change is measured with the help of a subsequent probe pulse. The probe pulse is delayed from the pump gradually to recover the change in the signal in the time domain. The idea is to mix fast events with arbitrary low frequencies so that they can be measured in real-time at a cost of overall measurement time. Pump-probe measurements use pulsed lasers and the temporal resolution is limited by the pulse width of lasers. Pico-second and femto-second pulse lasers are mostly used in pump-probe measurements. Optical delay elements can be placed on a mechanical translational stage to provide different time delays for the probe with respect to the pump as shown in figure 4.1 (a) to reconstruct the whole time trace afterwards from all the consecutive measurements. However, the conventional pump-probe configuration using delay lines suffers from low scanning speed, manufacturing tolerances, measurement artefacts, among others. The delay can also be introduced by changing the relative phase of lasers that ASOPS (Asynchronous Optical Sampling System) configuration allows [119, 120]. Two lasers instead of one are used in the pump-probe system of ASOPS configuration where one of the lasers is electronically delayed from the other to recover the time trace as shown in figure 4.1 (b). The electronic delay system ensures high scan speed and improved beam point stability.
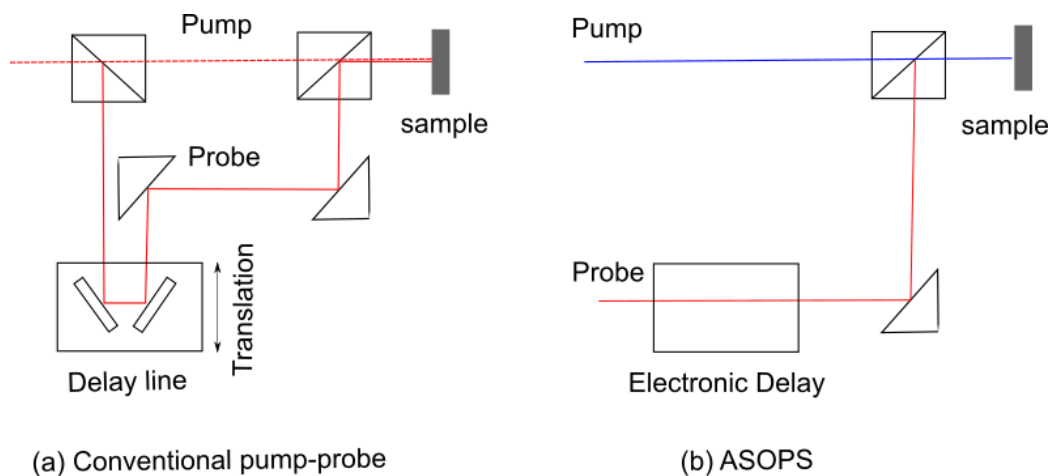
Figure 4.1: A simplified pump-probe set-up. (a) Conventional pump-probe configuration using mechanical delay line. (b) ASOPS pump-probe configuration where one of the laser pulses is electronically delayed from the other with high speed.

It can be seen in figure 4.2 that a co-incidence peak is generated each time from the sample when the pump pulse arrives where the time interval is the inverse of the pulse repetition frequency (PRF) of the pump laser. Detail about the co-incidence peak is described in section 4.4.1. The delay rate (DR) defines the rate at which the probe pulse is delayed from the pump pulse where the inverse of DR fixes the time interval when the pump and probe will be in synchronisation again. The number of pump and probe pulses in this time interval equals the ratio of PRF to DR.
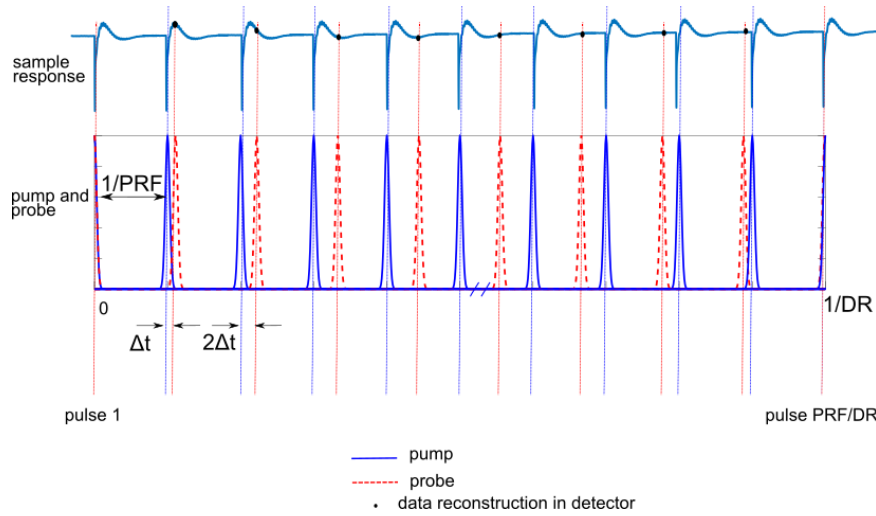
Figure 4.2: A basic pump-probe system where the probe pulse is delayed from the pump pulse to reconstruct the signal. The delay between the pump (blue) and probe (red) pulse is swept with an increment of Δt from 0 to the pulse repetition period. It can be seen from the sample response that a co-incidence peak is generated each time when the pump pulse arrives. The probe is delayed from the pump to reconstruct the whole signal as can be seen from the black points on the signal.

The experimental set-up used in this research was based on a dual Ti:Sapphire (Tsunami, Spectra-Physics) laser asynchronous optical sampling (ASOPS) system [114, 115] that had two femtosecond pulse lasers ($\sim 100\ f_s$ pulse width) where one laser had a PRF of 80 MHz and other laser had PRF of 80 MHz±DR. The probe pulse was delayed from the pump pulse from 0 to 12.5 ns for every 100 μs when the DR was 10 kHz. The number of pump or probe pulse was then 8000 as can be seen in figure 4.3. Pump pulse can also be delayed from the probe pulse in a pump-probe system where the probe laser acts as a master.
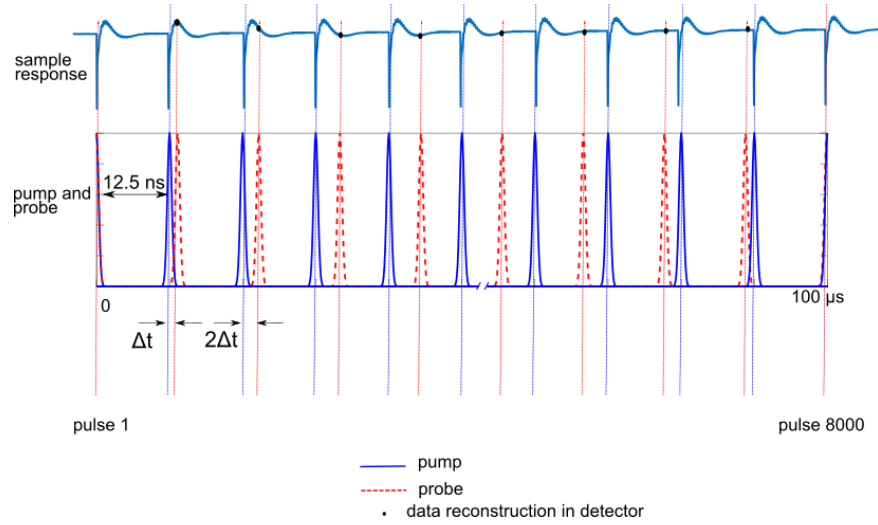
Figure 4.3: The applied pump-probe system where the probe was delayed from the pump to reconstruct the signal. The delay between the pump (blue) and the probe (red) pulses was set and swept from 0 to 12.5 ns in every 100 μs (10 kHz). It can be seen from the sample response that a co-incidence peak was generated each time when the pump pulse arrived. The probe was delayed from the pump from 0 to 12.5 ns to reconstruct the whole signal as can be seen from the black points on the signal.

4.3   Experimental set-up

The experimental set-up used in this project was designed in a way so that both UV-NIR and NIR-NIR modes could be used. The Laser wavelengths were tunable from 700 to 900 nm. The beam from one of the lasers was fed to a doubler to produce the UV beam. It was also possible to change the power and polarisation of light using the set-up. The designed system had the facility to detect the signal both in transmission and reflection. A schematic of the used experimental set-up is shown in figure 4.4.
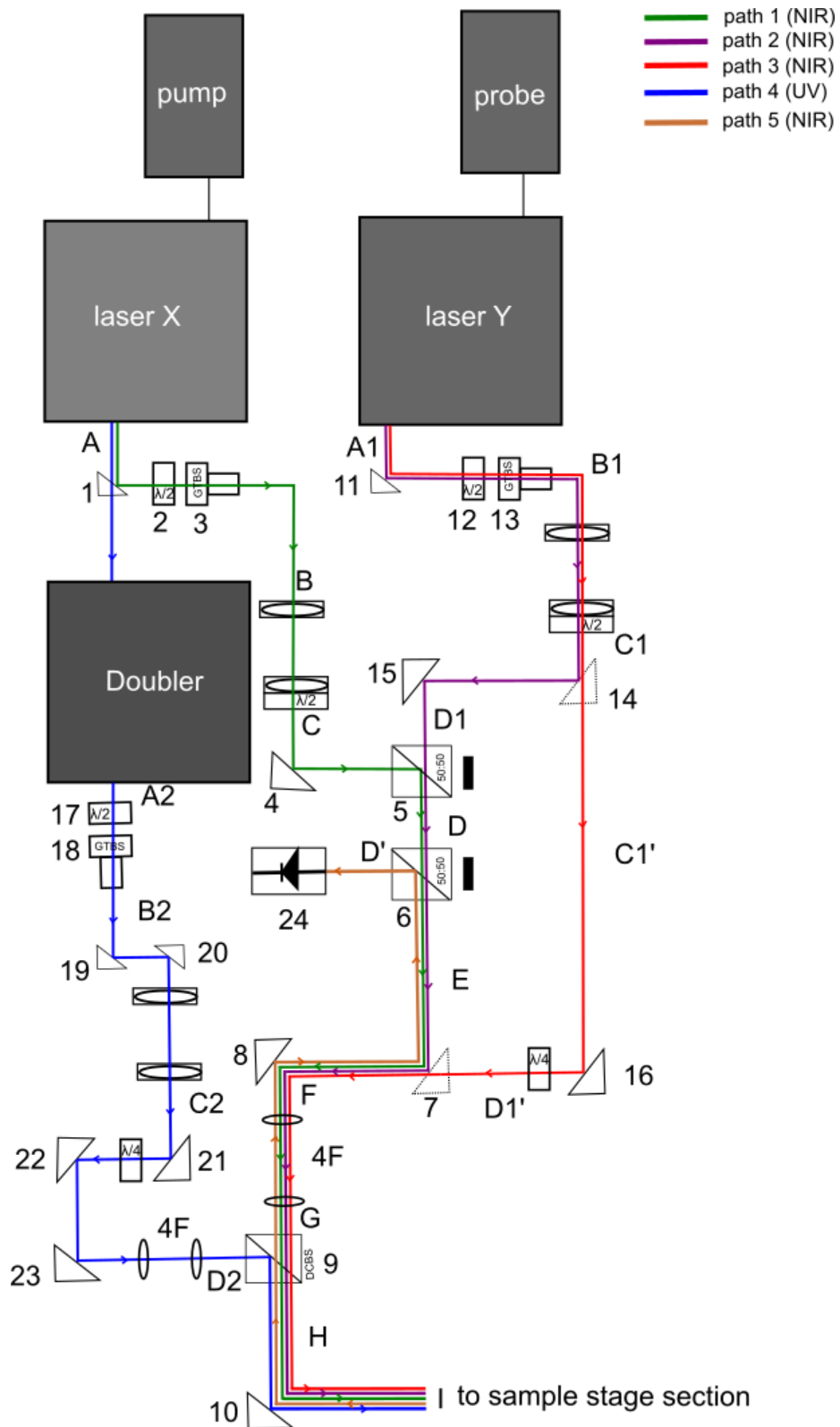
Figure 4.4: A schematic of the used experimental set-up (top view). This set-up had the facility to do an experiment in UV-NIR and NIR-NIR configurations. It was also possible to change the wavelength, power and polarisation of light (state and angle). The set-up was designed for adapting different types of experiments and it was easy to correct any anomaly. It is good to mention that the colour of light beam does not represent the wavelength of the light in the drawing.

Each optical path of the set-up is explained below.

1. Mirror 1 was a movable mirror that allowed switching between UV-NIR and NIR-NIR modes. The beam from laser X was reflected by this mirror (1) and passed through a half-wave plate $\lambda/2$ (2), Glan-Taylor Beam Splitter GTBS (3) and a beam expander following the path ABC. The power of the beam was controlled by the $\lambda/2$ and GTBS. Then, the beam was reflected by a mirror (4) and split by two 50:50 beam splitters (5 and 6) following the path CDE. Next, the beam was reflected by two mirrors (7 and 8) and passed through a 4F system following the path EFG. Finally, the beam was transmitted by a dichroic beam splitter (DCBS) (9) and entered the sample stage section after being reflected by a mirror (10) following the path GHI. In this way, the NIR beam from laser X was used as a pump or probe. The path ABCDEFGHI is called path 1 here to easily mention.

2. The beam from laser Y was reflected by a mirror (11) and passed through a half-wave plate $\lambda/2$ (12), Glan-Taylor Beam splitter GTBS (13) and a beam expander following the path A1B1C1. Then, the beam was reflected by mirrors (14,15) following the path C1D1. Next, the beam was passed through two 50:50 beam splitters (5,6) and reflected by mirrors (7,8) before entering a 4F system following the path D1DEFG. Finally, the beam passed through a dichroic (9) and entered the sample stage section after being reflected by a mirror (10) following the path GHI. In this way, the NIR beam reached the sample and was used as a pump or probe. Generally, this path was followed when a linearly polarised probe beam was required. However, a quarter-wave plate could be placed between mirror 7 and mirror 8 to make the beam circularly polarised. The path A1B1C1D1DEFGHI is called path 2 here to easily mention.

3. There was another way to direct the beam from laser Y to the sample stage section when two mirrors (14,7) were absent and the beam was reflected by a mirror (16) following the path A1B1C1C1′D1′FGHI. A quarter-wave plate was placed between mirror 16 and mirror 7 to make the light circularly polarised. Generally, this path was followed when the circularly polarised NIR probe beam was required for experiments. The path A1B1C1C1′D1′FGHI is called path 3 here to easily mention.

4. The UV beam was generated by feeding the beam from laser X (orange line) into a doubler (Model 3980 Spectra-Physics) when mirror 1 was absent. Then, the generated beam was passed through a half-wave plate $\lambda/2$ (17), a Glan-Taylor Beam Splitter (GTBS) (18) and reflected by two mirrors (19 and 20) before passing through a beam expander following the path A2B2C2. The power of the beam was controlled by the $\lambda/2$ and GTBS. Next, the beam was reflected by three mirrors (21, 22, 23) and entered a 4F system following the path C2D2. Then, the beam was reflected by a dichroic beam splitter (9) and another mirror (10) before entering the sample stage section following the path D2HI. A quarter-wave plate was placed between mirror 21 and mirror 22 to make the blue beam circularly polarised. In this way, the blue beam reached the sample and was used as a pump for the generation. The path A2B2C2D2HI is called path 4 here to easily mention.

5. The probe light reflected from the sample followed the path IHGFED$'$ to the detector (24). This path is called path 5 here to easily mention and was used to detect in the reflection mode.

24. sample stage
25. obejctive lens
26. dichroic beam splitter (DCBS)
27. a motor with half wave plate
28. polarizing beam splitter (PBS)
29. mirror
30. lens
31. detector (that detects horizontally)
32. lens
33. detcetor (that detects vertically)
34. light Emitting Diode (LED)
35. mirror
36. lens
37. beam splitter (50:50)
38. dichroic beam splitter (DCBS)

pump
probe

(a)

(b)
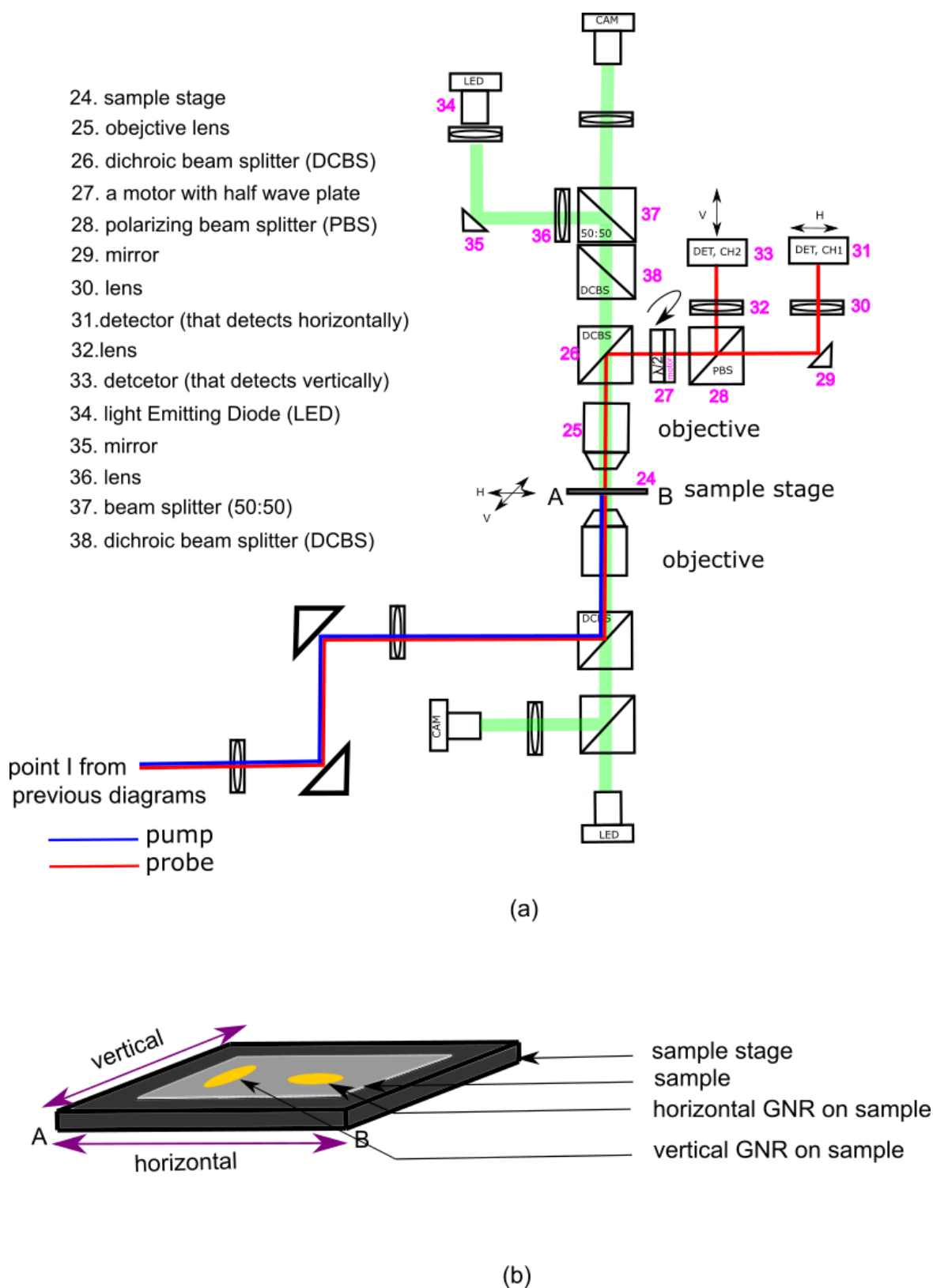
Figure 4.5: The sample stage section of the experimental set-up. (a) A schematic diagram (b) Assumptions about the direction of light and nanorod along and perpendicular to the sample stage.

94

The experimental set-up of the sample stage section where gold nanorods were excited by the pump beam and modulation of the scattered probe light was detected by the photo-detectors is shown in figure 4.5 (a). The sample was mounted on an electromechanical stage which was moved with a pre-set step motion to scan the sample. Fine step size ensures better quality of the results but at the cost of high scan time. The pump and probe beams were delivered from the bottom of the sample through the required objective and the scattered probe light was collected from above through another objective. Generally, 20x (Olympus LUCPlanFL N 20x, NA 0.45) or 40x (Olympus LUCPlanFL N 40x, NA 0.60) bottom objective and 20x (Mitutoyo Plan Apo, NA 0.42) top objective were used for the experiments of this project. Hence, the pump spot size (diameter) was $\sim$1 μm (for 20x) or $\sim$0.8 μm (for 40x) and the probe spot size (diameter) was $\sim$2 μm. In general, a maximum average power of 2 mW was used for both pump and probe at the sample which corresponded to a pulse energy of 25 pJ and peak power of 250 W, respectively.

In the case of detection in transmission, the probe light was passed through a dichroic beam splitter (dichroic beam splitter (DCBS) (26) to a polarising beam splitter (PBS, 28) that split the detected light into horizontally and vertically polarised beams. Each beam went to the respective photo-detector through a lens. A half-wave plate (27) was placed before the PBS and rotated by a motor automatically to change the angle of detection or polarisation of the linear probe light. The set-up permitted the detection of both cross-polarisations at the sample stage plane simultaneously using two photodetectors. The motor (HT08-221) was a NEMA 8 high torque step motor which was driven by a phidget stepper 1063. A sensor (QRD1114, phototransistor, reflective) was attached to the motor to detect the motor's home position. The motor surface was black and a small piece of Aluminium tape was attached to the surface of the motor so that the sensor could detect the difference in the reflection. The position of the Aluminium tape was set to $0°$ of the half-wave plate. The nanorod sample was scanned with this set-up frequently to detect the rods from different angles to demonstrate the orientation sensitivity of the nanorod to the polarisation of light. The sample was illuminated by a top and bottom LED to see in the top and bottom cameras, respectively. The labelled parts above the sample stage in figure 4.5 (a) can be compared with the image of the upper part of the sample stage section from the laser laboratory as shown in figure 4.6.

The orientation of a nanorod and the polarisation of light were very important matters for this project. It can be seen from figure 4.5 (b) that the direction along the sample stage was considered horizontal and the direction perpendicular to the sample stage was considered vertical. The polarisation axis of the half-wave plate matched the horizontal axis at the sample stage.
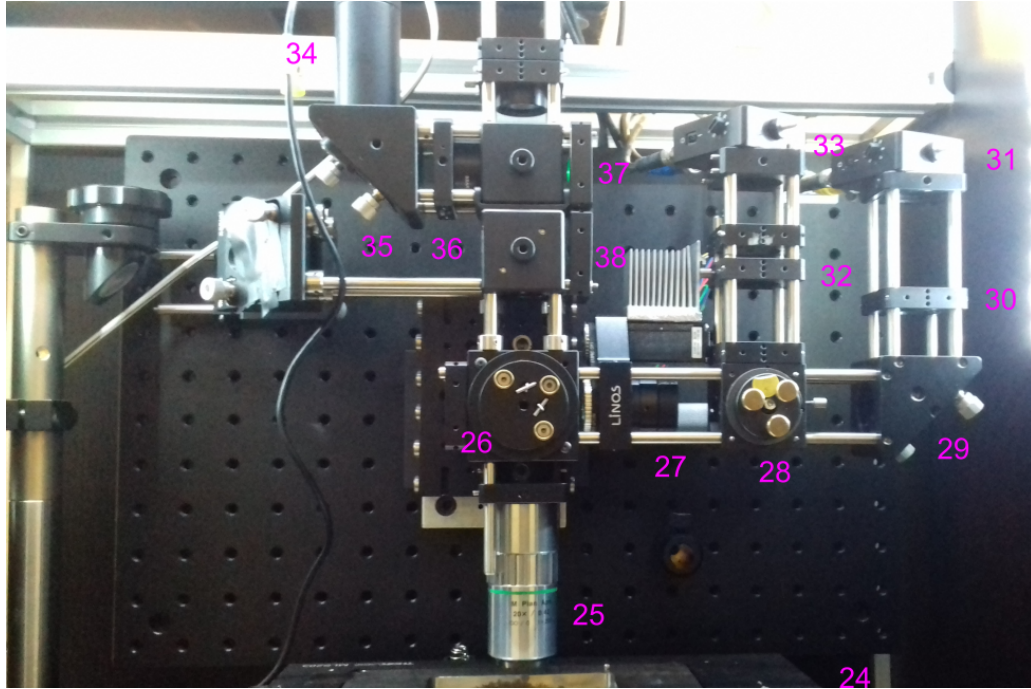
Figure 4.6: Laboratory image of the upper part of the sample stage section.

The signal from the detectors was split into DC and AC levels where the AC path was amplified before going to the oscilloscope because very small modulation depth can be observed in pico-second experiments. The amplifier (MiniCircuits ZFL-500+) introduced a gain of 20 dB. The DC was recorded with the help of analogue to digital cards. Responses from the photo-detectors (Thorlabs PDA 36A) were captured and averaged on a digital oscilloscope (Lecroy, wave Runner HRO 66Zi) as shown in figure 4.7 where the signal from an EBL fabricated GNR can be seen from two detectors. There were scope filters also (Mini-Circuits 15542, DC 7 MHz) to remove the noise. It is shown in section 3.3.1.1 through simulations that a nanorod is sensitive to its orientation to the light. It can be seen in figure 4.7 that the EBL fabricated GNR was detected along the major axis (yellow curve) but was not detected along the minor axis (blue curve). A signal detected at delay T on the digital oscilloscope (DSO) corresponds to a real delay between the laser pulses

of T/8000 at a DR of 10 kHz. It means that a frequency measured on the DSO of f_{scope} corresponds to a real frequency of 8000 f_{scope}. Generally, 10,000 averages took around 3 s to acquire. However, more averages can be taken to improve the SNR at the cost of high acquisition time.

Figure 4.7: Laboratory image of an oscilloscope showing a trace from an EBL fabricated GNR detected along the length (yellow) and the width (blue). It can be seen that the rod turned off when it was detected along the width.

4.4 Basic signal processing

In this research, acoustic images of gold nanorods were reconstructed by determining their sizes, orientations and locations. The size was determined from the acoustic resonant frequencies of gold nanorods. At first, the signal processing steps to get the frequency information of a nanorod from the obtained experimental raw traces are explained in this section. Then, different algorithms and signal processing steps are explained in detail. Those were used to predict the orientation and location of a nanorod. Finally, the processes of reconstructing the phononic images of gold nanorods and comparing the reconstructed images with the corresponding SEM images are explained. All the signal processing steps are shown using experimental results for better explanation.

4.4.1 Single trace analysis

An experimentally obtained raw time trace from a gold nanorod is shown in figure 4.8. It can be seen that each time trace consists of a co-incidence peak, thermal background, background coming from the laser electronics and oscillatory components on top of the thermal background. A co-incidence peak arises due to short-lived electronic effects while the pump and probe hit at the same time and the thermal background exists due to the temperature change of the particle. The oscillatory components carry the vibrational frequency information of the particle.
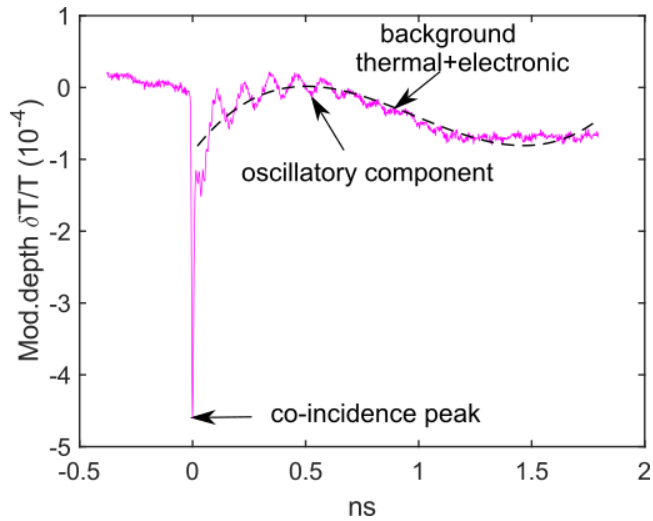
Figure 4.8: An experimentally obtained time trace from a gold nanorod which consists of a co-incidence peak, thermal background, background coming from the laser electronics and oscillatory components on top of the thermal background.

As a nanorod has both low and high frequency components, the raw data was processed for two different lengths of time windows. The signal processing steps are discussed for both long and short time windows below:

1. At first, the trace was truncated from the co-peak location at t = 0 up to the region of interest (long time trace/short time trace) to extract the information about the low and high frequencies. It is very important to find the proper location of the co-peak so that the desired signal is not cut. A default co-peak location and a range around it were used to find the location of the co-peak by searching for the location of the maximum value. If the obtained maximum value was above a chosen threshold value (set to separate signal and noise), the found co-peak location was

used, otherwise, the default co-peak location was used. Then, the truncated data was passed through a designed digital low-pass filter to remove the undesired high frequency components. The raw time trace is shown in figure 4.9 (a). The truncated traces for the long and short time windows after being filtered are shown in figure 4.9 (b) and figure 4.9 (c), respectively.

2. The next step was the removal of the thermal background from the traces. Hence, the traces were first fitted with polynomials (black lines) as can be seen in figure 4.9 (d) and figure 4.9 (e). Fitting with polynomials acted as a low pass filter. Then, the fitted polynomials were subtracted from the traces as shown in figure 4.9 (f) and figure 4.9 (g). Hence, when the fitted polynomials were subtracted from the raw traces, high pass filtering was carried out. Generally, polynomial fit orders of 3 and 5 were used for low and high frequency components, respectively. The choice of polynomial order is very important because it acts as a high pass filter and can remove the desired low frequency component if it is set too high. An initial offset from the co-peak location was also introduced to truncate the trace for excluding the co-peak transition point. Finally, only the oscillatory information was obtained which contains the vibrational information of the nanorod.

3. A fast Fourier Transform (FFT) was performed on the traces to obtain the low and high vibrational frequency modes as shown in figure 4.9 (i). It can be seen that the longitudinal mode (low frequency) and breathing mode (high frequency) of the gold nanorod were at 8.3 GHz and 64.8 GHz, respectively.
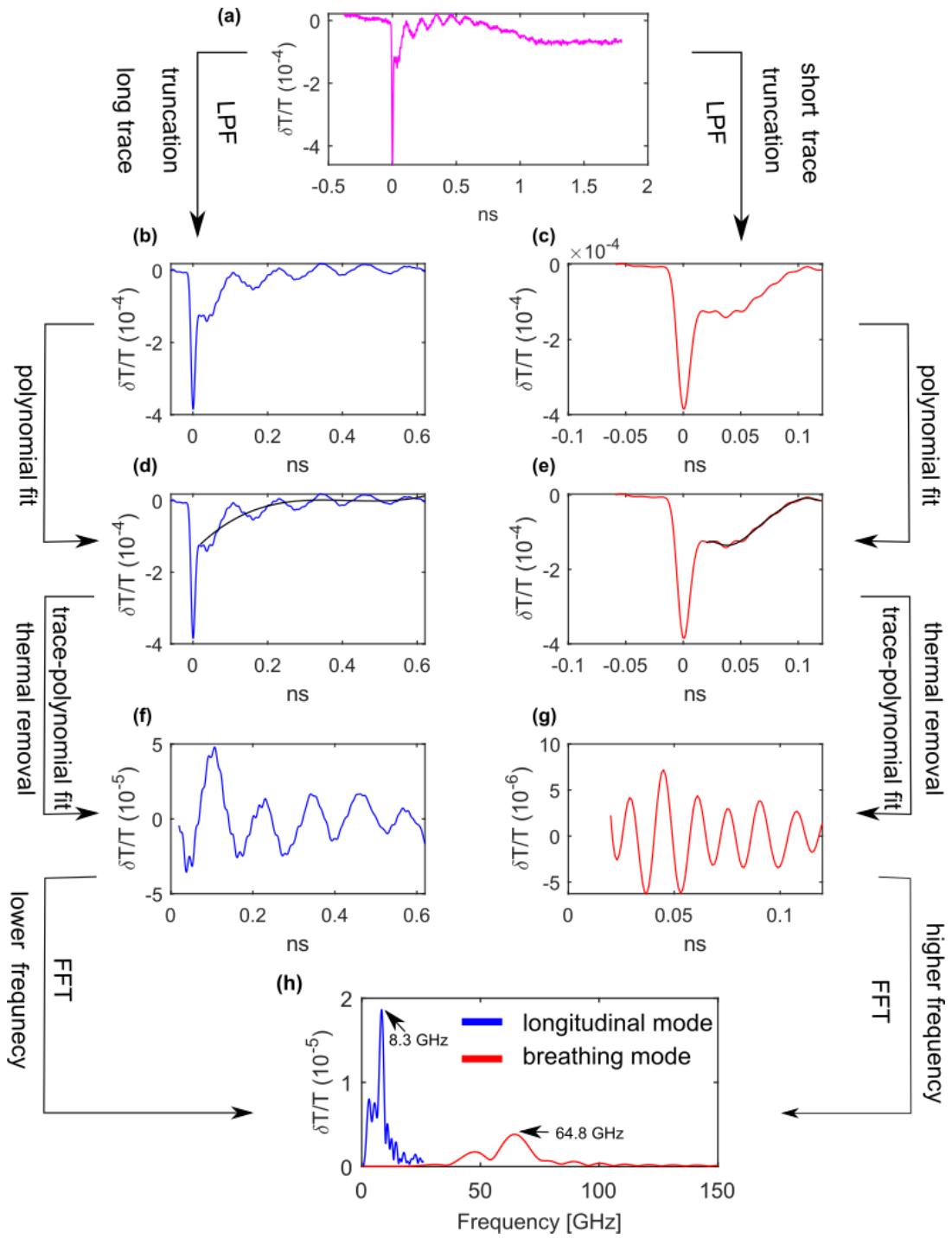
Figure 4.9: Basic signal processing steps on an experimental trace obtained from a gold nanorod to extract the vibrational frequency information. (a) Raw time trace of a gold nanorod showing the co-incidence peak, background coming from the laser electronics, thermal background and oscillatory signal. (b)(c) Truncated raw time traces for long and short time windows respectively after passing through a digital low pass filter. (d)(e) Filtered traces after fitting to a polynomial to remove the thermal background. (f)(g) Only oscillatory signal that contains the low and high vibrational frequency modes respectively after subtraction of the thermal background. (h) A fast Fourier transform (FFT) of the time traces that shows the low frequency (longitudinal mode) and high frequency (breathing mode) modes at 8.3 GHz and 64.8 GHz, respectively.

4.4.2 Imaging technique

Image reconstruction was a very important objective of this project. A single experimental trace of a GNR provided information about its DC, AC and vibrational frequency. The optical image, modulation depth map and frequency map were obtained from the DC information, ratio of AC to DC and FFT of the oscillatory components, respectively. To reconstruct the image of nanorods, additional parameters were needed such as size, location and orientation of nanorods. All these parameters were determined using the basic information obtained from the experimental traces. Applied image reconstruction techniques in this research are described below.

4.4.2.1 DC map

Objects can be detected from the DC map (optical picture) that shows the total amount of light reaching the detector after being absorbed by the object. The DC map can also show the presence of defects or any chemical leftovers on the sample in addition to the desired object. Though the resolution of the image is limited by optics, DC map is useful to find resolvable features for sample registration. The optical map of a nanorod is shown in figure 5.4 (a). It is the same nanorod for which the single trace analysis was shown in figure 5.4. It can be seen that the nanorod was not resolved optically.

4.4.2.2 Modulation depth map and frequency map

The modulation depth is the ratio of AC values to DC values. The modulation depth (expressed by $\delta T/T$, where T is the transmission) map plots the maximum of modulation depth. In this work, modulation depth was used as a way to assess the strength of the signal. Hence, the modulation depth map is also called the amplitude map in this thesis. Amplitude maps of the same nanorod for longitudinal mode and breathing mode are shown in figure 5.4 (b) and figure 5.4 (c), respectively. The frequency map plots the frequency of maximum FFT amplitude within the selected frequency range and a minimum threshold of modulation depth is set to remove the noise. Frequency maps of the nanorod for longitudinal and breathing mode are shown in figure 5.4 (d) and figure 5.4 (e), respectively.
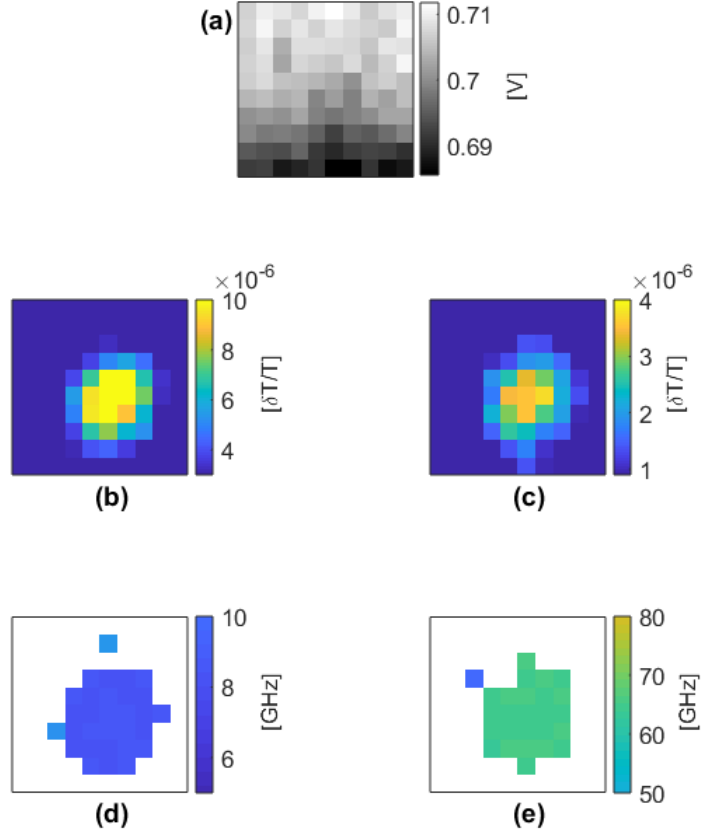
Figure 4.10: A scanned area of a GNR with 200 nm step size. (a) Optical picture. (b)(c) Amplitude maps at the longitudinal mode (8.3 GHz) and breathing mode (64.8 GHz), respectively. (d)(e) Frequency maps showing the longitudinal and breathing modes, respectively.

4.4.2.3 Centroid calculation and localisation

The localisation technique was based on calculating the centroid of the particle from the scanned image using the centre of mass formulae. The process is demonstrated here through a simulation. A fake data was created using a Gaussian window as can be seen in figure 4.11 (a). Gaussian window was created using a Gaussian function

$$f(x) = a \exp\left(\frac{(x-b)^2}{2c^2}\right) \tag{4.1}$$

where a is the height of the curve's peak, b is the position of the centre of the peak and c is width of the curve.
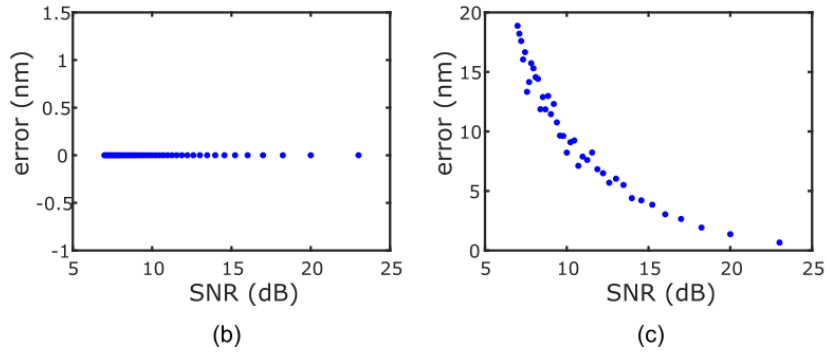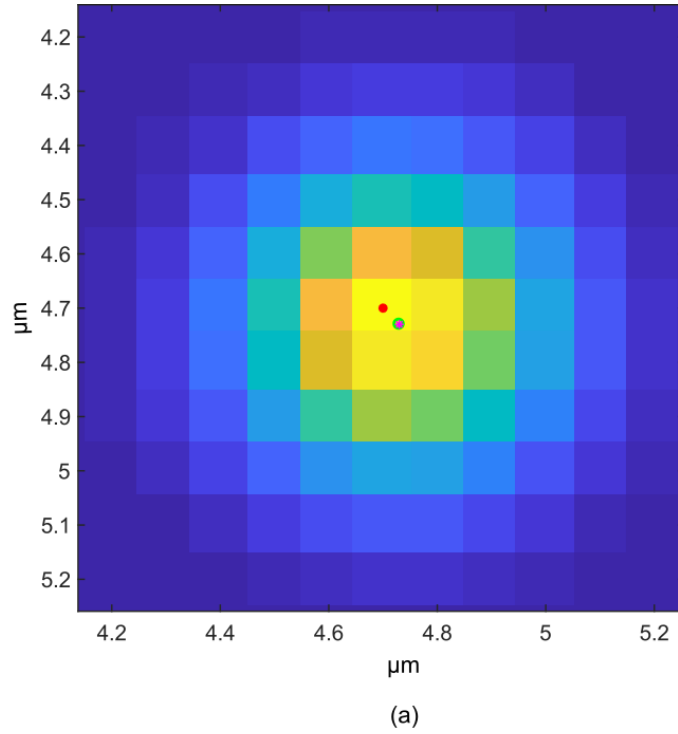
Figure 4.11: Centroid (centre of mass) calculation of a nanorod. (a) Noiseless fake data multiplied with a Hann window where the maximum amplitude, manually shifted centre of the data and calculated centre of mass are marked by a red dot, magenta dot and green dot, respectively. (b) There was no localisation error when there was no noise. (c) Localisation error reduced with an increase in SNR.

The centre of the fake data (Gaussian Window) was manually shifted (by changing b) by a fraction for testing, marked by a magenta dot in figure 4.11 (a). Next, the centre of the maximum amplitude location and the centre of mass were searched. Centre of mass x_{cm} formulae was used as follows:

$$x_{cm} = \frac{m_1 x_1 + m_2 x_2}{m_1 + m_2} \tag{4.2}$$

where m_1 is the mass of 1st object and x_1 is the position of 1st object. In ours case, the amplitude (as mass) and position of a pixel from the created data window were used in the equation to calculate the centre of mass for both x and y co-ordinates. It was observed that, a search for the maximum amplitude location returned the centre of the window as can be seen in figure 4.11 (a) marked by a red dot. On the other hand, a search for the centre of mass returned the manually shifted centre as can be seen in figure 4.11 (a) marked by a green dot. The green dot overlapped with the magenta dot when there was no noise.

Later, a random noise was added to the created fake data. Then, a Hann window was multiplied with the data plus noise to reduce the effect of noise outside the desired region. The Hann window has soft edges and hence is a better choice in comparison to the rectangular window. It was ensured that the Hann window size remains greater than the data plus noise width and a window of 23 pixels by 23 pixels was chosen. The distance between the obtained centroid point and the manually shifted point (b, actual centre) was calculated in pixels first and later the step size of the experiment was assumed as the value of one pixel. There was no error when there was no noise as can be seen in figure 4.11 (b). When noise was added, it can be seen from figure 4.11 (c) that there was an error which reduced with an increase in SNR. The experimental error in the centroid process can be estimated from this plot.

The size of the Hann window did not have a large impact on the localisation error. The window size was varied from 23 pixels by 23 pixels to 43 pixels by 43 pixels and the error was observed to increase from 10 nm to 25 nm at the SNR of 10 dB. The estimation was done for a scan step size of 100 nm. The SNR of the rod varied from 14 dB to 18 dB in the rod localisation results presented in this thesis that were taken with a step size of 100 nm. According to figure 4.11 (c), the location precision of this thesis results varied from 2 nm to 4.2 nm in the case of 100 nm scan step size and about 1 μm of data width. The same simulation was done for the data width and scan step size of each experiment to estimate the location precision.

| 1. Making a list of vibrational frequencies (longitudinal and breathing) of the nanorod (Frequency is used as a tag to identify the nanorod) |

| 2. Extracting the amplitude map of the rod at the desired frequency for four angles of detection |

| Amplitude maps at longitudinal and breathing modes at 0° | Amplitude maps at longitudinal and breathing modes at 90° | Amplitude maps at longitudinal and breathing modes at 45° | Amplitude maps at longitudinal and breathing modes at -45° |

| 3. Finding the location of maximum amplitude in all maps |

| 4. Amplitude map x Hann window mask centerd at the maximum amplitude location |

| 5. Finding the centroid (centre of mass) of rod in each map |

| 6. Calculating the weighted average of all centroids (for four angles) in the case of the longitudinal mode. Calculating the weighted average of all centroids (for four angles) in the case of the breathing mode (weight is the SNR of the rod for a speciifc angle of detection) |

| 7. Selecting one centroid (weighted average point) from either the longitudinal mode or the breathing mode to localize the rod |

| 8. Selectiion of a range around the selected location and calculating the average amplitude over that area for four angles (These are the angle amplitudes and either longitudinal or the breathing mode can be used in this calculation) |

| 9. Calculation of the nanorod's angle by using the phase stepping method and four angle amplitudes |

| 11. A rod was drawn of the calculated size and rotated by an amount of the calculated angle keeping the selected location as the centre | 10. Size characterization by converting the frequency to size by an analytical model |

| 12. The measured size, angle and location of the nanorod were combined to reconstruct its phononic image |

| 13. The reconstructed phononic image of the nanorod was overlaid to the SEM image for comparison |

Figure 4.12: Steps to calculate the location, size and angle of a nanorod to reconstruct its phononic image.

The whole process to locate a nanorod is explained in figure 4.12 through step 1 to step 7. As different sizes and shapes of nanorods have different frequencies, the vibrational frequency or mode was used as a tag to identify and locate a specific nanorod. At first, a list of frequencies (longitudinal and breathing modes) from all nanorods of the scanned

area was made. The next step was to extract the amplitude maps at those frequencies to identify a specific nanorod. This process acted as a frequency mask to filter out other rods to identify a specific rod (target rod) in that area. However, the situation became complex when the frequencies of other rods were close to the frequencies of the target rod. Hence, there was also one option to manually filter out other rods by multiplying the amplitude maps with a mask of zeros at specific areas to select the desired rod, if necessary. Otherwise, the centroid would be dragged to the rod which will have the higher FFT amplitude. Polarisation sensitivity of the rods also helped to separate them if they had different orientations. It is good to mention that the manual mask was used only to demonstrate the proposed technique. For practical applications of this technique, a gold nanorod set having a wide range of sizes and well separable frequencies is expected to be used. Although the orientations of nanorods in the distribution will be random, it can be said that the probability of all nanorods having the same orientation is very low. The distribution of nanorods will also be random. In the case of the cell imaging application of our technique, the distribution of gold nanorods will also depend on their binding to the cellular elements.

The experimental data was collected for four angles of detection (0°, 45°, 90°, 135°). Following this, the amplitude maps at the selected frequencies for all four angles were extracted. The next step was to find the location of the maximum amplitude in all maps. Then, the amplitude maps were multiplied by a Hann window mask where the centre of the Hann window was the obtained maximum amplitude location point. Next, the centroid was calculated using the centre of mass formula from all maps. In this way, there were eight estimated centroids for one rod, four for the longitudinal mode and four for the breathing mode. Then, the weighted average of all four centroids was calculated for both the longitudinal and breathing modes. Signal-to-noise ratios (SNRs) of the rod for four angles of detection were used as the weights in the calculation. Finally, one point (longitudinal or breathing) between the two obtained weighted average points was used as the location of the rod.
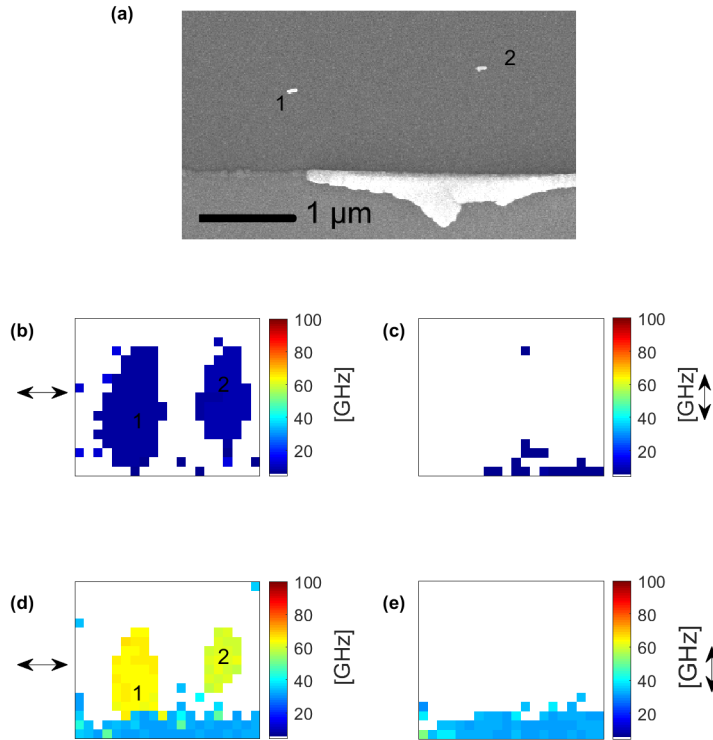
Figure 4.13: A scanned area showing two gold nanorods and their frequency maps. (a) The SEM image of the target gold nanorods. (b)(c) The longitudinal mode frequency maps where the almost horizontal nanorods were detected horizontally ('on' case) but were not detected vertically ('off'case), respectively. (d)(e) Breathing mode frequency maps where the almost horizontal nanorods were detected horizontally ('on' case) but not detected vertically ('off' case), respectively. The longitudinal modes of rod 1 and rod 2 were 7.69 and 8.24 GHz respectively and the breathing modes were at 64.51 GHz and 60.36 GHz, respectively.

The centroid calculation process and the localisation technique can be explained more with the help of a simple experimental result. In figure 4.13 (a), the SEM image of two gold nanorods can be seen where both of them were of similar size and produced approximately the same frequencies during the experiment as can be observed from the longitudinal and breathing mode frequency maps shown in figure 4.13 (b) and figure 4.13 (d), respectively. The experiment was done in water with the pump (415 nm) power of 0.5 mW and the probe (780 nm) power of 1 mW at the sample. Path 3 (probe) and path 4 (pump) were used for this experiment as explained before in section 4.3. To demonstrate the orientation sensitivity of both rods to the polarisation of light, the half-wave plate before the PBS

was rotated to change the angle of detection or the polarisation of the probe beam as was shown in figure 4.6 where two photo-detectors (orthogonal to each other) were used to detect in transmission. Two target rods were nearly horizontal and it was expected to detect those horizontally ('on' case) while miss those vertically ('off' case) as can be seen from figure 4.13 (b)(d) and figure 4.13 (c)(e), respectively. The detail of the angular response of a nanorod will be explained later in this section.

Following the centroid calculation and the localisation process described earlier in figure 4.12, all the amplitude maps were extracted at the frequencies of rod 1 (7.69 GHz, 64.51 GHz) for 0°, 45°, 90° and 135° angles of detection as shown in figure 4.14. It is important to mention that as the frequencies of two rods were very close, rod 2 was also visible in the maps when the frequency of rod 1 was used. For this reason, a manual mask was applied in addition to separate both rods. The obtained location of the maximum amplitude and the centre of mass for the rod are marked by a red cross and a green cross respectively on each map. The obtained position of the centre of mass was close to the maximum amplitude location, though it varied by a little amount. As the rod was almost horizontal, it was expected that the rod will be visible horizontally as can be seen in figure 4.14 (a)(c) and will not be visible vertically. However, the rod was not exactly a 0° rod and hence was slightly detected in figure 4.14 (b) but was not detected in 4.14 (d) for being close to the noise level. When the detection was at 45° or -45°, it was expected that the rod will be 'on' in both cases as can be seen in figure 4.14 (e) and 4.14 (f). However, the breathing modes were just detected and were close to the noise level as can be seen in figure 4.14 (g) and 4.14 (h). During the signal processing, a mask was applied to clean up the image to exclude the points below the noise threshold. However, it was ensured that the mask does not exclude any desired signal component. The optical image of the nanorod is shown in figure 4.14 (i) and it can be seen that the rod was not visible optically. As described before in figure 4.12, the calculated weighted average of all centroids for the longitudinal mode was chosen as the final point to localise the rod. The FFT traces at the selected point are shown in figure 4.14 (j) where it can be seen that the longitudinal and breathing modes of rod 1 were at 7.69 GHz and 64.51 GHz, respectively.

Similarly, all the amplitude maps were extracted at the frequencies (8.24 GHz, 60.36 GHz) of rod 2 for 0°, 45°, 90° and 135° angles of detection as shown in figure 4.15. Rod 2

was also almost horizontal and was 'on' for horizontal detection as shown in figure 4.15 (a) and (c). In contrast, the rod was slightly detected vertically as can be seen in figure 4.15 (b) and was not detected at all in 4.15 (d). When the detection was at 45° or -45°, it was expected that the rod will be 'on' in both cases as can be seen in figure 4.15 (e) and 4.15 (g). The rod was partially detected at -45° as can be seen in figure 4.15 (f) but was not detected at all in figure 4.15 (h) for being below the noise level. The obtained location of the maximum amplitude and the centre of mass for the rod are marked by a red cross and a green cross respectively in each map. The calculated weighted average of all centroids for the longitudinal mode was chosen as the final point to localise the rod. The optical image of the nanorod and FFT traces at the chosen location are shown in figure 4.15 (i) and 4.15 (j), respectively. It can be seen that the longitudinal and breathing modes of rod 2 were at 8.24 GHz and 60.36 GHz, respectively. It can be understood from the two experimental results that the vibrational frequency of a nanorod can be used as a tag to predict its location.
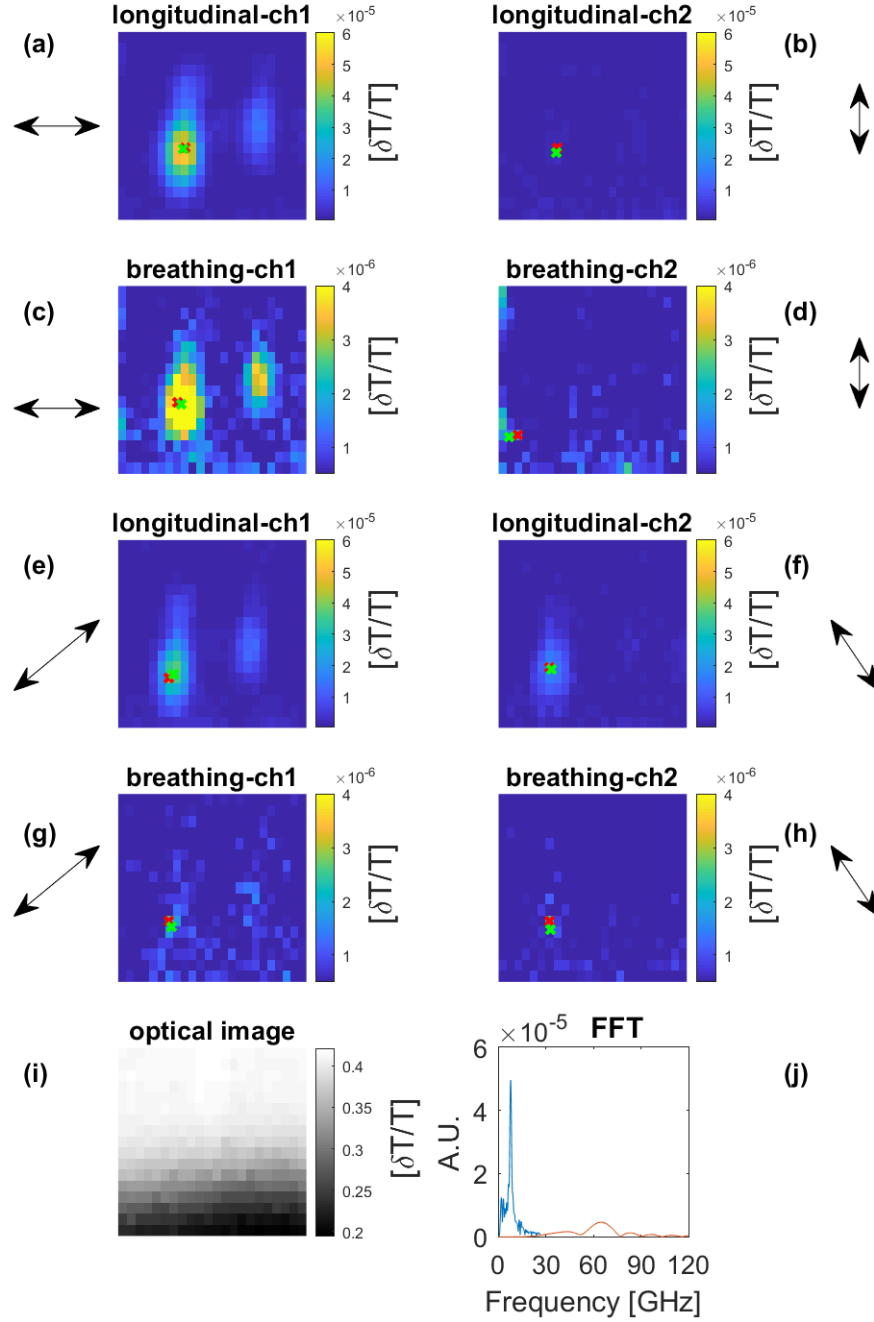
Figure 4.14: Amplitude maps extracted at the longitudinal and breathing modes of rod 1 to determine the location of the rod using the orthogonal detectors. (a)(b) Amplitude maps at the longitudinal mode (7.69 GHz) of rod 1 when were detected horizontally and vertically, respectively. (c)(d) Amplitude maps at the breathing mode (64.51 GHz) of rod 1 when were detected horizontally and vertically, respectively. (e)(f) Amplitude maps at the longitudinal mode of rod 1 when were detected along +45° and -45° respectively. (g)(h) Amplitude maps at the breathing mode of rod 1 when were detected along +45° and -45° respectively. The maximum amplitude location and the centre of mass of the rod are marked with a red cross and green cross respectively on each map. (i)(j) Optical image and FFT traces at the chosen location of the rod.
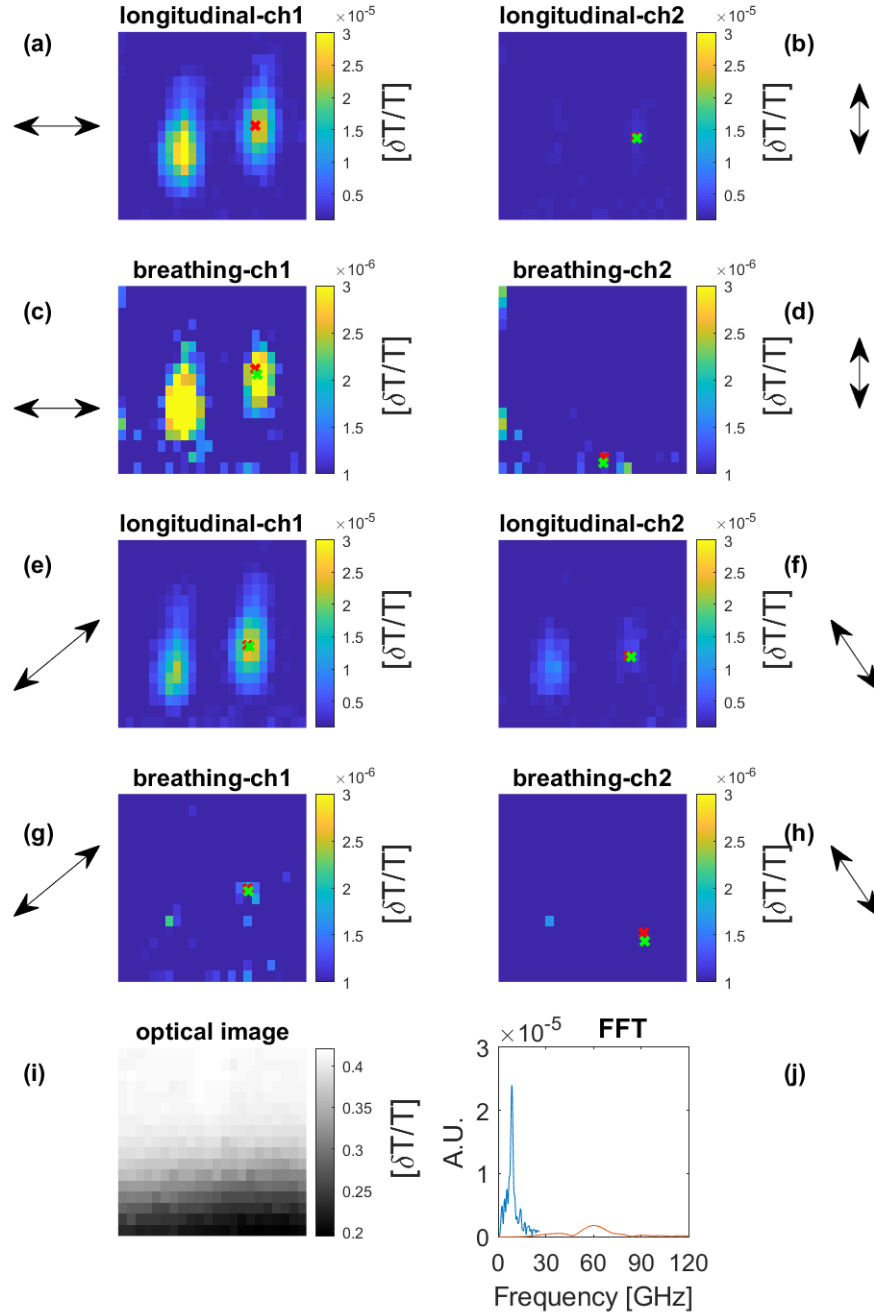
Figure 4.15: Amplitude maps extracted at the longitudinal and breathing modes of rod 2 to determine the location of the rod using orthogonal detectors. (a)(b) Amplitude maps at the longitudinal mode (8.24 GHz) of rod 2 when were detected horizontally and vertically, respectively. (c)(d) Amplitude maps at the breathing mode (60.36 GHz) of rod 2 when were detected horizontally and vertically, respectively. (e)(f) Amplitude maps at the longitudinal mode of rod 2 when detected along +45° and -45° respectively. (g)(h) Amplitude maps at the breathing mode of rod 2 when were detected along +45° and -45° respectively. The maximum amplitude location and centre of mass of the rod are marked with a red cross and green cross respectively on each map. (i)(j) Optical image and FFT traces at the chosen location of the rod.

4.4.2.4   Angle determination of a nanorod

The angle of a nanorod can be determined by using its sensitivity to the polarisation of light. In this research, a circularly polarised generation beam was used and the changed responses of a nanorod due to changes in the polarisation of the detection beam were recorded to determine its angle. The concept can be easily explained with the help of a cartoon image shown in figure 4.16. For example, the detected response will be maximum along 0° (or 180 °) for a 0° rod as can be seen in figure 4.16 (a). In contrast, the detected response will be minimum along 90° (or -90°) and half of the maximum along +45° (or -45°). The trend will be same for a 45° and a 90° rod as can be seen in figure 4.16 (b) and (c), respectively.
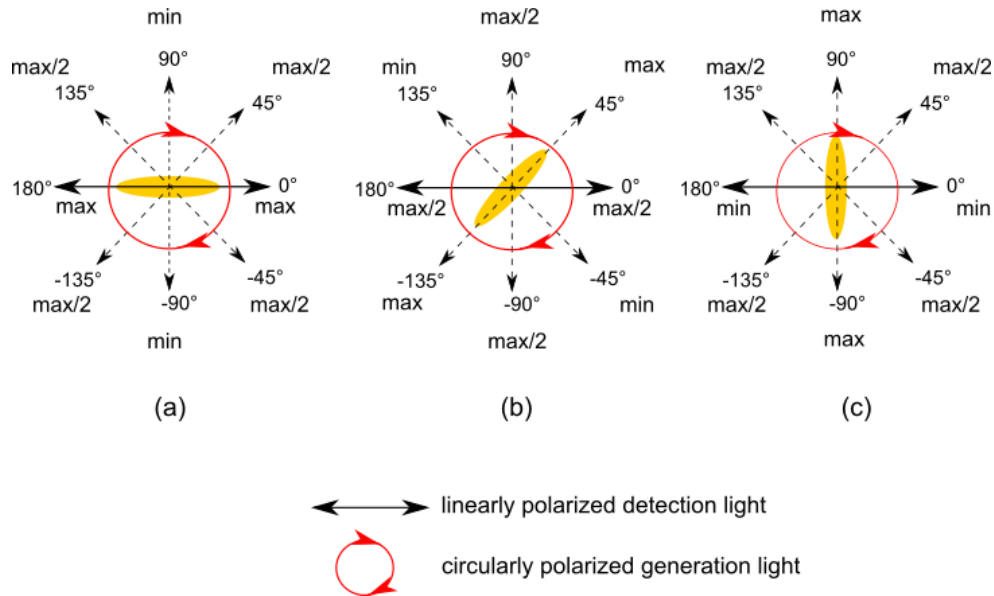
Figure 4.16: A cartoon image showing the circularly polarised generation beam on the rod and linearly polarised detection beam in different angles.

So, the phase of the detected signal changes if the rod angle changes and in turn the intensity at the selected detection angles also changes as can be seen in figure 4.17. The simulated responses changed according to the $cos^2\theta$ relation. Also, the curves were symmetric because of the shape of a rod which has two pulse symmetries. The change of phase can be determined by using two points, three points or four points phase stepping algorithm [223, 224]. In this research, four points phase stepping method was chosen to ensure good signal-to-noise ratio. The rod response was detected via $1 + cos(2\theta)$ form

during phase stepping to calculate the phase or angle of the rod. Four points phase stepping method was also a convenient method for the project because two orthogonal detectors were used in the experimental set-up and it was possible to get information about four angles of detection from two angles of detection.

According to the four points phase stepping algorithm, the phase distribution,

$$\phi = tan^{-1} \frac{I_4 - I_2}{I_1 - I_3} \tag{4.3}$$

where I_1 to I_4 are intensity values at $0°$, $90°$, $180°$ and $270°$.

In this thesis, four measurements at $0°$, $45°$, $90°$ and $135°$ were taken to determine the angle of a rod by using four points phase stepping method. The used formulae for the angle determination of a rod is as follows

$$\phi_{nanorod} = 0.5\, tan^{-1} \frac{I_4 - I_2}{I_1 - I_3} \tag{4.4}$$

where I_1, I_2, I_3 and I_4 are detected amplitudes at $0°$, $45°$, $90°$ and $135°$, respectively. It was tested theoretically that the phase stepping algorithm can estimate the angle of a rod correctly with four points. Hence, the phase stepping algorithm was a reliable technique to determine the angle of the rod. It was also a time saving solution because it used only four points. It can be very time consuming to use many points to determine the angle of a rod, specially if the angle responses come from area scans with fine step size and reasonable averages. However, fine angular scan of a rod can be done by just taking the data from a single point on the rod with high averages as shown later in this section (figure 4.19).
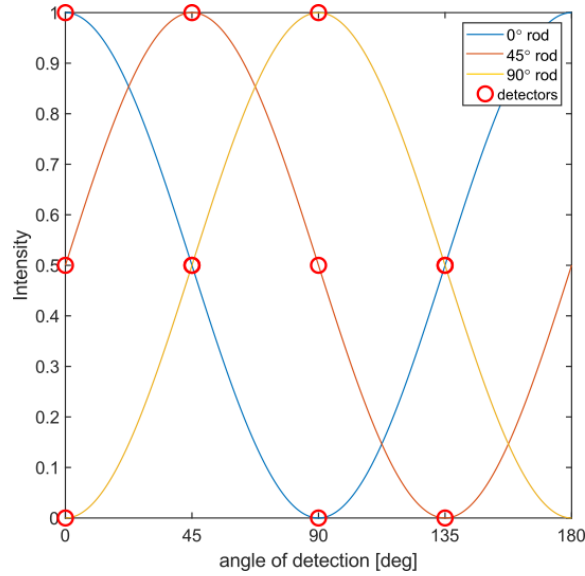
Figure 4.17: Simulated responses of a rod at 0°, 45° and 90°. It can be seen that the intensity of the detected signal changed as the phase of the rod changed. There were four detectors at 0°, 45°, 90° and 135° to record the amplitudes. These four amplitudes were used to determine the angle of the rod by the phase stepping method.

However, the phase stepping algorithm may not work reliably if noise is present in the signal. Experimentally obtained signals contain noise and reliability of any technique depends on the signal to noise ratio (SNR). The error between the true angle and the calculated angle by the phase stepping method was estimated as a function of SNR as can be seen in figure 4.18. At first, a specific amount of random noise was added 100 times to the signal of the rod per angle and the mean SNR for each angle was calculated. Then, the standard deviation of error between the noise free and the noisy signal per rod angle was calculated. The mean of all SNRs from different angles was the final SNR and the maximum of error was plotted vs final SNR as can be seen in figure 4.18. The same procedure was repeated by introducing different amount of random noise and the variation of error with SNR was observed. It can be seen that error was high for low SNR and low for high SNR. Hence, the calculated angle of the rod by the phase stepping method can deviate from the true value if the SNR is not high enough during the experiment. However, it is possible to estimate the deviation of the calculated angle from the expected angle as a function of SNR. High SNR can be ensured by using high power but that can damage the particles. Number of averages can also be increased to increase the SNR but at the cost of high acquisition time (low speed). Alternatively, pump/probe wavelengths can be

chosen in a way where the target GNR has high sensitivity to maximise the amplitude in generation and detection. Generally, SNR was observed to vary from 6 dB to 15 dB in the obtained results of this thesis. Hence, the angle precision of the phase stepping method was 3.6° to 0.4°.
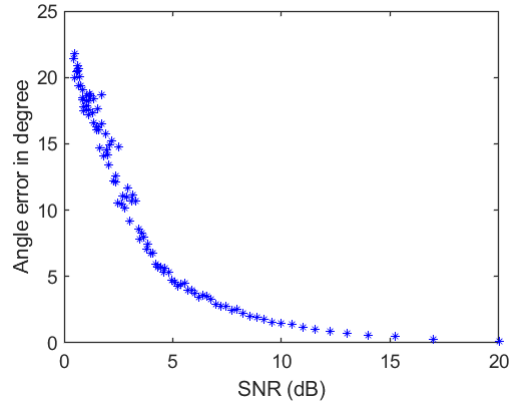
Figure 4.18: Angle error of a nanorod calculated by the four points phase shifting method vs SNR. It can be seen that the error was high for low SNR and reduced as the SNR improved.

To apply the four points phase shifting method on the experimental data, step 8 and 9 were followed as shown in figure 4.12. A range was selected around the chosen position of localisation as described before and the average amplitudes were calculated over the range for all 0°, 45°, 90° and 135° angles of detection at first. Then, all four amplitudes were used to determine the angle of the rod following the equation 4.4. Either longitudinal or breathing mode amplitude sets can be used to determine the angle of a nanorod using the phase shifting method. In this case, longitudinal mode amplitude set was used to determine the angle of rod 1 and rod 2 as breathing modes were not well detected each time. The obtained angles of rod 1 and rod 2 using the phase stepping method were -11.3±0.4°and -22.5±0.5°. The deviation came from the effect of noise on the angle error predicted by the phase shifting method as shown in figure 4.18. Experimentally, SNRs of the rods were calculated from the ratio of rod amplitudes to the noise where noise was the mean of the signal level (absolute of FFT map at the rod frequency) with no particle. Angles of rod 1 and rod 2 were 0±5° according to the SEM image.

The reasons behind the angle deviation can be low SNR, non-sinusoidal response of the rod, improper beam shape, not proper circularly polarised light, minor mismatch in the orientation of the sample on the SEM stage and the experimental stage, minor calibration fault of the rotary parts in the set-up and misalignment of optics. It was ensured that the last three options could not contribute to the error. It is sensible to think that the low SNR and non-sinusoidal response of the rod were the main reasons behind the angle deviation. The reason for the non-sinusoidal behaviour of the rod can be optics and slow movement of the substrate due to the pressure caused by air bubbles in the gasket chamber. Air bubble problem can be solved by degassing the water. Increasing the number of averages can increase the SNR but that would be very time consuming if the angular responses of a nanorod come from a point of area scans. Fine angular scan with high averages can be done on a single point on the rod to improve the situation instead of collecting angular responses from the area scans. Fine angular scan was done on a single point on the rod by rotating the half-wave plate automatically with the motor and detecting the rod with different polarisations of light in two orthogonal channels. As the rods were almost horizontal, it was expected that the maximum amplitude will be detected near 0 degree in the horizontal channel, ch1 and will be opposite in the orthogonal channel, ch2 as can be seen in figure 4.19 (setup is shown in figure 4.6). A gridded cover-slip was used to track the position of the rod and also the orientation of the sample. However, it was tricky to manually maintain the exact same orientation (or angle) of the sample on the experimental scan stage and the SEM stage because it is not possible for any human. During SEM, a digital ruler was used to fix the sample at $0°$. During laser scanning, vertical and horizontal lines on the sample stage were used to place the sample at $0°$. Also, a digital ruler on the optical camera image was used for the alignment. Although this matter was considered very carefully, the process could have minor error or misalignment. This error was computed by calculating the offset of grid lines between the optical camera image taken during the laser scan and the SEM image. In general, maximum $2°$ error was found and this was considered as a systematic error. This error can be considered as an error affected by human efficiency. The angles of the two rods predicted by the phase stepping method, measured from the SEM image and estimated from the fine angular scan are listed in table 4.1 to see all together.
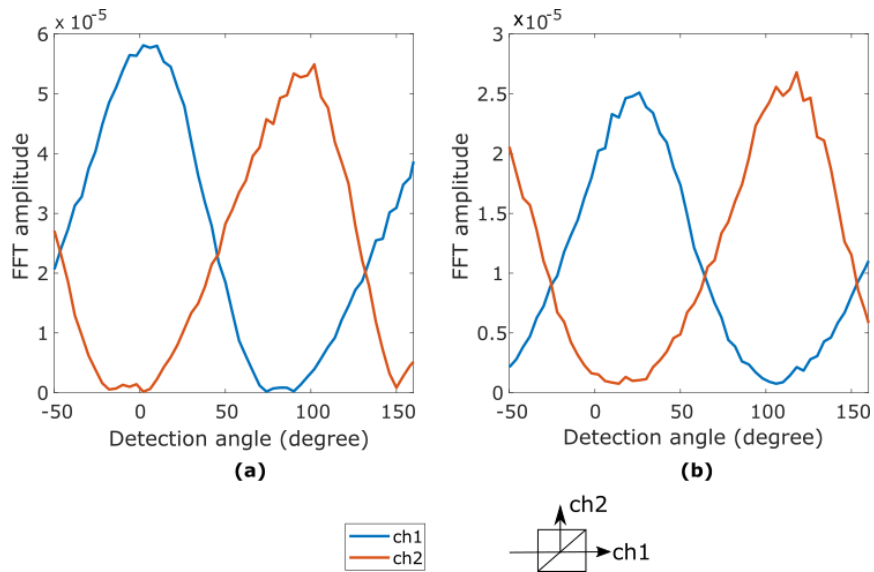
Figure 4.19: Angular scan of almost horizontal gold nanorods on a single point with fine steps. (a) Detected responses of an almost horizontal nanorod (rod 1) in two orthogonal channels. (b) Detected responses of an almost horizontal nanorod (rod 2) in two orthogonal channels.

Table 4.1: Angular measurements of two almost horizontal gold nanorods.

Rod	Angle (SEM) (°)	Angle (Phase stepping method) (°)	Angle (fine scan) (°)
Rod 1	0±5	-11.3±0.4	6
Rod 2	0±5	-22.5±0.5	26

4.4.2.5 Size precision and size accuracy

The size characterisation technique of nanorods in this research was based on the obtained vibrational frequencies from the rod. An analytical model developed by Hu et al. [162] was used to convert the frequency to the size of the rod where the length was determined from the extensional mode (low frequency) and the width was determined from the breathing mode (high frequency). The detail about this method was described in chapter 3 in section 3.3.3.2. This step (step 10) can also be seen in the diagram shown in figure 4.12.
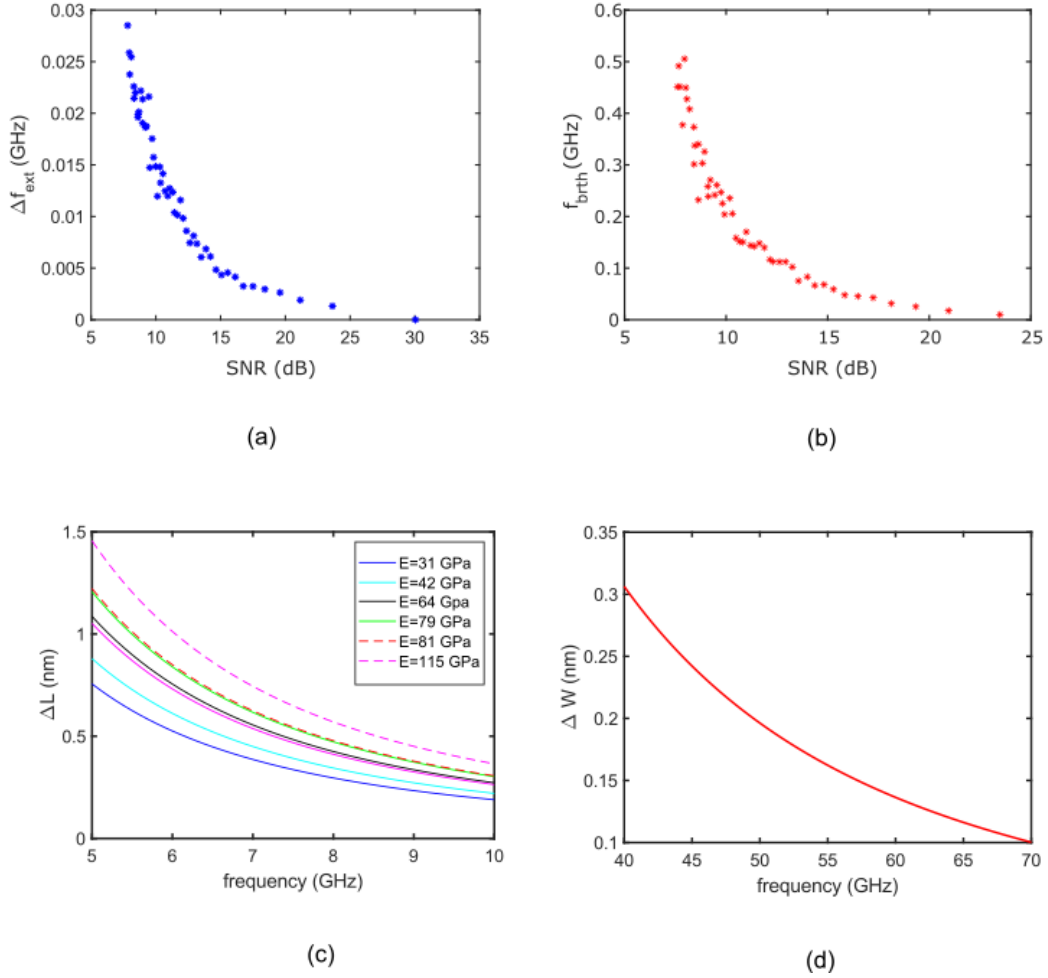
Figure 4.20: Size precision of gold nanorods. (a) Low frequency deviation (Δf_{ext}) vs SNR. (b) High frequency deviation (Δf_{brth}) vs SNR. (c) Length precisions for the used low frequency range for different E values. (d) Width precision for the used high frequency range.

The size precision was calculated by adding different amount of random noise to a decaying sinusoid and calculating the deviation of frequency as a function of noise. The deviation was calculated for the low frequency (Δf_{ext}) and the high frequency (Δf_{brth}) separately. The obtained graphs for Δf_{ext} vs SNR and Δf_{brth} vs SNR are shown in figure 4.20 (a) and 4.20 (b), respectively. In this thesis, it was observed that the SNR of the rod varied from 8 dB to 11 dB for the longitudinal mode that caused a maximum frequency deviation of about 0.03 GHz according to figure 4.20 (a). On the other hand, the SNR of the rod varied from 10 dB to 13 dB for the breathing mode that caused a maximum frequency deviation of about 0.2 GHz according to figure 4.20 (b). The obtained Δf_{ext} was added to the used low frequency range and Δf_{brth} was added to the used high frequency

range. Then, the frequency to size conversion was carried out to obtain ΔL and ΔW by using the analytical model [162]. It was discussed before in section 2.6 of chapter 2 that Young's modulus value (E) of a gold nanorod depends on the crystal structure and growth direction of the nanorod fixed by the used synthesis process. Hence, the extensional mode is dependent on the E value of a rod along a specific growth direction [162–167]. In contrast, the effect of crystallinity on the breathing mode is very low and the E value of bulk gold (E_{bulk}=79 GPa) can be used [165]. So, the conversion of the low frequency to length (figure 4.20 (c)) was performed for different values of E of gold nanorods as the actual value was unknown. These E values were mostly used and predicted by the researchers for gold nanorods [162–167]. It can be seen that ΔL changed by a small amount due to a change in the E value. Hence, the E value of bulk gold (E_{bulk}=79 GPa) was used as a reasonable reference and the size precision values were calculated using this value in this thesis. According to the figures shown in figure 4.20 (c) and figure 4.20 (d), the worst-case length and width precisions of the technique for the whole research were approximately 1 nm and 0.3 nm, respectively.

In the above paragraph, the worst-case size precision of the technique for the whole research was calculated. The same process was applied for any specific experiment and the size precision was estimated. For example, SNR of rod 1 for the case of longitudinal mode was calculated as before and Δf_{ext} was estimated from figure 4.20 (a). Then, Δf_{ext} was added to the used low frequency range and frequency to length conversion was performed as can be seen in figure 4.21 (a). Finally, ΔL at the longitudinal mode (7.6 GHz) of the rod was collected which was the length precision (0.3 nm) as marked by a blue dot in figure 4.21 (a). In the similar way, the width precision of rod 1 (0.05 nm) was collected at the breathing mode (64.4 GHz) of the rod. Following the similar process, the obtained length and width precisions of rod 2 were 0.15 nm and 0.06 nm, respectively.
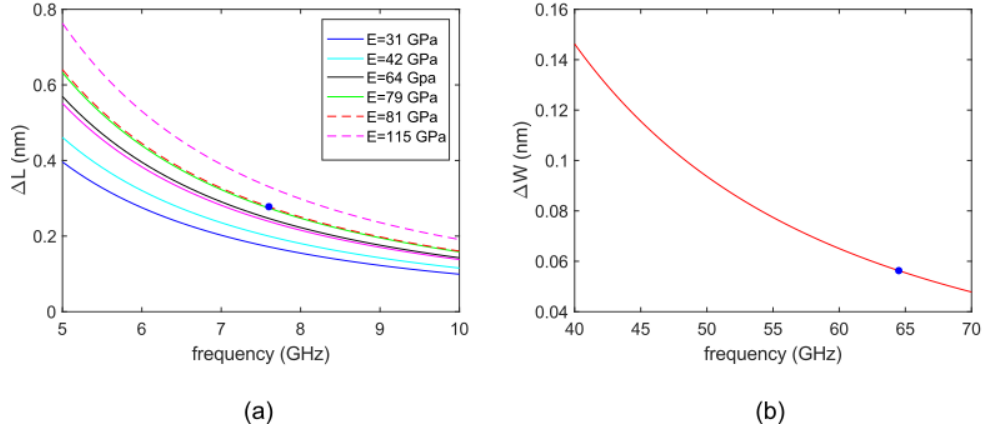
Figure 4.21: Size precision of rod 1. (a) Length precisions for the used low frequency range for different values of E. Length precision of rod 1 using E_{bulk}=79 GPa is marked by a blue point. (b) Width precision for the used high frequency range. Width precision of rod 1 is marked by a blue point.

The measured sizes of two rods are listed in table 4.2. It can be seen in table 4.2 that the predicted size of rod 1 closely matched the size measured by the SEM when $E_{[110]} = 64\,GPa$ was used. However, E_{bulk} or E_{poly} (for polycrystalline) was used as a reasonable reference in this research as the actual E was unknown and the difference between the measured size and the size from the SEM image was calculated. It can be observed that the length differences were 14.5±10.1 nm using E_{poly} and 1.4±10.1 nm using $E_{[110]}$. The predicted width of rod 1 was 36.3±0.6 nm and the difference with respect to the width measured from the SEM image was 2.63±10.0 nm as can be seen in the table 4.2. It is important to focus on the fact that the difference was calculated with respect to the size measured manually from the SEM images by multiplying the total pixel numbers with the pixel size. Hence, the measurement was affected by the human error. The measurement accuracy could also have been affected by the adjustment of the machine, noise, contrast, and magnification, among others.

Similarly, it can be seen from table 4.2 that the predicted size of rod 2 closely matched the size measured by the SEM when $E_{[110]} = 64$ GPa was used. It can be observed that the length differences were 15.8±10.1 nm using E_{bulk} and 3.5±10.1 nm using $E_{[110]}$. The predicted width of rod 2 was 38.9±0.9 nm and the difference with respect to the width measured from the SEM image was 0.86±10.0 nm as can be seen in the table 4.2.

In addition to the E value of the gold nanorod, the predicted size was also a function

Table 4.2: Measured sizes of two horizontal GNRs.

Rod	Frequency	E	Growth direction	Measured Size	Size from SEM	Size difference SEM and Measured
—	GHz	GPa		nm	nm	nm
Rod 1	7.7±0.1	31	[100]	82.4±1	117±10	34.6±10.1
		42	[100]	96±1.2		21.0±10.0
		64	[110]	118.4±1.5		1.4±10.1
		79	Bulk/poly	131.5±1.7		14.5±10.1
		81	[110]	133.2±1.7		16.2±10.2
		115	[111]	158.7±2.0		41.7±10.2
	64.51±1	79	Bulk/poly	36.36±0.57	39±10	2.63±10.0
Rod 2	8.24 ± 0.1	31	[100]	76.9 ± 0.94	107 ± 10	30.1 ± 10
		42	[100]	89.5 ± 1		17.5 ± 10.0
		64	[110]	110.4 ± 1.35		3.5 ± 10.1
		79	Bulk/poly	122.8 ± 1.5		15.76 ± 10.1
		81	[110]	124.3 ± 1.5		17.31 ± 10.1
		115	[111]	148.11 ± 1.8		41.1 ± 10.2
	60.36 ± 1.3	79	Bulk/poly	38.86 ± 0.85	38 ± 10	0.86 ± 10.0

of the shape of the rod. The analytical model which was used to convert the frequency of the rod to size was only applicable for rods of cylindrical shape. However, the rods used in the experiments were not perfect cylinders. The shape difference can introduce frequency difference and in turn affect the size difference. In figure 3.12, the effect of shape difference on the vibrational frequency of a nanorod was shown using a simulated result. It could be seen that the effect of shape difference was different for rods of different sizes. The reason is that the change of the tip shape affects the small and big rods differently. So, it is important to normalise the size by any parameter such as volume to estimate the effect of shape difference on the frequency properly. In addition, the shape of a purchased rod may be slightly different from a standard shape. So, the SEM image of the rod can be loaded in COMSOL Multiphysics and a matched geometry can be designed to reduce the error in the frequency estimation. Moreover, the shape factor should also be considered during SEM measurements. Hence, an estimation of the size error for the rods due to shape error requires further investigation and modelling. In summary, it can be said that the E value, unexpected errors coming from SEM measurements, shape difference between the rod used in the experiment and the rod used in modelling, among others contributed to the size error.

4.4.2.6 Overlay of predictions and SEM measurements

The final step was to overlay the obtained predictions and the captured SEM image. A rod of the predicted size (using $E_{bulk} = 79$ GPa) using the size characterisation method was drawn and rotated by an amount of the calculated angle, keeping the chosen location of the rod as the centre as mentioned in figure 4.12 (step 11). All three informations; locations (calculated from centroids), sizes (calculated from the vibrational frequencies) and angles (calculated using the phase stepping method) of the rods were overlaid with the SEM image to see the matching as can be seen in figure 4.22.

Rod SNRs were calculated experimentally using the ratio of PSF height to noise where noise was the mean of the signal level (absolute of FFT map at the rod frequency) with no particle. According to figure 4.11 (c) (location error vs SNR), the location error of rod 1 and rod 2 were 2.6 nm and 3 nm, respectively. To estimate the location accuracy, centre-to-centre distances of drawn rods from the SEM rods were calculated. Obtained location errors for rod 1 and rod 2 were 82 nm and 222 nm, respectively. There could be some reasons behind the location deviation, such as tiny movement of the particle/substrate because of water flow or air bubble pressure inside the chamber, elongated beam shape because of the sample movement, improper beam shape because of optics, low SNR, use of SEM scale bar and microscope stage positional information as references, among others. Degassing of water, assurance of proper beam shape, high SNR, among others can reduce the location error.
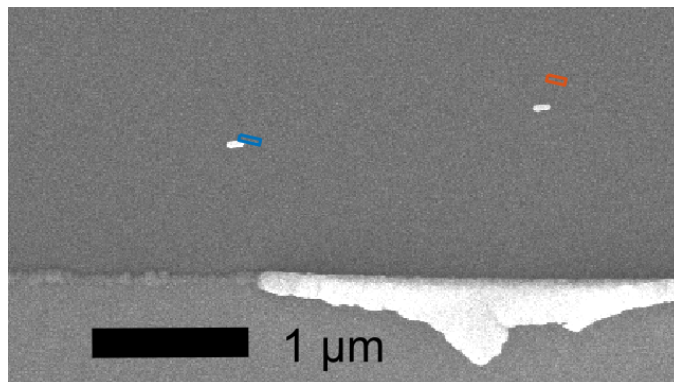
Figure 4.22: Overlay of experimental measurements of nanorod with the SEM image.

4.5 Sample preparation

In this section, different sample preparation methods have been described in detail. It was important to track the same nanorod or the same area of the sample effectively for this project. For this reason, a gridded cover-slip was used as the substrate of the sample that provided a coordinate system to track the particle. At first, the preparation method of this gridded cover-slip is described in this section. Then, different techniques to prepare samples using purchased gold nanorods are described. Electron beam lithography is a direct writing technique that offers more flexibility to fabricate nanostructures. Hence, gold nanorods were also fabricated by EBL in this work and the applied fabrication methods are briefly described. Finally, the chapter is concluded by describing the preparation methods to image samples using Scanning Electron Microscopy (SEM).

4.5.1 Making of gridded glass cover-slip by photolithography

At first, the desired mask was designed and then step-by-step photolithographic process was followed to prepare the gridded cover-slip. The whole process is decribed below.

Photomask design:

Matlab was used to create, read and modify files in the GDSII library format to prepare the design and Klayout software was used to view or check the design [225]. The designed pattern had an array of 20 by 20 squares where each square was 45 μm in size and the adjacent gap between the squares was 2 μm as can be seen in figure 4.23. Each row had a number and each column had a letter so that each cell could be identified uniquely. This identification was important to find the same nanorod under different measurement instruments at different times.
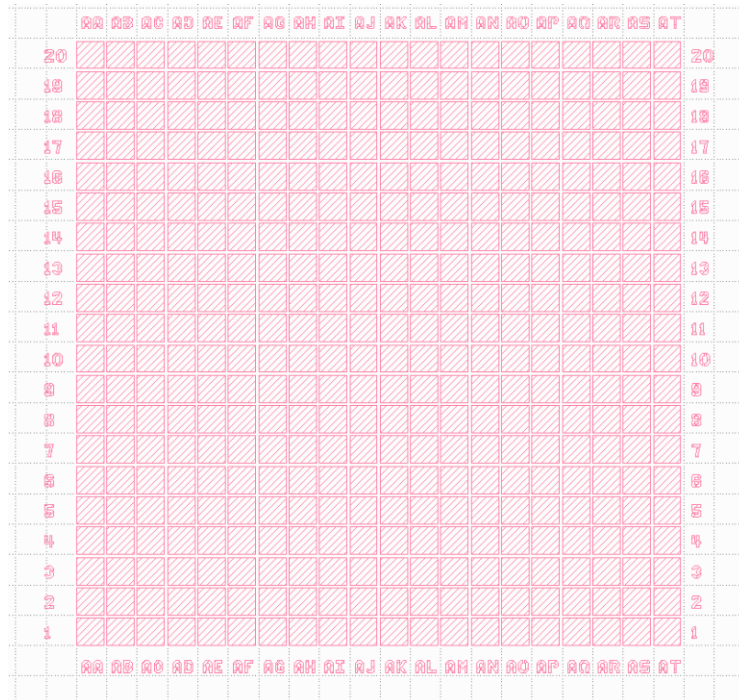
Figure 4.23: Mask pattern viewed in KLayout that consists of an array of 20 by 20 squares where each square is 45 μm and adjacent gap between squares is 2 μm.
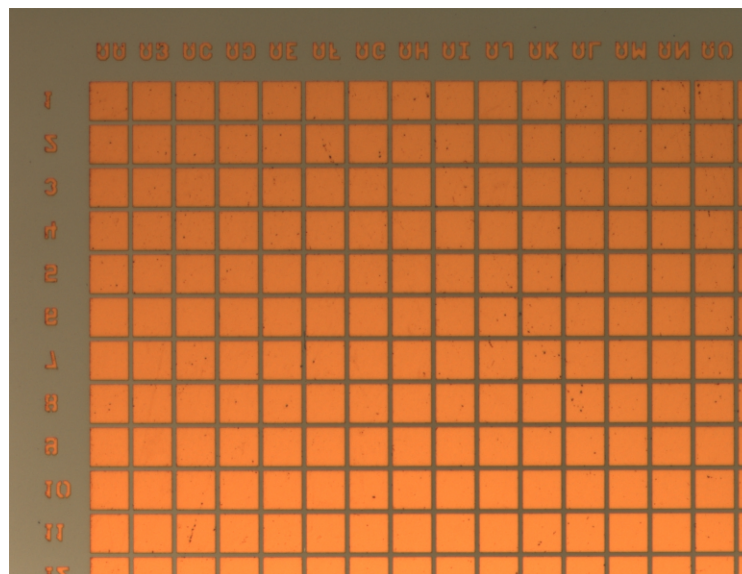
Figure 4.24: Optical microscope image (in reflection) of the printed light field mask on glass where bright areas (squares, numbers and letters) are of Chrome. Each square is 45 μm and adjacent gap between squares is 2 μm.

The pattern was designed to work with positive photo-resist to fabricate the gridded cover-slip. Finally, the mask was printed from JD Photo on a 4 inch by 4 inch glass

substrate as a light field mask where the designed squares and letters/numbers were of chrome as shown in figure 4.24.

Step-by-step photolithography process

The step-by-step process to fabricate the gridded cover slip following the photolithography process is explained below.

1. Surface cleaning

    The first step to fabricate a gridded cover slip was to clean the substrate with solvents because there may be organic impurities on the surface. The substrate was cleaned with ethyl lactate, acetone, methanol, and isopropanol in sequence as shown in figure 4.25 (a). It was a significant step because the presence of moisture and other molecules can create problems to the resist adhesion to the surface. In consequence, the developer or other etchant can penetrate the coated photoresist and undercut the photoresist pattern.

2. Photoresist coating

    Photoresist is a light sensitive polymer which is used to transfer an image on the underlying substrate. The exposed region of a positive resist gets soft and becomes soluble in an organic solvent whereas the unexposed region is soluble for a negative photoresist. The choice of the photoresist and polarity of the mask should be compatible to create the desired pattern. To match with our designed mask for the gridded cover slip, a positive photoresist BPRS 150 was spin coated at 4000 rpm for 30 s to create an uniform layer of photoresist on the glass substrate as shown in figure 4.25 (b). The layer was expected to be about 1.3 μm according to the applied spin parameters.

3. Soft Bake

    Soft bake of the coated photoresist was an important step to remove the residual solvents from the photoresist and improve the resist adhesion to the surface. If the photoresist is under baked, air bubbles may develop due to evaporation of residual solvent and can lead to inaccurate pattern. On the other hand, too strong baking can cause partial destruction of the light sensitive component and eventually reduce the

sensitivity requiring longer exposure time. For the current application, the coated substrate was soft baked on a hot plate for about 5 min at 90°C.

4. Cooling

   After the soft-bake, the substrate was cooled to the room temperature.

5. Exposure

   The sample was exposed to the UV light through the mask where the whole layer of the photoresist was exposed except the regions under the chrome squares as shown in figure 4.25 (c). UV exposure was performed using a Karl Suss MJB3 mask aligner for 8 s from a mercury lamp at power of 7 mW/cm^2.

6. Development of the pattern

   The exposed sample was immersed with gentle agitation in a 1:8 developing solution of AZ400K and deionised (DI) water for 20-25 seconds. Then, the sample was washed in deionised (DI) water and blow dried with Nitrogen. The exposed positive photoresist became soft and dissolved in the developer while the unexposed hard photoresist remained in the squares as shown in figure 4.25 (d).

7. Metal coating

   A thin layer of 10 nm ITO was coated by a sputterer at first which works as the adhesion layer for gold. Then a layer of 20 nm Au (gold) was coated as shown in figure 4.25 (e).

8. Lift-off

   Lift-off is an additive process to create a pattern in contrary to subtractive etching process. It removes unwanted metal regions on top of the photo-resist pattern while the coated metal at other regions stays that forms the desired structure. This method is simple and cheap. However, the disadvantage is the quality of lift-off depends on the coating technique and resist profile. If the side-wall of the structure gets coated, the lift-off may not be successful. Creating undercut resist profile and coating using thermal evaporation are promising for successful lift-off for critical nano-structures.

(a) ← cleaned glass substrate

(b) ← coated photoresist

← UV exposure

← optical mask

(c)

(d) ← remaining photoresist after development

coated metal layer (Au)

coated metal layer (ITO)

(e)

(f) metals after lift-off
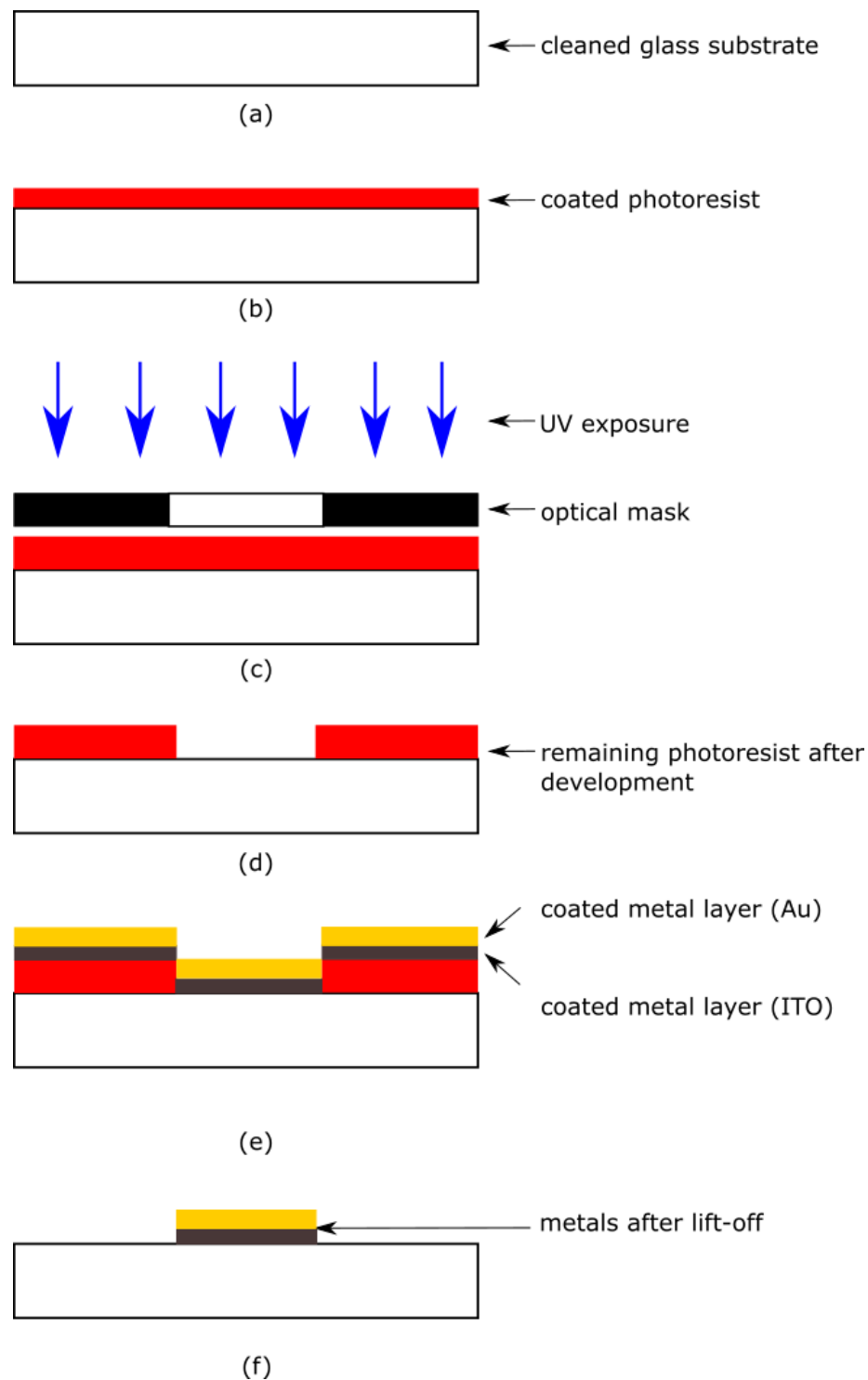
Figure 4.25: A schematic of the optical photolithography process used to make gridded cover-slip. (a) A glass cover slip was solvent cleaned to use as a substrate. (b) A positive photoresist BPRS 150 was spin coated on the substrate followed by a soft bake. (c) UV light was exposed through the designed optical mask. (d) The UV exposed sample was developed with AZ400K to create the pattern. (e) A thin gold metal layer was deposited by a sputterer. (f) The metal coated substrate was dissolved in warm acetone to do the lift-off and create the desired pattern.

During the lift-off in this case, at first acetone was warmed at 60°C on a hot plate for 10 min by covering it with a parafilm. Then, the sample was immersed in warm acetone and kept on a hot plate for another 10 min. Next, the sample with warm acetone was put in ultrasonic bath for 8 minutes. The sample was then washed by fresh acetone and isopropanol (IPA). Finally, the sample was blow dried with Nitrogen and collected. The coated gold came off with the photoresist during the lift-off reacting with acetone as shown in figure 4.25 (f). According to the designed pattern, it was expected to have a gridded cover-slip of clear squares separated by gold lines and marked with gold letters/numbers. The optical microscope image of the fabricated gridded cover-slip in reflection is shown in figure 4.26 where the bright areas are of gold and the dark regions are of clear glass.
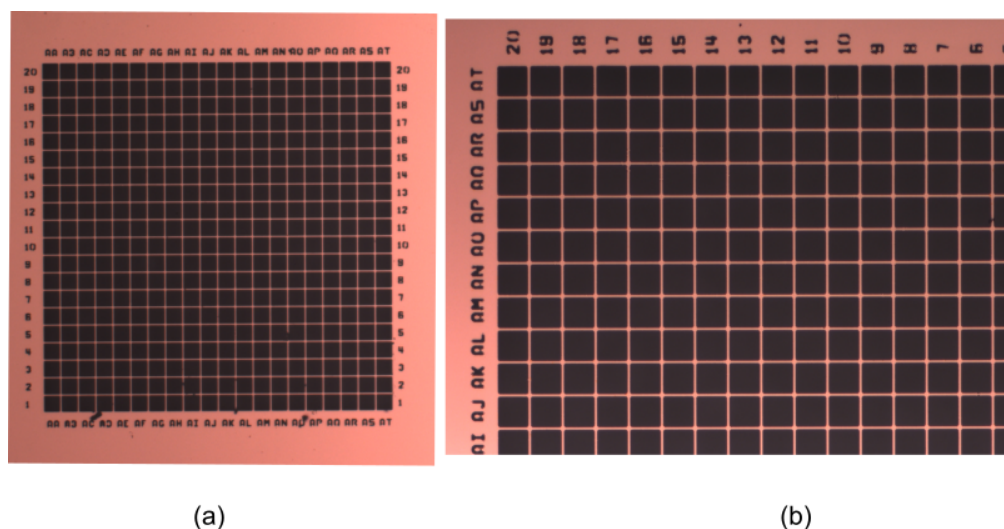
Figure 4.26: Fabricated gridded glass cover-slip. (a) the whole gridded cover-slip. (b) A zoom of the gridded cover-slip.

(a)

100 µm
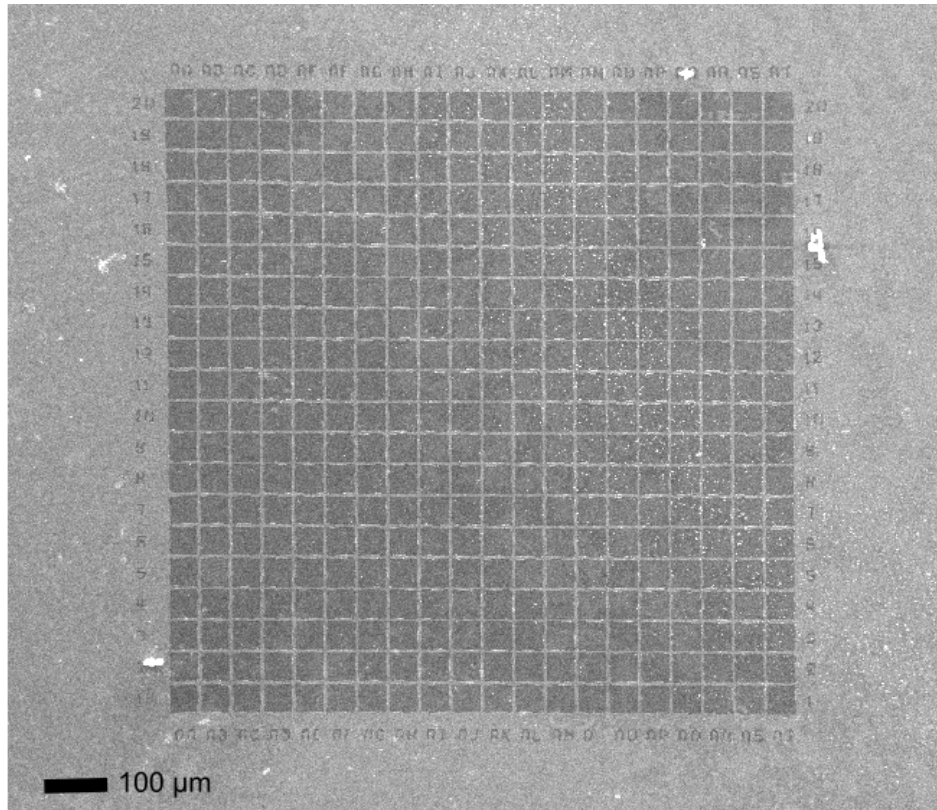
(b)
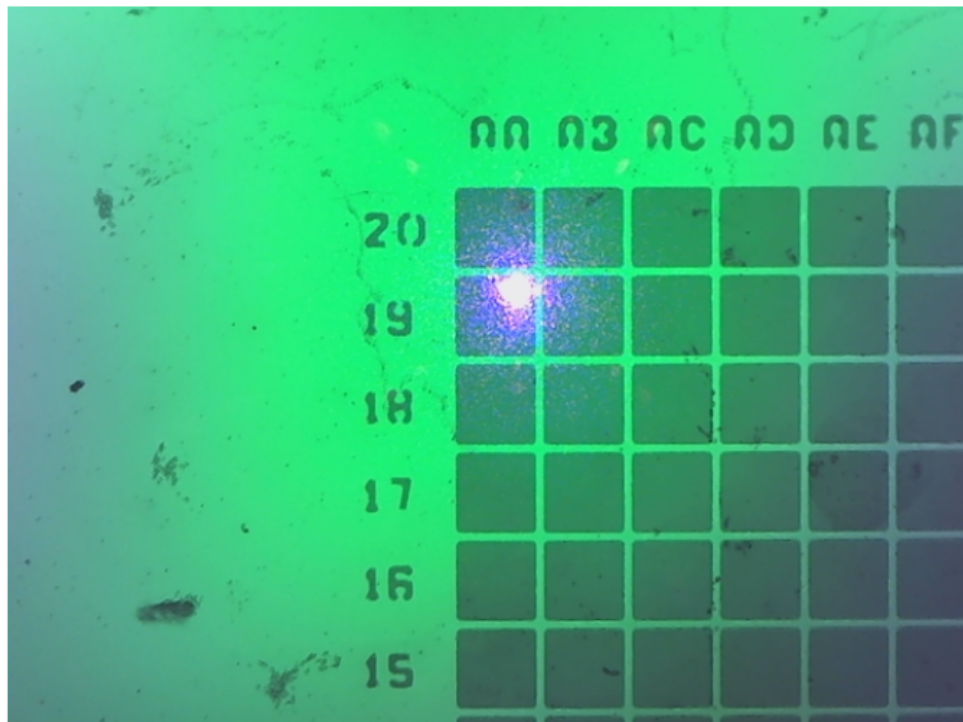
Figure 4.27: Fabricated gridded glass cover-slip on the SEM stage and the experimental stage. (a) The SEM image of the gridded cover-slip. (b) Optical microscope image of the gridded cover-slip on the experimental stage in the reflection mode.

Major part of the gridded cover-slip had gold on top and hence provided good conductivity during SEM. In contrast, the clear regions had only ITO on it. However there was a possibility that ITO layer got affected during lift-off. Hence, a layer of Indium Tin Oxide (ITO) was coated to provide enough conductivity to the clear glass regions before depositing or attaching nanoparticles on it. The SEM image of a sample made on a gridded cover-slip is shown in figure 4.27 (a) where it can be seen that the gridded cover-slip was clearly visible in SEM. Hence, it was possible to image particles effectively in SEM where the location of the particles were tracked by the co-ordinates of the gridded cover-slip. During the laser experiments, the sample was placed on the experimental stage and the desired area was identified for scanning. Hence, using a gridded cover-slip as a substrate was very helpful to track the particles when sample was moved between different instrumentations in different times. The aim of the thesis work was to characterise and image gold nanorods. Hence, it was required to scan the same area of the sample and same rod again and again. The gridded cover-slip was also important to observe any thermal effect on nanorod with time. The optical microscope image of the gridded cover-slip on the experimental stage in the reflection mode is shown in figure 4.27 (b).

4.5.2   Drop-casting nanorods

Drop-casting is a simple process which is frequently used for depositing nanoparticles [226]. A drop of liquid containing a suspension of the gold nanorods was deposited on the surface of a cover-slip as shown in figure 4.28 (a). Then, the sample was left overnight to dry.

Although this process is very simple, it is hard to obtain a uniform distribution and aggregation of nanorods can happen if proper sonication of the solution is not done before making the sample. It is also important to put the nanorod solution in room temperature for a while and shake it before making the sample to avoid the aggregation. On the other hand, as the nanorods are not well attached to the surface, water or any solvent can wash the rods from the sample. The SEM image of a sample made with this process is shown in figure 4.28 (b). A 18 mm by 18 mm gridded glass cover slip was coated first with 50 nm of Indium Tin Oxide (ITO) to produce conductivity for the SEM imaging. Then, 50 μL of GNR solution (145 nm by 50 nm, purchased from Nanopartz, A12-50-800) and deionised (DI) water (1:8 mixture) was deposited on the substrate.
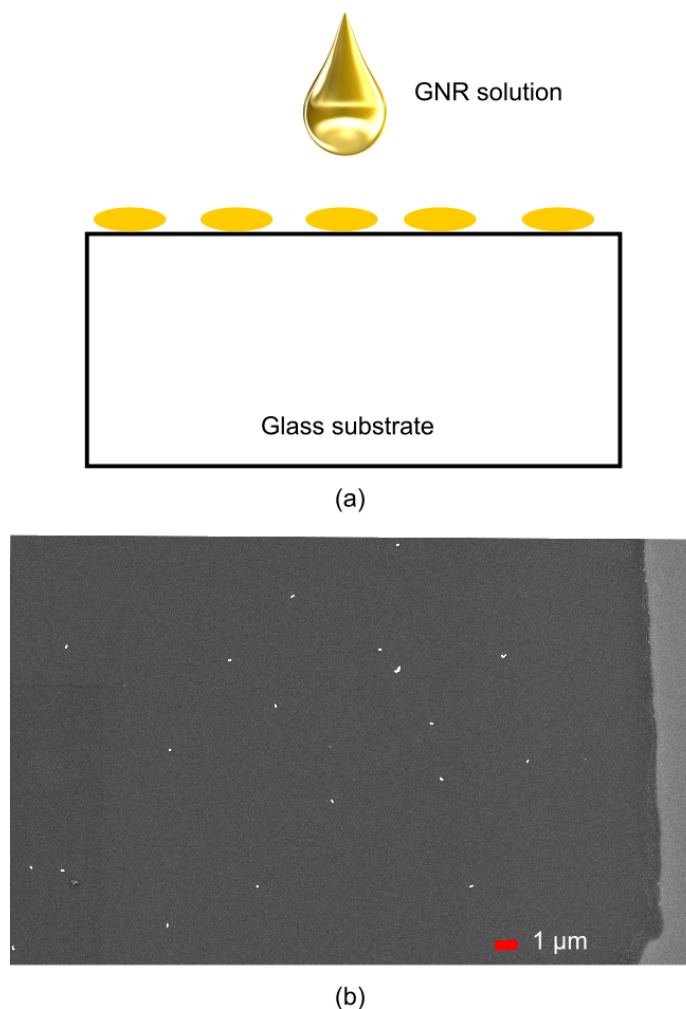
Figure 4.28: Drop casting gold nanorods on the surface of a sample. (a) A cartoon image showing the drop casting method. (b) The SEM image of a sample made with 1:8 mixture of GNR solution (145 nm by 50 nm) with DI water on a 50 nm ITO coated gridded cover slip following the drop casting method. It can be seen that nanorods are well dispersed and deposited on the sample surface.

4.5.3 Bonding nanorods to the substrate

An electrostatic layer-by-layer self-assembly process [227, 228] was used to attach gold nanorods to the substrate for measuring the nanorod response in water. This method is based on the electrostatic attraction between oppositely charged electrolyte layers. Electrostatic layers bond the particles to the substrate so that they do not wash away by any liquid. The whole process is described with the help of figure 4.29.
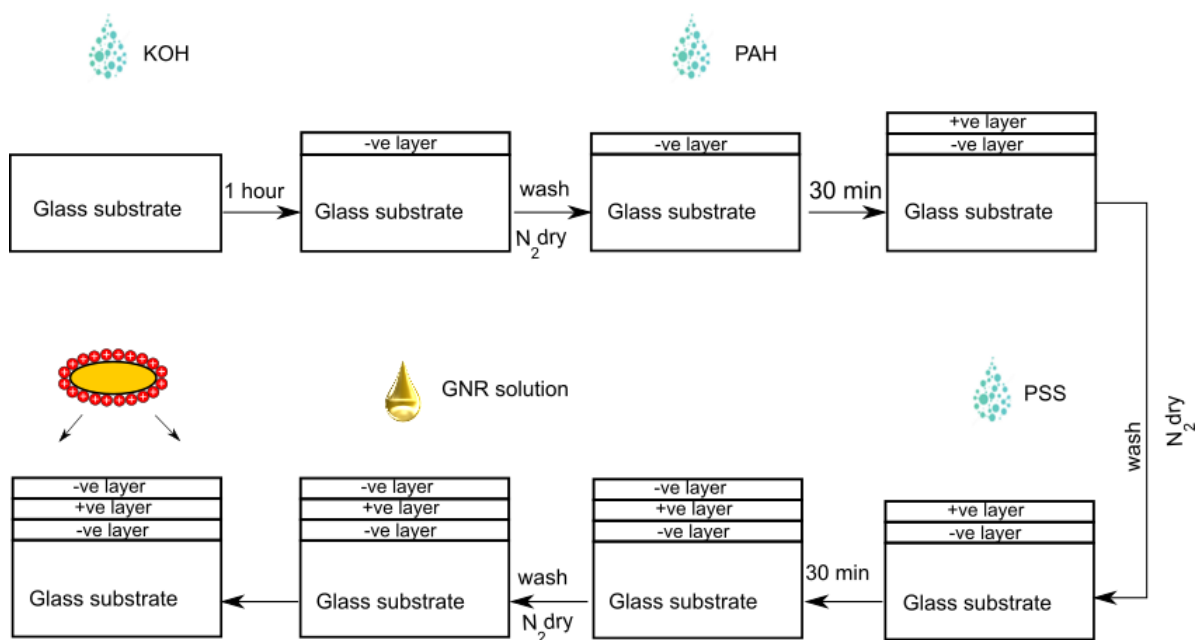
Figure 4.29: Electrostatic layer-by-layer self-assembly to attach gold nanorods to the surface of a sample.

At first, Potassium Hydroxide KOH was deposited on the ITO-coated gridded coverslip and left for 1 hour to form OH groups on the surface. The solution was kept in an orbital shaker for better mixing. Deposition of KOH made the surface of the substrate negatively charged. Then, positively charged poly (allylamine hydrochloride) (PAH) was deposited and left for 30 min so that it can attach to the previous layer. Finally, negatively charged poly (sodium 4-styrenesulfonate) (PSS) was deposited and left for 30 min. The sample was always washed with deionised water and dried with Nitrogen gas before the addition of successive layers. The protocol to prepare the mentioned solutions is described below.

- KOH solution was made by mixing $\sim$ 500 mg KOH pellets and a solution of 4 mL:
  6 mL of H_2O:Ethanol (2:3) in an orbital shaker.

- PAH solution was made by mixing $\sim$ 17 mg PAH powder into 10 mL of H_2O and adding 125 μL of NaOH (1M). This was mixed in an orbital shaker until it was completely dissolved.

- PSS solution was made by mixing $\sim$ 44 mg of PSS powder into 10 mL of H_2O and mixing it in an orbital shaker to dissolve.
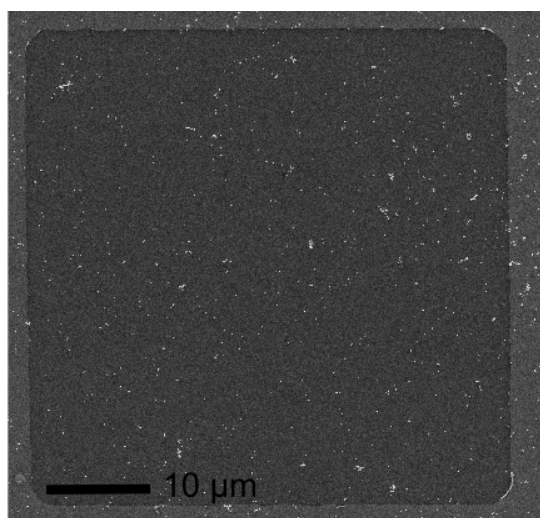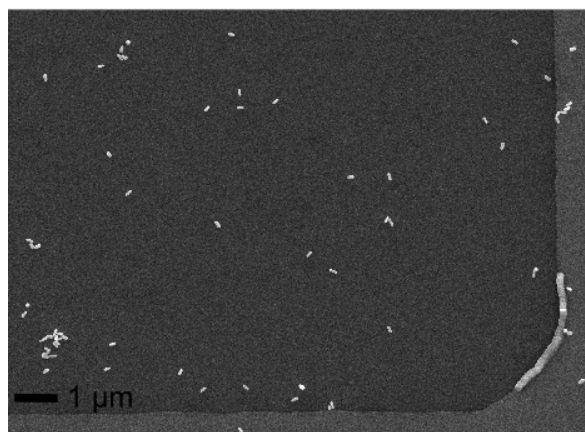
Figure 4.30: A sample made by electrostatic layer-by-layer self-assembly process. (a) The SEM image of a sample made with a 1:6 mixture of GNR solution (145 nm by 50 nm) and DI water on a 200 nm ITO- coated gridded cover-slip following the layer-by-layer self-assembly process. It can be seen that many nanorods were attached to the sample. (b) A zoom-in view of the SEM image of the right bottom corner.

When the layer by layer assembly was completed, the substrate surface was ready with negative charges on the top. Then, the purchased gold nanorod solution (diluted according to necessity) was deposited on the surface. Purchased nanorod solution had capping agent Hexadecyltrimethylammonium bromide (CTAB) to direct the growth of Au nanorods and stabilise them after synthesis. Gold nanorods got polarity from the positively charged CTAB surfactant and attached to the negatively charged surface through electrostatic interactions. In this way, gold nanorods well bonded to the surface. Finally, the sample

was left to dry and washed with DI water before doing experiments.

The scanning Electron Microscopy (SEM) image of a sample made with the electrostatic layer-by-layer self-assembly process is shown in figure 4.30. A 25 mm gridded glass cover-slip was coated with 200 nm of Indium Tin Oxide (ITO) to produce conductivity for the SEM imaging and 60 μL of KOH, PAH and PSS were used during the layer-by-layer process. The ITO thickness was high to avoid damaging it by the chemical reaction with electrostatic layers. Finally, 60 μL 1:6 mixture of GNR solution (145 nm by 50 nm, purchased from Nanopartz, A12-50-800) and DI water was deposited on the substrate. It is clear from figure 4.30 (a) and (b) that the layer-by-layer self-assembly was successful and many nanorods were attached to the surface.

4.5.4 Design and fabrication of gold nanorods by electron beam lithography (EBL)

Gold nanorods were also fabricated by electron beam lithography (EBL) in this research where nB5 EBL tool at the Nanoscale and Microscale Research Centre (nmRc) of University of Nottingham (UON) was used. The attractive features of nB5 EBL are [229]

1. Accelerating voltage of 80 KV

2. Beam current of between 2 and 40 nA

3. Main field (500 μm) stitching of less than 20 nm

4. Sub field (20 μm) stitching of less than 15 nm

5. 65 MHz Processor Clock speed

The system accepted some specific file formats and GDSII (Graphic Database System Information Interchange) was one of them. Matlab was used to create, read and modify files in the GDSII library format and Klayout software was used to open and check the designed GDSII files [225]. The script was written in a way so that the size, orientation and distribution of nanorods can be changed easily in the design.
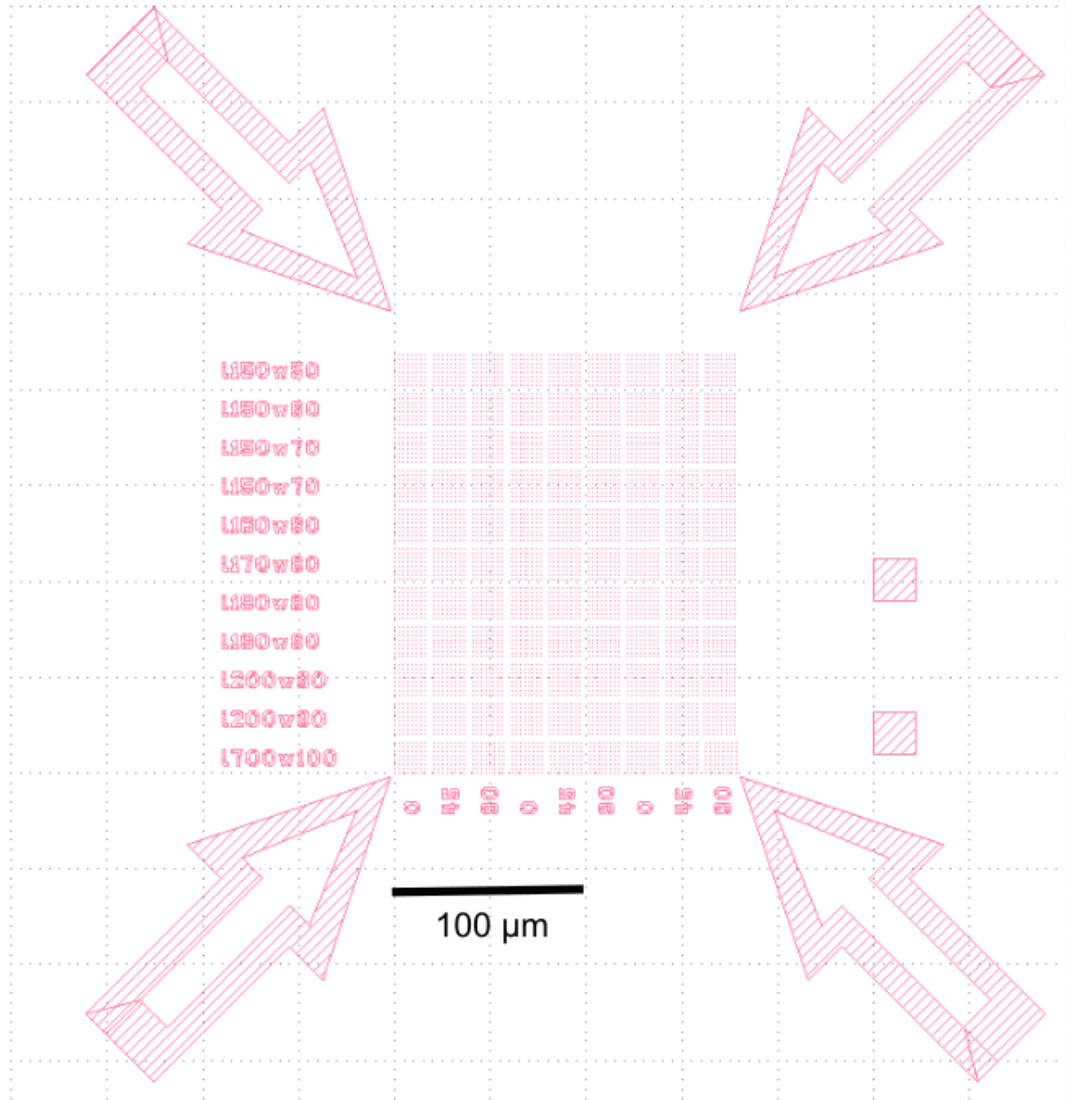
Figure 4.31: A design view from Klayout showing different sizes of nanorod in different orientations. The big arrows and texts helped to locate the desired area under the optical microscope. The gold squares were used to test and optimise the signal initially.

It was necessary to know some field design parameters of the EBL tool before finalising the designs. The nB5 fractured the GDSII file into a 500 μm main field that consisted of 20 μm sub-fields. It was ensured that the sub-field boundary does not split the deigned pattern. A zoom-out and zoom-in view of the design from Klayout are shown in figure 4.31 and 4.32 respectively. In the showed designs, the area of one GNR set was 18 μm by 18 μm and the gap between the adjacent GNR sets was 2 μm to avoid the splitting of the designs. The arrows and texts were added to find the position of the set easily under the optical microscope and the gold squares helped to test the basic signal before starting the experiment on gold nanorods.
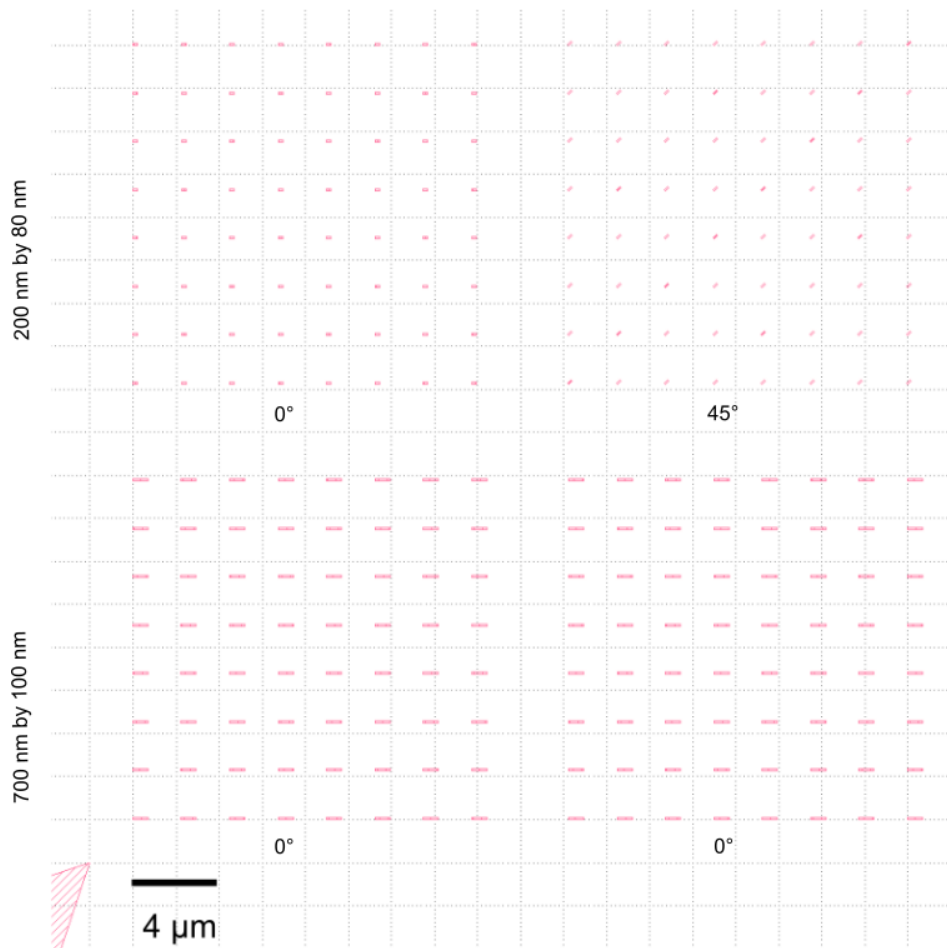
Figure 4.32: Zoom-in view of a design from Klayout showing different sizes of nanorod in different orientations.

The basic steps that were followed to fabricate samples by EBL are summarised in table 4.3. Bilayer resist process [230] was used to make the samples and the exact followed protocols are discussed in detail in the appendix. The SEM image of a sample showing gold nanorods fabricated by EBL on a glass substrate is shown in figure 4.33.

Table 4.3: Followed steps to fabricate GNRs by EBL.

Number	Steps
1.	Cleaning the substrate (a glass cover slip in this case) with solvents
2.	Coating the desired e-beam resist on the substrate
3.	Prebaking the resist
4.	Coating a conductive layer
5.	Exposing the substrate to the electron beam
6.	Developing the substrate
7.	Coating metals on the substrate.
8.	Doing lift-off to get desired metal nanostructures.
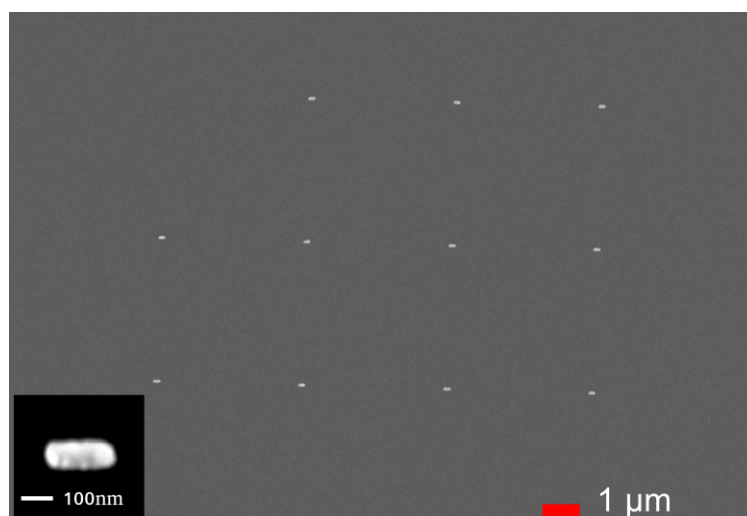
Figure 4.33: The SEM image of an array which consists of 200 nm by 80 nm GNRs in 0° angle fabricated by electron beam lithography (EBL). The inset shows the zoom in of one of the rods.

4.6 Scanning Electron Microscopy of used samples

The gold nanorod samples were imaged using JEOL 7100F FEG-SEM electron microscope at nmRC, UON. Generally, accelerating voltage of 15 kV, 10kV and 5kV were used to image samples. The choice of the accelerating voltage depends on the type of the sample and the required information. High accelerating voltage ensures high resolution but the beam penetrates more into the sample and provides less information from the surface structure. In addition, high voltage can damage the sample or can cause a charging effect if the sample surface has poor conductivity. The substrate of all used samples in the experiments was a gridded glass cover-slip where the major portion of the sample surface had ITO (50 nm)

on top of coated gold (20 nm) except the grid pattern. On the grid pattern, gold nanorods were deposited on top of coated ITO (50 nm) on clear glass. Hence, the sample provided good conductivity during the SEM imaging and an accelerating voltage of 15 kV did not produce any charging effect. Some of the used samples were prepared using electrostatic layers to attach gold nanorods to the surface and less conductivity was observed for those types of samples. The reason can be the chemical reaction between the conductive coating (ITO) and the electrostatic layers. Hence, a thick conductive layer (approximately 200 nm) was chosen for those samples.

The preparation to make the sample compatible for the SEM imaging varies according to the sample type. The preparation to image nanoparticles deposited on a glass substrate under scanning electron microscopes is simple. It is also not time consuming. The sample needs to be dry before placing it inside the vacuum chamber, otherwise water vaporisation can obstruct the beam and reduce the image clarity. For this reason, enough time was given to dry the sample before carrying out SEM. The sample also needs to be clean to avoid contamination. This is why the substrate of the sample was solvent cleaned at the first stage of preparing the sample.

The sample was mounted on a 25 mm aluminium stub using aluminium tapes at the edges. Most of the used samples were 18 mm by 18 mm squares or 25 mm circular glass cover-slips. The aluminium tape not only attached the sample to the stub but also provided conductivity to the edges of the sample. Double sides carbon tape can also be used to stick the sample and provide conductivity. However, a thin glass sample (170 μm) can break easily while removing it from the sticky carbon tape. It was more convenient to use aluminium tapes to remove the glass sample from the stub. The stub was then placed on a 25 mm specimen holder for inserting into the SEM chamber in a high vacuum ($\approx$ 10^{-4}). The microscopy was done with a working distance of $\approx$ 10 mm using a secondary electron detector. The image of a sample on the SEM stage is shown in figure 4.34.
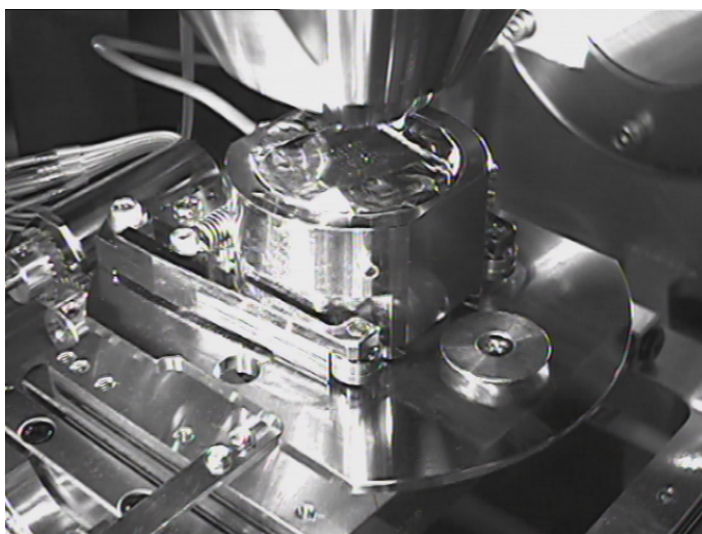
Figure 4.34: A sample on the SEM stage of JEOL 7100F FEG-SEM at nmRC, UON.

4.7 Summary

The used experimental set-up and laser scanning techniques were described in detail. In addition, the basic signal processing steps and algorithms were described to determine the size, angle and location of gold nanorods for reconstructing their phononic images. Also, the used sample preparation methods and protocols were described briefly. It was very important for this project to capture the images of gold nanorods by SEM. The used technique and parameters for SEM operation were also explained in this chapter.

Chapter 5

Phononic image reconstruction of gold nanorods by characterising their sizes, angles and locations

5.1 Introduction

In this chapter, phononic image reconstruction of different gold nanorods are shown by combining their sizes, angles and locations using the techniques as described before in chapter 4. Size characterisation of gold nanorods is shown first and explained in detail. Sizes of gold nanorods are determined from their vibrational frequencies obtained using time-resolved pump-probe spectroscopy. The predicted sizes of gold nanorods are compared with the sizes measured from their SEM images. In addition, the size precision of the technique is also estimated. Then, angle measurements of gold nanorods are presented using some basic examples. Detected amplitudes or intensities of a nanorod for different polarisations of the probe beam are used to determine the angle of the rod. Measured angles of the rods are compared with the angles measured from their SEM images and the angle precision of the technique is also estimated and presented in this chapter.

Finally, the location information of the rods is extracted to reconstruct the phononic images of gold nanorods. The image reconstruction of the rods is shown in both air and water media in this chapter. It is also shown that the technique can reconstruct the

phononic images of gold nanorods even when they are inside the same optical point spread function and thus can image them with super-optical resolution.

5.2 Size characterisation of gold nanorods

It is very important to characterise the size of metal nanoparticles because their optical and mechanical properties mostly depend on their sizes and shapes. In this research, time-resolved pump-probe spectroscopy was used to measure the vibrational frequencies of gold nanorods in both air and water media. Then, the obtained frequencies were converted to size dimensions by using an analytical model [162].

5.2.1 Size characterisation of gold nanorods in an air medium

The size characterisation of gold nanorods in an air medium is more straightforward than in a water medium because the sample preparation process is simple and less time-consuming as described before in section 4.5. In addition, there is no need to refresh the water intermittently to prevent the bacteria and the formation of water bubbles. A commercially available GNR (145 nm by 50 nm according to the product sheet, batch A12-50-800, purchased from Nanopartz) was scanned in an air medium using the UV-NIR (generation-detection) set-up to characterise the size. The experiment was done with the pump wavelength of 415 nm and the probe wavelength of 780 nm. The experimental set-up for the UV-NIR configuration was shown and explained before in section 4.3 (figure 4.4) where path 3 (NIR) and path 4 (UV) were used for this experiment. It can be seen from the absorption and scattering cross section spectra shown in figure 3.18 that the applied pump and probe wavelengths were suitable to excite and detect the target rod in an air medium. A maximum average power of 2 mW was used for the pump and the probe at the sample which corresponded to pulse energy of 25 pJ and peak power of 250 W, respectively. The probe laser was delayed at a rate of 5 kHz to reconstruct the signal using the pump-probe configuration as explained before in section 4.1. The sample was scanned by moving the electromechanical stage holding the sample with a step motion of 200 nm. The fine step size ensures a better quality of the result but at the cost of high scan time. However, the experimental time can also be optimised by setting different delay rates and averages.

Circularly polarised pump and probe beams were provided from the bottom of the sample using the configuration shown in figure 4.6 (a) and focused by a 0.45 NA objective lens (Olympus LUCPlanFL N 20x)). Hence, the diameters of the probe beam and the pump beam were $\sim 2~\mu m$ and $\sim 1~\mu m$, respectively. The SEM image of the target nanorod can be seen in figure 5.1 (a). Having one SEM image of the rod before the laser scan is helpful to be sure that there is only one nanorod inside the optical point spread function, not a group of nanorods which can misinterpret the size characterisation result. The raw trace which consists of the co-incidence peak, thermal background, background coming from the laser electronics and oscillatory components, is shown in figure 5.1 (b). As a nanorod has both low and high frequencies, the data was processed for both long and short time windows separately. After removing the thermal background, the traces (called as processed traces here) for the long time window (left) and the short time window (right) are shown in figure 5.1 (c). Finally, the FFT traces of the processed traces can be seen in figure 5.1 (d). It can be observed that the obtained longitudinal and breathing modes from the rod were at 6.5 GHz and 45.04 GHz, respectively. Only two main vibrational modes were observed because the excitation was uniform. However, higher order modes might be present there but were difficult to detect or were outside the measurement bandwidth of our system.

A frequency difference between different pixels of the frequency map of the rod area was collected. Frequency differences of 0.1 GHz and 0.9 GHz were found for the longitudinal and the breathing modes, respectively. The obtained frequencies were converted to sizes by using an analytical model [162]. It was discussed before in section 2.6 of chapter 2 that Young's modulus value (E) of a gold nanorod depends on the crystal structure and growth direction of the nanorod fixed by the used synthesis process. Hence, the extensional mode is dependent on the E value of a rod along the growth direction [162–167]. In contrast, the effect of crystallinity on the breathing mode is very small and the E value of polycrystalline bulk gold (E_{poly}=79 GPa) can be used [165]. In this research, the actual E values of the used gold nanorods were unknown because the crystal structure of the rods was not determined by using TEM and also was not available in the product sheet provided by the manufacturer. Hence, the predicted lengths of the rod for different values of Young's modulus were calculated as can be seen in the table 5.1. These E values were mostly used and predicted for gold nanorods by the researchers [162–167]. It can

be seen in table 5.1 that the predicted size of the rod closely matched the size measured by SEM when the E value along the [111] direction was used. However, E_{poly}=79 GPa was used as a reasonable reference in this research as the actual E was unknown and the corresponding difference was also calculated. It can be observed that the length differences with respect to the SEM measurements were 50.4±20.1 nm using E_{poly} and 18.2±20.2 nm using $E_{[111]}$. The predicted width of the rod was 52±1 nm and the difference with respect to the width measured from the SEM image was 45±20 nm as can be seen in the table 5.1. It is important to focus on the fact that the difference was calculated with respect to the size measured manually from the SEM images by multiplying the total pixel numbers with the pixel size. Hence, the measurement was affected by the human error and an addition or subtraction of 1 pixel by mistake caused a 10 nm error for this case. The measurement accuracy of SEM also depends on the adjustment of the machine, noise, contrast, and magnification, among others. Hence, SEM precision cannot be generalised. However, all the size characterisation results presented in this thesis showed that the worst case SEM precision was 36 nm. In addition, the experiment was done in an air medium and it could have been possible that the laser power slightly modified the size and shape of the rod. Thermal effect of gold nanorods are discussed in chapter 7.

The SNR of the rod was calculated using the ratio of the rod amplitude in the FFT response to the mean of noise level. The size precision was extracted in the same way as described in section 4.4.2.5 on chapter 4 (figure 4.20). It was shown in figure 4.20 that E value has a very little effect on the size precision. Hence, the size precision values were calculated using $E_{poly} = 79$ GPa in this thesis. It was found that the length and width precisions for the rod were 0.2 nm and 0.1 nm compared to SEM measurements, respectively using E_{poly}. A rod of the predicted size using E_{poly} was drawn on the SEM image for a comparison as can be seen in figure 5.2. It can be observed that the predicted size was close to the SEM measured size, even when the actual E of the rod was unknown and E_{poly} was used.

In addition to the E value of the gold nanorod, the predicted size was also dependent on the shape of the rod. The analytical model which was used to convert the frequency of the rod to size was only applicable for cylindrical rods. However, the rods used in the experiments were not cylindrical. This shape difference introduced a frequency difference

and in turn affected the size measurement. In figure 3.12, the effect of shape difference on the vibrational frequency of a nanorod was shown using a result simulated by COMSOL Multiphysics. It could be seen that the effect of shape difference was different for rods of different sizes. The reason is that the change of the tip shape affects the small and big rods differently. To estimate the effect of shape difference on the frequency properly, it is important to normalise the size by any parameter such as volume, which was not done in the current thesis but can be done for further improvements. In addition, the shape of a purchased rod may be slightly different from a standard shape. So, the SEM image of the rod can be loaded in COMSOL Multiphysics and a matched geometry can be designed to reduce the error in the frequency estimation for further improvements in future. Moreover, the shape factor should also be considered during the SEM measurements. Hence, an estimate of the size error for the rods due to shape error requires further investigation and modelling. In summary, it can be said that the E value, unexpected errors coming from the SEM measurements, shape difference between the rod used in the experiment and in the modelling, and heat from the laser, among others contributed to the size error.
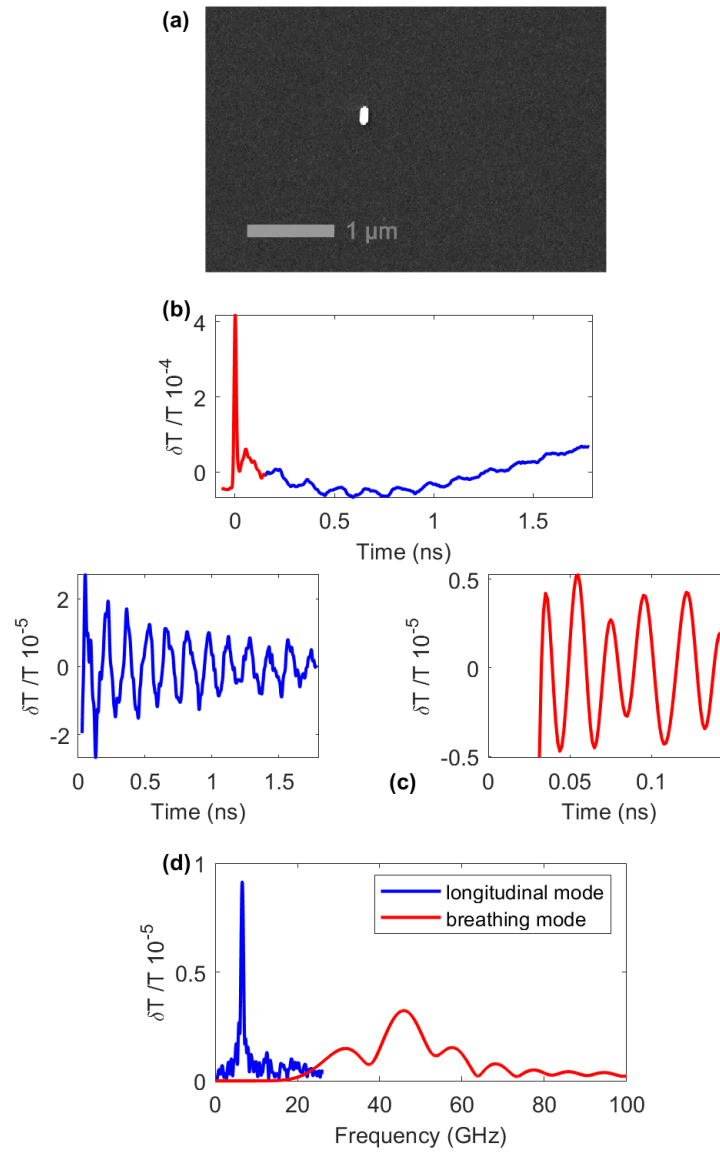
Figure 5.1: The SEM image and experimental traces from a GNR (145 nm by 50 nm according to the product sheet, batch A12-50-800, purchased from Nanopartz) in an air medium. (a) The SEM image of the target GNR. (b) Raw time trace. (c) Processed traces for 1.8 ns (left), for 0.15 ns (right). (d) Obtained longitudinal (low frequency) mode at 6.5 GHz and breathing mode (high frequency) at 45.08 GHz after performing an FFT of the processed traces for the long and short time windows, respectively.

Table 5.1: Predicted size dimensions of a GNR in an air medium.

Frequency	E	Growth direction	Measured Size	Size from SEM	Size difference SEM and Measured
GHz	GPa		nm	nm	nm
6.5 ± 0.1	31	[100]	97.4 ± 1.5	206 ± 20	108.5 ± 20
	42	[100]	113.5 ± 1.8		92.5 ± 20.1
	64	[110]	140 ± 2.1		65.9 ± 20.1
	79	polycrystalline	155.6 ± 2.43		50.4 ± 20.1
	81	[110]	157.6 ± 2.46		48.4 ± 20.1
	115	[111]	187.8 ± 2.9		18.2 ± 20.2
45.04 ± 0.9	79	polycrystalline	52 ± 1	97 ± 20	45 ± 20
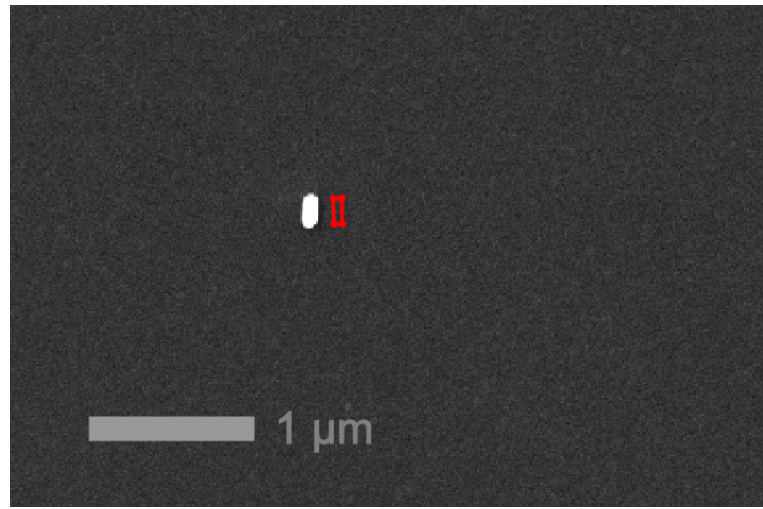
Figure 5.2: A comparison of the predicted size (using E_{poly}=79 GPa) and the size measured from the SEM image for a scanned GNR (batch size, 145 nm by 50 nm) in an air medium. It can be seen that the predicted size was close to the size seen in the SEM image. It should be noted that the orientation and position of the drawn rod are random in this image and can be ignored.

5.2.2 Size characterisation of gold nanorods in a water medium

The size characterisation of metal nanoparticles in a water medium is very important because it enhances their applications in bio-medical fields such as cell imaging by gold nanorods [61, 62]. Some ways to use gold nanorods for cell imaging are described briefly in the future work (please see chapter 9). In biomedical applications, NIR light is mostly used because it can penetrate the body. In this research, experiments on gold nanorods were done using both UV-NIR and NIR-NIR configurations. However, mostly UV-NIR configuration was used to avoid the thermal effect on nanorods which was observed while using the NIR-NIR configuration (please see chapter 6, section 6.5). In addition, the

system complexity was low for the UV-NIR configuration. However, there is no problem to carry out experiments on gold nanorods using the NIR-NIR set-up with a controlled laser power and proper wavelength.

The samples for the experiment in a water medium were made by using electrostatic layers to attach the gold nanorods on the surface so that the water could not wash them as described in section 4.5.3 of chapter 4. Though attempting experiments in a water medium is more challenging than in an air medium, careful steps can lead to the success. Water was centrifuged before filling the sample chamber with it and also refreshed many times to prevent the bacteria and formation of bubbles. The experimental results below show the size characterisation of a GNR (112 nm by 40 nm according to the product sheet, batch A12-40-750, purchased from Nanopartz) in a water medium and the SEM image of the rod can be seen in figure 5.3 (a). The experiment was done with the pump wavelength of 415 nm and probe wavelength of 780 nm. It can be seen from the simulations shown in figure 3.18 of chapter 3 that the chosen wavelengths were applicable to excite and detect this rod in a water medium. The experimental set-up for the UV-NIR configuration was shown and explained before in section 4.3 where path 3 (NIR) and path 4 (UV) were used for this experiment. The used experimental parameters are mentioned in the table 5.2.

Table 5.2: Experimental parameters used for a GNR in a water medium.

Pump wavelength nm	Probe wavelength nm	Pump power mW	Probe power mW	delay rate kHz	step size nm
415	780	0.5	1	4	200

The raw time trace, processed trace for the long time window of 1 ns, processed trace for the short time window of 0.15 ns and corresponding FFT traces are shown in figure 5.3 (b), (c) and (d), respectively. It can be seen that the rod had the longitudinal mode at 8.4 GHz and breathing mode at 64.4 GHz. The scanned rod area is shown through maps in figure 5.4. It can be seen from the optical image shown in figure 5.4 (a) that the nanorod was not resolved optically but was resolvable acoustically as can be seen from figure 5.4 (b) to (e). The amplitude maps were extracted at the obtained longitudinal mode (8.4 GHz) and the breathing mode (64.4 GHz) as shown in figure 5.4 (b) and (c), respectively. The frequency maps show the low frequency (longitudinal mode) and high

frequency (breathing mode) clearly in figure 5.4 (d) and 5.4 (e), respectively.
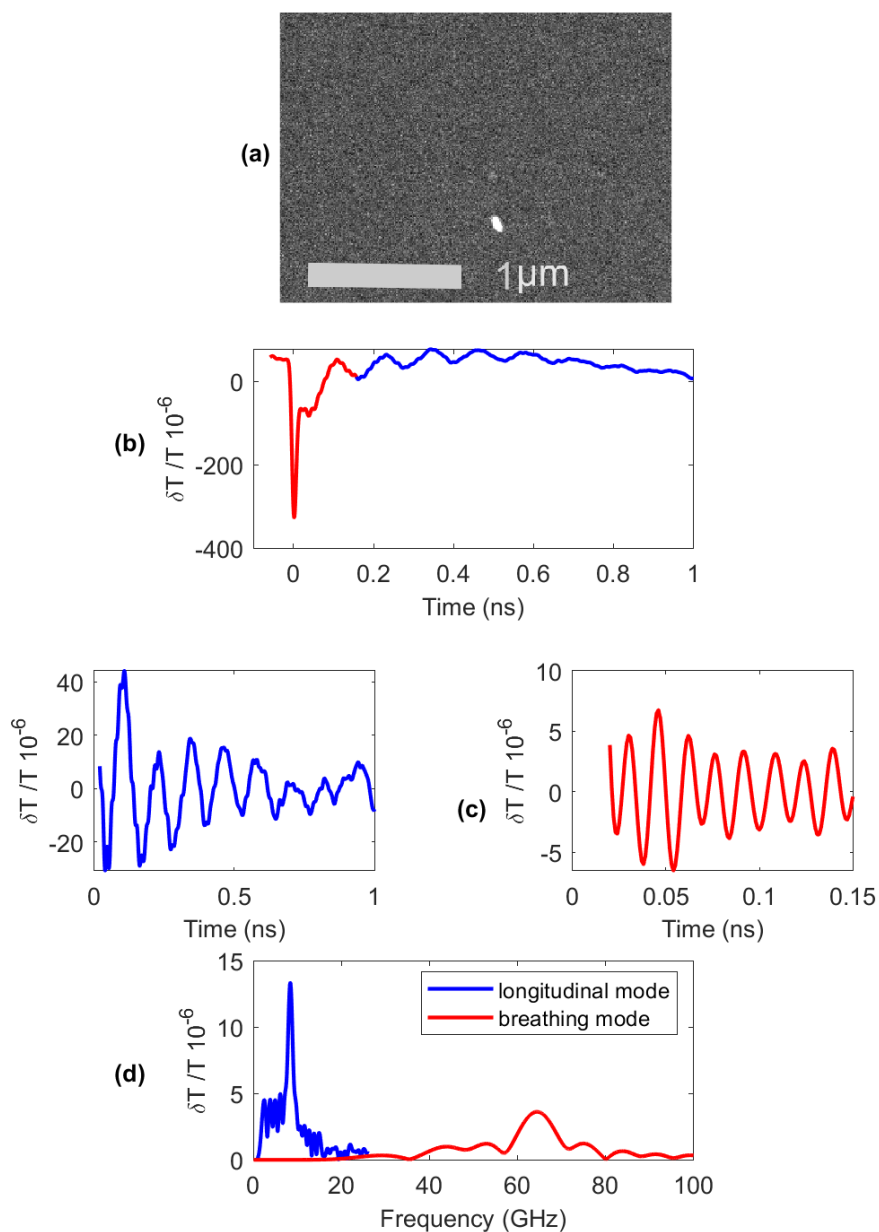
Figure 5.3: The SEM image and experimental traces from a GNR (112 nm by 40 nm according to the product sheet, batch A12-40-750, purchased from Nanopartz) in a water medium. (a) The SEM image of the nanorod. (b) Raw time trace. (c) Processed traces for 1 ns (left), for 0.15 ns (right). (d) Obtained longitudinal mode (low frequency) at 8.4 GHz and breathing mode (high frequency) at 64.4 GHz after performing an FFT of the processed traces for long and short time windows, respectively.
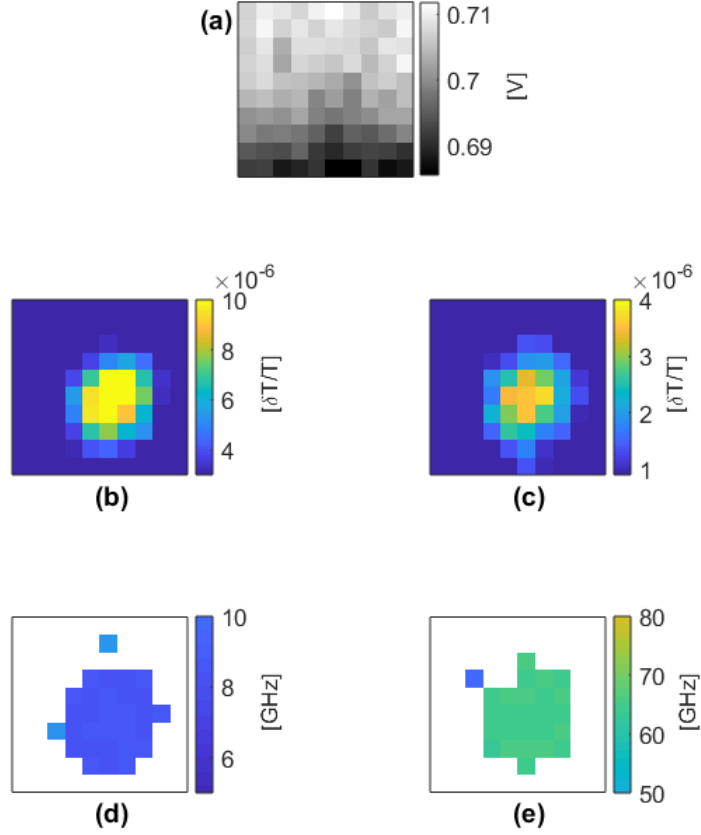
Figure 5.4: Scanned area of a GNR (112 nm by 40 nm according to the product sheet, batch A12-40-750, purchased from Nanopartz) with a step size of 200 nm. (a) Optical picture. (b)(c) Amplitude maps at the longitudinal mode (8.4 GHz) and the breathing mode (64.4 GHz), respectively. (d)(e) Frequency maps showing the longitudinal and the breathing modes, respectively.

Similar to the previous section, experimental measurements for this rod are listed in table 5.3. It can be seen that the predicted length of the rod closely matched to the length measured by the SEM if $E_{[110]} = 64$ GPa were used. However, the length differences with respect to the SEM measurements were 13.4±8.6 nm using E_{poly} and 1.4±8.5 nm using $E_{[110]} = 64$ GPa. The predicted width of the rod was 40±8 nm and the difference with respect to the width measured from the SEM image was 3.6±8 nm as can be seen in the table 5.3. The size precisions were extracted in the same way as was described before in section 4.4.2.5 of chapter 4. It was found that the length and width precisions for the rod were 0.4 nm and 0.06 nm compared to SEM measurements, respectively using E_{poly}. A

rod was drawn of the predicted size using E_{poly} on the SEM image for a comparison as can be seen in figure 5.5. It is visible that the predicted size was close to the SEM measured size, even when the actual E of the rod was unknown and E_{poly} was used. The factors that could affect the size accuracy were the same as described in the previous section.

Table 5.3: Predicted size dimensions of a GNR in a water medium.

Frequency	E	Growth direction	Measured Size	Size from SEM	Size difference SEM and Measured
GHz	GPa		nm	nm	nm
8.4 ± 0.2	31	[100]	75.4 ± 2	107 ± 8	31.5 ± 8.2
	42	[100]	87.8 ± 2.4		19.1 ± 8.3
	64	[110]	108.4 ± 2.9		1.4 ± 8.5
	79	polycrystalline	120.4 ± 3.2		13.4 ± 8.6
	81	[110]	121.9 ± 3.3		15 ± 8.6
	115	[111]	145.3 ± 3.9		38.3 ± 8.9
64.4 ± 0.3	79	polycrystalline	36.4 ± 0.17	40 ± 8	3.6 ± 8
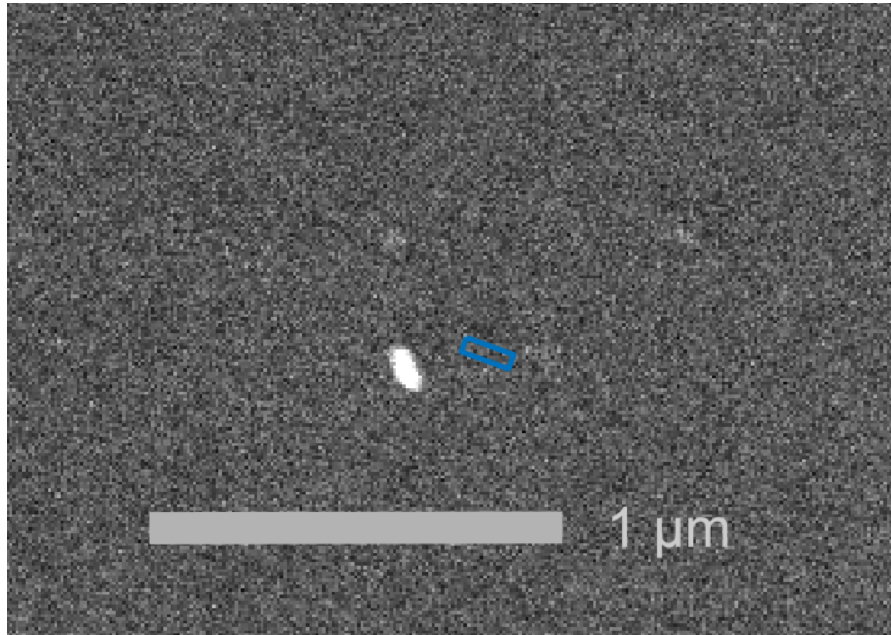
Figure 5.5: A comparison of the predicted size (using E_{poly}) and the size measured from the SEM image for a scanned single GNR (batch, 112 nm by 40 nm) in a water medium. It should be noted that the orientation and position of the rod are random in this image and can be ignored.

5.2.3   Summary of the size characterisation of gold nanorods

The size characterisation of gold nanorods was performed in both air and water media by using time resolved pump-probe spectroscopy in this research. At first, vibrational

frequencies of gold nanorods were obtained by using time-resolved measurements and then the obtained frequencies were converted to size dimensions by using an analytical model developed by Hu et al. [162]. The experimental results demonstrated that the predicted sizes were very close to the sizes measured by the SEM. It is also true that the E value, unexpected errors coming from the SEM measurements, shape difference between the rod used in the experiment and in the modelling, and heat from the laser, among others contributed to the size error. Hence, it is reasonable to say that the use of exact E value of the rod, taking account the exact shape of the rod in the modelling during the frequency to size conversion, use of reasonable laser power during scan, among others can improve the size accuracy.

5.3   Determination of the angle of a gold nanorod

It was shown through simulations in figure 3.3 and figure 3.6 that a nanorod is sensitive to its orientation to the light or the polarisation of light. This property of a nanorod can be demonstrated either by changing the polarisation of the pump beam or the probe beam. By using this property, it is possible to determine the orientation or angle of a nanorod. It can be understood from the simulations shown in figure 3.3 and figure 3.6 that a nanorod is not sensitive to the polarisation of the UV beam. Hence, NIR beam needs to be used for the generation to determine the angle of a nanorod by changing the polarisation of the pump beam. Either the generation beam or the detection beam can be used to determine the angle of a rod using the NIR-NIR configuration. In contrast, only detection beam can be used in the case of the UV-NIR set-up. In this research, UV-NIR (circularly polarised) configuration was used mostly and the polarisation of the NIR probe beam was changed to determine the angle of the rod. The reason was that the laser induced thermal effect on gold nanorods was observed while using the NIR beam for generation (please see chapter 6, section 6.5). Hence, the NIR beam was avoided as a pump beam. It is also possible to determine the angle of a rod by using linearly polarised beams and rotating the sample instead of changing the polarisation of beams. However, a rotating stage needs to be installed in the system which can make the set-up slightly complex.

The sample was made on a 50 nm ITO coated 18 mm by 18 mm gridded glass cover-slip

by drop casting 40 μL 1:8 mixture of GNR solution and DI water. The target GNR (145 nm by 50 nm according to the product sheet, batch A12-50-800, purchased from Nanopartz) for the experiment was almost vertical as can be seen in the SEM image (inside the red colour box) shown in figure 5.6 (a). It was ensured that the angle deviation between the sample on the SEM stage and the experiment stage was low. The considered polarisation directions of light and the orientation of the sample on the experiment stage are shown in figure 5.6 (b, left) to avoid any confusion. It can be seen that the directions along and perpendicular to the experiment stage were considered as horizontal and vertical, respectively. So, if it is said in this thesis that the rod is vertical or the beam is vertically polarised, it means that the rod and beam were perpendicular to the experiment stage. As the UV beam was used for the generation, the nanorod was always 'on' because it was insensitive to the polarisation of the UV beam. The polarisation of the detection beam was changed as shown in figure 5.6 (b, right) to determine the angle of a rod. The response of a nanorod will be different for different polarisations of the detection or probe beam. For example, a vertical rod will be 'off' and 'on' when the detection beam angles would be 0° and 90°, respectively. In contrast, the rod will be 'on' in both cases when the detection angles would be 45° and -45°.

The experiment was done with the same experimental set-up as explained in section 4.3 where path 3 (NIR) and path 4 (UV) were used for this experiment. The experimental parameters are mentioned in the table 5.4. To change the polarisation of the probe beam, the half wave plate before the PBS was rotated automatically using a motor as shown in figure 4.6 where two photo-detectors (orthogonal with each other) were used for the detection in transmission. The nanorod response was measured in an air medium.

Table 5.4: Experimental parameters to demonstrate the polarisation sensitivity of a vertical rod.

Pump wavelength	Probe wavelength	Pump power	Probe power	delay rate	step size
nm	nm	mW	mW	kHz	nm
415	780	1.77	1.5	4	100

The amplitude maps of the target rod are shown in figure 5.7. It can be seen from the amplitude maps at the longitudinal and breathing modes shown in figure 5.7 (a) and

5.7 (c), respectively that the target vertical rod was 'off' when the detection angle was 0°. In contrast, the rod was 'on' when the detection angle was 90° as can be seen from the amplitude maps at the longitudinal and breathing modes shown in figure 5.7 (b) and 5.7 (d), respectively.

(a)

(b)
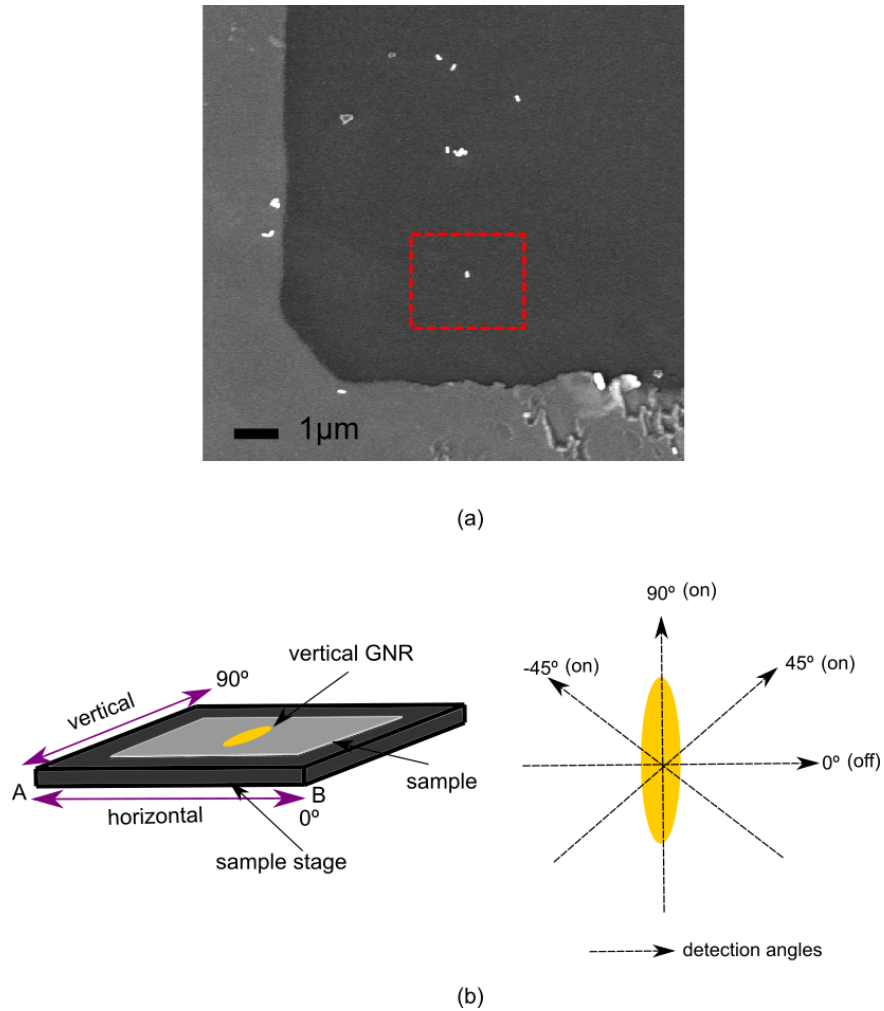
Figure 5.6: SEM image of the target sample, considered beam polarisation directions on the sample and detection of a rod from different angles. (a) The target vertical GNR can be seen inside the red colour box. (b) The sample stage is shown where AB is the front side. It was assumed that the direction along the sample stage was horizontal and the direction perpendicular to the stage was vertical. So a vertical rod was perpendicular to the sample stage. Similarly, a vertically polarised beam was perpendicular to the sample stage. (c) The polarisation sensitivity of a GNR can be demonstrated by changing the detection angle. It can be expected that a vertical rod will be 'off' (minimum detection point) for the detection angle of 0° and 'on' (maximum detection point) for the detection angle of 90°. On the other hand, the vertical rod will be 'on' (half way of maximum detection point) for both the detection angles of 45° and -45°.

On the other hand, the rod was 'on' in both cases when the detection angles were

+45° and -45° as can be seen from the amplitude maps at the longitudinal mode as shown in figure 5.7 (e) and 5.7 (f), respectively. The same observation can be made for the amplitude maps at the breathing mode as shown in figure 5.7 (g) and 5.7(h) when the detection angles were +45° and -45°, respectively. The optical image of the nanorod is shown in figure 5.7 (i) where it can be seen that the nanorod was not resolved optically. The longitudinal and breathing modes of this rod were at 7.3 GHz (blue curve) and 40.6 GHz (red curve) as can be seen from figure 5.7 (j).

Frequency maps of the rod at the longitudinal and breathing modes are shown in figure 5.8 for the detection angles of 0°, 90°, 45° and -45° and changed responses of the rod according to the detection angle can be observed as before. It is also important to see the difference between the 'on' and 'off' signal amplitudes. All the experimental traces from this rod for different detection angles are shown in figure 5.9. Raw time traces, processed traces and FFT traces are shown in figure 5.9 (a)(b) and (c), respectively for 0° (orange+blue) and 90° (violet+yellow) where short length traces are shown by orange and violet colours. It can be seen that no longitudinal or breathing modes (blue and orange curves) were detected when the detection angle was at 0° (along width, turn-off case). In contrast, the longitudinal mode at 7.3 GHz (yellow curve) and breathing mode at 40.6 GHz (violet curve) were detected when the detection angle was at 90° (along length, turn-on case). It can be seen from 5.9 (c) that the difference between the 'turn on' and 'turn off' signal amplitudes was high as expected.

On the other hand, raw time traces, processed traces and FFT traces are shown in figure 5.9 (d)(e) and (f) respectively for +45° (orange+blue) and -45° (violet+yellow) where short length traces are shown by orange and violet colours. It can be seen that the longitudinal and breathing modes were detected for both cases when the detection angles were at +45° and -45°. It was expected that the signal amplitudes for +45° and -45° angles of detection would be same because the rod was almost vertical. However, the reason behind this deviation can be that the rod was not exactly at 90° and the light was not perfectly circularly polarised. It can be seen that the signal amplitudes were more close in the case of the longitudinal mode than the breathing mode.

It was described in chapter 4 (section 4.4.2.4) that four points phase stepping method was used in this thesis to determine the angle of a gold nanorod where amplitudes at 0°, 45°,

90° and 135° were used. Experimentally obtained amplitudes for the longitudinal mode of the rod at four angles of detection are marked by red dots in figure 5.10. The calculated angle of the rod was 85.3±0.8° according to the phase stepping method where the deviation came from the effect of noise on the accuracy of the phase stepping method (figure 4.18). It can be seen that the experimental points were slightly off from the theoretical trace (blue curve) and also did not maintain a sinusoidal response. All size and angle measurements of this rod are listed in table 5.5.

The reason for the angle deviation can be low SNR, obtained non-sinusoidal response of the rod, minor mismatch in the orientation of the sample between the SEM stage and the experiment stage, calibration fault of the rotary parts in the set-up, and misalignment of optics. However, it was ensured that the last three options could not contribute to the error. It is sensible to think that low SNR and non sinusoidal response of the rod were the main reasons behind the angle deviation. In addition, accuracy of the angle prediction also depended on the proper localisation of the rod in this thesis because a window was selected around the localised point of the rod and average amplitude over that window was the amplitude of the rod for any respective angle. Average amplitude of the rod can also depend on the beam shape and overlapping of the pump and probe beams during scanning.

One way to get rid of this problem is to increase the number of averages and increase the SNR but that would be very time consuming if the four points of the phase stepping method come from four area scans. A quick but fine angular scan can be taken on a single point on the rod to have more accurate result which is shown later in this chapter.
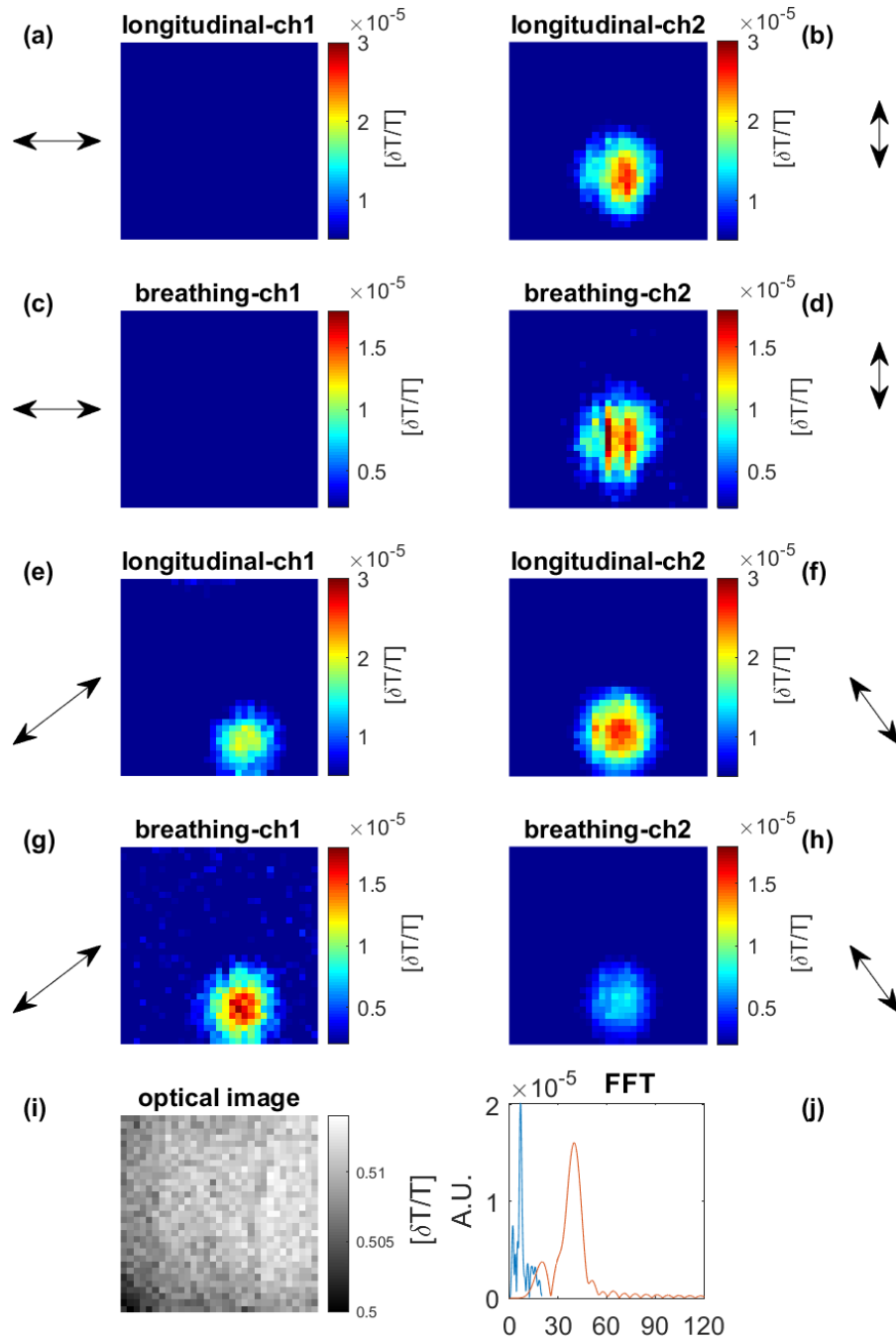
Figure 5.7: Changes in the response of a vertical gold nanorod in an air medium for different polarisations of the detection (probe) beam. (a)(c) Amplitude maps at the longitudinal and breathing modes respectively when the detection angle was at 0° (along width of rod). (b)(d) Amplitude maps at the longitudinal and breathing modes respectively when the detection angle was at 90° (along length of rod). (e)(g) Amplitude maps at the longitudinal and breathing modes respectively when the detection angle was at 45°. (f)(h) Amplitude maps at the longitudinal and breathing modes respectively when the detection angle was at -45°. (i) Optical image of the nanorod where it can be seen that nanorod was not resolved optically. (j) Obtained longitudinal and breathing modes of the rod at 7.3 GHz and 40.6 GHz, respectively. It can be seen that the vertical rod was 'off' when the detection angle was 0° and 'on' when the detection angle was 90° as expected. On the other hand the rod was 'on' for both cases when the detection angles were +45° and -45°, as expected.

156
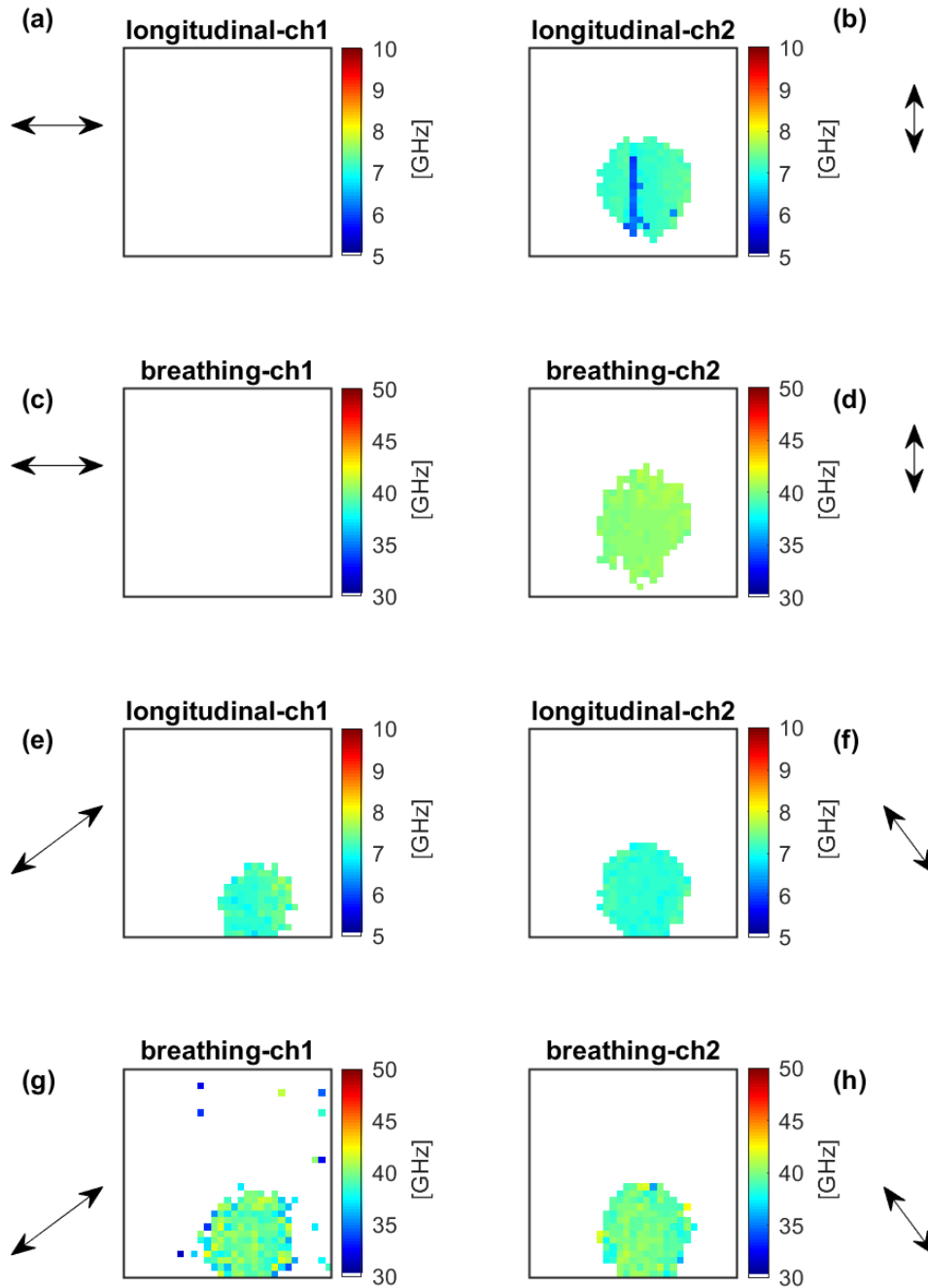
Figure 5.8: Frequency maps of a vertical gold nanorod in an air medium for different polarisations of the detection (probe) beam. (a)(c) Frequency maps at the longitudinal (7.3 GHz) and breathing modes (40.6 GHz) respectively when the detection angle was at 0° (along width of rod). (b)(d) Frequency maps at the longitudinal and breathing modes respectively when the detection angle was at 90° (along length of rod). (e)(g) Frequency maps at the longitudinal and breathing modes respectively when the detection angle was at 45°. (f)(h) Frequency maps at the longitudinal and breathing modes respectively when the detection angle was at -45°. It can be seen that the vertical rod was 'off' when the detection angle was 0° and 'on' when the detection angle was 90°, as expected. On the other hand the rod was 'on' for both cases when the detection angles were +45° and -45°, as expected.
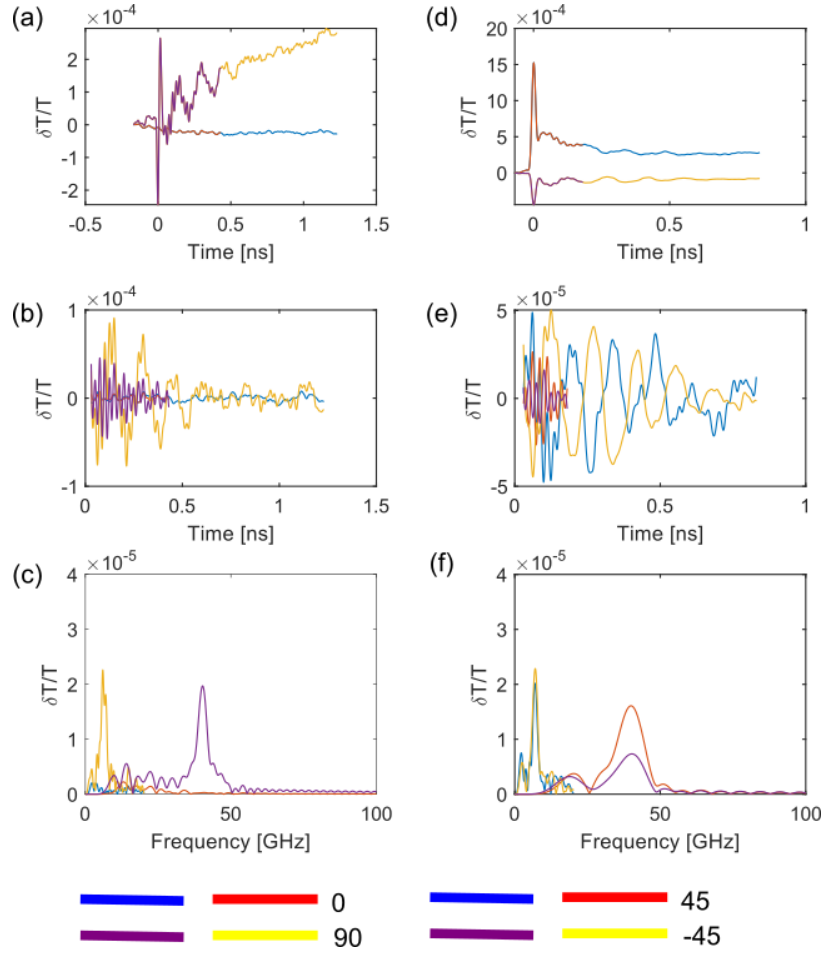
Figure 5.9: Experimental traces from a vertical gold nanorod detected for different polarisations of the detection (probe) beam in an air medium. (a)(b)(c) Raw time traces, processed traces and FFT traces for 0° (orange+blue) and 90° (violet+yellow) where short trace lengths are shown by orange and violet colours. No longitudinal and breathing modes (blue and orange curves) were detected when the detection angle was at 0° (along width, turn-off case). The longitudinal mode at 7.3 GHz (yellow curve) and breathing mode at 40.6 GHz (violet curve) were detected when the detection angle was at 90° (along length, turn-on case). It can be seen that the difference between the 'turn on' and 'turn-off' signal was high, as expected. (d)(e)(f) Raw time traces, processed traces and FFT traces for +45° (orange+blue) and -45° (violet+yellow) where short trace lengths are shown by orange and violet. The longitudinal and breathing modes were detected for both cases when the detection angles were at +45° and -45°. It was expected that signal amplitudes would be same if the rod was detected along +45° and -45° because the rod was vertical. The reason behind this deviation may be that the nanorod was not exactly at 90° or the probe light was not perfectly circularly polarised. It can be seen that signal amplitudes were more close for the longitudinal mode than the breathing mode.
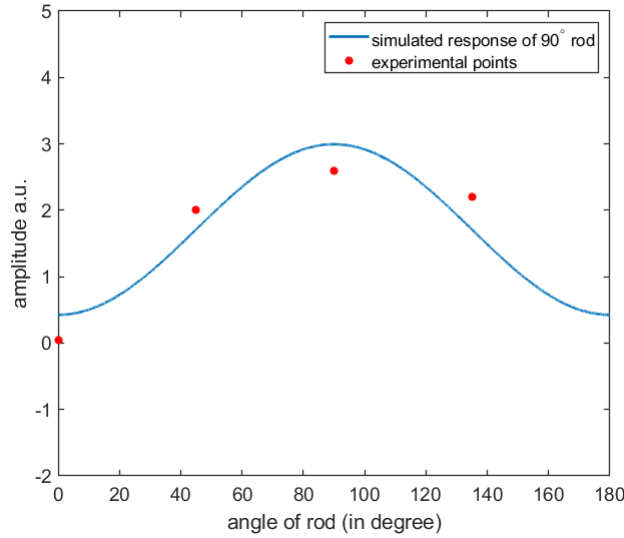
Figure 5.10: Angle determination of a vertical GNR using the phase stepping method. The blue curve is the theoretical response of the vertical GNR and hence has the maximum amplitude at 90°. Obtained experimental values at four angles 0°, 45°, 90° and 135° are marked with red dots which were used to determine the angle of the rod by the phase stepping method. The calculated angle using the longitudinal mode amplitudes were 85.3±0.8° where the deviation came from the effect of noise on the accuracy of the phase stepping method.

Table 5.5: Experimental measurements of a vertical GNR in an air medium.

Frequency	E	Size Measured	Size (SEM)	Size difference SEM and Measured	Angle (SEM)	Angle (Measured)
GHz	GPa	nm	nm	nm	°	°
7.3 ± 0.2	31 [100]	86.8 ± 1.9	163 ± 36	76.1 ± 36	90 ± 7	85.3±0.8
	42 [100]	101 ± 2.26		62 ± 36		
	64 [110]	124.7 ± 2.8		38.3 ± 36.1		
	79 (poly)	138.5 ± 3.1		24.4 ± 36.1		
	81 [110]	140.3 ± 3.1		22.7 ± 36.1		
	115 [111]	167.2 ± 3.7		4.2 ± 36.2		
40.6 ± 1.2	79 (poly)	57.8 ± 1.8	90 ± 36	32.2 ± 36		

Another interesting spot was selected to demonstrate the sensitivity of a nanorod to the polarisation of light as shown in figure 5.11 where three similar sizes of gold nanorods were in three different orientations. The experiment was done with the same set-up, parameters and external medium as were mentioned for the above experiment.
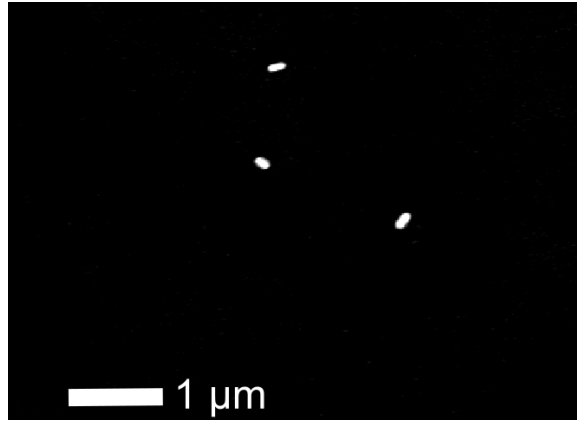
Figure 5.11: SEM image of the target area consisting three gold nanorods where three gold nanorods were almost of similar sizes and in different orientations.

It can be seen from the optical picture shown in figure 5.12 (a) and (b) that three rods were not visible because of the optical resolution limit set by the probe laser spot size (~ 2 μm). In contrast, they were clearly visible using acoustics set by the pump laser spot size (~ 1 μm). Rod 1, rod 2 and rod 3 were nearly 0°, -45° and +45°, respectively as can be seen from the SEM image shown in figure 5.11. When the rods were detected horizontally, it was expected to detect all rods simultaneously as can be seen from the amplitude maps at the longitudinal and breathing modes shown in figure 5.12 (c) and 5.12 (e), respectively. In contrast, only rod 2 and rod 3 were visible when rods were detected vertically because rod 1 was almost horizontal as can be seen from the amplitude maps at the longitudinal and breathing modes shown in figure 5.12 (d) and 5.12 (f), respectively. So, the sensitivity of a nanorod to the orientation of light can be understood from these experimental results. The same trend can be seen in the longitudinal mode frequency maps shown in figure 5.12 (g)(h) and breathing mode frequency maps shown in figure 5.12 (i)(j). However, the angles of rod 1, rod 2 and rod 3 were not exactly 0°, -45° and +45°. Hence, it could be expected that the rods will be slightly visible in other channels. However, the detection level could be lower than the noise level in those cases.
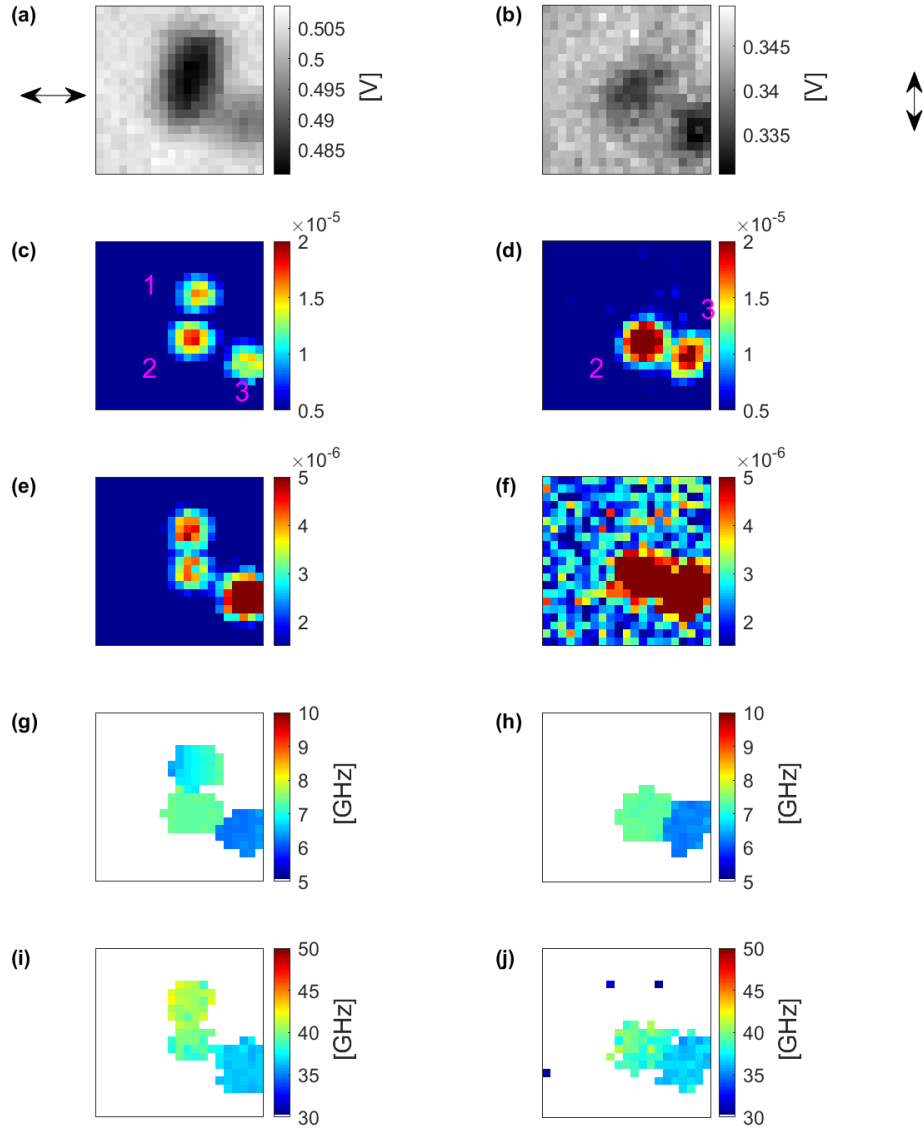
Figure 5.12: All maps corresponding to the three rods from the scanned area detected using the orthogonal detectors. (a)(b) Optical map. (c)(e) Amplitude maps for the longitudinal and breathing modes respectively when detected horizontally. (d)(f) Amplitude maps for the longitudinal and breathing modes respectively when detected vertically, (g)(i) Frequency maps for the longitudinal and breathing modes when detected horizontally. (h)(j) Frequency maps for the longitudinal and breathing modes when detected vertically. As rod 1, rod 2 and rod 3 were nearly at ~ 0 deg, $\sim$ -45 deg and $\sim$ +45 deg respectively, three rods were visible simultaneously when detected horizontally. In contrast, only rod 2 and rod 3 were visible when rods were detected vertically because rod 1 was almost horizontal.

Table 5.6: Experimental measurements of three GNRs in an air medium.

Frequency	E	Measured Size	Size from SEM	Size difference SEM and Measured	Angle (SEM)	Angle (Measured)
GHz	GPa	nm	nm	nm	°	°
Rod 1						
6.7 ± 0.2	31 [100]	94.6 ± 2.9	185 ± 14	90.4 ± 14.3	24.7 ± 4	7.3 ± 1.3
	42 [100]	110 ± 3.4		74.9 ± 14.4		
	64 [110]	135.9 ± 4.2		49.1 ± 14.6		
	79 (poly)	151 ± 4.6		34 ± 14.8		
	81 [110]	152.9 ± 4.7		32.1 ± 14.8		
	115 [111]	182.2 ± 5.6		2.8 ± 15		
41.3 ± 0.8	79 (poly)	56.9 ± 1.1	71 ± 14	14.1 ± 14		
Rod 2						
7.2 ± 0.07	31 [100]	88 ± 0.86	154 ± 14	66 ± 14	-38.65 ± 6	-7.1 ± 1.7
	42 [100]	102.4 ± 1		51.6 ± 14.6		
	64 [110]	126.4 ± 1.24		27.5 ± 14		
	79 (poly)	140.5 ± 1.4		13.5 ± 14		
	81 [110]	142.2 ± 1.4		11.7 ± 14		
	115 [111]	169.5 ± 1.7		15.5 ± 14		
40.16 ± 0.7	79 (poly)	58.41 ± 1	80 ± 14	21.6 ± 14		
Rod 3						
6.3 ± 0.12	31 [100]	100.6 ± 2	183 ± 14	82.4 ± 14.1	47.72 ± 3	30.6 ± 1.4
	42 [100]	117 ± 2.2		65.9 ± 14.1		
	64 [110]	144.5 ± 2.8		38.5 ± 14.3		
	79 (poly)	160.6 ± 3.1		22.4 ± 14.3		
	81 [110]	162.6 ± 3.2		20.4 ± 14.4		
	115 [111]	193.7 ± 3.8		10.7 ± 14.5		
36.25 ± 0.36	79 (poly)	64.7 ± 0.64	85 ± 14	20.3 ± 14		

Angle of three rods were calculated using the phase stepping method and are mentioned in the table 5.6 with the size characterisation results. The probable reasons behind the angle deviation are the same as mentioned before.

5.4   Phononic image reconstruction of gold nanorods

In the last two sections, characterisation of size and angle of gold nanorods were shown. In this section, phononic image reconstruction of gold nanorods are shown by combining their size, angle and location information and some advanced level examples are presented.

5.4.1 Phononic image reconstruction of gold nanorods in an air medium

In the previous section, experimentally obtained size and angle measurements of three rods in an air medium were shown in table 5.6. Following the described localisation process of GNRs in section 4.4.2.3, those three rods were localised. Then, obtained sizes, angles and locations of those rods were overlaid with the previously captured SEM image of the rod area for comparison as shown in figure 5.13. It can be seen that the reconstructed phononic images of the rods were not perfect but close to the originals.

The same simulation as shown in figure 4.11 (c), was generated for the used step size (200 nm) of this experiment and the location precision for each rod was estimated. The estimated location precisions for rod 1, rod 2 and rod 3 were 26 nm, 16 nm and 29 nm, respectively. The localisation errors (centre-to-centre) of the rods with respect to the SEM image were 147±20 nm, 303±20 nm and 124±20 nm for rod 1, rod 2 and rod 3, respectively. Improper beam shape because of optics, low SNR, use of SEM scale bar and microscope stage positional information as references, among others could contribute to the location accuracy.

The reasons behind the size error could be the unknown E value of the rod, unexpected errors coming from the SEM measurements, shape difference between the rod used in the experiment and the modelling, and heat from the laser, among others, as were mentioned in the last chapter. The reasons behind the angle deviation could be the low SNR, not fully circularly polarised light, obtained non-sinusoidal response of the rod, minor mismatch in the angle of the sample between the SEM stage and the laser scan stage, calibration fault of the rotary parts in the set-up, and misalignment of optics, as were mentioned in the previous chapter. However, it was ensured that the last three options could not contribute to the error. It is sensible to think that the low SNR and non-sinusoidal response of the rod were the main reasons behind the angle deviation. All the probable reasons behind the deviations are mentioned again in this chapter for clarity and to remind the reader.
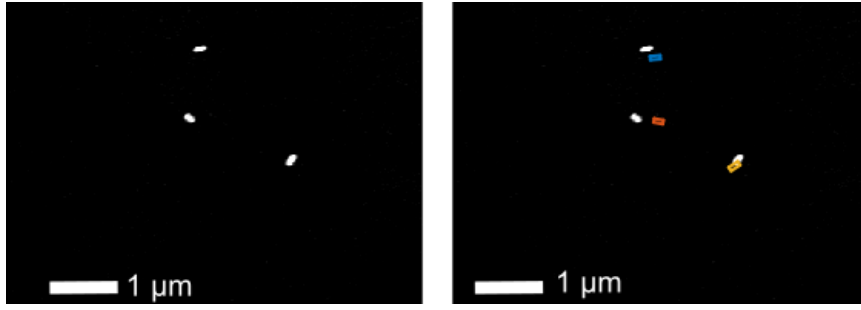
Figure 5.13: Overlay of experimentally measured sizes, angles and locations of GNRs with the SEM image. It can be seen that the reconstructed phononic image of the target rod area was not perfect but close to the original.

5.4.2 Phononic image reconstruction of gold nanorods in a water medium

In this section, phononic image reconstruction of GNRs in a water medium is presented. The SEM image of the target area is shown in figure 5.14 (a) where it can be seen that the rods were of different sizes and in different orientations. As rods were of different sizes, they provided different frequencies and hence their frequencies could be used to identify and separate them. In addition, orientations or angles of rods could be used to separate them because nanorods are sensitive to their orientations to the light. The sample was made by using electrostatic layers to attach GNRs on the substrate as described in section 4.5.3 and the experiment was carried out in a water medium.

The experiment was performed using path 4 (UV) and path 3 (NIR) of the experimental set-up explained in section 4.3. The experimental parameters are mentioned in the table 5.7. The half-wave plate before the PBS was rotated to change the angle of the detection beam as shown in figure 4.5 of chapter 4 where two photo-detectors were used for detecting orthogonal light beams simultaneously in the transmission mode.

Table 5.7: Experimental parameters to image three gold nanorods.

Pump wavelength nm	Probe wavelength nm	Pump power mW	Probe power mW	delay rate kHz	step size nm
415	780	0.5	1	4	200
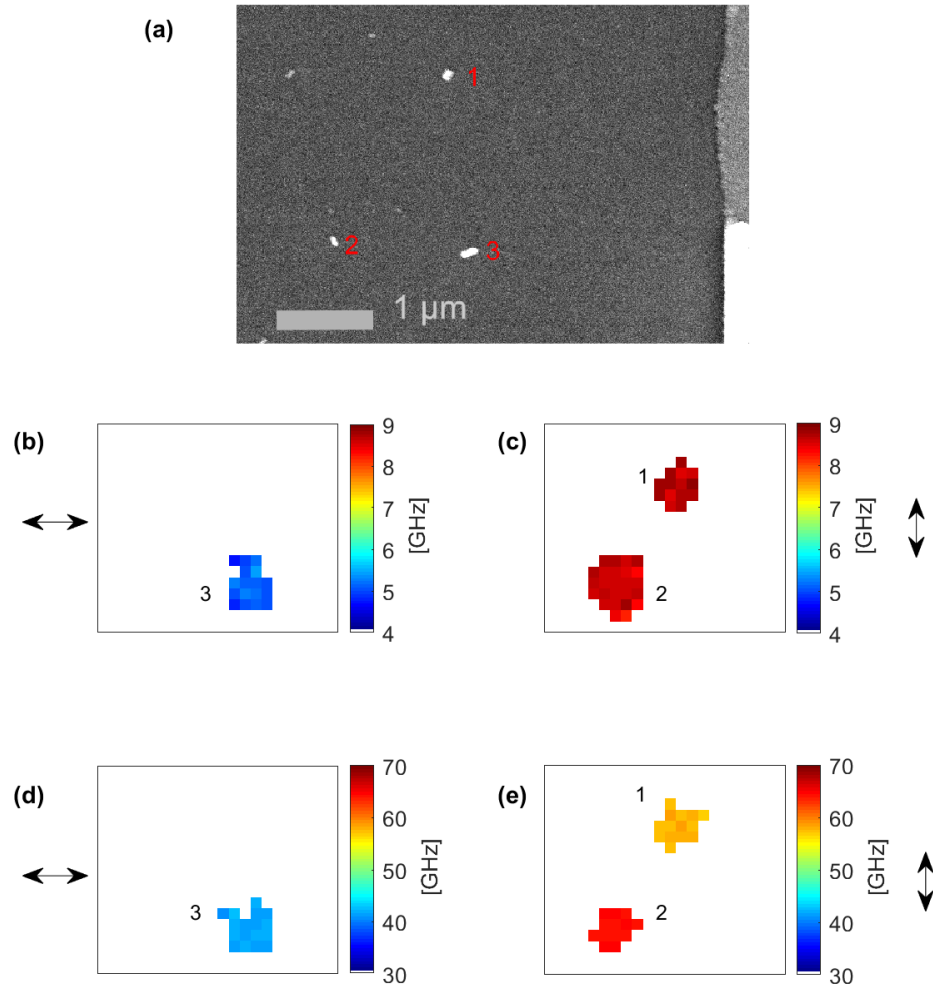
Figure 5.14: A scanned area showing three GNRs and their frequency maps. (a) SEM image of GNRs of different sizes and orientations. (b) The longitudinal mode frequency map of rod 3 (5.3 GHz). (c) The longitudinal mode frequency maps of rod 1 (8.7 GHz) and rod 2 (8.4 GHz). (d) The breathing mode frequency map of rod 3 (41.3 GHz). (e) The breathing mode frequency maps of rod 1 (58.17 GHz) and rod 2 (64.4 GHz).

As in the target area rod 1 and rod 2 were smaller than rod 3, expected frequencies from rod 1 and rod 2 were higher than that of rod 3. Rod 3 had the longitudinal and breathing modes at 5.3 GHz and 41.8 GHz, respectively as can be seen from the frequency maps shown in figure 5.14 (b) and (d), respectively. On the other hand, rod 1 and rod 2 had the longitudinal modes at 8.7 and 8.4 GHz respectively as can be seen in figure 5.14 (c) and breathing modes at 58.17 GHz and 64.4 GHz respectively as can be seen in figure

5.14 (e). So, rods could be identified and separated by using their frequencies as tags. It can also be observed that rod 1 and rod 2 appeared in the vertical channel (vertical with respect to the sample stage) as their orientations were nearly vertical and rod 3 appeared in the horizontal channel (horizontal with respect to the sample stage) as its orientation was nearly horizontal. Hence, the orientation difference of rods could be used to identify and separate them as well. However, the rods were not exactly horizontal and vertical. Hence, it was expected that those would be detected minimally in other channels also. However, the detection level might be below the noise level.

To separate and locate each rod, an amplitude map at the frequency of the rod was extracted and the centroid algorithm was applied to localise the rod as described before in section 4.4.2.3. All amplitude maps at the longitudinal and breathing mode frequencies of rod 1 were extracted for four angles of detection ($0°$, $45°$, $90°$, $135°$), as shown in figure 5.15. It can be seen that rod 2 was also visible with rod 1 in some cases because the frequency and orientation of rod 2 were very close to the frequency and orientation of rod 1. Hence, a manual mask was applied to filter out rod 2 so that the centroid algorithm could properly identify rod 1. This mask was applied to demonstrate the ability of the technique only and became necessary because the frequencies of the used rods were close to each other. For practical applications, it is recommended to use rods whose frequencies are far apart from each other to avoid this problem. However, the orientation difference of the rods still would be helpful to separate them even if the frequencies are the same. Red and green crosses point to the maximum amplitude location and centre of mass (centroid) on all maps, respectively. It is important to focus on the fact that in figure 5.15 (f), the red cross did not point to the maximum amplitude location, the bottom rod, because that rod was manually filtered out so that rod 1 could be identified. This type of situation can also be seen in some other places in the thesis which occurred due to the same reason just explained above. Following the process described in figure 4.12, the calculated weighted average of all centroids for the longitudinal mode was chosen as the final point to localise the rod.

The measured angle of the rod from the SEM image was $50\pm3°$. It was expected that the rod would be visible for $0°$, $45°$, and $90°$ angles of detection. The rod was detected for $90°$ and $45°$ as can be seen in figure 5.15 (b)(d) and 5.15 (e)(g), respectively. However, the

rod was not detected at $0°$ as can be seen in figure 5.15 (a) and 5.15 (c). The reason may be that the detection level was below the noise level. On the other hand, the rod was not detected along $-45°$ as can be seen in figure 5.15 (f) and 5.15 (h) because the rod was close to $+45°$. The results predicted that the rod angle ϕ could be defined by the expression, $45° < \phi \leq 90°$. The calculated angle of the rod using the phase stepping method was $18.2\pm3.2°$. The reasons behind the angle deviation were the same as mentioned in the previous section. It is worth mentioning that the angle deviation of the sample between the SEM stage and experimental stage was found very low, about $2°$ which could contribute to the systematic error. On the other hand, the zero position of the half-wave plate might not be in the right place or the aluminium tape which was used on the motor to fix the home position was not aligned perfectly with the zero position of the half-wave plate. However, this was tested and adjusted to have no error as can be seen from figure 5.16. This test was carried out by placing a polariser instead of the sample on the experimental stage and recording the DC (amount of light) for both orthogonal channels by rotating the $\lambda/2$ plate before the PBS. It can be seen that when the angle of light was $0°$, channel 1 (detector 1) which was horizontal with respect to the stage, had the maximum power. On the other hand, when the angle of light was $90°$, channel 2 (detector 2) which was vertical with respect to the stage, had the maximum power. Hence, there was no error in the alignment and rotation of the half-wave plate. Another point was that the shape of the rod was not properly like a rod, as can be seen from the SEM image. This shape diversity could also be a reason behind the angle deviation because the response of a rod to different polarisations of light also depends on its shape. The optical image of the rod and FFT traces at the chosen location point (weighted average point) are shown in figure 5.15 (i) and 5.15 (j), respectively. It can be seen that the rod was not resolved optically.
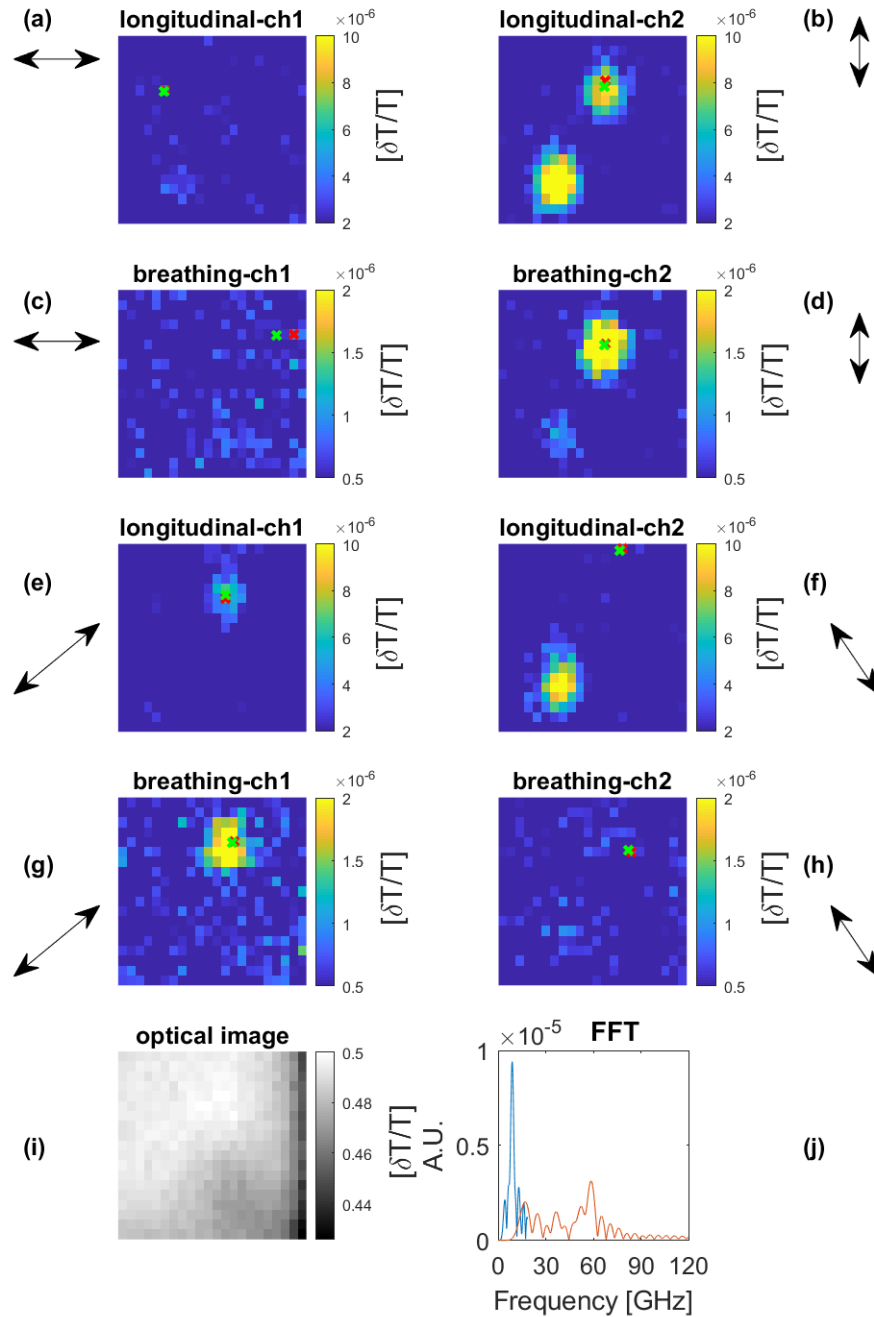
Figure 5.15: Amplitude maps extracted at the longitudinal and breathing modes of rod 1 for four angles of the detection beam to determine the location and angle of the rod. (a)(b) Amplitude maps at the longitudinal mode (8.7 GHz) of rod 1 when detected horizontally and vertically, respectively. (c)(d) Amplitude maps at the breathing mode (58.17 GHz) of rod 1 when detected horizontally and vertically, respectively. (e)(f) Amplitude maps at the longitudinal mode (8.7 GHz) of rod 1 when detected along +45° and -45°, respectively. (g)(h) Amplitude maps at the breathing mode (58.17 GHz) of rod 1 when detected along +45° and -45°,respectively. (i)(j) Optical image and FFT at the chosen location (weighted average point) for the rod. The maximum amplitude location and the centroid are marked by red and green crosses on each map, respectively.

Amplitude maps at the longitudinal and breathing mode frequencies of rod 2 for four angles of detection are shown in figure 5.17. As previously, the calculated weighted average of all centroids for the longitudinal mode was chosen as the final point to localise the rod. Rod 2 was also close to 90° (or -90°) and the measured angle was -65±2° from the SEM image. Hence, the rod was not detected at 0° as can be seen in figure 5.17 (a)(c). The rod was detected at 90° as can be seen in figure 5.17 (b)(d). On the other hand, the rod was not detected along +45° as can be seen in figure 5.17 (e)(g) while was detected along -45° as can be seen in figure 5.17 (f)(h). The results predicted that the rod angle ϕ could be defined by the expression, $-45° < \phi < -90°$. However, the calculated angle of rod 2 was -22.6±0.8°. The optical image of the rod and FFT traces at the chosen location point (weighted average point) are shown in figure 5.17 (i) and 5.17 (j), respectively. It can be seen that the rod was not resolved optically.

Amplitude maps at the longitudinal and breathing mode frequencies of rod 3 for four angles of detection are shown in figure 5.18. As previously, the calculated weighted average of all centroids for the longitudinal mode was chosen as the final point to localise the rod. Rod 3 was close to 0° and the measured angle from the SEM was 25±2°. So, this rod was expected to be detected at 0° and +45° as can be seen in figure 5.18 (a)(c) and figure 5.18 (e)(g), respectively. On the other hand, the rod was not detected at 90° as can be seen in figure 5.18 (b) for being below the noise level and was slightly visible in figure 5.18 (d). The rod was not detected at -45° as can be seen in figure 5.18 (f)(h) because the rod was close to +45°. The results predicted that the rod angle ϕ could be defined by the expression, $0° < \phi < 45°$. However, the calculated angle was -18.1±1.4°. The optical image of the rod and FFT traces at the chosen location point (weighted average point) are shown in figure 5.18 (i) and 5.18 (j), respectively. It can be seen that the rod was not resolved optically.
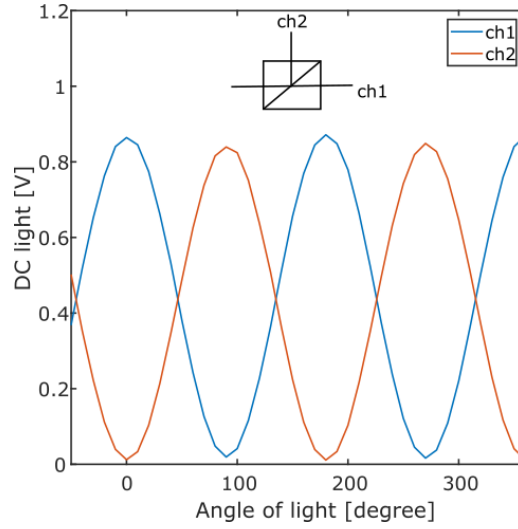
Figure 5.16: Alignment test of the half-wave plate rotation with respect to two orthogonal channels (detectors). This test was done by putting a polariser instead of the sample and it can be seen that there is no angle error.

Predicted values for all three rods are listed in table 5.8. The acoustically reconstructed images of the rods were overlaid with the SEM image for comparison as shown in figure 5.19. It can be seen that the reconstructed phononic images of the rods were not perfect, but close to the original. The same simulation as shown in figure 4.11 (c) was run for the applied step size of the scan (200 nm) and location precisions of the rods were estimated. The location precisions of rod 1, rod 2 and rod 3 were 20 nm, 19 nm and 61 nm respectively depending on the SNRs of the rods. The localisation errors (centre-to-centre) of the rods with respect to the SEM rods were 78±5 nm, 126±5 nm and 96±5 nm for rod 1, rod 2 and rod 3, respectively. The reasons behind the location error were the same as described before. In addition, a tiny movement of the particle/substrate because of the water flow or water bubble pressure inside the chamber could also contribute to the location error. Degassing the water before filling the chamber can reduce the location error.
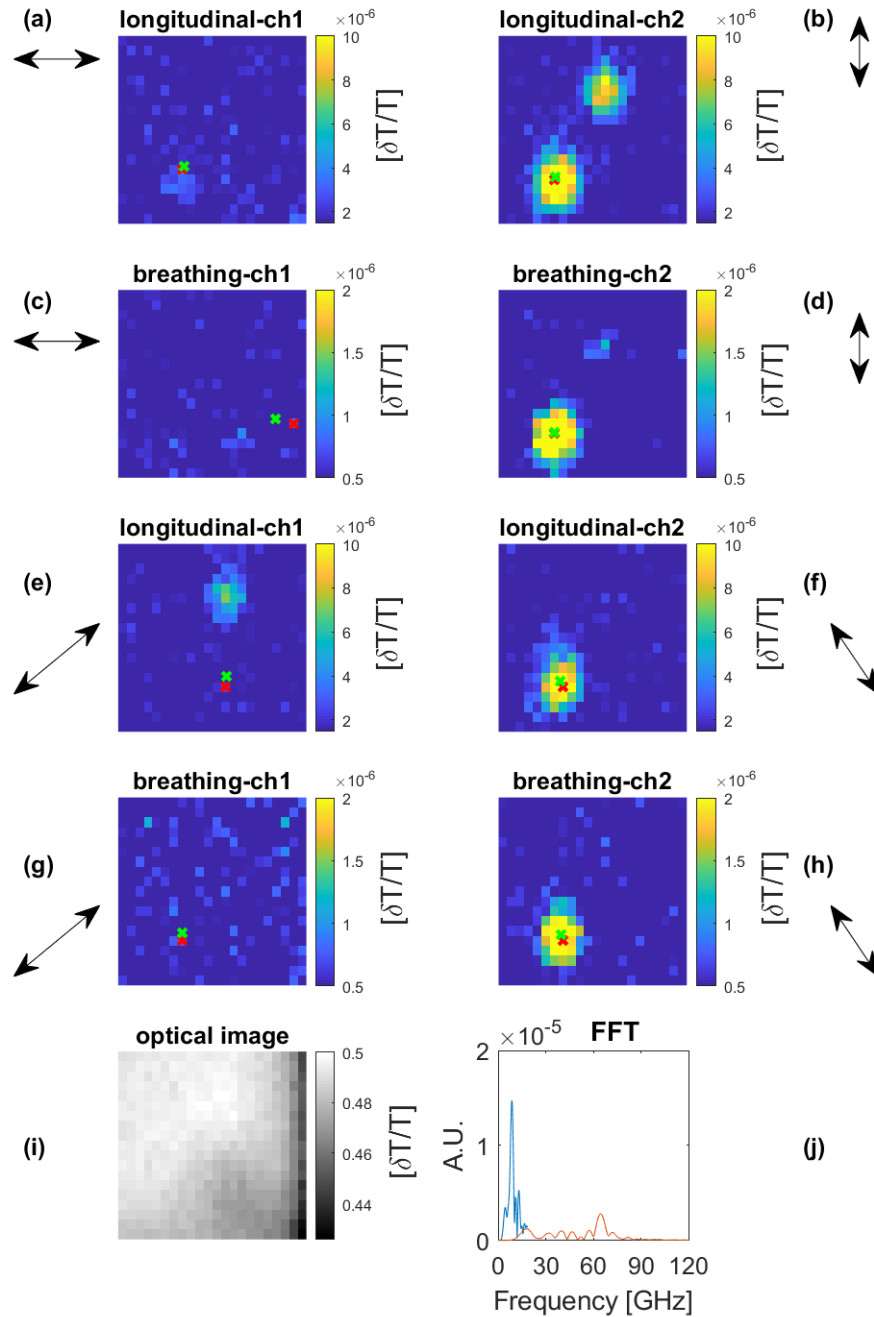
Figure 5.17: Amplitude maps extracted at the longitudinal and breathing modes of rod 2 for four angles of the detection beam to determine the location and angle of the rod. (a)(b) Amplitude maps at the longitudinal mode (8.1 GHz) of rod 2 when detected horizontally and vertically, respectively. (c)(d) Amplitude maps at the breathing mode (65.25 GHz) of rod 2 when detected horizontally and vertically, respectively. (e)(f) Amplitude maps at the longitudinal mode (8.1 GHz) of rod 2 when detected along +45° and -45°, respectively. (g)(h) Amplitude maps at the breathing mode (65.25 GHz) of rod 2 when detected along +45° and -45°, respectively. (i)(j) Optical image and FFT at the chosen location (weighted average point) for the rod. The maximum amplitude location and the centroid of the rod are marked by red and green crosses on each map, respectively.

171

Figure 5.18: Amplitude maps extracted at the longitudinal and breathing modes of rod 3 to determine the location and angle of the rod using orthogonal detectors. (a)(b) Amplitude maps at the longitudinal mode (5.3 GHz) of rod 3 when detected horizontally and vertically, respectively. (c)(d) Amplitude maps at the breathing mode (41.8 GHz) of rod 3 when detected horizontally and vertically, respectively. (e)(f) Amplitude maps at the longitudinal mode (5.3 GHz) of rod 3 when detected along +45° and -45°, respectively. (g)(h) Amplitude maps at the breathing mode (41.8 GHz) of rod 3 when detected along +45° and -45°, respectively. (i)(j) Optical image and FFT at the chosen location (weighted average point) for the rod. The maximum amplitude location and the centroid of the rod are marked by red and green crosses on each map, respectively.

Table 5.8: Experimental measurements of GNRs in a water medium.

Frequency	E	Measured Size	Size from SEM	Size difference SEM and Measured	Angle (SEM)	Angle (Measured)
GHz	GPa	nm	nm	nm	°	°
Rod 1						
8.7 ± 0.2	31 [100]	72.8 ± 1.7	100 ± 8	27.1 ± 8.2	50± 3	18.2± 3.2
	42[100]	84.8 ± 1.9		15.2 ± 8.2		
	64 [110]	104.6 ± 2.5		4.65 ± 8.4		
	79 (poly)	116.2 ± 2.7		16.3 ± 8.5		
	81 [110]	117.7 ± 2.8		17.7 ± 8.5		
	115 [111]	140.3 ± 3.3		40.3 ± 8.7		
58.2 ± 0.4	79 (poly)	40.3 ± 0.27	67 ± 8	26.7 ± 8.00		
Rod 2						
8.4 ± 0.2	31 [100]	75.4 ± 1.8	107 ± 8	31.6 ± 8.2	-65± 2	-22.6± 0.8
	42 [100]	87.8 ± 2.1		19.2 ± 8.3		
	64 [110]	108.3 ± 2.6		1.4 ± 8.4		
	79 (poly)	120.4 ± 2.9		13.4 ± 8.5		
	81 [110]	121.9 ± 3		14.9 ± 8.5		
	115 [111]	145.3 ± 3.5		13.3 ± 8.7		
64.4 ±0.3	79 (poly)	36.4 ± 0.17	40 ± 8	3.6 ± 8.0		
Rod 3						
5.3 ± 0.1	31 [100]	119.6 ± 2.3	178 ± 8	58.4 ± 8.3	25± 2	-18.1± 1.4
	42 [100]	139.1 ± 2.7		38.8 ± 8.4		
	64 [110]	171.8 ± 3.3		6.2 ± 8.7		
	79 (poly)	190.9 ± 3.7		12.9 ± 8.8		
	81 [110]	193.3 ± 3.7		15.3 ± 8.8		
	115 [111]	230.3 ± 4.4		52.3 ± 9.1		
41.8 ± 0.5	79 (poly)	56.1 ± 0.7	72 ± 8	15.9 ± 8		
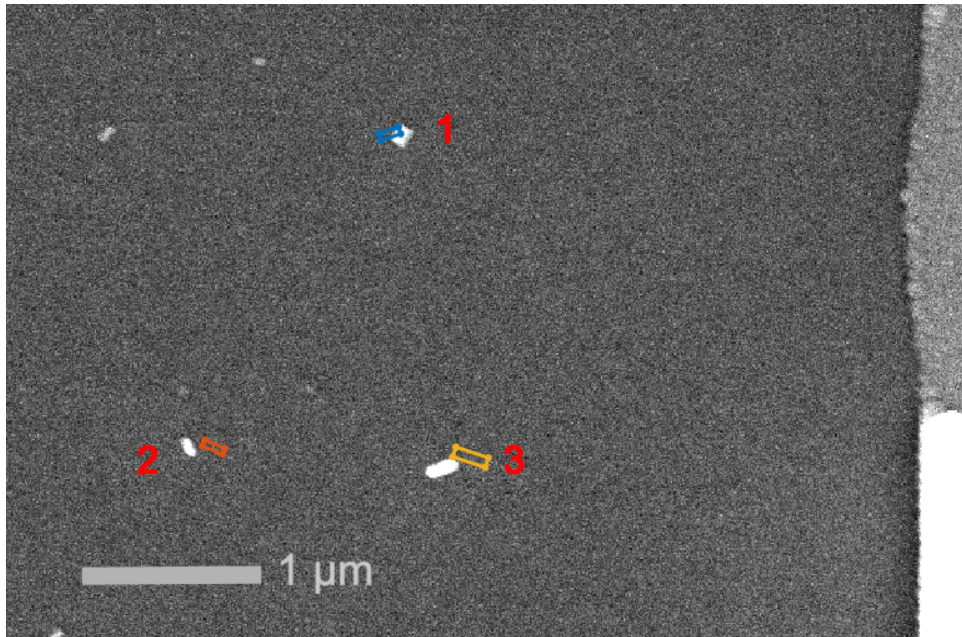
Figure 5.19: Overlay of measured sizes, locations and angles of rods with the SEM image. It can be seen that the reconstructed phononic images of the rods were not perfect, but close to the original.

5.4.2.1 Super-resolution of nanorods

It is described until now that the vibrational frequencies of nanorods and the polarisation of light can be used to determine the size, angle and location of nanorods. In the previously shown examples, nanorods were not inside the same optical PSF. The same techniques were repeated to super-resolve nanorods when they were inside the same optical PSF.

An example of resolving GNRs with super-optical resolution is shown here. It can be seen from the SEM image shown in figure 5.20 that two gold nanorods (rod 2 and rod 3) were inside the same optical PSF (1 μm). The rods were of different sizes and produced different frequencies. Hence, it was possible to use the frequency as a tag to differentiate them even they were inside the same PSF. The lengths of the rods were close but the widths of them were much different. As a result, the breathing modes were more separable than the longitudinal modes. In addition, rods were in different orientations that allowed to use the orientation or polarisation sensitivity of rods to separate them. The sample was scanned in an water medium with the same set-up and parameters mentioned for the previous examples by moving the electromechanical stage with 100 nm step size.
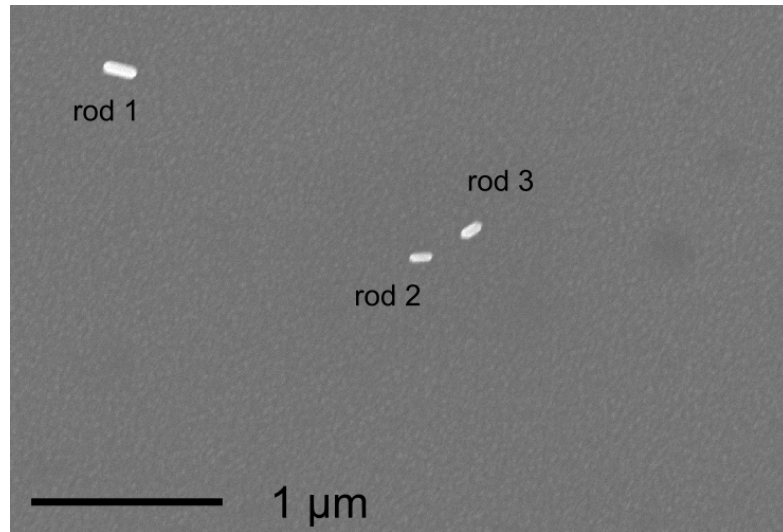
Figure 5.20: The SEM image of the target area where rod 2 and rod 3 are inside the same PSF and a good spot to attempt super-resolution imaging.

To separate and locate each rod, amplitude map at the frequency of the rod was extracted and centroid algorithm was applied to localise the rod as described before section 4.4.2.3. All the amplitude maps at the longitudinal and breathing mode frequencies of rod 1 were extracted for four angles of the detection beam as shown in figure 5.21. As previously, the calculated weighted average of all centroids for the longitudinal mode was chosen as the final point to localise the rod. As the rod was close to horizontal, it was well detected horizontally as can be seen in figure 5.21 (a) and (c). However, as the rod was not exactly horizontal, it was also detected vertically as can be seen from figure 5.21 (b). It was also expected to see the rod in 5.21 (d) but was below the noise level. On the other hand, the rod was close to -45° and this is why the longitudinal mode was very well detected in figure 5.21 (f) for -45° than in figure 5.21 (e) for +45°. Similarly, the breathing mode of the rod was expected to be detected in figure 5.21 (g) but it was missing for being below the noise level. However, the breathing mode was detected in figure 5.21 (h) according to the expectation. The red and green crosses point to the maximum amplitude location and the calculated centroid. According to the four point phase stepping method, the calculated angle of the rod was 22±1.1°. The deviation came from the effect of noise on the phase stepping method where the SNR of rod 1 was used in the estimation (figure 4.18).

Rod 2 and rod 3 were in the same optical PSF. The amplitude maps at the frequencies of the rod 2 were extracted as before for four angles of the detection beam as shown in figure 5.22. As two rods were inside the same PSF and their orientations were different, it was expected to detect a rod always for all the angles of the detection beams as can be seen in the figure. As previously, the calculated weighted average of all centroids for the longitudinal mode was chosen as the final point to localise the rod. The similar maps extracted for rod 3 are shown in figure 5.23 and calculated weighted average of all centroids for the breathing mode was chosen as the final point to localise the rod. The FFT traces at one point inside the PSF of two rods (rod 2 and rod 3) are shown in figure 5.24. It can be seen that when the detection angle was +45°, four frequencies were present that corresponded to rod 2 (longitudinal 8.7 GHz, breathing 68 GHz) and rod 3 (longitudinal 7.6 GHz, breathing 45 GHz). It can be seen from figure 5.20 that rod 2 was almost horizontal and rod 3 was close to +45°. Hence, both rods were detected along +45°. In contrast, when the detection angle was -45°, rod 3 was not detected properly and only frequencies

from rod 2 could be seen. It can also be observed that longitudinal modes of both rods were very close and breathing modes were far apart. All the obtained sizes and angles of the rods are listed in table 5.9. The predicted size, locations and angles of the rods were overlaid with the SEM image as shown in figure 5.25. According to the simulation shown in figure 4.11 (c), The location precisions of rod 1, rod 2 and rod 3 were 3 nm, 4.2 nm and 2 nm respectively depending on the SNRs of the rods. The localisation error (centre-to-centre) from SEM and acoustic reconstruction for rod 1, rod 2 and rod 3 are found as 222±3 nm, 28±3 nm and 92±3 nm respectively. The reasons behind the location and angle deviations are the same as described for the previous examples. Although the results have some limitations, it can be said that the results demonstrate that GNRs can be super-resolved using the vibrational frequencies and orientation differences of nanorods.
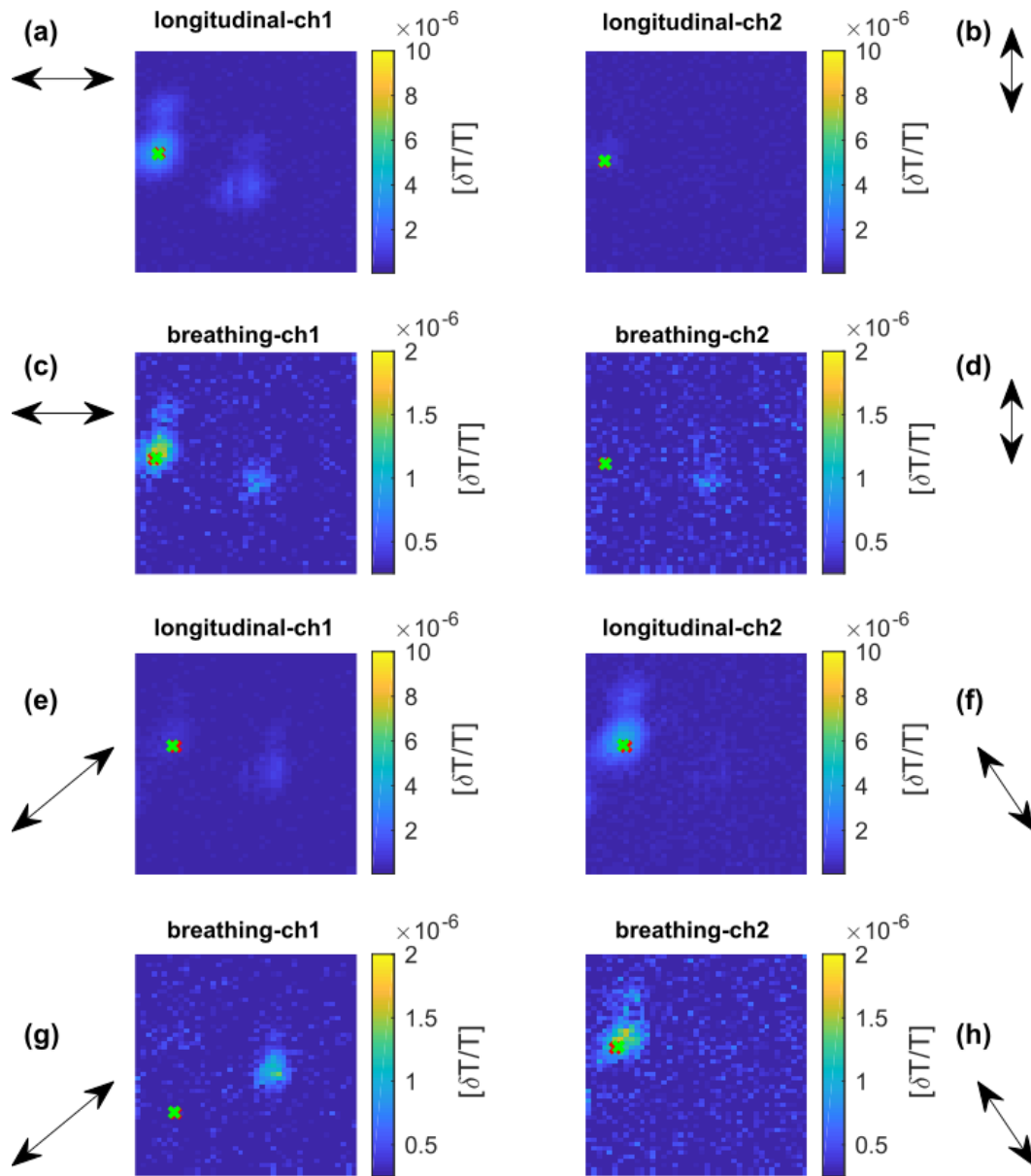
Figure 5.21: Amplitude maps extracted at the longitudinal and breathing modes of rod 1 for four angles of the detection beams to determine the location and angle of the rod. (a)(b) Amplitude maps at the longitudinal mode (4.8 GHz) of rod1 when detected horizontally and vertically, respectively. (c)(d) Amplitude maps at the breathing mode (42.24 GHz) of rod 1 when detected horizontally and vertically, respectively. (e)(f) Amplitude maps at the longitudinal mode of rod 1 when detected along $+45°$ and $-45°$, respectively. (g)(h) Amplitude maps at the breathing mode of rod 1 when detected along $+45°$ and $-45°$, respectively. Red and green crosses point to the maximum amplitude position and the calculated centroid.
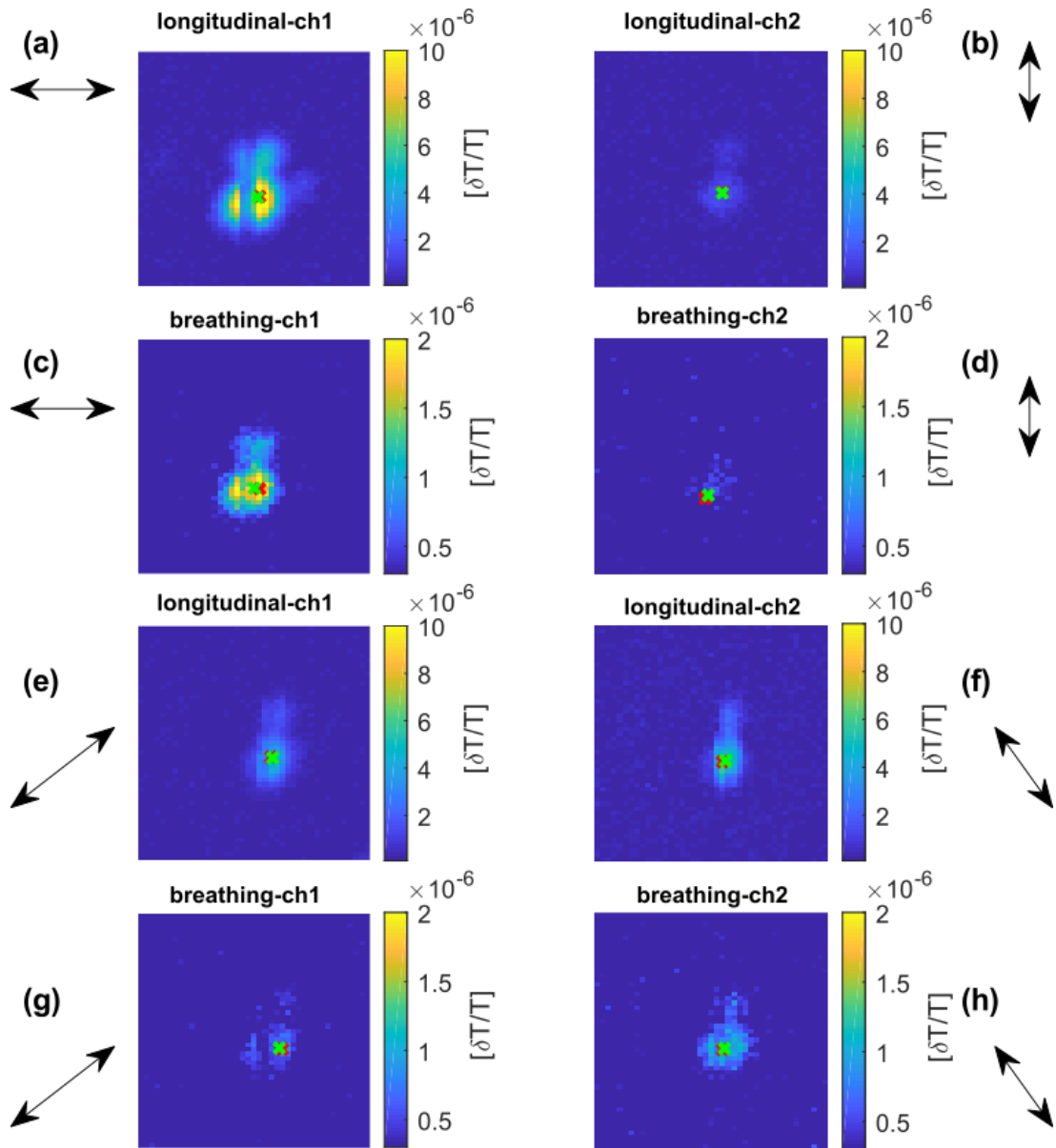
Figure 5.22: Amplitude maps extracted at the longitudinal and breathing modes of rod 2 for four angles of the detection beams to determine the location and angle of the rod. (a)(b) Amplitude maps at the longitudinal mode (8.7 GHz) of rod 2 when detected horizontally and vertically respectively. (c)(d) Amplitude maps at the breathing modes(68 GHz) of rod 2 when detected horizontally and vertically respectively. (e)(f) Amplitude maps at the longitudinal mode of rod 2 when detected along +45° and -45°respectively. (g)(h) Amplitude maps at the breathing mode of rod 2 when detected along +45° and -45° respectively. Red and green crosses point to the maximum amplitude position and the calculated centroid.
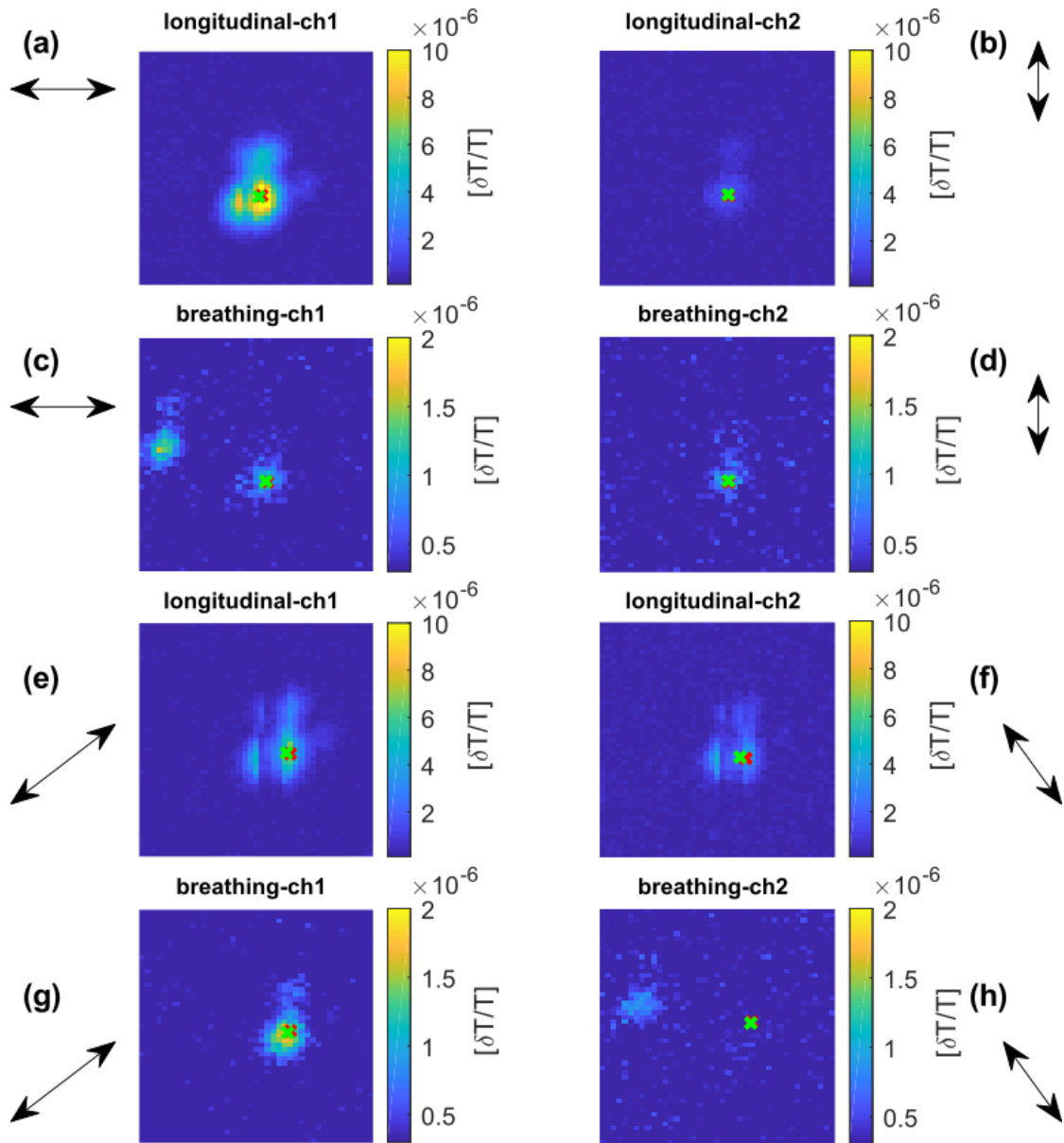
Figure 5.23: Amplitude maps extracted at the longitudinal and breathing modes of rod 3 for four angles of the detection beams to determine the location and angle of the rod. (a)(b) Amplitude maps at the longitudinal mode (7.6 GHz) of rod 3 when detected horizontally and vertically respectively. (c)(d) Amplitude maps at the breathing mode (45 GHz) of rod 3 when detected horizontally and vertically, respectively. (e)(f) Amplitude maps at the longitudinal mode of rod 3 when detected along +45° and -45°, respectively. (g)(h) Amplitude maps at the breathing mode of rod 3 when detected along +45° and -45°, respectively. Red and green crosses point to the maximum amplitude position and the calculated centroid.
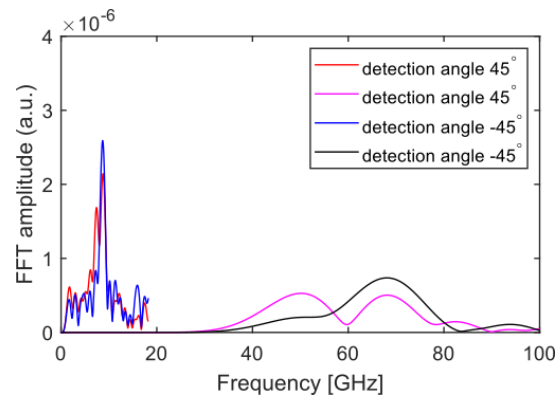
Figure 5.24: The FFT traces from two GNRs inside the same PSF. (a) The FFT traces in one point on the obtained amplitude maps of two rods. It can be seen that when the detection angle was +45°, four frequencies were present that corresponded to rod 2 (longitudinal 8.7 GHz, breathing 68 GHz) and rod 3 (longitudinal 7.6 GHz, breathing 45 GHz). Rod 2 was almost horizontal and rod 3 was close to +45°. Hence, both rods were detected along +45°. In contrast, when the detection angle was -45°, rod 3 was not detected properly and only frequencies from rod 2 could be seen.
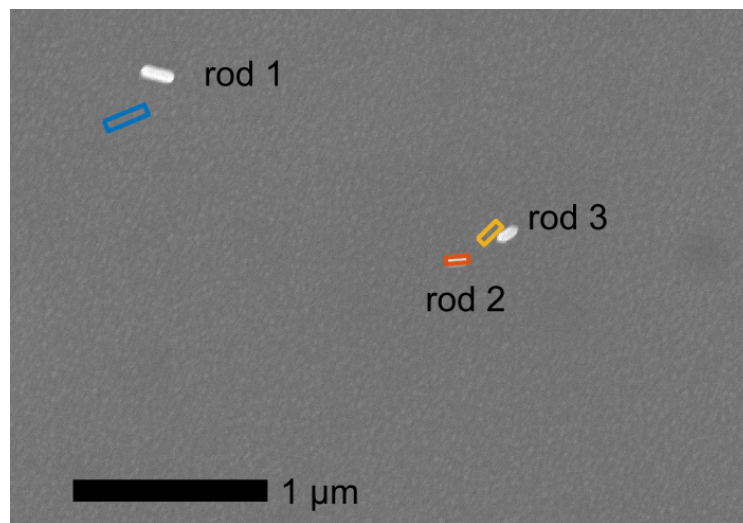
Figure 5.25: Overlay of the SEM image with the predicted sizes, locations and angles of rods.

Table 5.9: Experimental measurements for three rods where two rods are inside the same PSF.

Frequency	E	Measured Size	Size from SEM	Size difference SEM-Measured	Angle (SEM)	Angle (Measured)
GHz	GPa	nm	nm	nm	°	°
Rod 1						
4.8 ± 0.09	31 [100]	132 ± 2.5	173 ± 10	41 ± 10.3	-18.7 ± 5	22±1.1
	42 [100]	153.7 ± 2.9		19.3 ± 10.4		
	64 [110]	189.7 ± 3.6		16.7 ± 10.6		
	79 (poly)	210.7 ± 4		37.7 ± 10.8		
	81 [110]	213.4 ± 4		40.4 ± 10.8		
	115 [111]	254.3 ± 4.9		81.3 ± 1.1		
42.2 ± 1.3	79 (poly)	65.6 ± 1.8	63 ± 10	7.4 ± 10.2		
Rod 2						
8.7 ± 0.2	31 [100]	72.8 ± 1.7	126 ± 10	53.2 ± 10.1	3.2±5	5.5±0.8
	42 [100]	84.8 ± 2		41.2 ± 10.2		
	64 [110]	104.7 ± 2.4		21.3 ± 10.3		
	79 (poly)	116.3 ± 2.7		9.7 ± 10.4		
	81[110]	117.7 ± 2.8		8.3 ± 10.4		
	115 [111]	140.3 ± 3.3		14.3 ± 10.5		
68 ± 1.1	79 (poly)	34.5 ± 0.6	51 ± 10	16.5 ± 10		
Rod 3						
7.6 ± 0.1	31 [100]	83.4 ± 1.1	134 ± 10	50.6 ± 10	39.8±4	44.6±3.6
	42 [100]	97 ± 1.3		37 ± 10		
	64 [110]	119.8 ± 1.6		14.2 ± 10.1		
	79 (poly)	133.1 ± 1.8		0.9 ± 10.2		
	81 [110]	134.8 ± 1.8		0.8 ± 10.2		
	115 [111]	160.6 ± 2.1		26.6 ± 10.2		
45 ± 1.5	79 (poly)	52.1 ± 1.8	60 ± 10	7.9 ± 10.2		

5.5 Summary

Phononic image reconstruction of different gold nanorods were shown in this chapter by combining their sizes, angles and locations. The size characterisation of gold nanorods in air and water media was shown in this chapter at the beginning. It was found that the predicted sizes of gold nanorods were close to the sizes measured from the SEM images. Vibrational frequencies of metal nanoparticles are related with their Young's modulus (E) values. Young's modulus of a gold nanorod varies according to its crystal structure and applied preparation method. Hence, the sizes of gold nanorods were also predicted for different probable E values because the actual values were not available from manufacturers. However, 79 GPa (E value of bulk gold) was used as a reasonable reference in this thesis and size precision values were calculated using that E value. Moreover, it was

shown that a nanorod can be turned 'on' and 'off' by changing the polarisation of the light. The angles of the rods were determined by using their detected amplitudes for different polarisations of the probe light. The angle precision of the technique was also estimated. Finally, the rods were localised and their phonoic images were reconstructed in air and water environments. It was found that the reconstructed images of gold nanorods were close to their SEM images. It was also shown that gold nanorods could be imaged with super-optical resolution when they were inside the same optical point spread function. However, systemic errors affected the accuracy of the measurements.

Chapter 6

Phononic image reconstruction of gold nanorods fabricated by EBL and thermal effect on gold nanorods

6.1 Introduction

This chapter first describes the size characterisation and angle determination of GNRs fabricated by EBL on a glass substrate which is measured in an air medium using the same techniques as described before in chapter 4 and 5 for purchased gold nanorods. The reconstructed phononic images of GNRs are then shown. Although the fabricated GNR patterns were self-designed, reconstruction of their phononic images were helpful to test the reliability of our proposed technique in an easy fashion. It can also be said that phononic image reconstruction of EBL fabricated GNRs by using our proposed technique have added a new value to the characterisation of EBL fabricated GNRs. Also, the work has extended the application of these GNRs such as in phonon-based imaging and sensing.

Thermal effect on gold nanorods is an important matter which needs to be considered while working with them. This effect on EBL fabricated rods was observed during laser scan while using the UV-NIR set-up in this project and the effect is shown and explained

in this chapter. In addition, thermal effect on synthesised gold nanorods are shown when they were scanned using the NIR-NIR set-up. The laser induced heat in a controlled manner can be used to reshape or melt metal nanoparticles for using them in different applications [32, 227–229]. For this research work, it is a problem if the laser induced heat changes the shape or size of gold nanorods and in turn their vibrational frequencies. The reason is that the vibrational frequencies of gold nanorods were used to identify and separate them in this work. Hence, some possible ways to minimise the heat effect on gold nanorods are also mentioned at the last part of this chapter.

6.2 Size characterisation of EBL fabricated gold nanorods

Experiments on EBL fabricated GNRs were done in the air medium. Hence, different sizes of flat ended (free moving) gold nanorods were simulated in an air medium using COMSOL Multiphysics to select the appropriate size of GNR that can be excited and detected optically in the available experimental set-up. Gold nanorods of 200 nm by 80 nm and 150 nm by 70 nm were chosen and fabricated using the recipe shown in the appendix A.1. Nanorods were designed in a 4 by 4 array which covered 18 μm by 18 μm area and there was a gap of 4 μm between the adjacent rods as can be seen from the SEM image shown in figure 6.1. It can be seen that some rods were missing because they did not came out nicely during lift-off. The rods were scanned using path 3 (NIR) and path 4 (UV) as shown before in figure 4.4. The experimental parameters which were applied to scan the sample are mentioned in table 6.1.
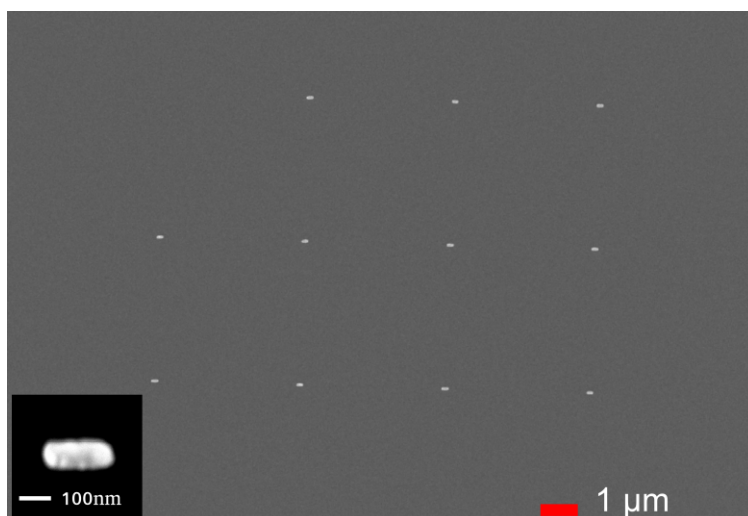
Figure 6.1: The SEM image of an array which consists of 200 nm by 80 nm GNRs in 0°
angle fabricated by electron beam lithography (EBL). The inset shows the zoom in of one
of the rods.

Table 6.1: Experimental parameters used to scan GNRs fabricated by EBL

Pump wavelength nm	Probe wavelength nm	Pump power mW	Probe power mW	delay rate kHz	step size nm
415	780	3.2	2.46	10	500

After the laser scan, the nanostructures could be seen in the dc map as shown in figure
6.2 (a). The obtained longitudinal and breathing mode amplitude maps are shown in figure
6.2 (b) and (c), respectively. The sizes of the rods were measured manually from the SEM
image and the average size was 237 nm by 109 nm which was bigger than the expected size
(200 nm by 80 nm). However, the SEM measurement can be limited by the precision of
the SEM scale bar size and human error. In addition, the actual size of the nanostructure
in EBL depends on the used dose, resist and other related parameters. The longitudinal
and breathing mode frequency maps are shown in figure 6.2 (d) and (e), respectively. It
can be said that the rods were of similar sizes and produced similar frequencies where the
longitudinal modes were nearly at 6.5 GHz and the breathing modes were nearly at 31
GHz.
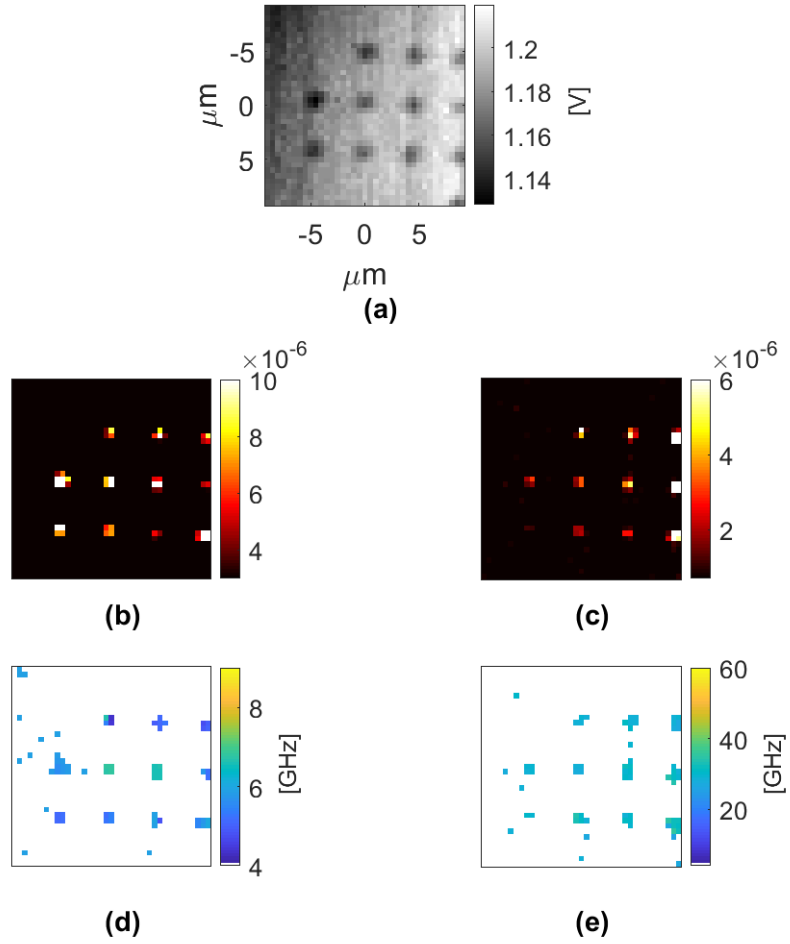
Figure 6.2: Scanned area of a 0° GNR set fabricated by EBL with 200 nm step size. (a) Optical picture. (b)(c) Amplitude maps at the longitudinal (6.5 GHz) and the breathing modes (31 GHz), respectively. (d)(e) Frequency maps showing the longitudinal and breathing modes, respectively.

.

The raw time trace, processed trace for the long time window (blue) and processed trace for the short time window (red) are shown in figure 6.3 (a), (b) and (c) respectively from one of the rods shown in figure 6.2. The obtained longitudinal and breathing modes were at 6.5 GHz and 31 GHz as can be seen in figure 6.3 (d) after performing an FFT of the long and short time window traces, respectively. It was important to compare signals from all rods for further understanding and analysis. The raw time traces, processed traces for long time window, processed traces for short time window, longitudinal modes and breathing modes obtained from all rods are shown in figure 6.4 (a), (b), (c), (d), and (e), respectively. It can be seen that the longitudinal modes slightly differed between

rods. It was found that the maximum frequency deviation of the highest peak was 2.6 GHz. This frequency deviation predicted that the rods differed in length on a small scale. Moreover, the thermal effect on nanorods during the laser scan can contribute to the shift of the longitudinal modes. On the other hand, almost the same breathing modes predicted that the rods had almost the same width. Some additional modes in the low frequency range can also be seen in figure 6.4 (d). Shape diversity of rods can be one of the possible reasons behind the existence of new modes. In addition, induced heat from the laser can change the size or shape of the rod. If the size and shape of a nanorod change due to the thermal effect, both optical and mechanical responses of the rod will change.

The designed size, measured size in SEM and the predicted size of the rod (traces shown in figure 6.3) were 200 nm by 80 nm, 237 nm by 109 nm and 155 nm by 77 nm, respectively as can be seen in figure 6.5. The same simulation as shown in figure 4.20 was done for the parameters of the rod and the length and width precision of the rod were 0.8 nm and 0.3 nm, respectively. In this research, the analytical model developed by Hu et al. [162] was used to convert the frequency of a gold nanorod to size. However, the used model was not a proper solution for nanorods fabricated by EBL. The model was only applicable to cylindrical rods in free space. The rods fabricated by EBL were not cylindrical and one side of the rods was bonded to the substrate which changed the boundary conditions and made them more complex for analysis. This bonding restricted the motion of the particle. As a result, different shapes and orders of modes might have been generated. Also, there could be a damping effect on the vibrational modes from the environment and the substrate which changed the boundary conditions and the vibrational frequencies as well. In addition, the shape of the rods was rectangular rather than round. Hence, there was a lack of symmetry in height and width which was also a reason behind the generation of extra modes. However, the detection of those modes was dependent on how strong they were and whether they were inside the measurement bandwidth of our system or not. Further investigation is needed to understand the full optical and mechanical properties of gold nanorods fabricated by EBL through advanced-level modelling and experimental works.
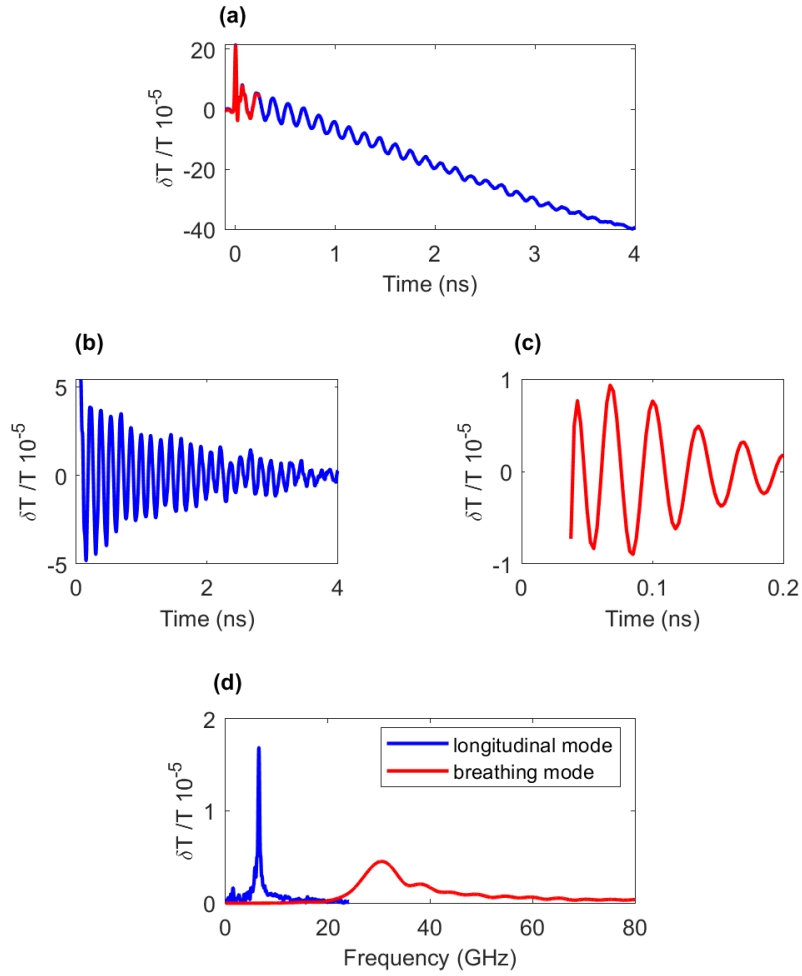
Figure 6.3: Experimental traces of a 200 nm by 80 nm EBL GNR in an air medium. (a) The raw time trace of a 200 nm by 80 nm GNR in an air medium. (c) The processed trace for 4 ns (left), a zoom-in of the trace for 200 ps (right). (d) The longitudinal (low frequency) mode is at 6.5 GHz and the breathing mode (high frequency) is at 30.8 GHz after performing an FFT of the processed traces for long and short time periods respectively.
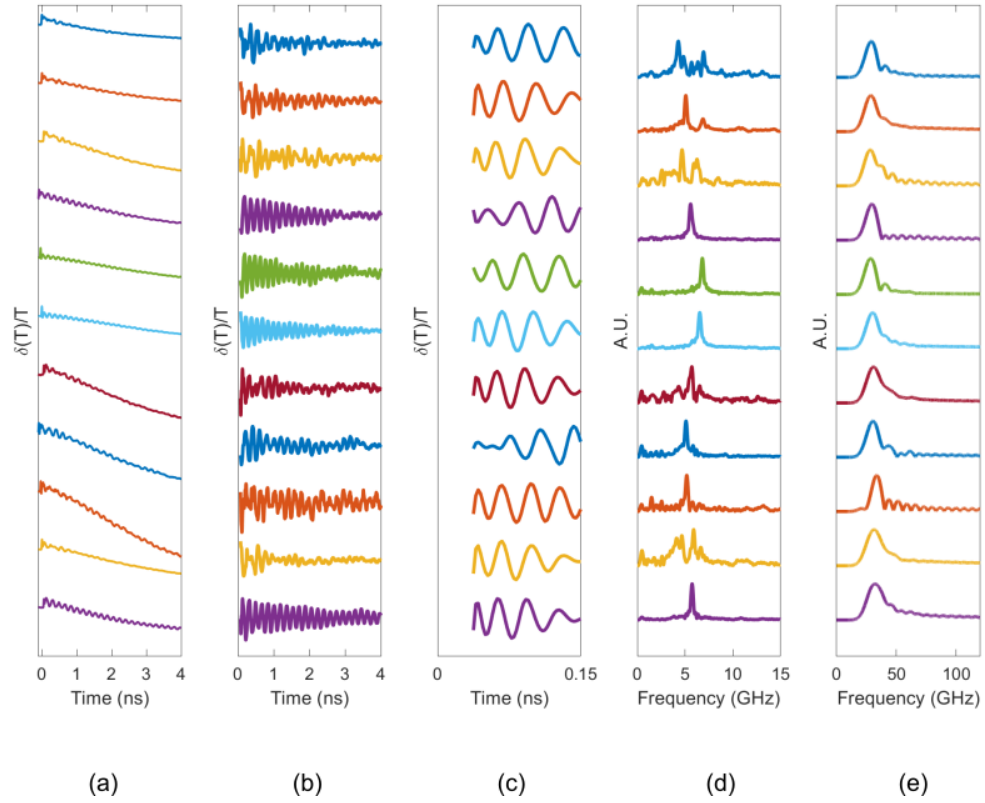
Figure 6.4: Experimental traces from eleven 200 nm by 80 nm GNRs fabricated by EBL. (a) Raw traces. (b) Processed traces for 4 ns. (c) Processed traces for 0.15 ns. (d) FFT traces that show the longitudinal modes. It can be seen that the longitudinal modes differed between rods. It was found that the maximum frequency deviation of the highest peak was 2.6 GHz. Also, some new modes were seen. The reasons behind the shift in the longitudinal modes can be the size or shape diversity between the rods and the laser induced heat effect on them. (e) FFT traces that show the breathing modes. It can be seen that breathing modes were the same for all rods.
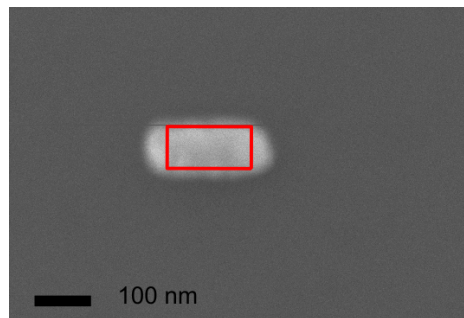
Figure 6.5: An approximate characterisation of the size of a gold nanorod fabricated by EBL. The reason behind the difference between the predicted size and the measured size in SEM is that the used model did not consider the effect of bonding to the substrate and other complex situations of nanorods fabricated by EBL. The designed size, size in SEM and predicted size of the rod were 200 nm by 80 nm, 237 nm by 109 nm and 155 nm by 77 nm, respectively.

6.3 Polarisation sensitivity and angle determination of EBL fabricated gold nanorods

It was also of great interest to test the sensitivity of a GNR fabricated by EBL to the polarisation of light. One of the rods shown in figure 6.1 was detected along the length and along the width to test the 'turn-on' and 'turn-off' mechanism, respectively. The half-wave plate before the PBS (shown previously in figure 4.5 (a)) was rotated to change the angle of detection.
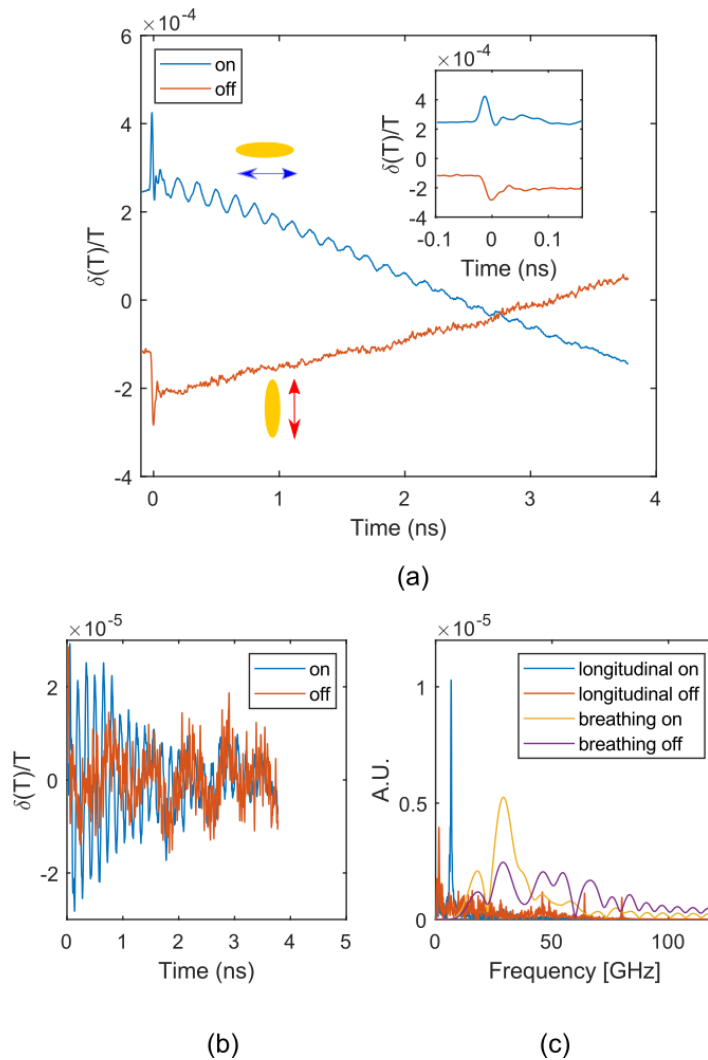
Figure 6.6: Sensitivity of a 0° 200 nm by 80 nm GNR fabricated by EBL to the polarisation of light in an air medium. (a) Raw traces (b) Processed traces and (c) FFT traces. It can be seen that the 0° rod was 'on' when it was detected along the length but was 'off' when it was detected along the width.

It can be seen from the raw traces shown in figure 6.6 (a) that the rod was 'on' when it was detected along the length but was 'off' when it was detected along the width. The inset shows a zoom-in of the raw traces to show the high frequency (breathing mode) clearly. The corresponding processed traces and FFT traces are shown in figure 6.6 (b) and (c), respectively. So, it can be said that a rod fabricated by EBL can also be turned on and off by changing the polarisation of light. The previously described phase stepping method was used to measure the angle of the rod. The obtained FFT amplitudes of the longitudinal mode from the rod at 0°, 45°, 90° and 135° were given as inputs to equation 4.4 and the calculated angle of the rod was -12.6±1.4° where the angle deviation came from the effect of noise on the phase stepping method (figure 4.18). Not fully circular light, non-sinusoidal response of the rod, thermal effect, minor mismatch between the orientation of the sample on the SEM stage and the experimental stage, and minor calibration fault in the rotary parts of the set-up affected the angle accuracy, as described before in chapter 5.

The 'turn-on' and 'turn-off' test was also carried out on a 90 degree 150 nm by 70 nm GNR and the obtained traces are shown in figure 6.7 for two orthogonal channels. The experimental set-up was shown in figure 4.4 and figure 4.6 before. UV-NIR configuration was used for this experiment where path 3 (NIR) and path 4 (UV) were used as was shown in figure 4.4 before. It is clear that the rod was 'off' in ch1 (transmitted channel, blue curve) and 'on' in ch2 (orthogonal to ch1, orange curve) when the detection angle was 0° before the PBS. In contrast, the rod was 'on' in ch1 (yellow curve) and 'off' in ch2 (violet curve) when the detection angle was 90° before the PBS. The obtained longitudinal mode was 9.6 GHz which was higher than 6.5 GHz obtained from 200 nm by 80 nm rod. It is true that the rod is not competently 'off' when the polarisation of the light is along the width. The reason can be that the rod is not exactly at 90°. However, no high frequency modes were observed during the trial. The previously described phase stepping method was used to measure the angle of the rod also. The obtained FFT amplitudes of the longitudinal mode at 0°, 45°, 90° and 135° were given as inputs to equation 4.4 and the calculated angle of the rod was 78.8±2.2° where the angle deviation came from the effect of noise on the phase stepping method (figure 4.18). The reasons that could affect the angle accuracy are the same as mentioned before. It can also be observed from figure 6.7 (c) that the

obtained longitudinal modes shifted during the experiments. The frequency shift of the longitudinal modes of the same rod implies that the rod was getting hot during the laser scan. The frequency shift was about 0.8 GHz for the 'on' case. The heat effect on the rod could also be a reason that the breathing mode was not detected because the rod was modified. To further investigate the thermal effect on the rod, the sample was checked under the SEM machine again and it is obvious from the SEM image that the rod was modified by the laser induced heat as shown at the end of the chapter (figure 6.9).
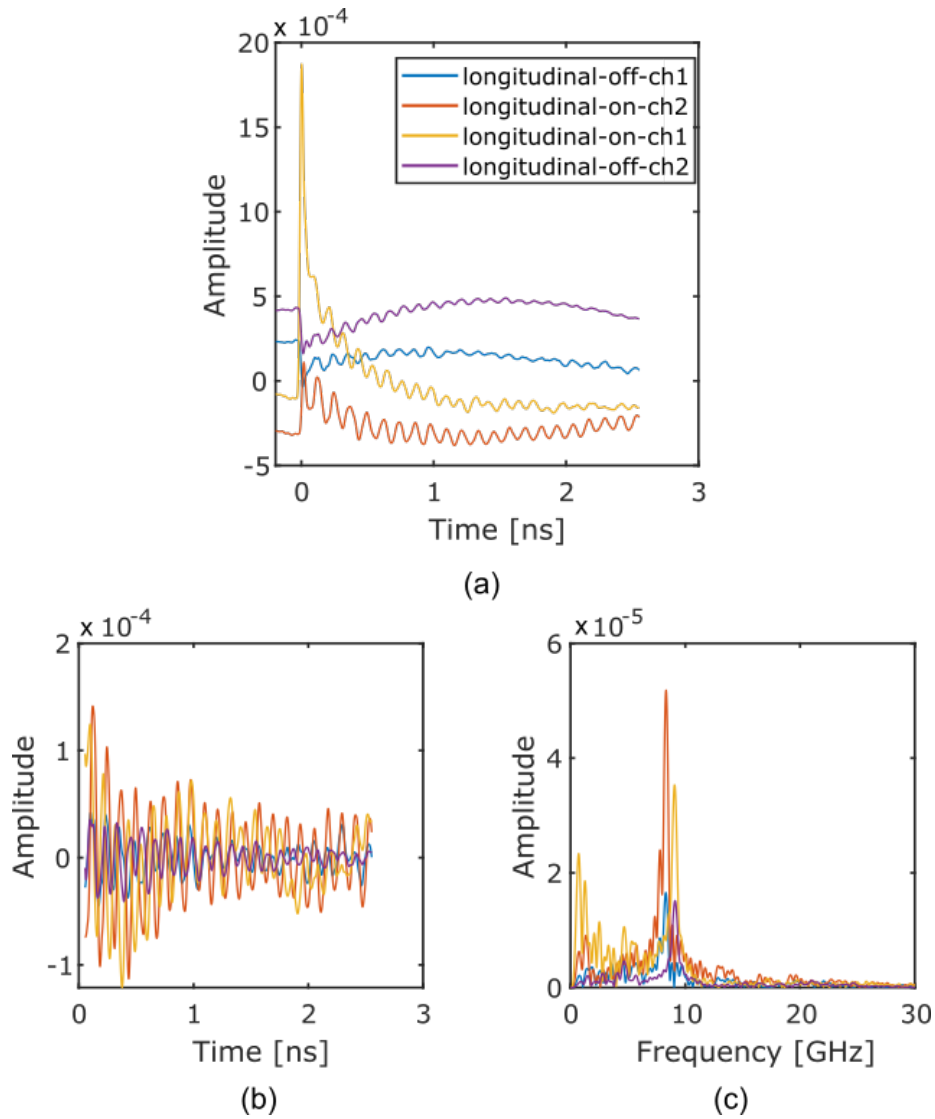
Figure 6.7: Sensitivity of a 90° 150 nm by 70 nm GNR fabricated by EBL to the polarisation of light in an air medium. (a) Raw traces (b) Processed traces and (c) FFT traces. It is clear that the rod was 'off' in ch1 (transmitted channel, blue curve) and 'on' in ch2 (orthogonal to ch1, orange curve) when the detection angle was 0° before the PBS. In contrast, the rod was 'on' in ch1 (yellow curve) and 'off' in ch2 (violet curve) when the detection angle was 90° before the PBS.

6.4 Reconstruction of the phononic image of an EBL fabricated gold nanorod array

The phononic image of the GNR set shown in figure 6.1 was reconstructed by combining the size, angle and location information of all rods as was shown for purchased GNRs in chapter 5 before. Unfortunately, the laser scanned data for the whole target area was available only for $0°$ and $90°$ angles of detection. Hence, those two data sets were used to predict the size and location of all rods. It is good to mention that for this case only the calculated centroid with high SNR ($0°$, longitudinal mode) was chosen as the location of rods instead of the weighted average of all centroids from four angles of detection. Manual masking was also used to remove undesired rods so that the desired rod could be found because the rods had almost the same frequencies and were at the same angle. The angle of one of the rods from the target area (figure 6.1) was calculated in section 6.3 and it was $-12.6\pm1.4°$. As all rods were of the same angle in the target area, that calculated angle was used for all rods in the reconstruction. The reconstructed phononic image of the target GNR set is shown in figure 6.8 where the angle of the rods was kept at $-12.6°$. It can be seen that the reconstructed phononic image was quite close to the SEM image. The same simulation as shown in figure 4.11 (c) was carried out for the parameters of the rods and average location precision of 35 nm was found. It is good to mention that the target area was very large and the laser scan was carried out with a 500 nm step size. So, the scan was carried out with a coarse step size, not with a fine step size. This can be one of the reasons of behind the big location error. In addition, low SNR of some rods and not fully circular light could contribute to the location error. The reasons that could affect the size and angle accuracy, were discussed before in this chapter.
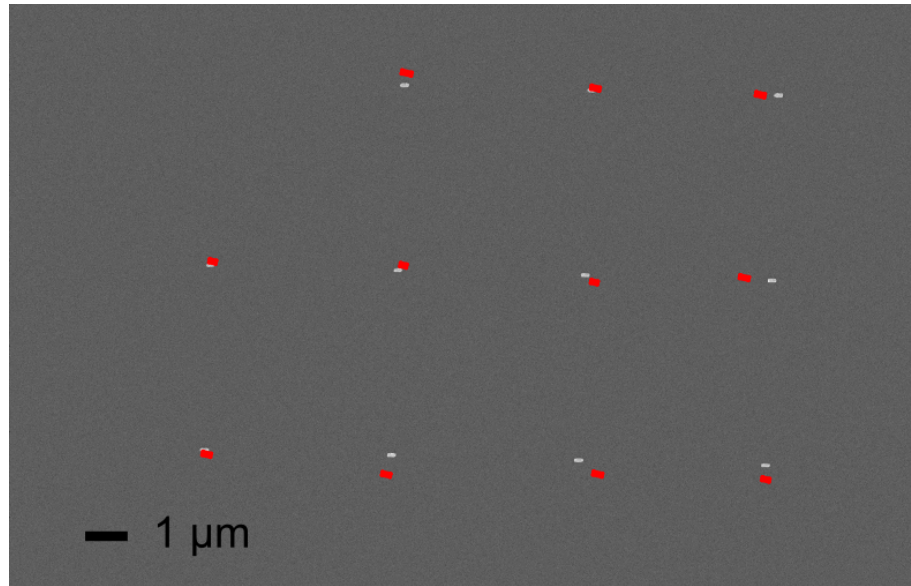
Figure 6.8: Reconstructed phononic image of a GNR set after combining the measured sizes, angles and locations of all rods.

To answer some questions regarding the shifting of the longitudinal frequencies, error in the determined angle and error in the predicted location of rods, the scanned area shown in figure 6.1 was looked again under a scanning electron microscope. The SEM image of a rod before and after the laser scan are shown in figure 6.9 (a) and figure 6.9 (b), respectively. It can be seen that the rod was damaged during the laser scan. However, it is hard to say at which point the rod was damaged because the rod was scanned many times. After observing the thermal effect on GNRs, low power was applied on GNRs during other experiments. In addition, change in the frequency of a nanorod with time and power was monitored during experiments. Thermal effect on purchased GNRs using the NIR-NIR set-up is discussed in the next section.
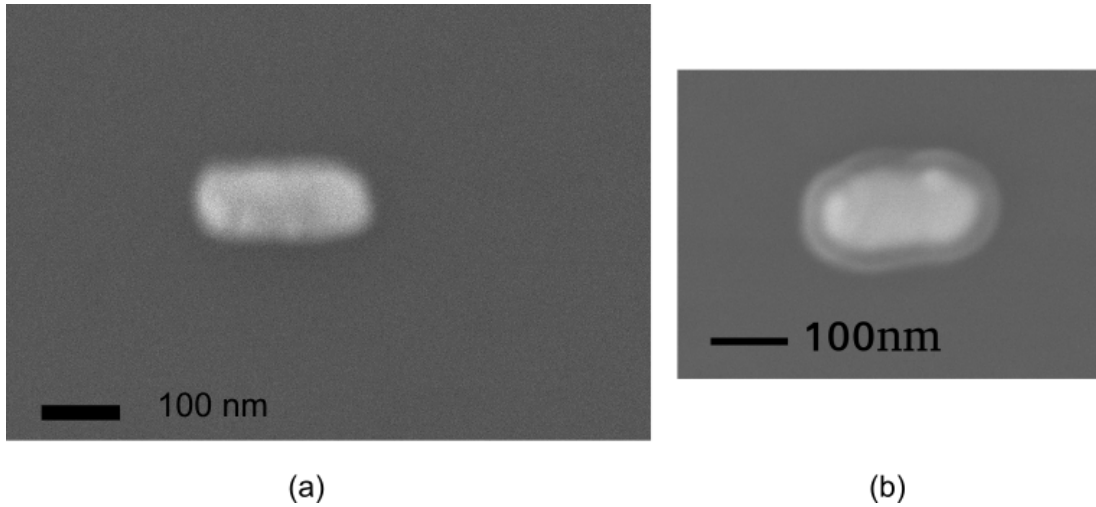
Figure 6.9: The SEM image of a GNR before and after the laser scan. (a) Before the laser scan. (b) After the laser scan. It can be seen that the rods were affected during the scan and melted.

6.5 Thermal effect on gold nanorods using NIR-NIR set-up

In the previous section, observed thermal effect on GNRs fabricated by EBL scanned with the UV-NIR setup was shown. In this project, thermal effect was also observed on synthesised GNRs while using the NIR-NIR setup. As GNRs have higher absorption and scattering cross-sections at NIR than UV, the possibility to damage GNRs by laser induced heat is higher at NIR than UV.

Analysis of such an experiment done with NIR-NIR setup is carried out in this section. Gold nanorods with an average length of 148 nm and an average width of 40 nm (batch A12-40-850, purchased from Nanopartz) were scanned in an air medium using the NIR-NIR (generation-detection) set-up with linearly polarised light. The target of the experiment was to demonstrate the polarisation sensitivity of gold nanorod by changing the polarisation of the generation (pump) light while keeping the polarisation of the detection light fixed. The motivation was to use the peak absorption wavelength for the pump and keep the probe wavelength sensitive enough for the nanorod detection. The experiment was done using the configuration shown in section 4.3 (figure 4.4) where path 1 (probe at 780 nm) and path 3 (pump at 740 nm) were used. The experiment was focused on the detection of the longitudinal mode only.

Some challenges were faced to do this experiment, for example, ensuring the desired

polarisation of the linear light on the sample, ensuring the same power on the sample when the polarisation of the pump beam was changed, and ensuring the same power in the detector when the polarisation of the probe beam was changed. The detail about the accomplished calibrations for the experiment is provided in appendix A.2.
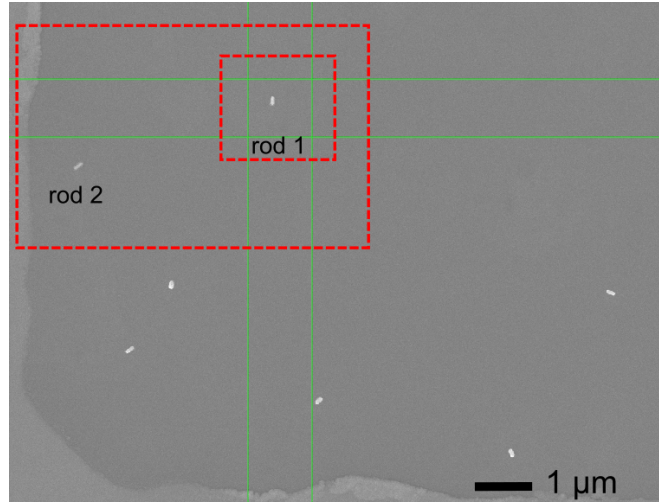
Figure 6.10: SEM image of the used sample made with 148 nm by 40 nm GNRs. The target rod is rod 1 (inside the small red box) which was used to demonstrate the polarisation sensitivity of a nanorod using the generation light. It can be seen that the rod was almost vertical.

The sample was made by drop-casting 40 μL 1:8 mixture of GNR solution (148 nm by 40 nm, purchased from Nanopartz, A12-40-850) and DI water on an 18 mm by 18 mm gridded glass cover-slip which had 50 nm ITO on it. The target GNR (rod 1, inside the small red colour box) for the experiment can be seen from the SEM image shown in figure 6.10. It can be seen that the rod was nearly vertical and it was ensured that the mismatch between the orientation of the sample on the SEM stage and the experiment stage was low during the experiment. To demonstrate the polarisation or orientation sensitivity of a nanorod using the generation beam, the plan of the experiment was to keep the detection (probe) beam vertically polarised (turn-on) but change the polarisation of the pump beam from vertical ('turn on') to horizontal ('turn off').
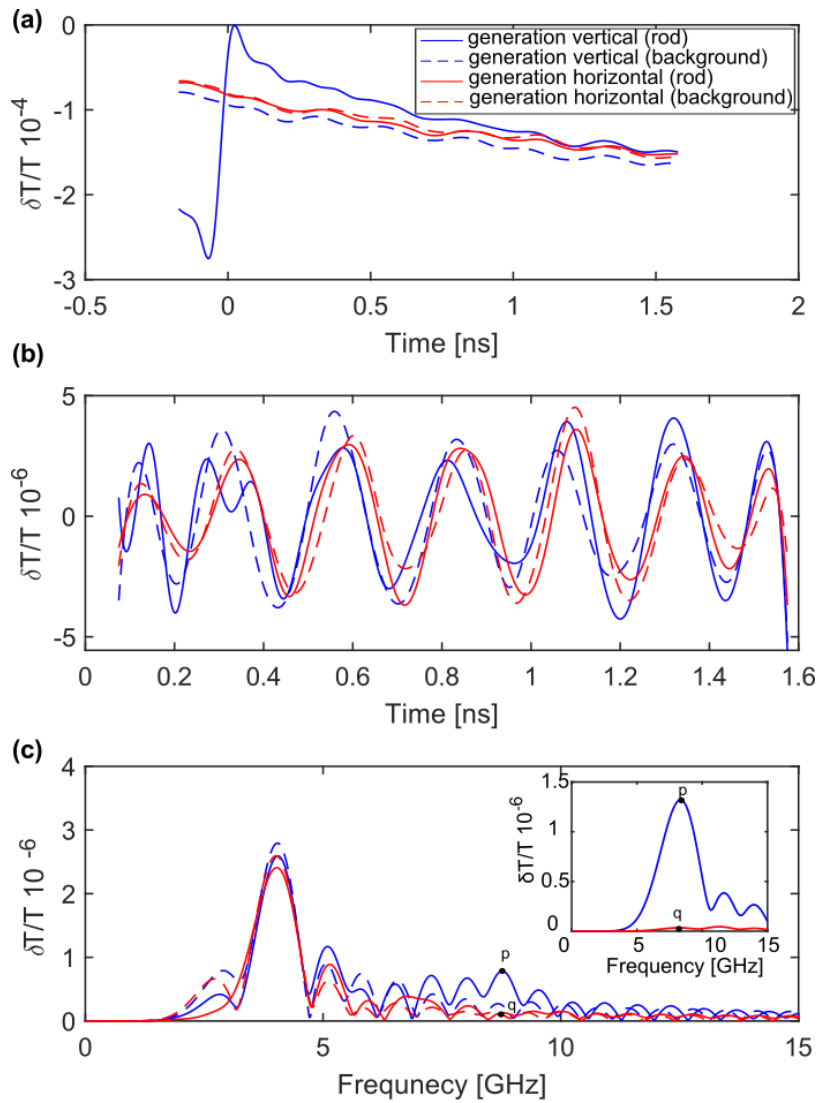
Figure 6.11: The experimental traces (attempt 1) from rod 1 (line) and the background of rod 1 (dash) in an air medium. (a) Raw time traces from rod 1 (line) and the background of rod 1 (dash). (b) Corresponding processed traces after removing the thermal background and undesired high frequency components. (c) Corresponding FFT traces after performing an FFT on the processed traces. Longitudinal mode of the rod can be seen at 8.7 GHz (blue line, point p). It can also be observed that rod 1 turned off when the polarisation of the generation beam was switched from vertical (blue line, point p) to horizontal (red line, point q).
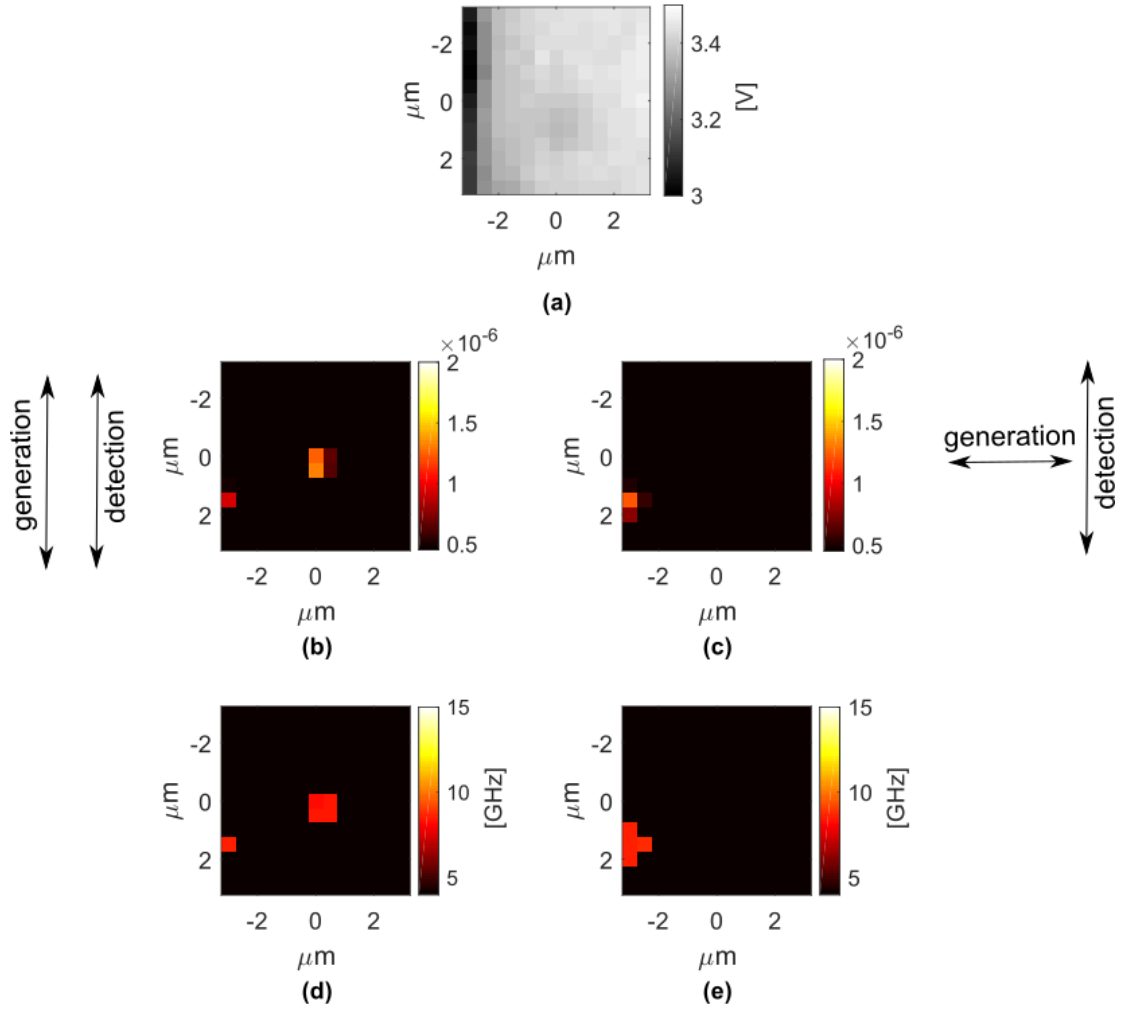
Figure 6.12: Scanned area with gold nanorods (148 nm by 40 nm) in an air medium with 500 nm step size. (a) Optical image. (b) (c) Amplitude maps at the longitudinal mode when the generation beam is polarised vertically and horizontally, respectively. (d)(e) Frequency maps showing the longitudinal mode (rod 1 at 8.3 GHz, rod 2 at 8.5 GHz) when the generation beam was polarised vertically and horizontally, respectively. It can be seen that the almost vertical rod 1 turned off when the polarisation of the pump beam (generation) was switched from vertical to horizontal. As rod 2 was close to 45°, it was 'on' for both vertically and horizontally polarised pump beams.

The area covering rod 1 and rod 2 was scanned in an air medium where rod 1 was the main target and the scan was considered as attempt 1. According to the calibration, the polarisation of the pump beam was switched from vertical to horizontal on the rod while the polarisation of the probe beam was vertical always. The obtained raw time traces, processed traces and FFT traces are shown in figure 6.11 (a), (b) and (c), respectively for rod 1 (line) and the background of the rod 1 (dash). The desired signal from the rod was

seen to stay for a comparatively shorter time than usual and a 4 GHz noise signal was seen to be present. To justify the fact, the background signals are also plotted. It can be seen clearly from figure 6.11 (c) that a 4 GHz noise was always present.

On the other hand, when the pump beam was vertically polarised, an extra peak at 8.7 GHz (blue line, point p) was seen in figure 6.11 (c) from the rod signal but it was absent when the pump beam was horizontal (red line, point q). The inset shows the zoom version so that 'on' and 'off' of the rod at 8.7 GHz can be seen properly. This was the expected longitudinal frequency from the rod. The noise at 4 GHz was often seen to be present in our system that sometimes went off automatically or after changing the wirings, alignments etc. Hence, for this case, data was processed for a short time length and the processed data could identify the locations of both rods as can be seen in figure 6.12.

The optical image of the nanorods can be seen in figure 6.12 (a). It can be seen from the amplitude and frequency maps shown in figure 6.12 (b) and 6.12 (d), respectively that the rod 1 was 'on' when the generation beam was vertically polarised. In contrast, the rod 1 was off when the generation beam was horizontally polarised as can be seen from the amplitude and frequency maps shown in figure 6.12 (c) and (e), respectively. The measured angle of rod 2 was 39° as can be seen form the SEM image shown in figure 6.10. As the angle of rod 2 was close to 45°, it was 'on' for both vertically and horizontally polarised pump beams.

The same experiment was repeated for examining the reliability where an area covering only target rod 1 was scanned. The sample was scanned by moving the electromechanical stage holding the sample with a step motion of 400 nm. The optical image of rod 1 can be seen in figure 6.13 (a). The observation was the same as explained before. Rod 1 was 'on' when the the pump beam was vertically polarised as can be seen from the amplitude and frequency maps shown in figure 6.13 (b) and (d), respectively. In contrast, rod 1 was 'off' when the pump beam was horizontally polarised as can be seen from the amplitude and frequency maps shown in figure 6.13 (c) and (e), respectively. The raw traces, processed traces and FFT traces obtained for rod 1 are shown in figure 6.14 (a) (b) and (c), respectively for both vertically (blue curve) and horizontally (red beam) polarised pump beams. It can be seen clearly from the traces that rod 1 turned off when the polarisation of the generation beam was switched from vertical to horizontal.
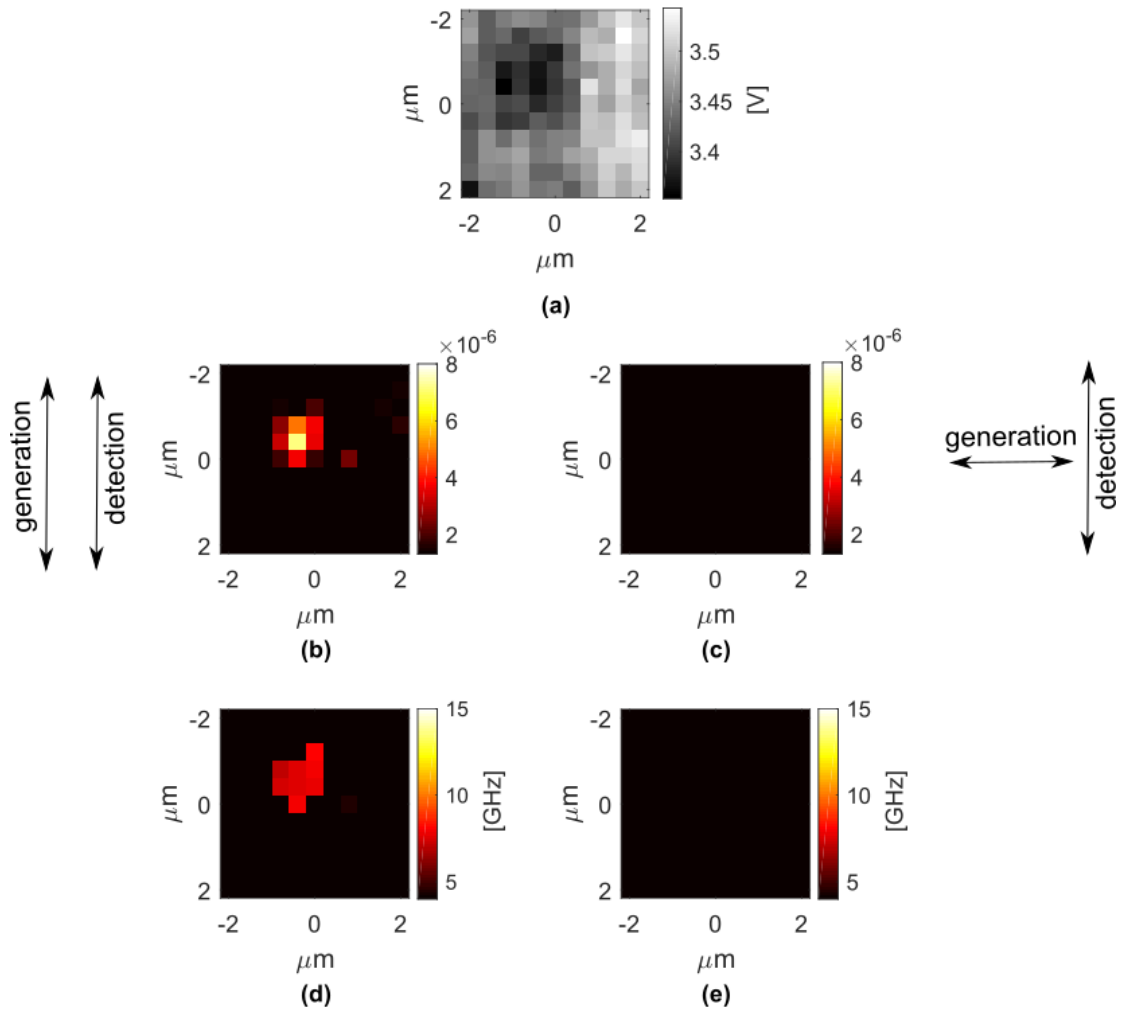
Figure 6.13: Scanned area with gold nanorods (148 nm by 40 nm) in air medium with 400 nm step size. (a) Optical image. (b) (c) Amplitude maps at the longitudinal mode when the generation beam is polarised vertically and horizontally, respectively. (d)(e) Frequency maps showing the longitudinal mode (7.4 GHz) when the generation beam was polarised vertically and horizontally, respectively. It can be seen that the almost vertical rod 1 turned off when the polarisation of the generation beam was switched from vertical to horizontal.
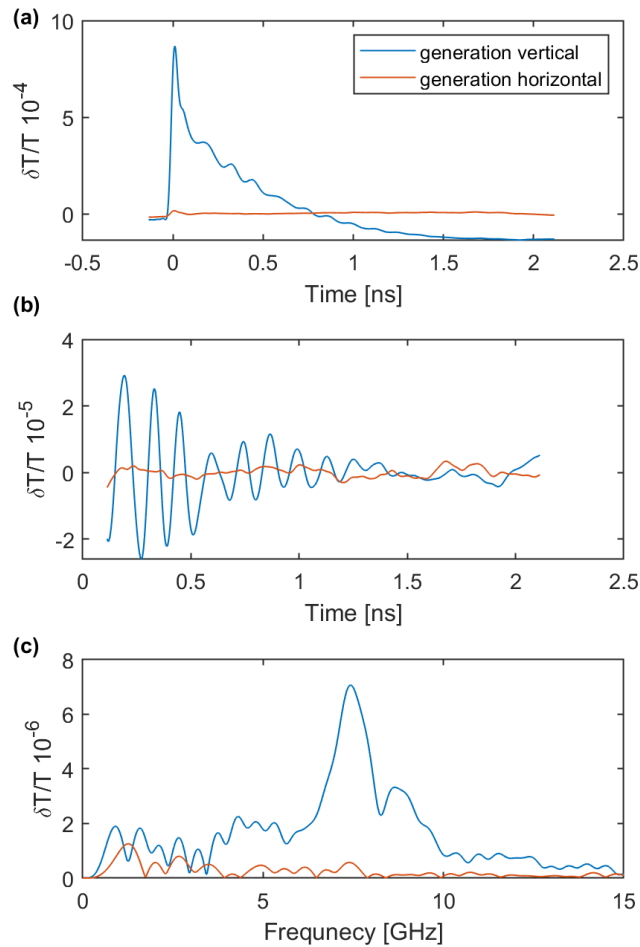
Figure 6.14: The experimental traces (attempt 2) of a 148 nm by 40 nm GNR (rod 1 from the SEM image) in an air medium. (a) Raw time traces. (b) Corresponding processed traces after removing the thermal background and undesired high frequency components. (c) Corresponding FFT traces after performing an FFT on the processed traces. The longitudinal mode of the rod was at 7.4 GHz (blue line).

Next plan of the experiment was to scan the rod by changing the polarisation of the pump beam in a reasonable step size so that the polarisation sensitivity and angle of the rod can be understood more clearly. An area covering rod 1 and rod 2 (as shown in figure 6.10) was scanned again for the pump beam angles of 0°, 22.5°, 45°, 67.5° and 90° as can be seen in figure 6.15 where the probe beam was vertically polarised all the time. The sample was scanned by moving the electromechanical stage holding the sample with a step motion of 200 nm.
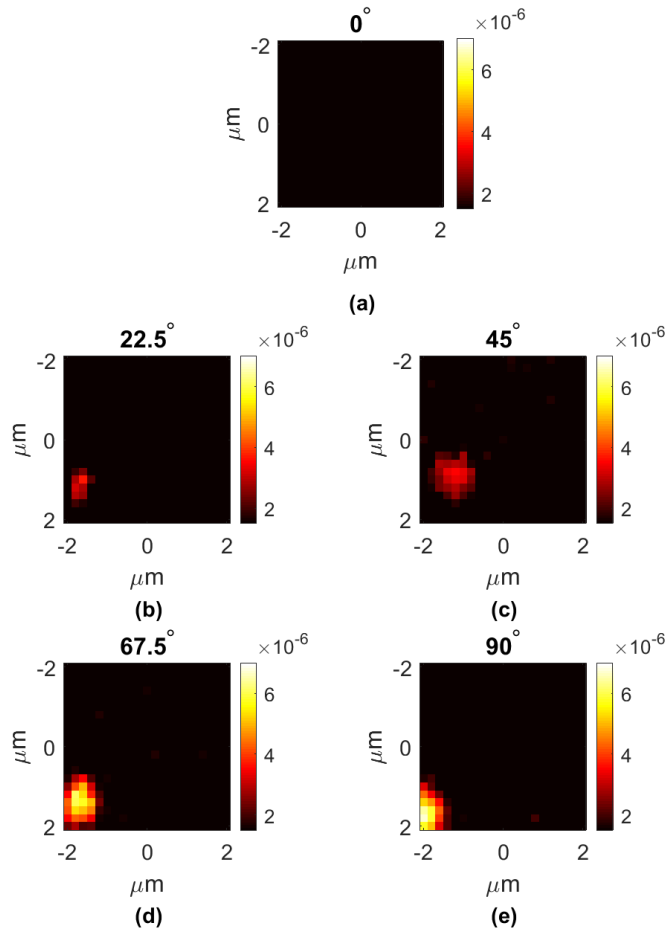
Figure 6.15: Scanned area with gold nanorods (148 nm by 40 nm) in an air medium with 400 nm step size. (a)(b)(c)(d)(e) Amplitude maps at the longitudinal mode for pump beam angles of 0°, 22.5°, 45°, 67.5° and 90°, respectively. It can be seen that rod 1 was not visible at all unexpectedly and rod 2 was visible for all angles as expected except at 0° unexpectedly.

It can be seen in figure 6.15 (a) that rod 2 was visible for all given pump beam angles except at 0° but it was visible at 0° in the previous trial as can be seen from figure 6.12 (b). The experiment seemed to be variable with time. The measured angle of rod 2 from the SEM image was 39° and it was expected to observe the rod for all pump beam angles. The visibility of the rod is also a function of SNR. If the rod is minimally detected for any angle and the detected signal level is lower than the noise level, the rod will not be visible. The obtained data suggested that the angle of rod 2 would be between 67.5° and 90° which was very far from what was measured from the SEM image. The error between the orientation of the sample on the SEM stage and the experiment stage was very low (2°). On the other hand, the input power was adjusted according to the calibration (Appendix

A.3) to compensate for the power variation on the sample when the polarisation of the pump beam was changed. As the power adjustment was done manually, any error in the pump power adjustment could cause a difference in the generation and resulted intensity difference which could be a probable reason for the angle error.
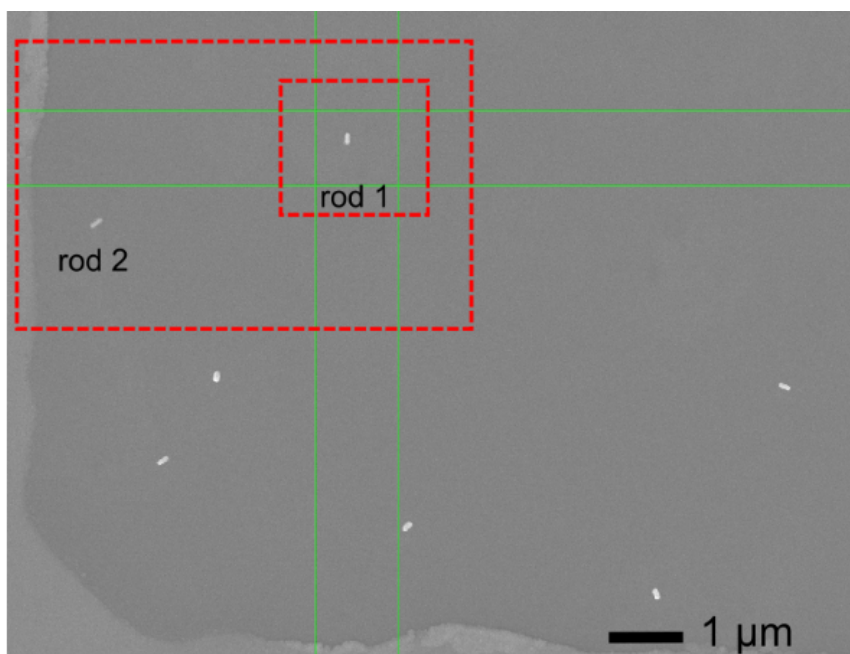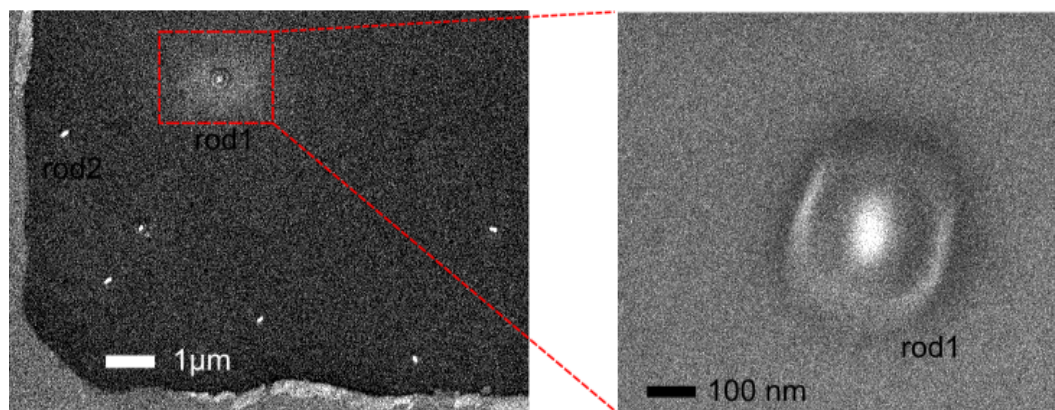
Figure 6.16: SEM image of rod 1 (synthesised GNR) before and after the laser scan using the NIR-NIR setup. (a) Before laser scan. (b) After laser scan.

The target rod 1 was not visible at all for any pump beam angle as can be seen in figure 6.15. As the rod was almost vertical, it was expected to be visible atleast from 45° to 90°. It is good to remind that rod 1 was visible in the previous trials as can be seen in

figure 6.12 (b) and figure 6.13 (b) when the pump beam was at 90°.

Anomaly was seen to continue the experiment and further investigation was done. The SEM was repeated on the sample to observe the condition. The SEM image of rod 1 before and after the laser scan are shown in figure 6.16 (a) and figure 6.16 (b), respectively. It can be seen from figure 6.16 (b) that rod 1 was damaged which was the reason that rod 1 was not visible in the scan. It can be said that rod 1 lost the desired optical property for generation. It can also be seen that rod 2 was not damaged like rod 1 but it is hard to say about any partial damage that can change the property of the nano-structure. If a nanorod is partially damaged then it may lose the proper orientation sensitivity. Hence, rod 2 was seen in the first trial when the pump beam was at 0° but not seen in the next trial when the pump beam was at 0°.

However, the experiment using the NIR-NIR (generation-detection) set-up was successful because it could be demonstrated that a nanorod can be 'turned on' and 'turned off' by changing the polarisation of the pump beam. As thermal effect on nanorod was observed using the NIR-NIR set-up, it was decided to continue future experiments with UV-NIR (generation-detection) set-up with low power.

More rigorous analysis of thermal effects on GNRs can be done by estimating the temperature of the rod as Peter Zijlstra and co-workers calculated in [165]. In addition, modelling can be done using COMSOL Multiphysics to estimate the temperature of a GNR bonded to different types of substrates. There are many ways to minimise the thermal effect on GNR during experiments. Some possible ways are listed in the following section.

6.6 Possible ways to minimise the thermal effect on gold nanorods

There are some possible ways to minimise the thermal effect on GNR as follows

1. Use of low pump laser power to excite the gold nanorod. A wavelength where the gold nanorod absorption cross-section is comparatively low but good enough for the excitation can be chosen.

2. If the probe wavelength is far away from the pump wavelength, it should not be

absorbed by the nanorod. However, it is good to keep the probe laser power low but sufficient for the detection. The wavelength where the nanorod detection sensitivity is high, can be chosen as the probe wavelength to reduce the required probe power.

3. Use of water as the external medium if applicable.

4. Use of a pulse picker to reduce the repetition rate of the laser so that the long term heating can be minimised.

5. Use of a material that has high thermal conductivity (such as diamond) as the substrate of gold nanorods to dissipate the heat. However, this option can only work when gold nanorods are hardly bonded to the substrate, for example, gold nanorods fabricated by electron beam lithography (EBL).

6. Use of small size gold nanorods if applicable because they have low absorption cross-sections and become less hot than the bigger ones.

6.7   Summary

The phononic image reconstruction of a gold nanorod array fabricated by EBL was discussed through characterising the size, angle and location of individual rods. Although the nanorod array was self designed, reconstructing the image using our technique was important to understand its reliability. It can be observed that an EBL fabricated rod can act a plasmonic switch with high quality factor. Moreover, the characterisation of EBL fabricated rods by our technique showed a way to use picosecond laser ultrasonics for characterising metal nanoparticles fabricated by lithographic processes. However, the exact shape of the rod and the effect of bonding to the substrate were not considered in the characterisation which needs further investigations. Furthermore, successful image reconstruction of the rods shown in this thesis extended their applications in phonon-based imaging and sensing.

Thermal effect of GNRs is a matter of concern when exciting them with a laser. Unfortunately, the heat effect on some EBL fabricated GNRs was observed during the experiments while scanning them using UV-NIR set-up. Also, thermal effect on some synthesised GNRs was observed while scanning them with NIR-NIR set-up. Absorption cross section

of a GNR is higher at NIR than UV and hence the damage is higher also. The damage effect on rods was confirmed by observing the change in the frequencies of the rods, absence of the signal from the desired rod and the SEM images of the rods taken after the laser scan. Further experiments were continued with low powers in this project. However, it needs more work to quantify the power which would be safe for a GNR under UV and NIR. There are other ways to minimise the thermal effect on gold nanorods, for example, use of pump/probe wavelengths where the nanorod is highly sensitive, use of water as an external medium to have the benefit of cooling, use of a pulse picker to reduce the repetition rate of the laser, use of thermally conductive materials for the substrate, and use of small gold nanorods, among others. In this thesis, low pump/probe power, sensitive pump/probe wavelengths and water as the external medium were used to minimise the thermal effect on gold nanorods.

Chapter 7

Conclusions and Future work

7.1 Introduction

Metal nanoparticles are of special interest due to their localised surface plasmon resonances [68, 69] usable in different applications such as sensing [1–4], photothermal therapy [5–8], drug delivery [9–11], optoelectronics [12–15], imaging [16–20] and optical data storage [21–26], among others. The optical and mechanical properties of metal nanoparticles depend mostly on their sizes and shapes [27–30]. Various techniques are available for characterising the size of metal nanoparticles such as SEM [31], TEM [32, 33], AFM [34, 35], DLS [39–42], and UV-VIS spectroscopy [43–45], among others. However, all of these techniques can not precisely work in all environments in a non-destructive way. The unavailability of a precise and non-destructive size characterisation technique for metal nanoparticles which can work in any external environment, is one of the background problems where this PhD research was focussed on.

The resolution limitation of optical microscopy was another concerning issue which was dealt with in this current research. The resolution of an optical system is limited to a few hundred nanometres for visible wavelengths, even using the highest available NA (1.4). In this PhD work, acoustic images of gold nanorods were reconstructed using time-resolved pump-probe picosecond ultrasonics by measuring their sizes, orientations and locations, even when they were inside the same optical point spread function. Hence, it was also possible to image gold nanorods with super-optical resolution. This chapter provides the conclusion of this PhD work by briefly discussing the applied approaches, key findings,

significances and limitations of this research work. Some promising future works are also recommended and described at the end of this chapter.

7.2 Conclusions

This PhD research work aimed to characterise gold nanorods and reconstruct their phononic or acoustic images in air and water media by using a combination of optical and GHz ultrasound measurements. The proposed technique is summarised in this section including the key findings, challenges, long-term motivation, limitations and contributions to the knowledge of this research.

7.2.1 Applied approaches

Gold nanorods were designed to work as optoacoustic transducers in this work. Optical and mechanical responses of gold nanorods of different sizes and shapes in different external environments were simulated to select the size, shape, medium, pump wavelength, probe wavelength, pump power and probe power of the rods for different experiments. A non-commercial Matlab code package SMARTIES [136] and a commercial finite element model tool COMSOL Multiphysics were used to simulate the optical responses of gold nanorods. The mechanical responses of gold nanorods were simulated by using an established analytical model developed by Hu et al. [162] and finite element models designed using COMSOL Multiphysics. The simulated results by those tools not only helped to design the experiments but also to verify and explain the obtained experimental results.

Gold nanorods were excited by circularly polarised femtosecond optical pump pulses. Circularly polarised probe pulses were focussed on them, and the modulation of the scattered probe light intensity caused by the vibration of the particle was used to determine their acoustic or vibrational frequencies. The size was determined from the acoustic resonant frequencies, the orientation by measuring the response as the probe polarisation was varied, and the location by spatially tracking the strength of the vibration. Finally, the obtained sizes, orientations, and locations of gold nanorods were combined to reconstruct their acoustic images. Metal nanoparticles are of sub-optical dimensions and many of them could be placed inside the optical point spread function. Acoustic frequencies of

metal nanoparticles were used to separate them if their frequencies were separable, and the optical diffraction limit was defeated. In addition, the sensitivity of gold nanorods to the polarisation of light was used to separate them.

Vibrational frequencies of gold nano-spheres were used as tags in [60] to super-localise and image them with super-optical resolution. However, the limitation was that it was not possible to separate two spheres of the same sizes using the frequency as a tag because they produced the same frequencies. In contrast, nanorods are asymmetric in shape and hence sensitive to their orientation to the light or the polarisation of light. The use of gold nanorods solves the problem because their orientation or the polarisation of light can be used to separate them inside the point spread function when their frequencies are the same. In addition, nanorods have two vibrational frequencies, the longitudinal mode and the breathing mode. These modes give more information about the particles simultaneously and increase the degree of freedom to separate particles using frequencies. There is a limit to the number of particles or frequencies that can be measured simultaneously within one point spread function. This capacity can be increased if the amount of information from the particle increases to separate them simultaneously for accommodating more particles. So, polarisation selective generation or detection and two main vibrational frequencies of GNRs can be used to increase the number of accessible channels that can be detected simultaneously in the same optical point spread function. However, physical dimensions of the particles inside the PSF would be the final limiting factor to increase the number of channels.

7.2.2 Key findings

The obtained results indicated that the reconstructed acoustic images of gold nanorods were very close to the SEM images in both air and water media. It was also possible to image gold nanorods with super-optical resolution. The predicted length and width precisions of gold nanorods were 1 nm and 0.3 nm in the worst case compared to SEM measurements. The size characterisation results in this thesis showed that the worst case SEM precision was ± 36 nm. However, the SEM measurement was a function of human error because measurements were done manually from the pixels of the SEM images. In addition, the precision of SEM measurements also depends on the setting of the machine,

noise, magnification, contrast, and aberration, among others. Hence, the SEM precision depends on the quality of the image. The size accuracies were affected by other factors such as Young's modulus and shape diversity of gold nanorods. The minimum angle precision for gold nanorods was 0.4° using the proposed technique. The result presented in this thesis showed that the minimum angle precision was ±7° from SEM. It can be said that the measurements by the proposed technique had higher precision than the SEM measurements. However, the angle accuracy was affected by low SNR, thermal effect, non-sinusoidal response of rod, not fully circularly polarised light, minor mismatch in the orientation of the sample on the SEM stage and the experimental stage, and minor calibration fault in the rotary parts of the set-up. The estimated minimum location precision was 2 nm during imaging but the location accuracy was affected by the tiny movement of the particles in water because of water flow or air bubble pressure inside the gasket chamber, temperature drift, improper beam shape because of optics, low SNR, use of SEM scale bar and the positional information from the microscope stage as references, among others.

In this research, gold nanorods were also fabricated by EBL and their phononic images were reconstructed by applying the same techniques as applied for the purchased gold nanorods. Although the bonding of the EBL fabricated rods to the substrate was not considered, their reconstructed acoustic images were very close to their SEM images.

The thermal effect on gold nanorods was observed during some experiments of this research. It was shown how heat from the laser modified the gold nanorods, especially when a NIR-NIR (generation-detection) set-up was used. Hence, it was decided to continue the experiments using a UV-NIR set-up because nanorods have a lower absorption cross-section at UV than NIR (7 times lower, measured for a 112 nm by 40 nm GNR). For this reason, the orientation of the gold nanorod was determined by measuring the response of it as the probe polarisation was varied, since nanorod is not sensitive to the polarisation of light at UV. Although the heat effect was avoided in this work by using the UV-NIR configuration and water as the external medium, partial heating could have affected the accuracy of the measurements. The heat effect on gold nanorods was undesired for this project. However, the heat effect on gold nanorods can be used in many applications such as photothermal therapy, drug delivery, among others.

7.2.3 Long term motivation

The long-term motivation behind this PhD research is to help make progress towards a phonon-based super-resolution imaging technique in biology. Although imaging any biological nanostructure using gold nanorods is out of the scope of the current work, the achievements of this research are significant steps to offer a phonon based super-resolution imaging technique that can image biological nanostructures. Gold nanorods can be easily functionalised and are well-tolerated by biological cells. Most commonly used super-resolution techniques such as STED [50–52], STORM [53–55], and PALM [46] are based on fluorophores. The high photon dose used in these techniques damage fluorophores and they bleach. As a result, repetitive or time-consuming imaging destroys the specimen (for example cell death) and the super-resolution capability deteriorates. Gold nanorods can be used as labels like fluorophores and the demonstrated technique can be used to image living biological cells with super-resolution. Imaging cells in this way may be more stable than fluorescence microscopy because nanoparticles do not bleach like fluorophores. As the technique is phonon-based, it will not damage cells and can also provide mechanical information (such as viscosity or sound velocity) about the surrounding environment.

7.2.4 Current limitations of the technique

The nano-structures used in this work were relatively large. However, smaller nanoparticles can be used to allow better cell uptake while keeping the optical properties in the NIR region. Although the demonstrated technique is beneficial for live cell imaging, there are still some challenges. The acquisition speed is not yet practical for imaging live cells. In this project, it took approximately 4 hours to scan a 5 μm by 5 μm area with a step motion of 100 nm which may negatively affect live cells. The time can be reduced by decreasing the scan step size but at the cost of imaging detail. However, the survival time of a cell depends on the cell type, cell handling protocol and human efficiency to work with cells, among others. In addition, there are dynamic phenomena in cells at all time scales and the current speed of the technique may not be sufficient to monitor these. The situation may be improved by the use of an alternative approach which is to track a single point on the cell rather than imaging the whole to monitor its dynamic behaviour. However,

exciting/detecting a single point with a laser continuously will increase the thermal effect on gold nanorods as well as on biological cells. The speed of the technique can be increased, for instance, through a wide field detection technique which may require expensive and complex hardware facilities. However, parallel excitation/detection techniques can also increase the heat effect. Thermal effect on gold nanorods can also be thought as one of the limitations of the technique. However, it is possible to avoid or minimise this effect by optimising the pump and probe power and wavelengths, using highly conductive surfaces, and selecting small particles, among others. Frequently used super-resolution imaging techniques like STED, STORM etc. were mostly tested on fixed cells. If the thermal effect on gold nanorods and on cells can be controlled, it can be said the proposed phonon-based technique is ready for imaging fixed cells.

7.2.5 Contributions to knowledge at a glance

1. A detailed analysis of the optical and mechanical responses of gold nanorods was carried out using the simulated results from the analytical and designed FEM-based models. The modelling methods can be used to simulate the optical and mechanical responses of gold nanorods of any arbitrary size and shape in any external medium. The modelling works can also be used to estimate the experimental parameters of gold nanorods and verify the experimental results.

2. Gold nanorods were designed as optoacoustic transducers and experiments were carried out using picosecond laser ultrasonics. A polarisation-sensitive experimental system was designed and built to carry out experiments. The successful experiments on metal nanoparticles using picosecond laser ultrasonics focused on an important application of picosecond ultrasonics.

3. Size, orientation and location of gold nanorods were measured with high precision in air and water media. Then, the images of gold nanorods were reconstructed by combining their sizes, orientations and locations. The characterisation of size is itself an important contribution separately. The proposed technique can characterise the size of metal nanoparticles with high precision in any external environment. It does not need any vacuum environment like TEM and SEM. It does not touch the sample

with any sharp tip like AFM and is non-destructive. It also can measure a single particle precisely and does not give average measurements like DLS and UV-VIS spectroscopy. The above benefits are also true when the technique does imaging. Hence, the proposed technique can be applied to living specimens.

4. It was possible to image gold nanorods with super-optical resolution. By using the acoustic frequencies and orientations of gold nanorods as tags, they could be identified and separated in the same optical point spread function and the optical diffraction barrier was defeated.

5. It is possible to measure Young's modulus of metal nanoparticles using this technique if the size and shape information are known before which is an important elastic property.

6. The demonstrated imaging technique opens a path toward a phonon-based super-resolution imaging technique for biology where the metal nanoparticles can be used as labels like fluorophores. As the particles do not bleach like fluorophores, this phonon-based imaging technique can be more stable than fluorescence microscopy. If the thermal effect on gold nanorods and on cells can be controlled, it can be said the proposed phonon-based technique is ready for imaging fixed cells.

7.3 Future Work

There are scopes to do several interesting works in the future based on this PhD work. Some promising future works are recommended and described below.

7.3.1 Biological cell imaging using gold nanorods as labels

Significant amount of researches have been done where biological cells were imaged by using gold nanorods inside the cells [231–235]. The proposed technique in this research can be applied to biological cells by following the procedures described below. It is good to mention that only the major steps are listed here as shown in figure 7.1, not the exact protocol. The described process is one of the possible ways to apply the proposed technique to image biological cells.
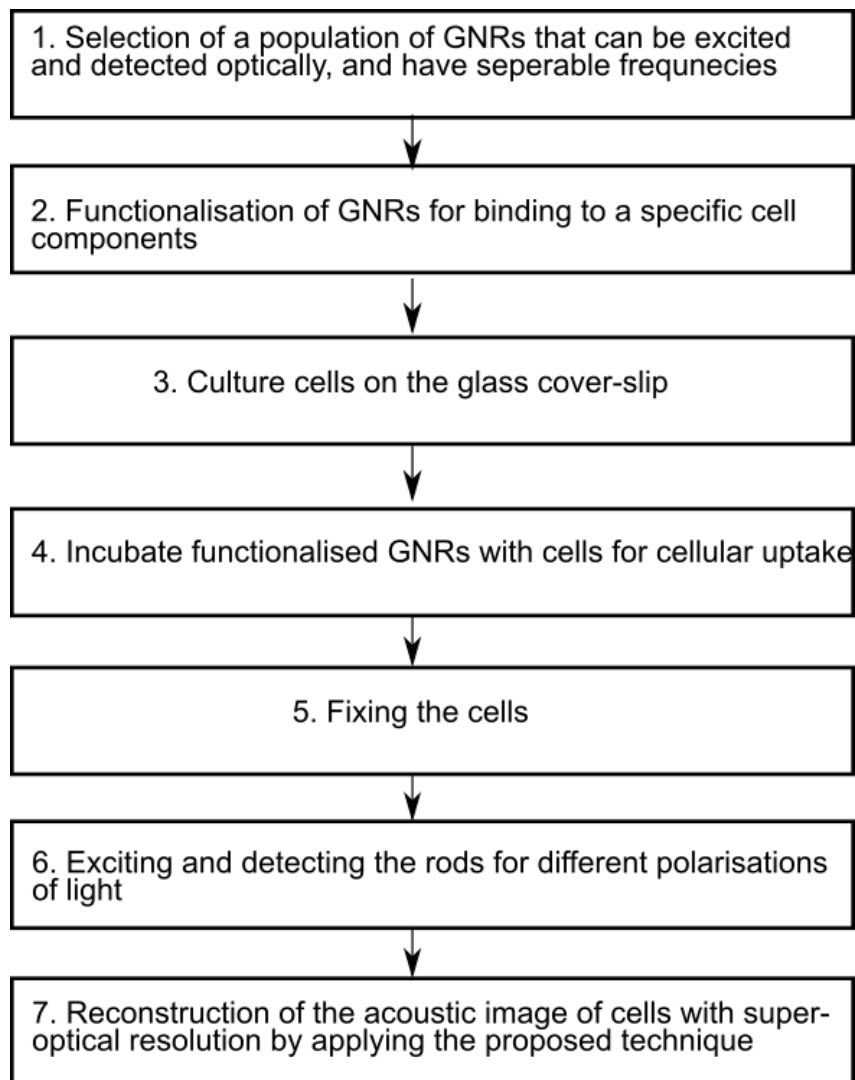
Figure 7.1: A tentative workflow to apply the proposed imaging technique to image biological cells.

1. The first step is to select a population of gold nanorods that can be excited and detected optically using a specific experimental system. It is also important to make sure that the selected gold nanorods have separable frequencies.

2. The second step is the functionalisation of gold nanorods which is required to reduce the toxicity, increase the bio-compatibility and selectively target various cellular structures [233]. The seed-mediated process [83, 84] is the most frequently used method for synthesising gold nanorods where the cationic surfactant cetyltrimethylammonium bromide (CTAB) is used as a structure directive agent. CTAB shows cytotoxicity and there are many ways to reduce the toxicity from CTAB, such as,

214

centrifugation, using polymers to modify the surface of GNRs by electrostatic absorption, and coating GNRS with bovine serum albumin (BSA), among others [233, 236]. Current approaches for the functionalisation of GNRs generally involve the use of either one or a combination of functional groups including oligo or polyethylene glycol (PEG), bovine serum albumin (BSA), acids and polypeptides, oligonucleotides, antibodies, receptors, and similar diverse particles [233]. Gold nanorod surface chemistry has effect on the cellular response also [237] . Useful data are provided in [238] (table 2) where different functional groups, their ligands and the types of cells they bind with can be seen. Some dark field images of functionalised GNRs inside different types of cells are shown in figure 7.2.

3. The glass cover-slip next needs to be coated with either poly-lysine or gelatine to stick the cell on it [239–241].

4. Functionalised gold nanorods can be inserted into cells by following the appropriate process [242–244].

5. To fix the cell, organic solvent methods or a cross-linking method can be used [245]. The goal of fixation is to stop the decomposition of cells and freeze the cellular proteins and sub-cellular structures in place. The proposed technique can also be applied to living cells. However, imaging living cells would be complex and time-consuming. Hence, applying the proposed technique to fixed cells can be considered as a reasonable first attempt.

6. Optical excitation and detection of gold nanorods inside the cell for different polarisations of light can be done in the same manner as has been demonstrated in this thesis. It is important to control the laser power so that the thermal effect of gold nanorods on living cells can be minimised. In this work, acoustic images of gold nanorods were reconstructed using UV-NIR set-up because of the excessive thermal effect on gold nanorods when NIR-NIR set-up was used. However, NIR light is used in biomedical applications because it can penetrate the body. More analysis and advanced level modelling can be done to estimate the applicable power for gold nanorods at NIR. In addition, bio-cells are very sensitive to wavelength less than 600
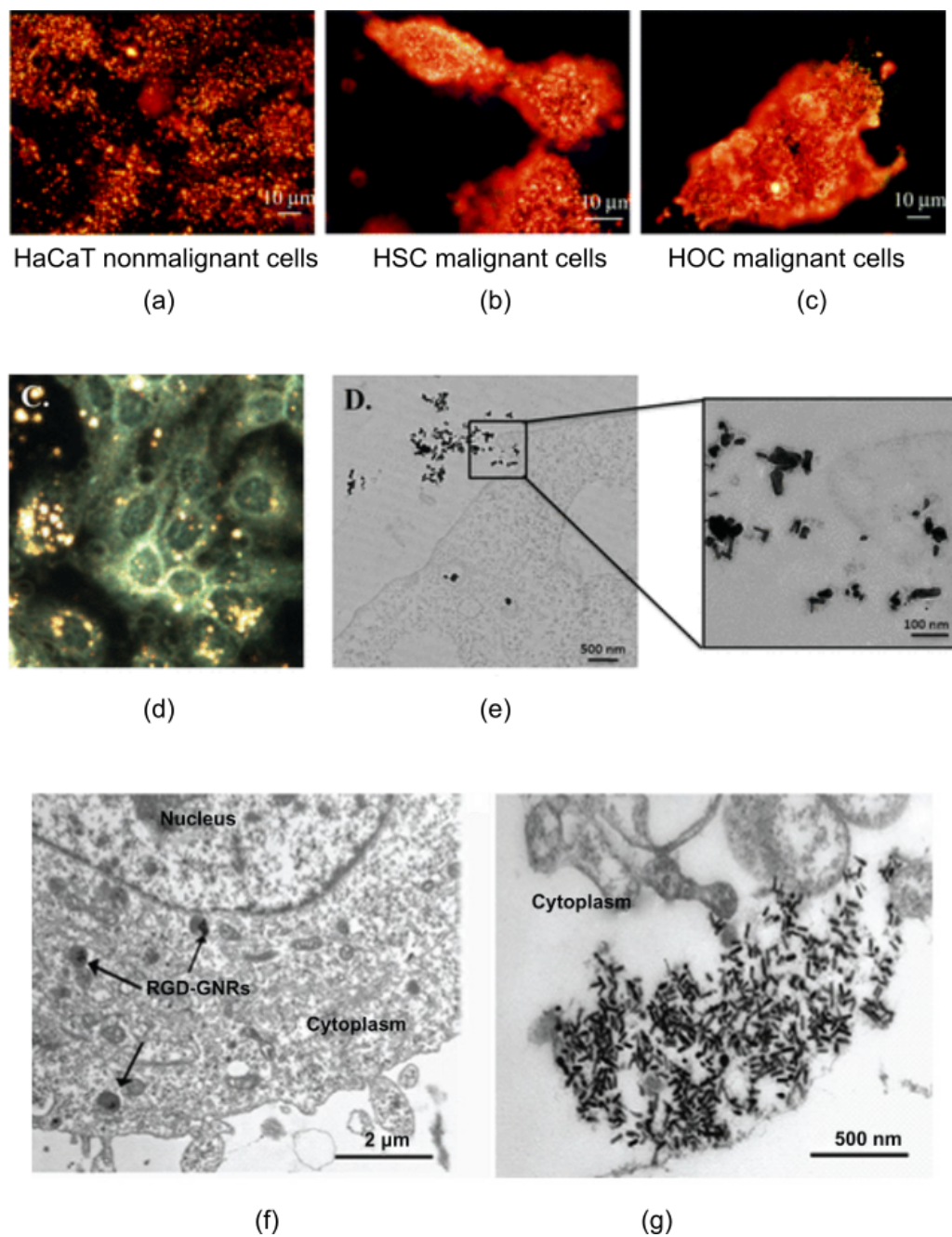
Figure 7.2: Dark field images of functionalised GNRs inside cells. (a)(b)(c) Light scattering images of anti-EGFR/Au nanorods after incubation with cells for 30 min at room temperature [232]. Nanorods strongly scatter orange to red light due to their strong longitudinal surface plasmon oscillation with a frequency in the NIR region. (d)(e) Cell uptake of GNR-MHDA in HaCaT cells [237]. (f)(g) A375 melanoma cell shows evidence of internalised RGD-GNRs [234]. Reproduced with permission.

nm. However, UV-NIR can also be used to image cell if the power is tolerable [118].

7. The functionalised gold nanorods bond to the target cells. The acoustic image of the target cells can then be reconstructed by locating the gold nanorods using the proposed super localisation technique as has been described in this thesis. Using the frequency and orientation difference of gold nanorods, it is possible to super-locate them and image the cell with super-optical resolution. There is no need to know any information about the size, frequency, distribution and orientation of the nanorod population initially.

It is also possible to do a different type of cell imaging experiment where gold nanorods can act as sensors. The acoustic response of gold nanorods is related to their external environment [246]. Hence, the perturbation of the known acoustic frequencies of gold nanorods can be used to image the cell. A simple way to do this kind of experiment can be, placing a cell on top of a gold nanorod pattern fabricated by EBL and measuring the change in the known acoustic frequencies of gold nanorods in the pattern to image the cell. In essence, the principle is to detect the deviation in the acoustic frequency of a specific gold nanorod in the known pattern when the cell touches it and changes its resonant behaviour. Using a gold nanorod pattern for imaging cell in this way can be more promising for super-resolution imaging because an ideal sample can be designed by placing gold nanorods very close to each other and in desired orientations. Hence, more close points on the cell can be imaged. Also, the binding problem of synthesised gold nanorods to the cell can be avoided.

7.3.2 Imaging different shapes of metal nanoparticles with super-optical resolution

Imaging different shapes of metal nano-particles such as triangles, squares, pentagons etc. with super-optical resolution would be another promising future work based on the presented technique in this thesis. The first step could be modelling these structures to understand their vibrational behaviours and figure out their complex fabrication requirements. Multiple vibrational modes of these complex structures may be helpful to separate

them easily. Also, the proposed imaging technique needs to be updated to measure the orientation or angle of these complex nano-structures. Successful imaging of different shapes of metal nanoparticles with super-optical resolution can also help in imaging cell efficiently. However, the toxicity of different shapes of metal nanoparticles need to be analysed before.

Appendix A

Appendix

A.1 Protocols used for fabricating gold nanorods by EBL

The fabrication steps of GNRs by EBL were briefly discussed in section 4.5.4. In this section, the steps are discussed in detail and the followed protocol is presented. Bilayer resist process was followed to fabricate the samples shown in figure 4.33. Monolayer resist process may not ensure good lift-off for small nanostructures always. If the resist profile has too sharp undercut as shown in figure A.1 (a), the sidewall of the resist gets coated during the metal evaporation. This metal joins the desired metal structure as a tail and does not come out after the lift-off as shown in figure A.1 (b). In the worst case, this extra metal can pull out the whole structure during the lift-off process. Good lift-off needs an undercut resist profile that prevents side wall coating of the resist during the metal evaporation and the bilayer resist process [230] can serve this purpose. The process uses two different resists of different electron sensitivities defined by their molecular weight (MW) difference. The resist of lower molecular weight is used for the bottom layer and it is more sensitive to the electron beam than the top layer with the resist of high molecular weight. As a result, the bottom layer is overexposed to the electron beam and become more soluble in the developer than the top layer. In this way, an undercut profile can be created by using the bilayer stack of photoresist as shown in figure A.1 (c) where it can be seen that the bottom layer of resist is not in contact with the desired metal structure. Hence, proper lift-off can be ensured as shown in figure A.1 (d).
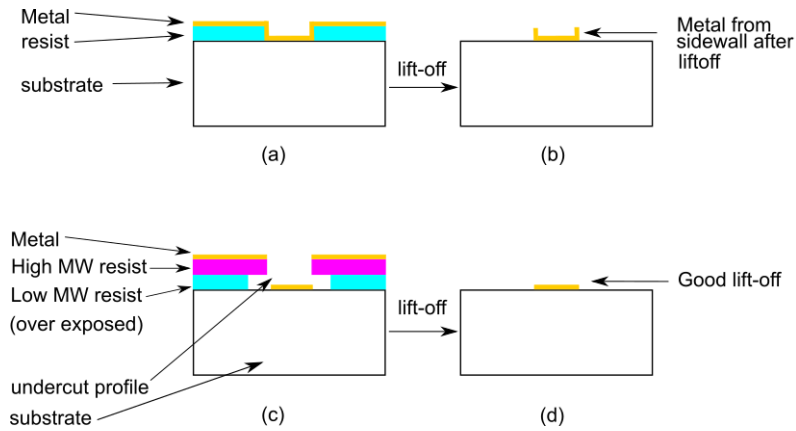
Figure A.1: Comparison of the lift-off quality between the monolayer and bi-layer resist processes. (a)(b) Too sharp undercut profile of the monolayer resist process and the resultant poor lift-off because of the coated sidewall during the metal evaporation, respectively. (c) An undercut profile created by the bilayer stack of resist which prevents the side-wall coating. (d) Better quality of lift-off using the bilayer resist process because the bottom layer of the resist is not connected to the metal.

The used protocol to fabricate GNRs by EBL following the bilayer resist process is explained below using a diagram as shown in figure A.2.

1. Cleaning of the substrate

   Glass cover slips of 25 mm were solvent cleaned to remove the surface organic impurities with ethyl lactate, acetone, methanol and isopropanol in sequence as shown in figure A.2 (a).

2. Coating of the resist and pre-bake

   A positive tone PMMA E-beam resist AR-P 662.04 of 600K MW (provided by ALL-RESIST GmbH) was spin-coated with 4000 rpm for 1 min to form the bottom layer of about 140 nm thick as shown in figure A.2 (b). This layer was then pre-baked at 150°C on a hot plate for 3 min. Next, a positive PMMA E-beam resist AR-P 679.02 of 950K MW was spin-coated with 4000 rpm for 1 min which formed the top layer (less sensitive) of about 70 nm thick as shown in figure A.2 (c). The thickness of a resist depends on several factors such as the spin speed, spin time, viscosity and temperature. Hence, it is important to look at the available data sheet of the resist before selecting the parameters for spin coating or the thickness can be self-monitored as a function of different parameters. This layer was also pre-baked at

150°C on a hot plate for 3 min. The images of resist coating and prebaking are shown in figure A.3 (a) and (b), respectively.
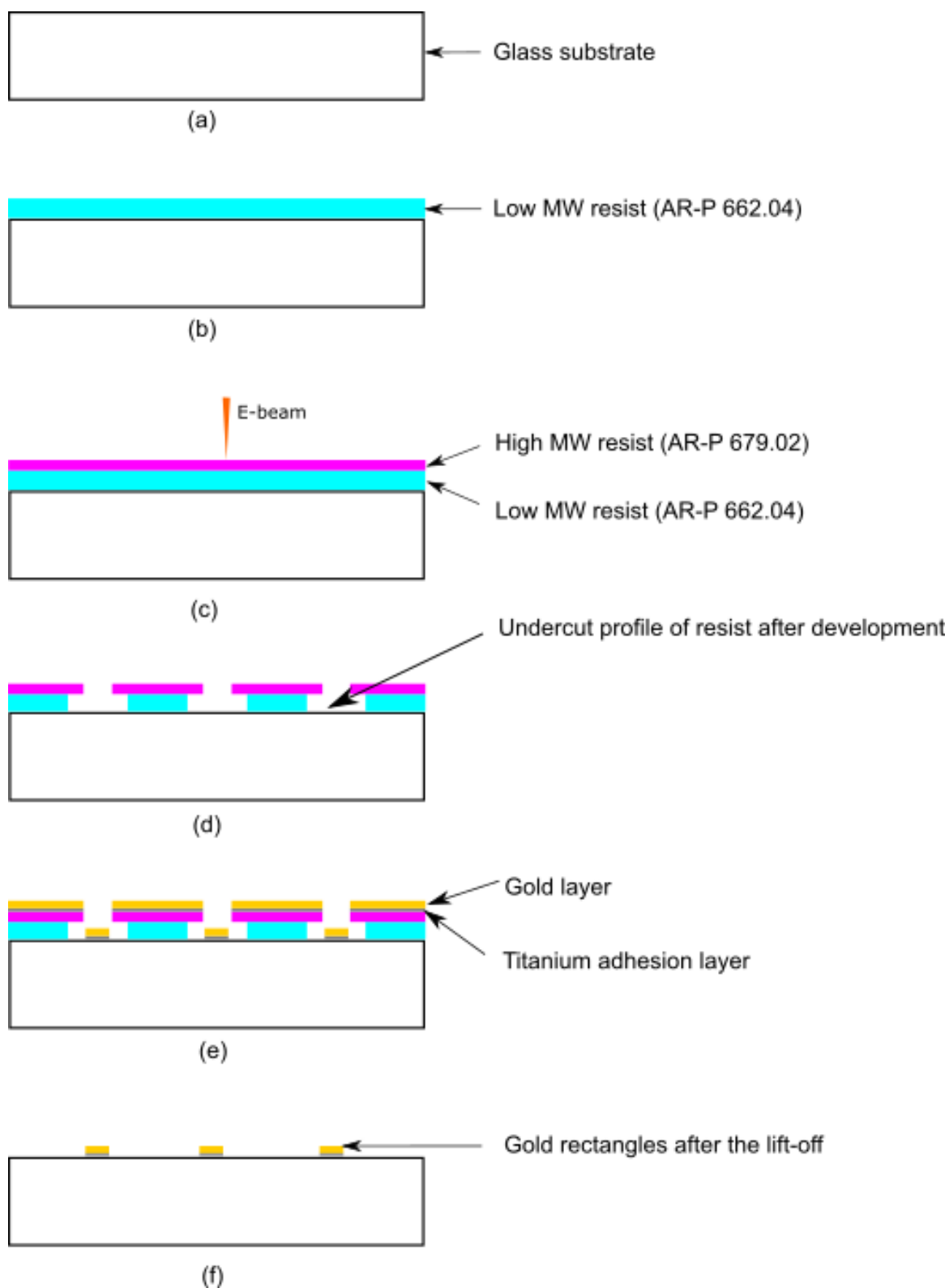
Figure A.2: Fabrication process of GNRs by Electron Beam Lithography (EBL).
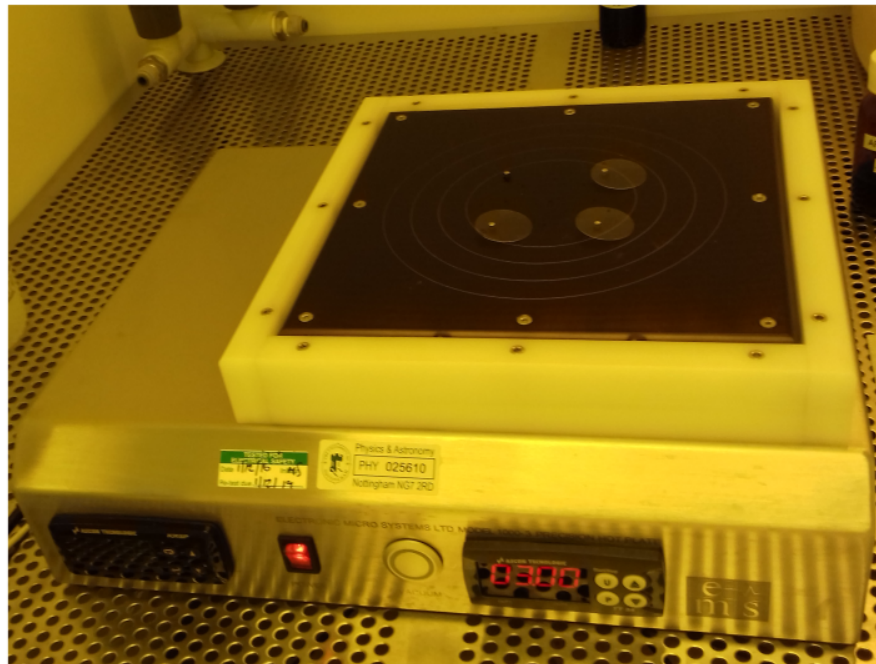
Figure A.3: Images taken during electron beam lithography process at the clean room, nmRC, UON. (a) Coating of the e-beam resist on a glass substrate using a spin coater. (b) Prebaking of the coated resist on a hot plate. (c) Coating of a conductive layer on the resist using a spin coater.

3. Coating of a conductive layer

   Electron beam fabrication is challenging on an insulating substrate because of the surface charging effect. The charge from the electron beam gets trapped on the substrate and can not dissipate. This charge accumulation on the surface creates

a strong electrostatic field at the sample surface and deflects the incident electron beam which results in pattern distortion. To overcome this problem, a conductive polymer PMMA Electra 92 (AR-PC 5090) was spin-coated with 2000 rpm for 1 min on top of the bilayer resist stack to provide a conductive surface. The conductive coating was then baked at 90°C for 2 min on a hot plate. This layer was not shown in the schematic diagram for simplicity. The image of coating the conductive layer is shown in figure A.3 (b). A conductive layer of ITO (Indium Tin Oxide) can also be coated at the beginning (before coating resist) to provide conductivity to the sample for EBL exposure. In this thesis work, ITO or PMMA Electra 92 were used as conductive layers. It can be said from the practical experience that the success rate for ITO coated samples were high.

4. Exposure

It is important to put some focus marks on the sample which can be used to estimate the focus parameters for the exposure. A small amount of silver conductive paint was heavily diluted in MIBK and then agitated. This solution was then passed through a 0.2 μm filter and the obtained solution was then placed on the corners of the sample using a fine pointer as shown in figure A.4 (a) to give focus marks. Three cover slips can be seen where the coverslip with black shade had PMMA Electra 92 as the conductive coating and the other two had ITO on them as the conductive layer. After this step, the samples were placed in the appropriate slot of the chuck as shown in figure A.4 (b) for loading into the chamber. Two samples were placed in two 25 mm slots and two extra dummy coverslips were used beneath the samples to adjust the required height. Then, the chuck was placed in the chuck holder as shown in figure A.4 (c) and the holder was loaded into the chamber as shown in figure A.4 (d). Exposure base doses of 500 $\mu C/cm^2$ to 600 $\mu C/cm^2$ were used to fabricate the rods (200 nm by 80 nm) using this recipe. However, the amount of dose can vary according to the resist, size and shape of the structure, among others.
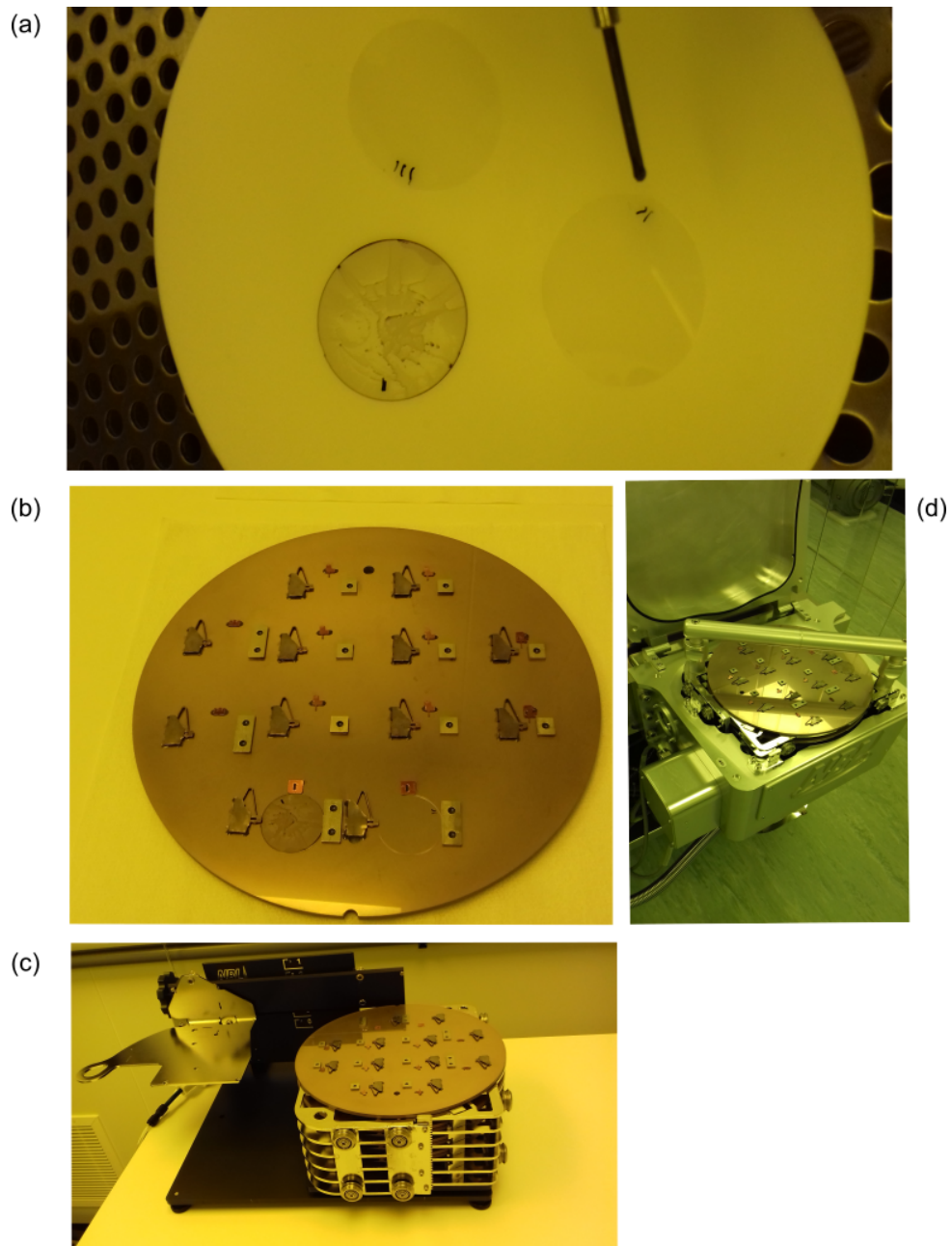
Figure A.4: Images taken during the electron beam lithography process at the clean room, nmRC, UON. (a) Silver conductive paint was dropped on the corner of the sample as focus marks to set the focus parameters for exposure. (b) Ready samples were placed in the appropriate slots of the chuck maintaining the proper height. (c) Chuck was placed in the chuck holder. (d) Chuck holder was loaded into the EBL chamber.

5. Development

At first, the sample was placed in DI water for 1 min to remove the conductive layer (if PMMA). If the sample had coated thin film like ITO on it, this step is not needed. Then, the sample was developed in a mixture of MIBK:IPA (1:3) for 3 min

on a stirrer. In the mixture, the MIBK acts as the developer and the IPA is used to dilute it and therefore slows down the development to increase the contrast. The benefit of MIBK is that it can be used for a wide range of resist thicknesses. Finally, the sample was placed in IPA for 30 s and then blow dried. The IPA step at the end was to stop the development and remove the developed resist from the sample.
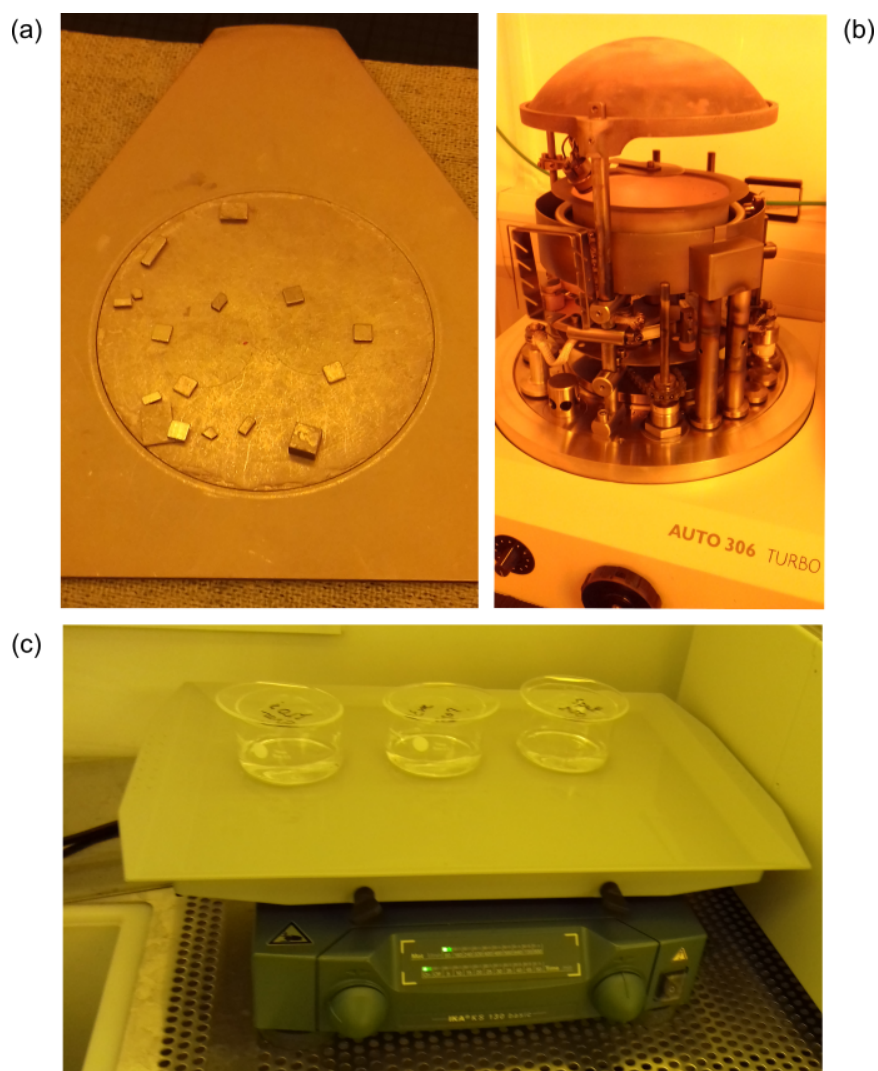
Figure A.5: Images taken during the electron beam lithography process at the clean room of Physics & Astronomy, UON and nmRC, UON. (a) Developed samples attached to the sample holder by using small magnets. (b) thermal evaporator (EDWARDS, AUTO 306) at Physics & Astronomy, UON to coat metal. (c) Samples left in AR 600-71 (remover) on a stirrer at nmRC, UON during lift-off.

6. Metallisation

Developed samples were well attached to the holder of the thermal evaporator with

the help of small magnets as shown in figure A.5 (a) before inserting into the chamber. Auto 306 thermal evaporator was used for coating metals as shown in A.5 (b). At first, 5 nm of Titanium was coated as an adhesion layer. Then, the required amount of gold was deposited on top of the Titanium layer. In this thesis work, 70 nm gold was used for 200 nm by 80 nm GNRs. The metal thickness can vary according to the necessity but it needs to be checked by the simulation at first because a change in the thickness will change the optical properties of the structure.

7. Lift-off

The final step was the lift-off. The coated sample was soaked in AR 600-71 (remover) for 1 hour on a stirrer as shown in figure A.5 (c). While the sample was immersed in a solvent, fresh AR 600-71 was sprayed from a squeeze bottle to remove the gold waste. Samples should not be out of the solvent because if the sample becomes dry, lift-off would not work properly. Then, the samples were collected carefully and placed in a beaker containing fresh AR 600-71 and left on the stirrer for another hour or overnight while AR 600-71 was sprayed occasionally. The lift-off time can vary according to the sample type and situation. Finally, the sample was rinsed with the directed stream of AR 600-71 on a tissue and blow dried.

A.2 Calculation of detectable number of gold nanorods

It is possible to increase the capacity of a system by detecting more particles simultaneously. In [60], GNSs were super-resolved by using their vibrational frequencies. The use of gold nanorods allows to increase the capacity of a system rather than using nanospheres. In this section, the maximum and average number of GNRs are calculated that can be detected simultaneously.

A.2.1 Simultaneously detectable maximum number of gold nanorods and gold nanospheres

Spheres have one main vibrational frequency but rods have two main vibrational frequencies. Hence, it is possible to use two frequencies of the rod to identify and separate them. For example, if there are 50 frequency channels (FCHs), it is possible to resolve 50 different GNSs simultaneously. On the other hand, as nanorods have two vibrational frequencies, it is possible to resolve more than 50 GNRs simultaneously using their two frequencies together. However, the actual number of resolvable GNRs simultaneously depends on the frequency overlap of rods. A 4 by 4 matrix of random frequency values can be taken as an example where the longitudinal mode frequencies are 5GHz, 6GHz, 7GHz, 8GHz and breathing mode frequencies are 30GHz, 31GHz, 32GHZ and 33GHz. As a result, 16 combinations of frequencies are possible but 16 GNRs can not be detected simultaneously because of the frequency overlap and confusion to identify the correct particle. To illustrate the frequency overlap, it can be assumed that three GNRS have frequencies as listed in the table A.1.

Table A.1: Assumed frequencies of GNRs to explain the frequency overlap.

Rod	Longitudinal mode GHz	Breathing mode GHz
GNR1	6	30
GNR2	5	31
GNR3	5	30

If we observe frequency two peaks at 5 GHz and 30 GHz in the experimental result, it is not sure that 5 GHz corresponds to GNR2 or GNR3 and 30 GHz corresponds to
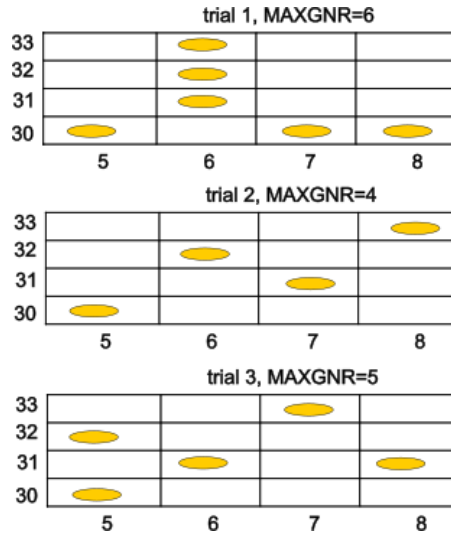
Figure A.6: Maximum number of GNRs that can be detected simultaneously shown for three random trials in the case of a 4 by 4 matrix. It can be seen that the maximum number of GNR (MaxGNR) varied in different trials because particles were chosen in a random order. However, the case when MaxGNR=6, was the best case which can happen for a 4 by 4 matrix without any frequency overlap.

GNR1 or GNR3. This means that GNR1, GNR2 and GNR3 can not be detected simultaneously. The maximum number of GNRs that can be detected simultaneously without any frequency overlap was estimated using Matlab for the 4 by 4 matrix mentioned before and shown simply in figure A.6 where the gold nanorods are placed in a valid position to avoid the frequency overlap. In the simulation, GNRs were chosen randomly one by one and the frequency overlap was checked before adding more GNRs to the valid set. In this way, it was possible to estimate the maximum number of GNRs that can be detected simultaneously.

The maximum number of GNRs (MaxGNR) was expected to vary in different trials because particles were chosen randomly as can be seen in figure A.6. However, the case when MaxGNR=6 was the best case for a 4 by 4 matrix without any frequency overlap problem. It can be seen that it was not possible to accommodate more particles. This gave a rule of thumb that MaxGNR=number of frequency channels (FCH)-2. This rule was also tested for a rectangular matrix and was found valid. It was also found out that the lowest MaxGNR=number of frequency channels (FCH)-4 but there was a condition that the matrix needs to be a regular matrix where all possible particles (matrix elements) are present. If the matrix is irregular (all particles or matrix elements are not present),

the rule of thumb for lowest MaxGNR will not work. In that case, lowest MaxGNR will be the maximum dimension of the irregular matrix. For example, if it is a 12 by 14 matrix, the lowest MaxGNR will be 14. The estimation of MaxGNR for an irregular matrix is discussed more later in this chapter.

A.2.2 Simultaneously detectable average number of gold nanorods and gold nanospheres

It is important to estimate the number of GNRs that can be detected simultaneously before there is the first clash of frequency overlap. It can be termed as the average number of GNRs representing the number of particles having a 50% chance of clash. The simulation was done in the same way as described before but this time the simulation was stopped when the first clash of GNR frequency was found rather than adding more GNRs later. Different sizes of square matrices were taken as examples as shown in figure A.7 and different numbers of trials were attempted to estimate the unique number of particles. The unique number of particles means the number of particles until a collision of frequency occurs and it also depends on the number of trials attempted. A general assumption was made for all square matrices by fixing the trial number equal to 100 times the number of possible GNRs. For example, the number of trials for 2 by 2 and 4 by 4 matrices were 400 and 1600, respectively. This assumption also helped to maintain the same ratio of the trial number for different sizes of matrices.

All data were then fitted with a Gaussian curve and mean values were extracted. The mean values represent the number of particles having a 50% chance of clash or the average number of GNRs that can be detected simultaneously. The mean values from all sets are plotted versus the number of frequency channels in figure A.8 (red curve). The increasing trend of the curve represents that if the number of frequency channels increases, more GNRs can be accommodated before there is a 50-50 chance of clash.

Two spheres of the same sizes (same frequency) can not be differentiated using their frequencies. If two spheres are taken randomly from a mixture of different sizes of spheres, the probability that they have the same frequency (same size) can be determined by using an approximate formula which is used to solve the birthday paradox [247]. The probability
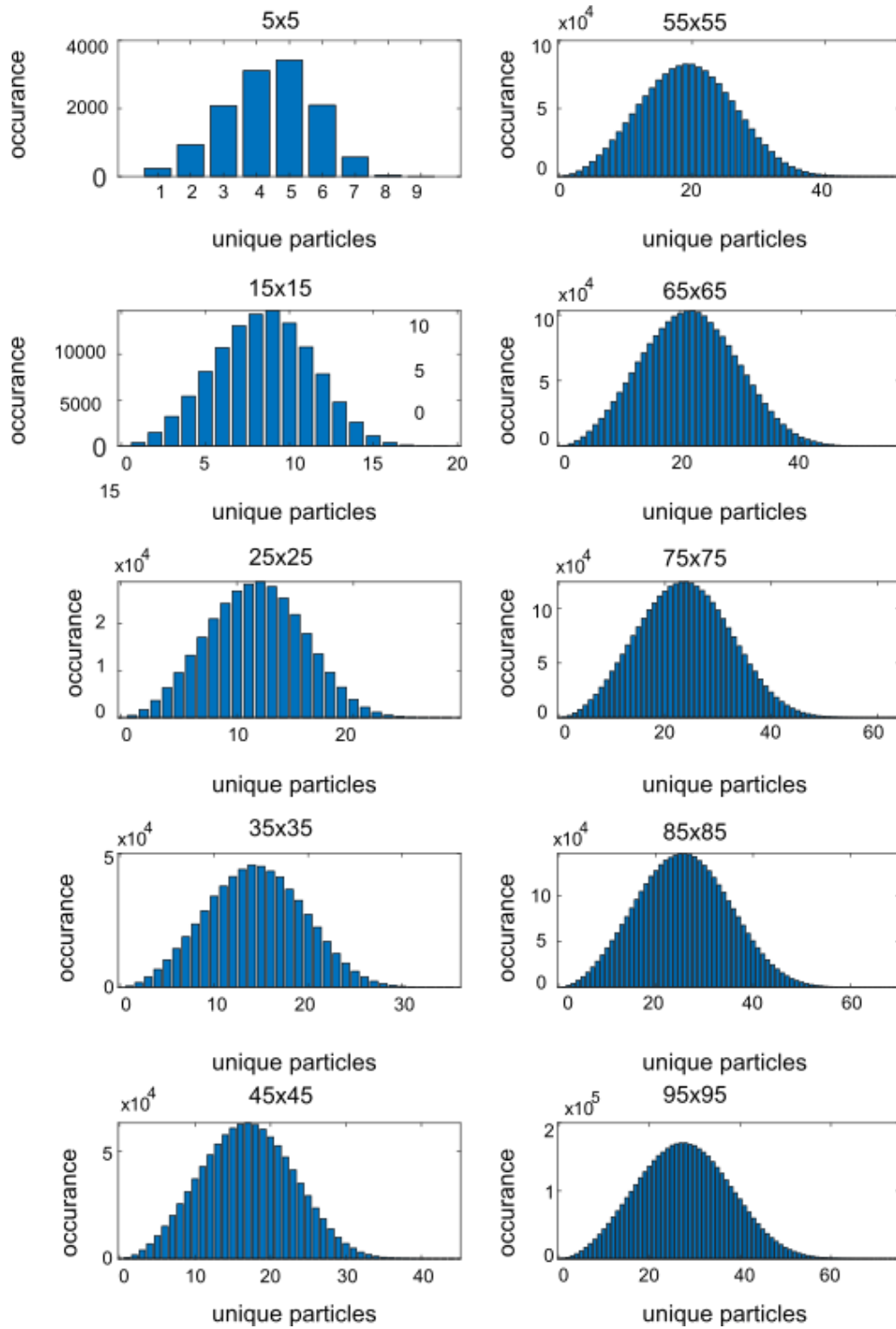
Figure A.7: Occurrence of the unique number of particles (GNRs) simulated for different sizes of square matrices.
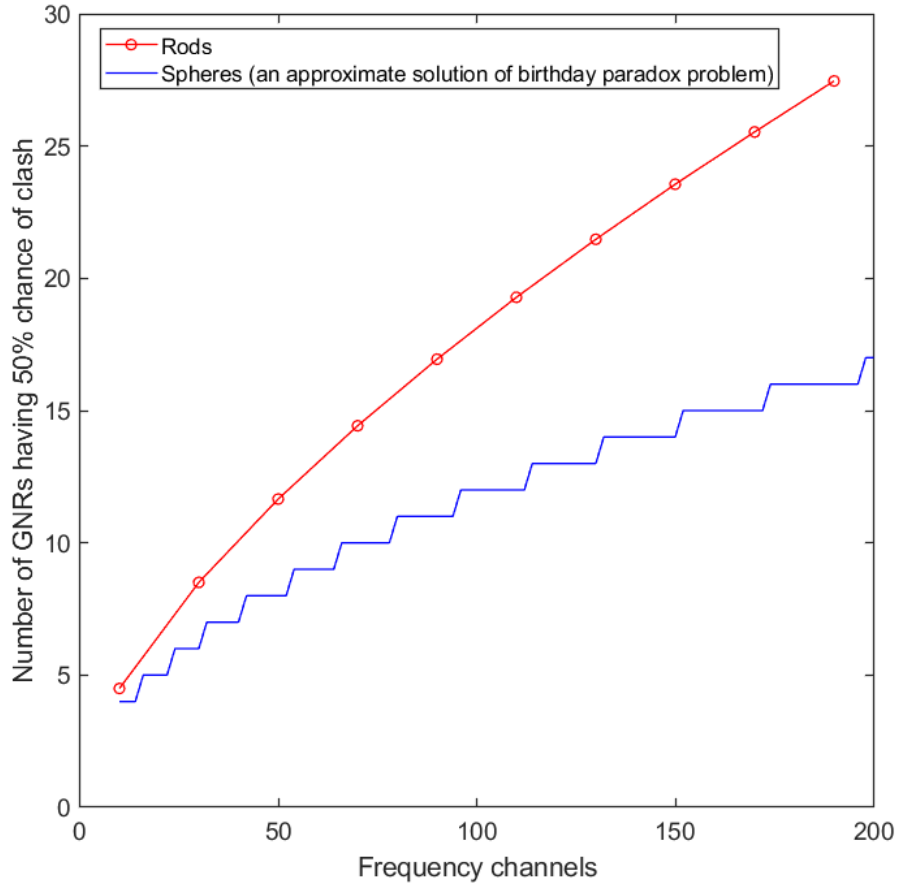
Figure A.8: Comparison of the number of rods and spheres that have 50% chance of a clash. It can be seen that the rod curve was above the sphere curve. It means that more rods were needed than spheres to have a 50% chance of clash. It can be said that for the same number of frequency channels, it is possible to detect more rods than spheres simultaneously.

of a match in birthday can be expressed as

$$P(n) = 1 - \left(\frac{364}{365}\right)^{n(n-1)/2} \tag{A.1}$$

where n is the number of people. So, the probability of a match in the frequency of spheres can be expressed as

$$P(n) = 1 - \left(\frac{FCH - 1}{FCH}\right)^{n(n-1)/2} \tag{A.2}$$

where FCH is the number of total frequency channels and n is the number of spheres.

The equation was solved and the plot (blue staircase curve) can be seen in figure A.8 for different numbers of FCHs to get the maximum value of n until 50% probability of a match happens. Hence, the calculated maximum value of n represents the number of spheres that have 50% chances of clash for a given number of FCHs. So the number of rods A.8 (red line) and spheres (blue staircase curve) that have 50% chance of clash can be compared as shown in figure A.8. It can be seen that the rod curve was higher than the sphere curve. It means that more rods were needed to have a 50-50 chance of collision. This comparison was done to justify the fact through a simulation that for the same number of frequency channels, it is possible to detect more rods than spheres simultaneously.

In these simulations, different practical factors were not considered such as the number of allowed frequency channels, frequency selections, adjacent frequency separability and optical sensitivity of GNR according to the wavelength. If a practical scenario is considered, the obtained matrix may be irregular where all possible GNRs may not be valid after passing through different criteria-based filters. However, the basic established rules will be same. For instance, the maximum number of GNRs that can be detected simultaneously is FCH-2 and it is possible to detect more nanorods than spheres for the same number of available frequency channels.

A.3 Performed Calibrations for experiments with NIR-NIR

The performed calibrations for the experiments explained in chapter 6 (section 6.5) are provided in this section. The experiments were done with a pump wavelength of 740 nm and a probe wavelength of 780 nm. The configuration was shown in section 4.3 where path 1 and path 3 were used for this experiment. Some challenges were faced to do those experiments as described below.

1. The beam from the laser passed through many optical elements before reaching the sample. Hence, it was needed to do some calibrations to ensure that the light was linearly polarised and had the desired polarisation on the sample stage. As a part of the calibration, a polariser was placed on the sample stage at first and its zero was set horizontally according to our assumptions about the directions with respect to the stage as shown in figure 4.5 (b). Then, the half-wave plate after the beam

expander in B1C1 path (set-up is shown in figure 4.4 of chapter 4) was rotated and the power on the sample stage was recorded. In this way, the position of the half wave plate was known to select the desired polarisation of the red beam from laser Y on the sample as shown in figure A.9. The same test was done to know the position of the half-wave plate in the BC path (set-up is shown in figure 4.4 of chapter 4) to select the desired polarisation of the red beam from laser X as can be seen in figure A.10.

2. It was observed that when the polarisation of the red beam from laser Y at 740 nm (acting as the pump) was changed, the power fluctuated on the sample stage as shown in figure A.11 (a). Little variation was seen in the power with the change of the polarisation when it passed through different optical elements in the set-up but the fluctuation was significant when the light passed through the bottom dichroic beam splitter (DCBS) as can be seen from figure 4.6. The DCBS worked for a certain range of wavelengths and its response to 740 nm was not flat. If the pump power on the sample fluctuates with a change in the polarisation of the pump beam, the mechanism to demonstrate the sensitivity of a nanorod to the polarisation of the pump beam can not be reliable. One solution was to replace the DCBS and select the desired one. However, the desired DCBS was not available in the market and it was very expensive to order a custom one. On the other hand, the used system was a shared system where it was needed to ensure that the new DCBS works for other users as well. As a reasonable solution, the input power was adjusted when the polarisation of the pump was changed to ensure a constant power on the sample as can be seen in figure A.11 (b). Hence, the polarisation was not changed in fine steps for those experiments because it was very time-consuming to adjust the power for every polarisation angle manually and efficiently. However, it is possible to automate the power adjustment procedure.

3. It was also important to check whether the power of the probe beam from laser X fluctuated at the detector end when the polarisation was changed. It was tested but it is not critical to discuss here because the probe light polarisation was not changed for those experiments.
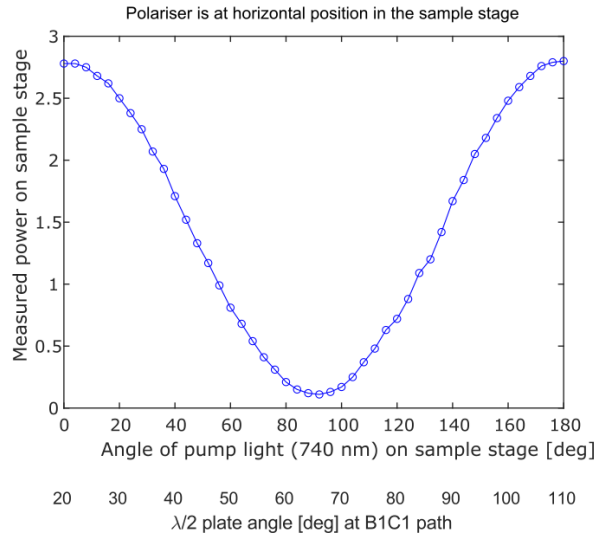
Figure A.9: Calibration to select the desired polarisation of the pump light on the sample. A polariser was set to the horizontal position on the sample stage and the half-wave plate at the B1C1 path was rotated to determine the angle of the half-wave plate to select the desired polarisation of the pump light on the sample stage. It can be seen that when $\lambda/2$ was at 20° and 65°, the measured power was maximum and minimum, respectively on the sample stage. So, when $\lambda/2$ was at 20° and 65°, the polarisation of the pump light was horizontal and vertical, respectively on the sample.
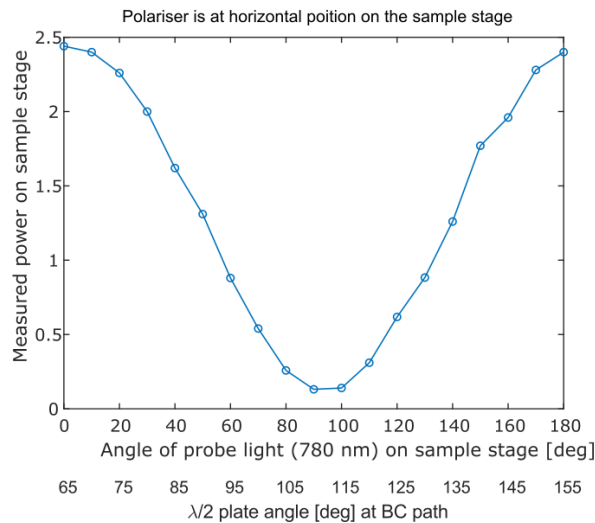
Figure A.10: Calibration to select the desired polarisation of the probe light on the sample. A polariser was set to the horizontal position on the sample stage and the half-wave plate at the BC path was rotated to determine the angle of the half-wave plate to select the desired polarisation of the probe light on the sample stage. It can be seen that when $\lambda/2$ was at 65° and 115°, the measured power was maximum and minimum, respectively on the sample stage. So when $\lambda/2$ was at 65° and 115°, the polarisation of the probe light was horizontal and vertical, respectively on the sample.
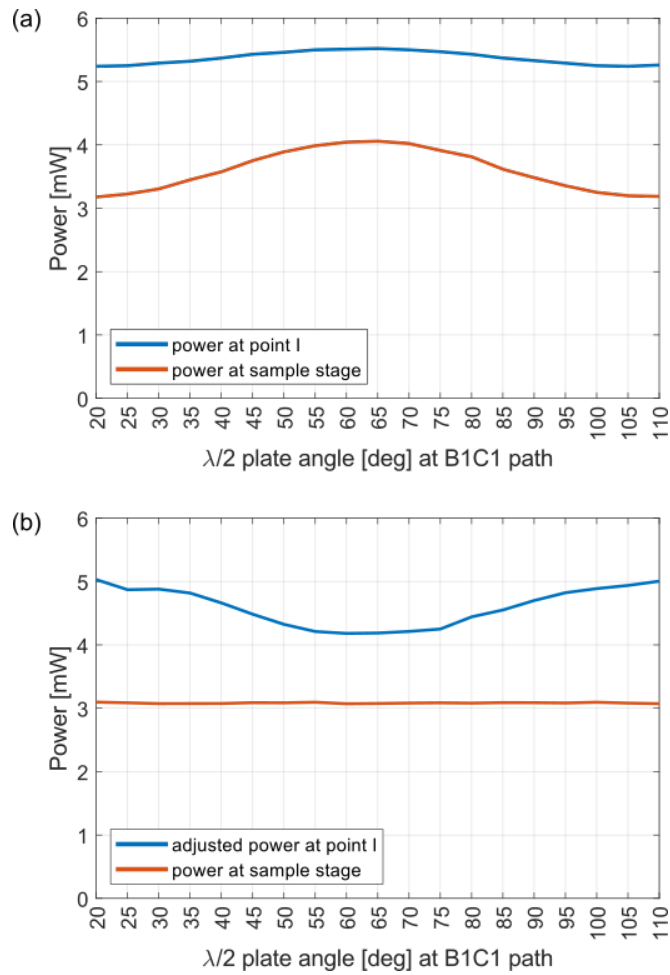
Figure A.11: Variation of the pump power on the sample with a change of the polarisation and adjustment of the input power to maintain a constant power on the sample. (a) The pump power on the sample at 740 nm was seen to vary with a change of the polarisation because of passing through a DCBS. (b) Adjustment of the given input power to compensate for the variation of power and assurance of the desired constant power on the sample with a change of the polarisation.

Bibliography

[1] ES Pavlenko, M Sander, Q Cui, and M Bargheer. Gold nanorods sense the ultrafast viscoelastic deformation of polymers upon molecular strain actuation. *The Journal of Physical Chemistry C*, 120(43):24957–24964, 2016. 1, 11, 12, 207

[2] Libing Wang, Yingyue Zhu, Liguang Xu, Wei Chen, Hua Kuang, Liqiang Liu, Ashish Agarwal, Chuanlai Xu, and Nicholas A Kotov. Side-by-side and end-to-end gold nanorod assemblies for environmental toxin sensing. *Angewandte Chemie*, 122(32): 5604–5607, 2010. 12, 13

[3] Neval A Cinel, Serkan Bütün, and Ekmel Özbay. Electron beam lithography designed silver nano-disks used as label free nano-biosensors based on localized surface plasmon resonance. *Optics express*, 20(3):2587–2597, 2012. 13

[4] Yongbin Lin, Yang Zou, Yuanyao Mo, Junpeng Guo, and Robert G Lindquist. E-beam patterned gold nanodot arrays on optical fiber tips for localized surface plasmon resonance biochemical sensing. *Sensors*, 10(10):9397–9406, 2010. 1, 11, 13, 207

[5] Xiaohua Huang and Mostafa A El-Sayed. Gold nanoparticles: Optical properties and implementations in cancer diagnosis and photothermal therapy. *Journal of advanced research*, 1(1):13–28, 2010. 1, 11, 13, 52, 207

[6] Hagar I Labouta, Nasrin Hooshmand, Tushar Upreti, and Mostafa A El-Sayed. Localized plasmonic photothermal therapy as a life-saving treatment paradigm for hospitalized covid-19 patients. *Plasmonics*, pages 1–5, 2021.

[7] Moustafa RK Ali, Yue Wu, Yan Tang, Haopeng Xiao, Kuangcai Chen, Tiegang Han,

Ning Fang, Ronghu Wu, and Mostafa A El-Sayed. Targeting cancer cell integrins using gold nanorods in photothermal therapy inhibits migration through affecting cytoskeletal proteins. *Proceedings of the National Academy of Sciences*, 114(28): E5655–E5663, 2017.

[8] Zhuoqian Lv, Sijia He, Youfu Wang, and Xinyuan Zhu. Noble metal nanomaterials for nir-triggered photothermal therapy in cancer. *Advanced Healthcare Materials*, 10 (6):2001806, 2021. 1, 11, 13, 52, 207

[9] Sibi Raj, Sartaj Khurana, Ramesh Choudhari, Kavindra Kumar Kesari, Moham-mad Amjad Kamal, Neha Garg, Janne Ruokolainen, Bhudev C Das, and Dhruv Kumar. Specific targeting cancer cells with nanoparticles and drug delivery in can-cer therapy. In *Seminars in cancer biology*, volume 69, pages 166–177. Elsevier, 2021. 1, 11, 13, 207

[10] Haiyan Chen, Yingfeng Di, Dan Chen, Kyle Madrid, Min Zhang, Caiping Tian, Lip-ing Tang, and Yueqing Gu. Combined chemo-and photo-thermal therapy delivered by multifunctional theranostic gold nanorod-loaded microcapsules. *Nanoscale*, 7(19): 8884–8897, 2015.

[11] Falian Zhu, Guozhu Tan, Yingtao Zhong, Yaodong Jiang, Lulu Cai, Zhiqiang Yu, Shuwen Liu, and Fei Ren. Smart nanoplatform for sequential drug release and enhanced chemo-thermal effect of dual drug loaded gold nanorod vesicles for cancer therapy. *Journal of nanobiotechnology*, 17(1):1–15, 2019. 1, 11, 13, 207

[12] Mihee Heo, Heesook Cho, Jae-Woo Jung, Jong-Ryul Jeong, Soojin Park, and Jin Young Kim. High-performance organic optoelectronic devices enhanced by sur-face plasmon resonance. *Advanced Materials*, 23(47):5689–5693, 2011. 1, 11, 207

[13] Zhiqiang Liang, Jun Sun, Yueyue Jiang, Lin Jiang, and Xiaodong Chen. Plasmonic enhanced optoelectronic devices. *Plasmonics*, 9(4):859–866, 2014.

[14] Yoon Ho Lee, Tae Kyung Lee, Inho Song, Hojeong Yu, Jiwon Lee, Hyunhyub Ko, Sang Kyu Kwak, and Joon Hak Oh. Boosting the performance of organic optoelec-

tronic devices using multiple-patterned plasmonic nanostructures. *Advanced Materials*, 28(25):4976–4982, 2016.

[15] Chi-Shen Lin, Xingyu Du, and Wei-Chih Lin. High photoresponse of gold nanorods/zinc oxide photodetector using localised surface plasmon resonance. *Sensors and Actuators A: Physical*, 326:112714, 2021. 1, 11, 207

[16] Yun-Sheng Chen, Yang Zhao, Soon Joon Yoon, Sanjiv Sam Gambhir, and Stanislav Emelianov. Miniature gold nanorods for photoacoustic molecular imaging in the second near-infrared optical window. *Nature nanotechnology*, 14(5):465–472, 2019. 1, 11, 14, 207

[17] Haifeng Wang, Terry B Huff, Daniel A Zweifel, Wei He, Philip S Low, Alexander Wei, and Ji-Xin Cheng. In vitro and in vivo two-photon luminescence imaging of single gold nanorods. *Proceedings of the National Academy of Sciences*, 102(44): 15752–15756, 2005. 14

[18] Tianxun Gong, Malini Olivo, US Dinish, Douglas Goh, Kien Voon Kong, and Ken-Tye Yong. Engineering bioconjugated gold nanospheres and gold nanorods as label-free plasmon scattering probes for ultrasensitive multiplex dark-field imaging of cancer cells. *Journal of biomedical nanotechnology*, 9(6):985–991, 2013. 14

[19] Amy L Oldenburg, Matthew N Hansen, Tyler S Ralston, Alexander Wei, and Stephen A Boppart. Imaging gold nanorods in excised human breast carcinoma by spectroscopic optical coherence tomography. *Journal of materials chemistry*, 19 (35):6407–6411, 2009. 14

[20] Mohammad Eghtedari, Alexander Oraevsky, John A Copland, Nicholas A Kotov, Andre Conjusteau, and Massoud Motamedi. High sensitivity of in vivo detection of gold nanorods using a laser optoacoustic imaging system. *Nano letters*, 7(7): 1914–1918, 2007. 1, 11, 14, 207

[21] James WM Chon, Craig Bullen, Peter Zijlstra, and Min Gu. Spectral encoding on gold nanorods doped in a silica sol–gel matrix and its application to high-density

optical data storage. *Advanced Functional Materials*, 17(6):875–880, 2007. 1, 11, 207

[22] Jorge Pérez-Juste, Benito Rodríguez-González, Paul Mulvaney, and Luis M Liz-Marzán. Optical control and patterning of gold-nanorod–poly (vinyl alcohol) nanocomposite films. *Advanced Functional Materials*, 15(7):1065–1071, 2005.

[23] Peter Zijlstra, James WM Chon, and Min Gu. Five-dimensional optical recording mediated by surface plasmons in gold nanorods. *nature*, 459(7245):410–413, 2009. 52

[24] Adam B Taylor, Pierrette Michaux, Abu SM Mohsin, and James WM Chon. Electron-beam lithography of plasmonic nanorod arrays for multilayered optical storage. *Optics Express*, 22(11):13234–13243, 2014.

[25] Min Gu, Qiming Zhang, and Simone Lamon. Nanomaterials for optical data storage. *Nature Reviews Materials*, 1(12):1–14, 2016.

[26] Adam B Taylor, Jooho Kim, and James WM Chon. Detuned surface plasmon resonance scattering of gold nanorods for continuous wave multilayered optical recording and readout. *Optics Express*, 20(5):5069–5081, 2012. 1, 11, 207

[27] Anthony S Stender, Gufeng Wang, Wei Sun, and Ning Fang. Influence of gold nanorod geometry on optical response. *ACS nano*, 4(12):7667–7675, 2010. 1, 10, 59, 207

[28] Hui Bin Jeon, Philippe Vuka Tsalu, and Ji Won Ha. Shape effect on the refractive index sensitivity at localized surface plasmon resonance inflection points of single gold nanocubes with vertices. *Scientific reports*, 9(1):1–8, 2019.

[29] Otto L Muskens, Guillaume Bachelier, Natalia Del Fatti, Fabrice Vallee, Arnaud Brioude, Xuchuan Jiang, and Marie-Paule Pileni. Quantitative absorption spectroscopy of a single gold nanorod. *The Journal of Physical Chemistry C*, 112(24): 8917–8921, 2008.

[30] William J Kennedy, Sarah Izor, Bryan D Anderson, Geoffrey Frank, Vikas Varshney, and Gregory J Ehlert. Thermal reshaping dynamics of gold nanorods: influence of

size, shape, and local environment. *ACS applied materials & interfaces*, 10(50): 43865–43873, 2018. 1, 10, 59, 61, 68, 207

[31] Nidhi Raval, Rahul Maheshwari, Dnyaneshwar Kalyane, Susanne R Youngren-Ortiz, Mahavir B Chougule, and Rakesh K Tekade. Importance of physicochemical characterization of nanoparticles in pharmaceutical product development. In *Basic Fundamentals Of Drug Delivery*, pages 369–400. Elsevier, 2019. 1, 21, 207

[32] David B Williams and C Barry Carter. The transmission electron microscope. In *Transmission electron microscopy*, pages 3–17. Springer, 1996. 1, 21, 184, 207

[33] Guojun Weng, Ying Qi, Jianjun Li, and Junwu Zhao. Size-dependent production of radicals in catalyzed reduction of eosin y using gold nanorods. *Journal of Nanoparticle Research*, 17(9):1–11, 2015. 1, 22, 207

[34] Peter Eaton and Paul West. *Atomic force microscopy.* Oxford university press, 2010. 1, 2, 22, 207

[35] Yves F Dufrêne, Toshio Ando, Ricardo Garcia, David Alsteens, David Martinez-Martin, Andreas Engel, Christoph Gerber, and Daniel J Müller. Imaging modes of atomic force microscopy for application in molecular and cell biology. *Nature nanotechnology*, 12(4):295–307, 2017. 2, 22, 207

[36] A Rao, M Schoenenberger, E Gnecco, Th Glatzel, E Meyer, D Brändlin, and L Scandella. Characterization of nanoparticles using atomic force microscopy. In *Journal of Physics: Conference Series*, volume 61, page 192. IOP Publishing, 2007.

[37] Shuchen Hsieh, Sheffer Meltzer, CR Chris Wang, Aristides AG Requicha, Mark E Thompson, and Bruce E Koel. Imaging and manipulation of gold nanorods with an atomic force microscope. *The Journal of Physical Chemistry B*, 106(2):231–234, 2002. 22, 23

[38] D Grainger and D Castner. Surface analysis and biointerfaces: Vacuum and ambient in situ techniques. In *Comprehensive Biomaterials*, pages 1–22. Elsevier, 2011. 1, 2, 22, 23

[39] Emilia Tomaszewska, Katarzyna Soliwoda, Kinga Kadziola, Beata Tkacz-Szczesna, Grzegorz Celichowski, Michal Cichomski, Witold Szmaja, and Jaroslaw Grobelny. Detection limits of dls and uv-vis spectroscopy in characterization of polydisperse nanoparticles colloids. *Journal of Nanomaterials*, 2013, 2013. 1, 2, 23, 207

[40] Michael Glidden and Martin Muschol. Characterizing gold nanorods in solution using depolarized dynamic light scattering. *The Journal of Physical Chemistry C*, 116(14):8128–8137, 2012. 24

[41] J Naveen, D Gajanan, and R Menon. Dynamic light scattering: advantages and applications. *Acta Sci Nutr Health*, 3(3):50–52, 2017. 2, 24

[42] Helin Liu, Nickisha Pierre-Pierre, and Qun Huo. Dynamic light scattering for gold nanorod size characterization and study of nanorod–protein interactions. *Gold bulletin*, 45(4):187–195, 2012. 1, 2, 23, 24, 207

[43] Rahul Kumar, Leonardo Binetti, T Hien Nguyen, Lourdes SM Alwis, Arti Agrawal, Tong Sun, and Kenneth TV Grattan. Determination of the aspect-ratio distribution of gold nanorods in a colloidal solution using uv-visible absorption spectroscopy. *Scientific reports*, 9(1):1–10, 2019. 1, 2, 25, 207

[44] Hui Bin Jeon, Philippe Vuka Tsalu, and Ji Won Ha. Shape effect on the refractive index sensitivity at localized surface plasmon resonance inflection points of single gold nanocubes with vertices. *Scientific reports*, 9(1):1–8, 2019. 25

[45] Johan Grand, Baptiste Auguié, and Eric C Le Ru. Combined extinction and absorption uv–visible spectroscopy as a method for revealing shape imperfections of metallic nanoparticles. *Analytical chemistry*, 91(22):14639–14648, 2019. 1, 2, 25, 207

[46] Bonnie O Leung and Keng C Chou. Review of super-resolution fluorescence microscopy for biology. *Applied spectroscopy*, 65(9):967–980, 2011. 3, 44, 211

[47] Rainer Heintzmann and Thomas Huser. Super-resolution structured illumination microscopy. *Chemical reviews*, 117(23):13890–13908, 2017. 3, 44, 45, 46

[48] Yicong Wu and Hari Shroff. Faster, sharper, and deeper: structured illumination microscopy for biological imaging. *Nature methods*, 15(12):1011–1019, 2018. 45

[49] Tianyu Zhao, Zhaojun Wang, Tongsheng Chen, Ming Lei, Baoli Yao, and Piero R Bianco. Advances in high-speed structured illumination microscopy. *Frontiers in Physics*, 9:298, 2021. 3, 44, 45, 46

[50] Stefan W Hell and Jan Wichmann. Breaking the diffraction resolution limit by stimulated emission: stimulated-emission-depletion fluorescence microscopy. *Optics letters*, 19(11):780–782, 1994. 3, 44, 46, 211

[51] Dominik Wildanger, Johanna Bückers, Volker Westphal, Stefan W Hell, and Lars Kastrup. A sted microscope aligned by design. *Optics Express*, 17(18):16100–16110, 2009. 47

[52] Steffen J Sahl and Stefan W Hell. High-resolution 3d light microscopy with sted and resolft. *High resolution imaging in microscopy and ophthalmology*, pages 3–32, 2019. 3, 44, 46, 48, 211

[53] Michael J Rust, Mark Bates, and Xiaowei Zhuang. Sub-diffraction-limit imaging by stochastic optical reconstruction microscopy (storm). *Nature methods*, 3(10): 793–796, 2006. 3, 44, 48, 211

[54] Eric Betzig, George H Patterson, Rachid Sougrat, O Wolf Lindwasser, Scott Olenych, Juan S Bonifacino, Michael W Davidson, Jennifer Lippincott-Schwartz, and Harald F Hess. Imaging intracellular fluorescent proteins at nanometer resolution. *Science*, 313(5793):1642–1645, 2006.

[55] Bo Huang, Wenqin Wang, Mark Bates, and Xiaowei Zhuang. Three-dimensional super-resolution imaging by stochastic optical reconstruction microscopy. *Science*, 319(5864):810–813, 2008. 3, 44, 48, 49, 211

[56] MP McDonald, F Vietmeyer, D Aleksiuk, and M Kuno. Supercontinuum spatial modulation spectroscopy: detection and noise limitations. *Review of Scientific Instruments*, 84(11):113104, 2013. 3, 44, 51

[57] Subhasis Adhikari, Patrick Spaeth, Ashish Kar, Martin Dieter Baaske, Saumyakanti Khatua, and Michel Orrit. Photothermal microscopy: imaging the optical absorption

of single nanoparticles and single molecules. *ACS nano*, 14(12):16414–16445, 2020. 3, 44, 51

[58] Rafael Fuentes-Domínguez, Shakila Naznin, Leonel Marques, Fernando Pérez-Cota, Richard J Smith, and Matt Clark. Characterising the size and shape of metallic nano-structures by their acoustic vibrations. *Nanoscale*, 12(26):14230–14236, 2020. 3, 27, 28, 37, 39, 78

[59] Rafael Fuentes-Domínguez, Richard J Smith, Fernando Pérez-Cota, Leonel Marques, Ovidio Peña-Rodríguez, and Matt Clark. Size characterisation method and detection enhancement of plasmonic nanoparticles in a pump–probe system. *Applied Sciences*, 7(8):819, 2017. 3, 39

[60] Rafael Fuentes-Domínguez, Fernando Pérez-Cota, Shakila Naznin, Richard J Smith, and Matt Clark. Super-resolution imaging using nano-bells. *Scientific Reports*, 8(1): 1–9, 2018. 3, 4, 27, 28, 37, 40, 78, 209, 227

[61] Anton Liopo, André Conjusteau, Dmitri Tsyboulski, Boris Ermolinsky, Alexander V Kazanksy, and Alexander Oraevsky. Biocompatible gold nanorod conjugates for preclinical biomedical research. *Journal of nanomedicine & nanotechnology*, 2012. 4, 146

[62] Ravi Shukla, Vipul Bansal, Minakshi Chaudhary, Atanu Basu, Ramesh R Bhonde, and Murali Sastry. Biocompatibility of gold nanoparticles and their endocytotic fate inside the cellular compartment: a microscopic overview. *Langmuir*, 21(23): 10644–10654, 2005. 13, 146

[63] Shouju Wang and Guangming Lu. Applications of gold nanoparticles in cancer imaging and treatment. *Noble and Precious Metals—Properties, Nanoscale Effects and Applications*, 1:291–309, 2018. 4

[64] Ian Freestone, Nigel Meeks, Margaret Sax, and Catherine Higgitt. The lycurgus cup—a roman nanotechnology. *Gold bulletin*, 40(4):270–277, 2007. 9

[65] Michael Faraday. X. the bakerian lecture.—experimental relations of gold (and other

metals) to light. *Philosophical Transactions of the Royal Society of London*, (147): 145–181, 1857. 10

[66] Gustav Mie. Contributions to the optics of turbid media, particularly of colloidal metal solutions. *Contributions to the optics of turbid media*, 25(3):377–445, 1976. 10

[67] R v Gans. Über die form ultramikroskopischer silberteilchen. *Annalen der Physik*, 352(10):270–284, 1915. 10

[68] Eliza Hutter and Janos H Fendler. Exploitation of localized surface plasmon resonance. *Advanced materials*, 16(19):1685–1706, 2004. 10, 207

[69] SS Verma and Jagmeet Singh Sekhon. Influence of aspect ratio and surrounding medium on localized surface plasmon resonance (lspr) of gold nanorod. *Journal of Optics*, 41(2):89–93, 2012. 10, 11, 207

[70] MAC Potenza, Ž Krpetić, T Sanvito, Q Cai, M Monopoli, JM De Araujo, C Cella, L Boselli, V Castagnola, P Milani, et al. Detecting the shape of anisotropic gold nanoparticles in dispersion with single particle extinction and scattering. *Nanoscale*, 9(8):2778–2784, 2017. 12

[71] Joseph R Cole, Nikolay A Mirin, Mark W Knight, Glenn P Goodrich, and Naomi J Halas. Photothermal efficiencies of nanoshells and nanorods for clinical therapeutic applications. *The Journal of Physical Chemistry C*, 113(28):12090–12094, 2009. 12

[72] Yang Liu, Jeffrey R Ashton, Everett J Moding, Hsiangkuo Yuan, Janna K Register, Andrew M Fales, Jaeyeon Choi, Melodi J Whitley, Xiaoguang Zhao, Yi Qi, et al. A plasmonic gold nanostar theranostic probe for in vivo tumor imaging and photothermal therapy. *Theranostics*, 5(9):946, 2015. 12

[73] Ferenc Liebig, Radwan M Sarhan, Matias Bargheer, Clemens NZ Schmitt, Armen H Poghosyan, Aram A Shahinyan, and Joachim Koetz. Spiked gold nanotriangles: formation, characterization and applications in surface-enhanced raman spectroscopy and plasmon-enhanced catalysis. *RSC Advances*, 10(14):8152–8160, 2020. 12

[74] Younan Xia, Weiyang Li, Claire M Cobley, Jingyi Chen, Xiaohu Xia, Qiang Zhang, Miaoxin Yang, Eun Chul Cho, and Paige K Brown. Gold nanocages: from synthesis to theranostic applications. *Accounts of chemical research*, 44(10):914–924, 2011. 12

[75] B Karlik, MF Yilmaz, M Ozdemir, CT Yavuz, and Y Danisman. A hybrid machine learning model to study uv-vis spectra of gold nanospheres. *Plasmonics*, 16(1): 147–155, 2021. 12

[76] Tamara Muñoz-Ortiz, Jie Hu, Dirk H Ortgies, Shreya Shrikhande, Paula Zamora-Perez, Miriam Granado, Daniel González-Hedström, María de la Fuente-Fernández, Ángel Luis García-Villalón, Laura Andrés-Delgado, et al. Molecular imaging of infarcted heart by biofunctionalized gold nanoshells. *Advanced Healthcare Materials*, 10(10):2002186, 2021. 12

[77] Ren Odion, Yang Liu, and Tuan Vo-Dinh. Plasmonic gold nanostar-mediated photothermal immunotherapy. *IEEE Journal of Selected Topics in Quantum Electronics*, 27(5):1–9, 2021. 12

[78] Joachim Koetz. The effect of surface modification of gold nanotriangles for surface-enhanced raman scattering performance. *Nanomaterials*, 10(11):2187, 2020. 12

[79] Huamei He, Lanlan Liu, Shengping Zhang, Mingbin Zheng, Aiqing Ma, Ze Chen, Hong Pan, Haimei Zhou, Ruijing Liang, and Lintao Cai. Smart gold nanocages for mild heat-triggered drug release and breaking chemoresistance. *Journal of Controlled Release*, 323:387–397, 2020. 12

[80] Jeremy B Vines, Jee-Hyun Yoon, Na-Eun Ryu, Dong-Jin Lim, and Hansoo Park. Gold nanoparticles for photothermal cancer therapy. *Frontiers in chemistry*, 7:167, 2019. 13

[81] Huang-Chiao Huang, Sutapa Barua, David B Kay, and Kaushal Rege. Simultaneous enhancement of photothermal stability and gene delivery efficacy of gold nanorods using polyelectrolytes. *Acs Nano*, 3(10):2941–2952, 2009. 13

[82] Partha Ghosh, Gang Han, Mrinmoy De, Chae Kyu Kim, and Vincent M Rotello.

Gold nanoparticles in delivery applications. *Advanced drug delivery reviews*, 60(11): 1307–1315, 2008. 13

[83] Xiaohua Huang, Svetlana Neretina, and Mostafa A El-Sayed. Gold nanorods: from synthesis and properties to biological and biomedical applications. *Advanced materials*, 21(48):4880–4910, 2009. 14, 214

[84] Nikhil R Jana, Latha Gearheart, and Catherine J Murphy. Seed-mediated growth approach for shape-controlled synthesis of spheroidal and rod-like gold nanoparticles using a surfactant template. *Advanced Materials*, 13(18):1389–1393, 2001. 14, 214

[85] Nikhil R Jana, Latha Gearheart, and Catherine J Murphy. Wet chemical synthesis of high aspect ratio cylindrical gold nanorods. *The Journal of Physical Chemistry B*, 105(19):4065–4067, 2001. 15

[86] Babak Nikoobakht and Mostafa A El-Sayed. Preparation and growth mechanism of gold nanorods (nrs) using seed-mediated growth method. *Chemistry of Materials*, 15(10):1957–1962, 2003. 15

[87] Jie Cao, Tong Sun, and Kenneth TV Grattan. Gold nanorod-based localized surface plasmon resonance biosensors: A review. *Sensors and actuators B: Chemical*, 195: 332–351, 2014. 15, 62

[88] Xingchen Ye, Linghua Jin, Humeyra Caglayan, Jun Chen, Guozhong Xing, Chen Zheng, Vicky Doan-Nguyen, Yijin Kang, Nader Engheta, Cherie R Kagan, et al. Improved size-tunable synthesis of monodisperse gold nanorods through the use of aromatic additives. *ACS nano*, 6(3):2804–2817, 2012. 15

[89] Xiaolong Xu, Yuanyuan Zhao, Xiangdong Xue, Shuaidong Huo, Fei Chen, Guozhang Zou, and Xing-Jie Liang. Seedless synthesis of high aspect ratio gold nanorods with high yield. *Journal of Materials Chemistry A*, 2(10):3528–3535, 2014. 15

[90] Yu-Ying Yu, Ser-Sing Chang, Chien-Liang Lee, and CR Chris Wang. Gold nanorods: electrochemical synthesis and optical properties. *The Journal of Physical Chemistry B*, 101(34):6661–6664, 1997. 15

[91] Franklin Kim, Jae Hee Song, and Peidong Yang. Photochemical synthesis of gold nanorods. *Journal of the American Chemical Society*, 124(48):14316–14317, 2002. 15

[92] Colby A Foss Jr, Gabor L Hornyak, Jon A Stockert, and Charles R Martin. Template-synthesized nanoscopic gold particles: optical spectra and the effects of particle size and shape. *The Journal of Physical Chemistry*, 98(11):2963–2971, 1994. 15

[93] Huanjun Chen, Xiaoshan Kou, Zhi Yang, Weihai Ni, and Jianfang Wang. Shape-and size-dependent refractive index sensitivity of gold nanoparticles. *Langmuir*, 24(10): 5233–5237, 2008. 15

[94] Sathish Sugumaran, Mohd Faizal Jamlos, Mohd Noor Ahmad, Chandar Shekar Bellan, and Dominique Schreurs. Nanostructured materials with plasmonic nanobiosensors for early cancer detection: a past and future prospect. *Biosensors and Bioelectronics*, 100:361–373, 2018. 15

[95] J Orloff. Focused ion beam characterization techniques. 2016. 15

[96] Choloong Hahn, Akram Hajebifard, and Pierre Berini. Helium focused ion beam direct milling of plasmonic heptamer-arranged nanohole arrays. *Nanophotonics*, 9 (2):393–399, 2020. 15

[97] Gediminas Seniutinas, Armandas Balčytis, Yoshiaki Nishijima, Achim Nadzeyka, Sven Bauerdick, and Saulius Juodkazis. Ion beam lithography with gold and silicon ions. *Applied Physics A*, 122(4):383, 2016. 16

[98] Michal Horák, Kristỳna Bukvišová, Vojtěch Švarc, Jiří Jaskowiec, Vlastimil Křápek, and Tomáš Šikola. Comparative study of plasmonic antennas fabricated by electron beam and focused ion beam lithography. *Scientific reports*, 8(1):1–8, 2018.

[99] Priscila Romagnoli, Maki Maeda, Jonathan M Ward, Viet Giang Truong, and Síle Nic Chormaic. Fabrication of optical nanofibre-based cavities using focussed ion-beam milling: a review. *Applied Physics B*, 126:1–16, 2020. 15

[100] Vitor R Manfrinato, Lihua Zhang, Dong Su, Huigao Duan, Richard G Hobbs, Eric A Stach, and Karl K Berggren. Resolution limits of electron-beam lithography toward the atomic scale. *Nano letters*, 13(4):1555–1558, 2013. 16

[101] Christophe Vieu, F Carcenac, A Pepin, Y Chen, M Mejias, A Lebib, L Manin-Ferlazzo, L Couraud, and H Launois. Electron beam lithography: resolution limits and applications. *Applied surface science*, 164(1-4):111–117, 2000. 16

[102] Shaurya Prakash and Junghoon Yeom. *Nanofluidics and microfluidics: systems and applications.* William Andrew, 2014. 17

[103] Bryan Cord, Joel Yang, Huigao Duan, David C Joy, Joseph Klingfus, and Karl K Berggren. Limiting factors in sub-10 nm scanning-electron-beam lithography. *Journal of Vacuum Science & Technology B: Microelectronics and Nanometer Structures Processing, Measurement, and Phenomena*, 27(6):2616–2621, 2009. 17

[104] Neval A Cinel, Serkan Bütün, and Ekmel Özbay. Electron beam lithography designed silver nano-disks used as label free nano-biosensors based on localized surface plasmon resonance. *Optics express*, 20(3):2587–2597, 2012. 19

[105] Kosei Ueno, Saulius Juodkazis, Masahiro Mino, Vygantas Mizeikis, and Hiroaki Misawa. Spectral sensitivity of uniform arrays of gold nanorods to dielectric environment. *The Journal of Physical Chemistry C*, 111(11):4180–4184, 2007. 19

[106] Wei-Shun Chang, Fangfang Wen, Debadi Chakraborty, Man-Nung Su, Yue Zhang, Bo Shuang, Peter Nordlander, John E Sader, Naomi J Halas, and Stephan Link. Tuning the acoustic frequency of a gold nanodisk through its adhesion layer. *Nature communications*, 6(1):1–8, 2015. 19

[107] Yongbin Lin, Yang Zou, Yuanyao Mo, Junpeng Guo, and Robert G Lindquist. E-beam patterned gold nanodot arrays on optical fiber tips for localized surface plasmon resonance biochemical sensing. *Sensors*, 10(10):9397–9406, 2010. 19

[108] Adam B Taylor, Pierrette Michaux, Abu SM Mohsin, and James WM Chon. Electron-beam lithography of plasmonic nanorod arrays for multilayered optical storage. *Optics Express*, 22(11):13234–13243, 2014. 20

[109] Shaoli Zhu, Han-Hao Cheng, Idriss Blakey, Nicholas Stokes, Kostya Ken Ostrikov, and Michael Cortie. Plasmonic 'top-hat'nano-star arrays by electron beam lithography. *Microelectronic Engineering*, 139:13–18, 2015. 20

[110] Luis Gutierrez-Rivera, Robert F Peters, Steven K Dew, and Maria Stepanova. Application of ebl fabricated nanostructured substrates for surface enhanced raman spectroscopy detection of protein a in aqueous solution. *Journal of Vacuum Science & Technology B, Nanotechnology and Microelectronics: Materials, Processing, Measurement, and Phenomena*, 31(6):06F901, 2013. 19, 20

[111] AA Maznev, Kara J Manke, Kung-Hsuan Lin, Keith A Nelson, Chi-Kuang Sun, and Jen-Inn Chyi. Broadband terahertz ultrasonic transducer based on a laser-driven piezoelectric semiconductor superlattice. *Ultrasonics*, 52(1):1–4, 2012. 26

[112] FE Lytle, RM Parrish, and WT Barnes. An introduction to time-resolved pump/probe spectroscopy. *Applied spectroscopy*, 39(3):444–451, 1985. 26, 88

[113] C Thomsen, J Strait, Z Vardeny, Humphrey J Maris, J Tauc, and JJ Hauser. Coherent phonon generation and detection by picosecond light pulses. *Physical Review Letters*, 53(10):989, 1984. 26, 28, 29, 78

[114] C Thomsen, Holger T Grahn, Humphrey J Maris, and Jan Tauc. Surface generation and detection of phonons by picosecond light pulses. *Physical Review B*, 34(6):4129, 1986. 26, 28, 29, 78, 89

[115] Léon Brillouin. Diffusion de la lumière et des rayons x par un corps transparent homogène. In *Annales de physique*, volume 9, pages 88–122, 1922. 27, 34, 89

[116] C Thomsen, HT Grahn, HJ Maris, and J Tauc. Picosecond interferometric technique for study of phonons in the brillouin frequency range. *Optics communications*, 60 (1-2):55–58, 1986. 27

[117] Richard J Smith, Fernando Perez Cota, Leonel Marques, Xuesheng Chen, Ahmet Arca, Kevin Webb, Jonathon Aylott, Micheal G Somekh, and Matt Clark. Optically excited nanoscale ultrasonic transducers. *The Journal of the Acoustical Society of America*, 137(1):219–227, 2015. 27, 31, 34

[118] Fernando Pérez-Cota, Richard J Smith, Emilia Moradi, Leonel Marques, Kevin F Webb, and Matt Clark. High resolution 3d imaging of living cells with sub-optical wavelength phonons. *Scientific reports*, 6(1):1–11, 2016. 27, 28, 34, 35, 52, 53, 217

[119] Paul A Elzinga, Fred E Lytle, Yanan Jian, Galen B King, and Normand M Laurendeau. Pump/probe spectroscopy by asynchronous optical sampling. *Applied spectroscopy*, 41(1):2–4, 1987. 27, 88

[120] Albrecht Bartels, Roland Cerna, Caroline Kistner, Arne Thoma, Florian Hudert, Christof Janke, and Thomas Dekorsy. Ultrafast time-domain spectroscopy based on high-speed asynchronous optical sampling. *Review of Scientific Instruments*, 78(3): 035107, 2007. 27, 88

[121] Fernando Pérez-Cota, Richard J Smith, Emilia Moradi, Leonel Marques, Kevin F Webb, and Matt Clark. Thin-film optoacoustic transducers for subcellular brillouin oscillation imaging of individual biological cells. *Applied optics*, 54(28):8388–8398, 2015. 27, 28, 31

[122] Thomas Dehoux, Maroun Abi Ghanem, OF Zouani, J-M Rampnoux, Yannick Guillet, Stefan Dilhaire, M-C Durrieu, and Bertrand Audoin. All-optical broadband ultrasonography of single cells. *Scientific reports*, 5(1):1–5, 2015. 27

[123] Osamu Matsuda, Maria Cristina Larciprete, Roberto Li Voti, and Oliver B Wright. Fundamentals of picosecond laser ultrasonics. *Ultrasonics*, 56:3–20, 2015. 28

[124] O Matsuda and OB Wright. Reflection and transmission of light in multilayers perturbed by picosecond strain pulse propagation. *JOSA B*, 19(12):3028–3041, 2002. 28, 34, 35

[125] T Stratoudaki, JA Hernandez, M Clark, and Michael Geoffrey Somekh. Cheap optical transducers (chots) for narrowband ultrasonic applications. *Measurement Science and Technology*, 18(3):843, 2007. 28

[126] P Babilotte, P Ruello, D Mounier, T Pezeril, G Vaudel, M Edely, Jean-Marc Breteau, V Gusev, and K Blary. Femtosecond laser generation and detection of high-frequency

acoustic phonons in gaas semiconductors. *Physical Review B*, 81(24):245207, 2010. 28

[127] Serguei Stepanov and Fernando Pérez Cota. Transient two-wave mixing in a linear configuration of an adaptive interferometer based on er-doped fiber with saturable absorption. *Optics letters*, 32(17):2532–2534, 2007. 29, 78

[128] RK Ing and J-P Monchalin. Broadband optical detection of ultrasound by two-wave mixing in a photorefractive crystal. *Applied physics letters*, 59(25):3233–3235, 1991. 29

[129] Jean-Pierre Monchalin. Optical detection of ultrasound at a distance using a confocal fabry–perot interferometer. *Applied Physics Letters*, 47(1):14–16, 1985. 29

[130] Jouni V Knuuttila, Pasi T Tikka, and Martti M Salomaa. Scanning michelson interferometer for imaging surface acoustic wave fields. *Optics letters*, 25(9):613–615, 2000. 29

[131] Takehiro Tachizaki, Toshihiro Muroya, Osamu Matsuda, Yoshihiro Sugawara, David H Hurley, and Oliver B Wright. Scanning ultrafast sagnac interferometry for imaging two-dimensional surface wave propagation. *Review of Scientific Instruments*, 77(4):043713, 2006. 29, 78

[132] D Karabacak, T Kouh, CC Huang, and KL Ekinci. Optical knife-edge technique for nanomechanical displacement detection. *Applied physics letters*, 88(19):193122, 2006. 29, 78

[133] M Clark. Optical detection of ultrasound on rough surfaces using speckle correlated spatial filtering. In *Journal of Physics: Conference Series*, volume 278, page 012025. IOP Publishing, 2011. 30

[134] SD Sharpies, RA Light, SO Achamfuo-Yeboah, M Clark, and Michael Geoffrey Somekh. The sked: speckle knife edge detector. In *Journal of Physics: Conference Series*, volume 520, page 012004. IOP Publishing, 2014. 30, 78

[135] N Chigarev, C Rossignol, and B Audoin. Beam distortion detection technique for picosecond ultrasonics. In *Journal of Physics: Conference Series*, volume 92, page 012178. IOP Publishing, 2007. 31, 78

[136] WRC Somerville, B Auguié, and EC Le Ru. Smarties: User-friendly codes for fast and accurate calculations of light scattering by spheroids. *Journal of Quantitative Spectroscopy and Radiative Transfer*, 174:39–55, 2016. 32, 55, 58, 59, 208

[137] Gary L Eesley, Bruce M Clemens, and Carolyn A Paddock. Generation and detection of picosecond acoustic pulses in thin metal films. *Applied physics letters*, 50(12):717–719, 1987. 34, 35

[138] Hirotsugu Ogi, Tomohiro Shagawa, Nobutomo Nakamura, Masahiko Hirao, Hidefumi Odaka, and Naoto Kihara. Elastic-constant measurement in oxide and semiconductor thin films by brillouin oscillations excited by picosecond ultrasound. *Japanese Journal of Applied Physics*, 48(7S):07GA01, 2009. 35

[139] Carmen M Hernandez, Todd W Murray, and Sridhar Krishnaswamy. Photoacoustic characterization of the mechanical properties of thin films. *Applied physics letters*, 80(4):691–693, 2002.

[140] P Emery and A Devos. Acoustic attenuation measurements in transparent materials in the hypersonic range by picosecond ultrasonics. *Applied physics letters*, 89(19): 191904, 2006. 35

[141] CJ Morath and HJ Maris. Phonon attenuation in amorphous solids studied by picosecond ultrasonics. *Physical Review B*, 54(1):203, 1996. 35

[142] Simon Ayrinhac, Marie Foret, Arnaud Devos, Benoît Rufflé, Eric Courtens, and René Vacher. Subterahertz hypersound attenuation in silica glass studied via picosecond acoustics. *Physical Review B*, 83(1):014204, 2011.

[143] H-N Lin, RJ Stoner, HJ Maris, and J Tauc. Phonon attenuation and velocity measurements in transparent materials by picosecond acoustic interferometry. *Journal of applied physics*, 69(7):3816–3822, 1991. 35

[144] C Rossignol, Bernard Perrin, S Laborde, L Vandenbulcke, MI De Barros, and P Djemia. Nondestructive evaluation of micrometric diamond films with an interferometric picosecond ultrasonics technique. *Journal of applied physics*, 95(8): 4157–4162, 2004. 35

[145] DH Hurley, OB Wright, O Matsuda, VE Gusev, and OV Kolosov. Laser picosecond acoustics in isotropic and anisotropic materials. *Ultrasonics*, 38(1-8):470–474, 2000. 35

[146] F Yang, TJ Grimsley, S Che, GA Antonelli, HJ Maris, and AV Nurmikko. Picosecond ultrasonic experiments with water and its application to the measurement of nanostructures. *Journal of Applied Physics*, 107(10):103537, 2010. 35

[147] Salvatore La Cavera, Fernando Pérez-Cota, Rafael Fuentes-Domínguez, Richard J Smith, and Matt Clark. Time resolved brillouin fiber-spectrometer. *Optics express*, 27(18):25064–25071, 2019. 35

[148] Sorasak Danworaphong, Motonobu Tomoda, Yuki Matsumoto, Osamu Matsuda, Toshiro Ohashi, Hiromu Watanabe, Masafumi Nagayama, Kazutoshi Gohara, Paul H Otsuka, and Oliver B Wright. Three-dimensional imaging of biological cells with picosecond ultrasonics. *Applied physics letters*, 106(16):163701, 2015. 35

[149] Liwang Liu, Alexis Viel, Guillaume Le Saux, Laurent Plawinski, Giovanna Muggiolu, Philippe Barberet, Marco Pereira, Cédric Ayela, Hervé Seznec, Marie-Christine Durrieu, et al. Remote imaging of single cell 3d morphology with ultrafast coherent phonons and their resonance harmonics. *Scientific reports*, 9(1):1–12, 2019.

[150] Fernando Pérez-Cota, Rafael Fuentes-Domínguez, Salvatore La Cavera, William Hardiman, Mengting Yao, Kerry Setchfield, Emilia Moradi, Shakila Naznin, Amanda Wright, Kevin F Webb, et al. Picosecond ultrasonics for elasticity-based imaging and characterization of biological cells. *Journal of Applied Physics*, 128(16):160902, 2020. 35, 53

[151] Clément Rossignol, Nikolay Chigarev, M Ducousso, B Audoin, Guillaume Forget,

F Guillemot, and MC Durrieu. In vitro picosecond ultrasonics in a single cell. *Applied Physics Letters*, 93(12):123901, 2008.

[152] Mathieu Ducousso, Omar El-Farouk Zouani, Christel Chanseau, Céline Chollet, Clément Rossignol, Bertrand Audoin, and Marie-Christine Durrieu. Evaluation of mechanical properties of fixed bone cells with sub-micrometer thickness by picosecond ultrasonics. *The European Physical Journal Applied Physics*, 61(1):11201, 2013.

[153] Vitalyi E Gusev and Pascal Ruello. Advances in applications of time-domain brillouin scattering for nanoscale imaging. *Applied Physics Reviews*, 5(3):031101, 2018.

[154] Marie-Fraise Ponge, Liwang Liu, Christophe Aristégui, and Bertrand Audoin. Scattering of ghz coherent acoustic phonons by silica nanoparticles in water probed with the time-domain brillouin spectroscopy. *Applied Physics Letters*, 115(13):133101, 2019. 35

[155] Salvatore La Cavera, Fernando Pérez-Cota, Richard J Smith, and Matt Clark. Phonon imaging in 3d with a fibre probe. *Light: Science & Applications*, 10(1): 1–13, 2021. 34, 36

[156] Horace Lamb. On the vibrations of an elastic sphere. *Proceedings of the London Mathematical Society*, 1(1):189–212, 1881. 36

[157] VA Dubrovskiy and VS Morochnik. Natural vibrations of a spherical inhomogeneity in an elastic medium. *Izv. Earth Phys*, 17:494–504, 1981. 36

[158] Hervé Portales, L Saviot, Eugene Duval, Minoru Fujii, Shinji Hayashi, N Del Fatti, and F Vallée. Resonant raman scattering by breathing modes of metal nanoparticles. *The Journal of Chemical Physics*, 115(8):3444–3447, 2001. 36

[159] Mauro Nisoli, Sandro De Silvestri, A Cavalleri, AM Malvezzi, A Stella, Guglielmo Lanzani, P Cheyssac, and R Kofman. Coherent acoustic oscillations in metallic nanoparticles generated with femtosecond optical pulses. *Physical Review B*, 55(20): R13424, 1997. 36

[160] Anna L Tchebotareva, Meindert A Van Dijk, Paul V Ruijgrok, Vincent Fokkema, Marcel HS Hesselberth, Markus Lippitz, and Michel Orrit. Acoustic and optical

modes of single dumbbells of gold nanoparticles. *ChemPhysChem*, 10(1):111–114, 2009. 37

[161] Arman S Kirakosyan and Tigran V Shahbazyan. Vibrational modes of metal nanoshells and bimetallic core-shell nanoparticles. *The Journal of chemical physics*, 129(3):034708, 2008. 37

[162] Min Hu, Xuan Wang, Gregory V Hartland, Paul Mulvaney, Jorge Perez Juste, and John E Sader. Vibrational response of nanorods to ultrafast laser induced heating: theoretical and experimental analysis. *Journal of the American Chemical Society*, 125(48):14925–14933, 2003. 37, 55, 69, 76, 77, 84, 117, 119, 141, 142, 151, 187, 208

[163] Min Hu, Patrick Hillyard, Gregory V Hartland, Thomas Kosel, Jorge Perez-Juste, and Paul Mulvaney. Determination of the elastic constants of gold nanorods produced by seed mediated growth. *Nano Letters*, 4(12):2493–2497, 2004. 38

[164] Hristina Petrova, Jorge Perez-Juste, Zhenyuan Zhang, Jing Zhang, Tom Kosel, and Gregory V Hartland. Crystal structure dependence of the elastic constants of gold nanorods. *Journal of Materials Chemistry*, 16(40):3957–3963, 2006. 38

[165] Peter Zijlstra, Anna L Tchebotareva, James WM Chon, Min Gu, and Michel Orrit. Acoustic oscillations and elastic moduli of single gold nanorods. *Nano letters*, 8(10): 3493–3497, 2008. 38, 53, 119, 142, 204

[166] Bernhard Reischl, Andrew L Rohl, Antti Kuronen, and Kai Nordlund. Atomistic simulation of the measurement of mechanical properties of gold nanorods by afm. *Scientific reports*, 7(1):1–8, 2017. 38

[167] Mahmoud A Mahmoud, Daniel O'Neil, and Mostafa A El-Sayed. Shape-and symmetry-dependent mechanical properties of metallic gold and silver on the nanoscale. *Nano letters*, 14(2):743–748, 2014. 38, 76, 119, 142

[168] Yong Gan, Chengquan Wang, and Zhen Chen. Ultrafast laser-excited vibration and elastic modulus of individual gold nanorods. *Optics letters*, 40(3):340–343, 2015. 38

[169] Yong Gan, Zheng Sun, and Zhen Chen. Breathing mode vibrations and elastic properties of single-crystal and penta-twinned gold nanorods. *Physical Chemistry Chemical Physics*, 18(32):22590–22598, 2016. 39

[170] Aurélien Crut, Paolo Maioli, Natalia Del Fatti, and Fabrice Vallée. Anisotropy effects on the time-resolved spectroscopy of the acoustic vibrations of nanoobjects. *Physical Chemistry Chemical Physics*, 11(28):5882–5888, 2009. 39

[171] Lucien Saviot. Vibrations of single-crystal gold nanorods and nanowires. *Physical Review B*, 97(15):155420, 2018. 39

[172] Jian Wu, Dao Xiang, and Reuven Gordon. Characterizing gold nanorods in aqueous solution by acoustic vibrations probed with four-wave mixing. *Optics express*, 24 (12):12458–12465, 2016. 39

[173] Kuai Yu, John E Sader, Peter Zijlstra, Minghui Hong, Qing-Hua Xu, and Michel Orrit. Probing silver deposition on single gold nanorods by their acoustic vibrations. *Nano letters*, 14(2):915–922, 2014. 39

[174] Damon A Wheeler, Thomas D Green, Haining Wang, Cristina Fernández-López, Luis Liz-Marzán, Shengli Zou, Kenneth L Knappenberger, and Jin Z Zhang. Optical properties and coherent vibrational oscillations of gold nanostars. *Chemical Physics Letters*, 543:127–132, 2012. 40

[175] Hristina Petrova, Chien-Hua Lin, Min Hu, Jingyi Chen, Andrew R Siekkinen, Younan Xia, John E Sader, and Gregory V Hartland. Vibrational response of au-ag nanoboxes and nanocages to ultrafast laser-induced heating. *Nano letters*, 7(4): 1059–1063, 2007. 40

[176] Kuai Yu, Peter Zijlstra, John E Sader, Qing-Hua Xu, and Michel Orrit. Damping of acoustic vibrations of immobilized single gold nanorods in different environments. *Nano letters*, 13(6):2710–2716, 2013. 40

[177] Chongyue Yi, Man-Nung Su, Pratiksha D Dongare, Debadi Chakraborty, Yi-Yu Cai, David M Marolf, Rachael N Kress, Behnaz Ostovar, Lawrence J Tauzin, Fangfang Wen, et al. Polycrystallinity of lithographically fabricated plasmonic nanostructures

dominates their acoustic vibrational damping. *Nano letters*, 18(6):3494–3501, 2018. 40

[178] Todd A Major, Aurélien Crut, Bo Gao, Shun Shang Lo, Natalia Del Fatti, Fabrice Vallée, and Gregory V Hartland. Damping of the acoustic vibrations of a suspended gold nanowire in air and water environments. *Physical Chemistry Chemical Physics*, 15(12):4169–4176, 2013. 40

[179] Carolina Novo, Daniel Gomez, Jorge Perez-Juste, Zhenyuan Zhang, Hristina Petrova, Maximilian Reismann, Paul Mulvaney, and Gregory V Hartland. Contributions from radiation damping and surface scattering to the linewidth of the longitudinal plasmon band of gold nanorods: a single particle study. *Physical Chemistry Chemical Physics*, 8(30):3540–3546, 2006.

[180] Kuai Yu, Peter Zijlstra, John E Sader, Qing-Hua Xu, and Michel Orrit. Damping of acoustic vibrations of immobilized single gold nanorods in different environments. *Nano letters*, 13(6):2710–2716, 2013. 40

[181] George Biddell Airy. On the diffraction of an object-glass with circular aperture. *Transactions of the Cambridge Philosophical Society*, 5:283, 1835. 41

[182] Eugene Hecht and Alfred Zajac. *Optics*, volume 4. Addison Wesley San Francisco, 2002. 41

[183] SG Lipson. H. lipson nd ds tannhauser, optical physics, 1998. 41

[184] Lord Raleigh. Investigations in optics with special reference to the spectroscopy. *Philos. Mag*, 8:261, 1879. 41

[185] Carroll Mason Sparrow. On spectroscopic resolving power. *The Astrophysical Journal*, 44:76, 1916. 41

[186] George H Patterson. Fluorescence microscopy below the diffraction limit. In *Seminars in cell & developmental biology*, volume 20, pages 886–893. Elsevier, 2009. 44

[187] Mariya Georgieva and Marcelo Nöllmann. Superresolution microscopy for bioimaging at the nanoscale: from concepts to applications in the nucleus. *Research and Reports in Biology*, 6:157–169, 2015.

[188] Bo Huang, Mark Bates, and Xiaowei Zhuang. Super-resolution fluorescence microscopy. *Annual review of biochemistry*, 78:993–1016, 2009. 44

[189] Francisco Balzarotti, Yvan Eilers, Klaus C Gwosch, Arvid H Gynnå, Volker Westphal, Fernando D Stefani, Johan Elf, and Stefan W Hell. Nanometer resolution imaging and tracking of fluorescent molecules with minimal photon fluxes. *Science*, 355(6325):606–612, 2017. 50

[190] Klaus C Gwosch, Jasmin K Pape, Francisco Balzarotti, Philipp Hoess, Jan Ellenberg, Jonas Ries, and Stefan W Hell. Minflux nanoscopy delivers 3d multicolor nanometer resolution in cells. *Nature methods*, 17(2):217–224, 2020. 50

[191] Michael Weber, Marcel Leutenegger, Stefan Stoldt, Stefan Jakobs, Tiberiu S Mihaila, Alexey N Butkevich, and Stefan W Hell. Minsted fluorescence localization and nanoscopy. *bioRxiv*, 2020. 50

[192] Luc S De Clerck, Chris H Bridts, Annemie M Mertens, Marleen M Moens, and Wim J Stevens. Use of fluorescent dyes in the determination of adherence of human leucocytes to endothelial cells and the effect of fluorochromes on cellular function. *Journal of immunological methods*, 172(1):115–124, 1994. 50

[193] Mary Sajini Devadas, Tuphan Devkota, Samit Guha, Scott K Shaw, Bradley D Smith, and Gregory V Hartland. Spatial modulation spectroscopy for imaging and quantitative analysis of single dye-doped organic nanoparticles inside cells. *Nanoscale*, 7(21):9779–9785, 2015. 51

[194] Dmitry A Nedosekin, Stephen Foster, Zeid A Nima, Alexandru S Biris, Ekaterina I Galanzha, and Vladimir P Zharov. Photothermal confocal multicolor microscopy of nanoparticles and nanodrugs in live cells. *Drug metabolism reviews*, 47(3):346–355, 2015. 51

[195] Mona B Mohamed, Kamal Z Ismail, Stephan Link, and Mostafa A El-Sayed. Thermal reshaping of gold nanorods in micelles. *The Journal of Physical Chemistry B*, 102 (47):9370–9374, 1998. 51

[196] O Ekici, RK Harrison, NJ Durr, DS Eversole, M Lee, and A Ben-Yakar. Thermal analysis of gold nanorods heated with femtosecond laser pulses. *Journal of physics D: Applied physics*, 41(18):185501, 2008. 52

[197] Stephan Link, Clemens Burda, B Nikoobakht, and Mostafa A El-Sayed. Laser-induced shape changes of colloidal gold nanorods using femtosecond and nanosecond laser pulses. *The Journal of Physical Chemistry B*, 104(26):6152–6163, 2000. 52

[198] Guillermo González-Rubio, Pablo Díaz-Núñez, Antonio Rivera, Alejandro Prada, Gloria Tardajos, Jesús González-Izquierdo, Luis Bañares, Pablo Llombart, Luis G Macdowell, Mauricio Alcolea Palafox, et al. Femtosecond laser reshaping yields gold nanorods with ultranarrow surface plasmon resonances. *Science*, 358(6363):640–644, 2017. xii, 52

[199] Junuthula Narasimha Reddy. *Introduction to the finite element method.* McGraw-Hill Education, 2019. 55

[200] S Tungjitkusolmun, EJ Woo, H Cao, JZ Tsai, VR Vorperian, and JG Webster. Thermal—electrical finite element modelling for radio frequency cardiac ablation: effects of changes in myocardial properties. *Medical and Biological Engineering and Computing*, 38(5):562–568, 2000. 56

[201] Abdelwahed Barkaoui, Imane Ait Oumghar, and Rabeb Ben Kahla. Review on the use of medical imaging in orthopedic biomechanics: finite element studies. *Computer Methods in Biomechanics and Biomedical Engineering: Imaging & Visualization*, pages 1–20, 2021. 56

[202] Hao Yang, Xiangyang Xu, and Ingo Neumann. An automatic finite element modelling for deformation analysis of composite structures. *Composite Structures*, 212: 434–438, 2019. 56

[203] Pedro Duarte Menezes, Nikolaj Gadegaard, Renato M Natal Jorge, and Sónia IS Pinto. Modelling human liver microphysiology on a chip through a finite element based design approach. *International Journal for Numerical Methods in Biomedical Engineering*, 37(5):e3445, 2021. 55, 56

[204] Xuezhi Zheng. Dedicated boundary element modeling for nanoparticle-on-mirror structures incorporating nonlocal hydrodynamic effects. *Advanced Theory and Simulations*, page 2200480, 2022. 55

[205] Stephen Martin Kirkup. *The boundary element method in acoustics*. Integrated sound software, 2007. 55

[206] Edward M Purcell and Carlton R Pennypacker. Scattering and absorption of light by nonspherical dielectric grains. *The Astrophysical Journal*, 186:705–714, 1973. 55, 57

[207] Shermila Brito Singham and Craig F Bohren. Light scattering by an arbitrary particle: a physical reformulation of the coupled dipole method. *Optics Letters*, 12 (1):10–12, 1987. 57

[208] Bruce T Draine and Piotr J Flatau. User guide for the discrete dipole approximation code ddscat 7.3. *arXiv preprint arXiv:1305.6497*, 2013. 57

[209] Prashant K Jain, Kyeong Seok Lee, Ivan H El-Sayed, and Mostafa A El-Sayed. Calculated absorption and scattering properties of gold nanoparticles of different size, shape, and composition: applications in biological imaging and biomedicine. *The journal of physical chemistry B*, 110(14):7238–7248, 2006. 57

[210] Mohammed Alsawafta, Mamoun Wahbeh, and Vo-Van Truong. Simulated optical properties of gold nanocubes and nanobars by discrete dipole approximation. *Journal of Nanomaterials*, 2012, 2012. 57

[211] Paerhatijiang Tuersun, Taximaiti Yusufu, Adili Yimiti, and Aierken Sidike. Refractive index sensitivity analysis of gold nanoparticles. *Optik*, 149:384–390, 2017. 57

[212] E Stefan Kooij and Bene Poelsema. Shape and size effects in the optical properties of metallic nanorods. *Physical Chemistry Chemical Physics*, 8(28):3349–3357, 2006. 55, 57

[213] Kane Yee. Numerical solution of initial boundary value problems involving maxwell's equations in isotropic media. *IEEE Transactions on antennas and propagation*, 14 (3):302–307, 1966. 55, 57

[214] Montacer Dridi and Alexandre Vial. Fdtd modeling of gold nanoparticles in a nematic liquid crystal: quantitative and qualitative analysis of the spectral tunability. *The Journal of Physical Chemistry C*, 114(21):9541–9545, 2010. 57

[215] Martin O'Halloran, Raquel Cruz Conceicao, Dallan Byrne, Martin Glavin, and Edward Jones. Fdtd modeling of the breast: A review. *Progress In Electromagnetics Research*, 18:1–24, 2009. 57

[216] Jianqing Wang and Osamu Fujiwara. Fdtd computation of temperature rise in the human head for portable telephones. *IEEE Transactions on Microwave Theory and Techniques*, 47(8):1528–1534, 1999. 57

[217] Aramais R Zakharian, Jerome V Moloney, Colm Dineen, and Moysey Brio. Application of the finite-difference time-domain (fdtd) method with local grid refinement to nanostructure design. In *Integrated Optics: Devices, Materials, and Technologies IX*, volume 5728, pages 154–163. International Society for Optics and Photonics, 2005. 55

[218] PC Waterman. Matrix formulation of electromagnetic scattering. *Proceedings of the IEEE*, 53(8):805–812, 1965. 55, 58

[219] Lei Bi, Ping Yang, George W Kattawar, and Michael I Mishchenko. A numerical combination of extended boundary condition method and invariant imbedding method applied to light scattering by large spheroids and cylinders. *Journal of Quantitative Spectroscopy and Radiative Transfer*, 123:17–22, 2013. 58

[220] TA Nieminen, H Rubinsztein-Dunlop, and NR Heckenberg. Calculation of the t-

matrix: general considerations and application of the point-matching method. *Journal of Quantitative Spectroscopy and Radiative Transfer*, 79:1019–1029, 2003. 58

[221] Michael I Mishchenko, Larry D Travis, and Andrew A Lacis. *Scattering, absorption, and emission of light by small particles.* Cambridge university press, 2002. 55, 58

[222] Vivek Sharma, Kyoungweon Park, and Mohan Srinivasarao. Colloidal dispersion of gold nanorods: Historical background, optical properties, seed-mediated synthesis, shape separation and self-assembly. *Materials Science and Engineering: R: Reports*, 65(1-3):1–38, 2009. 60

[223] RJ Smith, Michael Geoffrey Somekh, SD Sharples, MC Pitter, I Harrison, and C Rossignol. Parallel detection of low modulation depth signals: application to picosecond ultrasonics. *Measurement science and technology*, 19(5):055301, 2008. 112

[224] Rigoberto Juarez-Salazar, Ceciibet Mendoza-Rodriguez, Jose E Hernandez-Beltran, and Carlos Robledo-Sanchez. How do phase-shifting algorithms work? *European Journal of Physics*, 39(6):065302, 2018. 112

[225] Richard J Smith. *How to GDSII for EBeam.* http://optics.eee.nottingham.ac.uk/wiki/How_to_GDSII_for_EBeam, 2017. Accessed: 2017-02-30. 123, 134

[226] Archana Kaliyaraj Selva Kumar, Yifei Zhang, Danlei Li, and Richard G Compton. A mini-review: How reliable is the drop casting technique? *Electrochemistry Communications*, 121:106867, 2020. 130

[227] Hua Ai, Steven A Jones, and Yuri M Lvov. Biomedical applications of electrostatic layer-by-layer nano-assembly of polymers, enzymes, and nanoparticles. *Cell biochemistry and biophysics*, 39(1):23–43, 2003. 131, 184

[228] Michael J McShane and Yuri M Lvov. Electrostatic self-assembly: layer-by-layer. In *Dekker encyclopedia of Nnanoscience and nanotechnology*, pages 1342–1358. CRC Press, 2014. 131

[229] NanoBeam. *NanoBeam nB5.* http://www.nanobeam.co.uk/index.php?option=com_content&view=article&id=26&Itemid=48. Accessed: 2018-05-18. 134, 184

[230] Falco CMJM van Delft. Bilayer resist used in e-beam lithography for deep narrow structures. *Microelectronic engineering*, 46(1-4):369–373, 1999. 136, 219

[231] Won Il Choi, Abhishek Sahu, Young Ha Kim, and Giyoong Tae. Photothermal cancer therapy and imaging based on gold nanorods. *Annals of biomedical engineering*, 40 (2):534–546, 2012. 213

[232] Xiaohua Huang, Ivan H El-Sayed, Wei Qian, and Mostafa A El-Sayed. Cancer cell imaging and photothermal therapy in the near-infrared region by using gold nanorods. *Journal of the American Chemical Society*, 128(6):2115–2120, 2006. 216

[233] Naseer Ullah Khan, Jing Lin, Muhammad Rizwan Younas, Xukun Liu, and Liming Shen. Synthesis of gold nanorods and their performance in the field of cancer cell imaging and photothermal therapy. *Cancer Nanotechnology*, 12(1):1–33, 2021. 214, 215

[234] Wencai Xu, Teng Luo, Ping Li, Chuanqing Zhou, Daxiang Cui, Bo Pang, Qiushi Ren, and Shen Fu. Rgd-conjugated gold nanorods induce radiosensitization in melanoma cancer cells by downregulating $\alpha v \beta 3$ expression. *International Journal of Nanomedicine*, 7:915, 2012. 216

[235] Sihua Yang, Fei Ye, and Da Xing. Intracellular label-free gold nanorods imaging with photoacoustic microscopy. *Optics express*, 20(9):10370–10375, 2012. 213

[236] Xin Shi, Hannah L Perry, and James DET Wilton-Ely. Strategies for the functionalisation of gold nanorods to reduce toxicity and aid clinical translation. *Nanotheranostics*, 5(2):155, 2021. 215

[237] Christin Grabinski, Nicole Schaeublin, Andy Wijaya, Helen D'Couto, Salmaan H Baxamusa, Kimberly Hamad-Schifferli, and Saber M Hussain. Effect of gold nanorod surface chemistry on cellular response. *ACS nano*, 5(4):2870–2879, 2011. 215, 216

[238] Sundus Jabeen Amina and Bin Guo. A review on the synthesis and functionalization of gold nanoparticles as a drug delivery vehicle. *International journal of nanomedicine*, 15:9823, 2020. 215

[239] G Invitrogen. Cell culture basics. life technologies. 2014. 215

[240] Curtis ASG. The mechanism of adhesion of cells to glass. *Journal of Cell Biology*, 20(2):199–215, 1964.

[241] Ephraim Yavin and Ziva Yavin. Attachment and culture of dissociated cells from rat embryo cerebral hemispheres on polylysine-coated surface. *The Journal of cell biology*, 62(2):540, 1974. 215

[242] Shahed Behzadi, Vahid Serpooshan, Wei Tao, Majd A Hamaly, Mahmoud Y Alka-wareek, Erik C Dreaden, Dennis Brown, Alaaldin M Alkilany, Omid C Farokhzad, and Morteza Mahmoudi. Cellular uptake of nanoparticles: journey inside the cell. *Chemical Society Reviews*, 46(14):4218–4244, 2017. 215

[243] Anna Lesniak, Anna Salvati, Maria J Santos-Martinez, Marek W Radomski, Kenneth A Dawson, and Christoffer Åberg. Nanoparticle adhesion to the cell membrane and its effect on nanoparticle uptake efficiency. *Journal of the American Chemical Society*, 135(4):1438–1444, 2013.

[244] Nathan D Donahue, Handan Acar, and Stefan Wilhelm. Concepts of nanoparticle cellular uptake, intracellular trafficking, and kinetics in nanomedicine. *Advanced drug delivery reviews*, 143:68–96, 2019. 215

[245] Scott J Rodig. Fixing attached cells for staining. *Cold Spring Harbor Protocols*, 2020 (8):pdb–prot099689, 2020. 215

[246] C Voisin, Dimitrios Christofilos, N Del Fatti, and F Vallée. Environment effect on the acoustic vibration of metal nanoparticles. *Physica B: Condensed Matter*, 316: 89–94, 2002. 217

[247] https://betterexplained.com/articles/understanding-the-birthday-paradox/. Accessed: 2018-12-01. 229